Design, finite element analysis and experimental testing of a customised instrumented humeral component prototype for a total elbow prosthesis to measure the 6 degree of freedom elbow joint reaction forces in vitro.

By

Marim Basiouny

A thesis submitted in fulfilment of the requirements for the degree of

Doctor of Philosophy (PhD)

In

Biomedical Engineering

Division of Surgery and Interventional Science

University College of London (UCL)

Date of Submission: 29 January 2025

Declaration

I, Marim Basiouny, confirm that the work presented in this thesis is my own.

This thesis is submitted in fulfilment of the requirements for the degree of Doctor of Philosophy at University College London (UCL). Except where explicitly acknowledged, the research and findings contained herein are the result of my independent work and have not been submitted, in whole or in part, for any other degree or qualification at this or any other institution.

All sources of information and contributions from others have been appropriately acknowledged, and any collaborative work or assistance has been fully disclosed. This thesis adheres to UCL's regulations regarding academic integrity and ethical research conduct.

Abstract

Total Elbow Arthroplasty (TEA) is an effective procedure for restoring elbow function in patients with conditions like rheumatoid arthritis, complex fractures, and joint instability. However, TEA exhibits a lower long-term survival rate than other joint arthroplasties, often due to complications like aseptic loosening and mechanical failure. This is often caused by the complex forces acting on the elbow during activities of daily living (ADLs).

Although previous studies have proposed load thresholds to mitigate TEA failure, direct in vivo measurements of joint forces during ADLs remain unavailable. Existing computational models are limited by assumptions that oversimplify muscle dynamics and joint kinematics, leaving a gap in our understanding real-world joint loading.

This thesis presents the development and early-stage validation of a novel prototype: an instrumented humeral component for TEA capable of measuring elbow joint reaction forces and moments across six degrees of freedom during ADLs. A modified Titanium (Ti-6Al-4V) humeral implant was designed with integrated instrumentation and subjected to mechanical fatigue testing to assess its structural durability. Calibration was performed across all six degrees of freedom, followed by in vitro validation under simulated physiological loading conditions.

The results demonstrate that the prototype implant can reliably capture joint forces and moments under controlled conditions, providing a proof of concept for future in vivo applications. This work represents a foundational step toward enabling real-time force monitoring in TEA, with the long-term goal of improving implant design, surgical decision-making, and patient outcomes.

Impact Statement

The lack of accurate, direct data acting on the elbow joint, particularly during activities of daily living (ADL) has hindered effective implant design, leading to complications like aseptic loosening in Total Elbow Arthroplasty (TEA). This study introduces a first-generation prototype of an instrumented humeral component designed to measure in vivo elbow joint reaction forces during activities of daily living (ADLs). Although in its early stages, this development has the potential to generate valuable biomechanical data on force magnitude, direction, and load distribution, offering new insights into stress patterns previously unquantified in the elbow joint.

Clinical Practice: This early-stage technology has the potential to significantly enhance surgical planning by enabling more informed implant selection based on patient-specific biomechanical needs. By providing real-world joint loading data, it may help reduce complications such as aseptic loosening and periprosthetic fractures. The data could also inform more personalised rehabilitation strategies, supporting faster recovery and long-term implant success.

Implant Design: Current prostheses are largely informed by theoretical models and cadaveric studies, which do not fully capture the dynamic forces experienced during daily activities. The data generated in this study may inform the design of more durable, functional, and patient-specific implants, better equipped to withstand real-life loading and reduce revision rates.

Biomechanical Understanding: This research addresses the current gap in in vivo elbow joint force data. The findings will contribute to validating and refining existing biomechanical models, allowing for more accurate simulations. A deeper

understanding of joint mechanics and muscle–implant interactions may help identify key factors in implant failure and inform preventative strategies.

Public Health: By supporting the development of more reliable implants and evidence-based rehabilitation, this research could ultimately reduce the need for costly and invasive revision surgeries. Enhancing implant performance and durability has the potential to improve patients' quality of life and reduce the burden on healthcare systems.

Future Research and Development: The prototype implant developed in this study lays the groundwork for future investigations into elbow joint biomechanics. It offers a platform for advanced modelling, regulatory development, and iterative design improvements in TEA. This foundational work can support the establishment of evidence-based clinical and engineering standards in the field.

In summary, this early-stage research introduces a novel instrumented implant with the potential to advance clinical practice, implant design, and biomechanical modelling. By generating previously unavailable in vivo data, it sets the stage for future improvements in patient care, research, and surgical outcomes.

Acknowledgements

First, I would like to express my gratitude to my supervisor, Professor Stephen Taylor, for his invaluable guidance and support throughout this research. His expertise and insights have been fundamental in shaping this thesis. I am also grateful to my secondary supervisors, Dr. Sara Ghoreishizadeh, Professor Mehran Moazen, and Professor Jia Hua, for their constructive feedback and mentorship.

I extend my sincere thanks to Mr. Simon Lambert and Mr. Kuen Chin for their significant contributions to this research. Their expertise and involvement in conducting part of the experiments were vital to the success of this project. I am also grateful to Jose Gorjon for developing the implant PCB and GUI instrumentation, both of which were critical components of this work. I am deeply appreciative of their time, support, and collaboration throughout the process.

I extend my heartfelt thanks to my colleagues and friends, whose insightful discussions and steadfast support have been a constant source of inspiration and motivation. I am profoundly grateful to my family for their unwavering love, patience, and sacrifices, which have been my anchor throughout this journey. To my parents, for their constant belief in me, encouragement, and understanding during the challenging moments - I could not have done this without you!

UCL Research Paper Declaration Form

Chapter 4

Please use this form to declare if parts of your thesis are already available in another format, e.g. if data, text, or figures:

- *have been uploaded to a preprint server*
- *are in submission to a peer-reviewed publication*
- *have been published in a peer-reviewed publication, e.g. journal, textbook.*

This form should be completed as many times as necessary. For instance, if you have seven thesis chapters, two of which containing material that has already been published, you would complete this form twice.

1. For a research manuscript that has already been published (if not yet published, please skip to section 2)

a) What is the title of the manuscript?

Fatigue test evaluation of a customised humeral component for an instrumented total elbow prosthesis and strain validation study

b) Please include a link to or doi for the work

https://doi.org/10.1016/j.medengphy.2025.104311

c) Where was the work published?

Medical Engineering & Physics

d) Who published the work? (e.g. OUP)

Elsevier

e) When was the work published?

24/02/2025

f) List the manuscript's authors in the order they appear on the publication

Marim Basiouny, Simon Lambert, Chin Kuenfoo, Stephen Taylor

g) Was the work peer reviewed?

Yes

h) Have you retained the copyright?

Yes

i) **Was an earlier form of the manuscript uploaded to a preprint server? (e.g. medRxiv). If 'Yes', please give a link or doi)**

Click or tap here to enter text.

If 'No', please seek permission from the relevant publisher and check the box next to the below statement:

☐

*I acknowledge permission of the publisher named under **1d** to include in this thesis portions of the publication named as included in **1c**.*

2. For multi-authored work, please give a statement of contribution covering all authors (if single-author, please skip to section 4)

Marim Basiouny: Conceptualisation, Investigation, Writing – original draft, Writing – review & editing.
Simon Lambert: Writing – review & editing
Chin Kuenfoo: Writing – review & editing
Stephen Taylor: Writing – review & editing

3. In which chapter(s) of your thesis can this material be found?

Chapter 4

4. e-Signatures confirming that the information above is accurate (this form should be co-signed by the supervisor/ senior author unless this is not appropriate, e.g. if the paper was a single-author work)

Candidate

Marim Basiouny

Date:

29/01/2025

Supervisor/ Senior Author (where appropriate)

Stephen Taylor

Date

29/01/2025

Table of Contents

List of Abbreviations

ADC	-	Analog-to-Digital Converter
ADL	-	Activities of Daily Living
CNC	-	Computer Numerical Control
d.o.f	-	Degree of Freedom
DES	-	Discovery Elbow System
FBD	-	Free Body Diagram
FEA	-	Finite Element Analysis
FMR	-	Force Magnification Ratio
FOS	-	Factor of Safety
GUI	-	Graphical User Interface
JRF	-	Joint Reaction Force
PCB	-	Printed Circuit Board
SG	-	Strain Gauge
TEA	-	Total Elbow Arthroplasty
TER	-	Total Elbow Replacement
THA	-	Total Hip Arthroplasty
Ti-6Al-4V	-	Titanium Alloy Grade 5
TKA	-	Total Knee Arthroplasty
VV	-	Varus- Valgus

List of Figures

Chapter 1: Introduction

1.1. Background and Problem Statement

Total Elbow Arthroplasty (TEA) is a surgical procedure designed to restore elbow function by replacing the joint surfaces with a prosthetic implant, either partially or entirely. TEA was initially designed to treat end-stage rheumatoid arthritis of the elbow joint, which is a chronic inflammatory autoimmune condition that primarily affects the synovial membrane (Dee, 1972). However, TEA has evolved alongside the advancements in our understanding of elbow pathology. The introduction of several different types of elbow prosthesis has broadened the indications for TEA to include acute comminuted irreparable distal humerus fractures in the elderly, as well as post-traumatic sequelae such as arthritis and instability of the joint (Kholinne et al., 2020). This makes TEA a versatile solution for patients suffering from significant loss of elbow function due to conditions such as arthritis, fractures, or other degenerative disorders, ultimately aiming to restore function and relieve pain for a wider range of patients. While TEA has been effective in providing pain relief and enhancing elbow stability, its survival rate stands at a comparatively lower rate of 79.2%, in contrast to the 10-year survival rates of 95% for total hip arthroplasty (THA) and 90% for total knee arthroplasty (TKA) (Welsink et al., 2017). Recent studies continue to show that total elbow arthroplasty (TEA) carries a relatively high risk of postoperative complications. A meta-analysis of 2,374 patients with rheumatoid arthritis undergoing TEA reported an overall complication rate of 31.6%, with a surgical site infection rate of 3.4% (Zhao et al., 2023). In the early postoperative period, national surgical database studies show that the 30-day complication rate following primary TEA is approximately 9.5%, with reoperation (4.0%) and readmission (5.1%) as the

most common events (Nguyen et al., 2023). For revision TEA, the 30-day complication rate rises to 13.9%, including surgical site infections (3.8%) and reoperation (1.9%) (Wasserman et al., 2024). These figures reflect both the technical complexity and higher failure burden associated with elbow arthroplasty compared to other joints. Common complications include infection, aseptic loosening, and periprosthetic fracture, all of which may necessitate revision surgery, with aseptic loosening being the primary reason for such interventions. Revision surgery is often more complex, associated with increased bone and soft tissue trauma, and tends to yield worse outcomes compared to primary TEA (Kuen & Lambert, 2021).

The elbow joint, although not a weight-bearing joint like the hip or knee, is still subjected to significant forces during everyday activities. These forces arise mainly from muscle contractions required to equilibrate external loads and are transmitted across a small contact area within the joint. The complex muscle actions surrounding the elbow generate considerable compressive forces due to the small lever arms of muscles that must counteract external loads (Morrey & An, 1983). These forces can be significant on the joint because even minor external torques require large internal muscle forces for equilibrium. For instance, even seemingly simple tasks, such as rising from a chair or steering a car, can generate significant loads on the elbow, despite not involving external weights (Schwab et al., 1980).

Understanding the magnitude of real-world forces acting on the elbow joint during activities of daily living (ADL) is vital for several reasons. First, accurate measurements of these forces are essential in determining the wear rates of elbow implant materials. Research has revealed that joint loads of approximately

110 N weight in hand (WIH) or more are sufficient to cause wear and damage to the elbow prosthetic components (Varadarajan & Kincaid, 2019).

Second, excessive joint forces have been shown to lead to micromotion between the implant and bone, increasing the risk of aseptic loosening, which is the leading cause of total elbow replacement (TER) failure. It was found that posteriorly directed forces contributed to humeral stem loosening in the GSB III prosthesis, while the Kudo Type V prosthesis exhibited better humeral osseointegration, though its ulnar component failed due to load transfer in the ulna bone-prosthesis interface (Kodama et al., 2017). Moreover, in unlinked prostheses, loosening occurred due to multi-axial forces at implant-cement interfaces (Morrey et al., 1993), while non-anatomical forces from ligament deficiencies and radial head resection were also found to increase eccentric loads on elbow hinges, causing stem loosening and TER failure.

Third, accurate force data is crucial in surgical planning because it allows for more precise and tailored decision-making in implant selection, positioning, surgical approaches, and rehabilitation protocols, all of which help reduce the risk of complications such as implant loosening or failure. By understanding the forces that act on the elbow joint during normal activities, surgeons can choose implants that are better equipped to withstand the stresses of daily use, thus improving long-term implant success. Additionally, this data also guides the customisation of implants to align with the unique biomechanics of individual patients, thereby enhancing both the function and longevity of the implant.

Finally, the absence of recognised international standards for assessing the risks to durability of total elbow replacements (TER) highlights the pressing need for in vivo force data. Such data are essential not only for validating biomechanical models of elbow joint loading but also for ensuring their accuracy in replicating

real-world conditions. Overloading the prosthesis during daily activities has been identified as a leading cause of total elbow arthroplasty (TEA) failure (Goldberg et al., 2008; lo & Lipman, 2009). Although some studies have proposed specific load thresholds that should not be exceeded to prevent TEA failure, the actual in vivo forces experienced by patients during activities of daily living (ADL) remain largely unknown. Without this knowledge, we must rely on limited data from models that have proven inadequate, often relying on assumptions and simplifications that fail to capture the dynamic nature of muscle actions and joint movements. Consequently, they can produce inaccurate estimates of joint forces, potentially leading to suboptimal clinical outcomes and inadequate rehabilitation guidelines. This thesis aims to address this issue by developing an instrumented elbow implant prototype capable of measuring all six degrees of freedom around the elbow hinge during real-life activities. As an early-stage design, this prototype will require further iterations, reproducibility testing, and refinement before it can be considered for human testing. By providing fundamental biomechanical force data, this research seeks to improve the understanding of elbow joint function.

Such physiological data, previously not measured in vivo, will be recorded and utilised to achieve three key objectives: (1) validate existing theoretical musculoskeletal models of elbow biomechanics; (2) enhance our understanding of elbow joint function, thereby improving rehabilitation programmes and daily activities to promote patient independence; and (3) provide fundamental data to guide the optimal redesign and testing of elbow implants.

1.2. Research Aims and Objectives

1.2.1. Aims

This doctoral thesis aims to develop the first-of-its-kind customised instrumented humeral component prototype for a total elbow prosthesis capable of measuring the six degree of freedom elbow joint reaction forces in vivo during normal activities of daily living (ADL). This instrumented elbow prototype will provide fundamental biomechanical force data that can be used to validate existing theoretical musculoskeletal models of elbow biomechanics, enhance the understanding of elbow joint function, inform surgical planning and procedures, and guide the optimal redesign and testing of elbow implants.

1.2.2. Objectives

The main objectives of this research study are twofold: the design and development of a customised humeral component prototype and instrumentation, and the preclinical testing of the instrumented humeral implant. The specific objectives are as follows:

1. Design and manufacture a modified Titanium (Ti-6Al-4V) elbow humeral component prototype suitable for housing implant instrumentation (Chapter 3).
2. Identify optimal strain gauge locations based on the strain distribution pattern observed on the implant (Chapter 3).
3. Develop humeral implant instrumentation (PCB circuit) and install the strain gauges (Chapter 3).
4. Evaluate the safety of the newly modified humeral component prototype under peak anticipated loads through an experimental fatigue test, while

also reporting and validating the measured implant strains against those predicted by finite element analysis (FEA) (Chapter 4).

5. Calibrate all six degrees of freedom of the instrumented humeral component and apply the matrix method to develop a calibration sensitivity matrix for the measurement of the three forces and three moments acting on the elbow joint (Chapter 5).
6. Perform total elbow arthroplasty (TEA) on a synthetic bone model to validate the functionality and performance of the instrumented humeral implant prototype in measuring the forces and moments acting on the elbow joint (Chapter 6).
7. Conduct an in vitro biomechanical study validating the six degrees of freedom measured by the calibrated instrumented humeral implant under simulated physiological loading conditions and comparing these measurements against modelled values for accuracy (Chapter 6).

1.3. Research Motivation and Rationale

The motivation behind this research stems from the absence of in vivo force data on elbow joint forces. Unlike other major joints, such as the hip, knee and shoulder, no direct in vivo measurements of elbow joint forces have been made to date. This project seeks to address this significant gap through this first-in-human study by developing an instrumented humeral component for a total elbow prosthesis to enable the direct measurement of elbow joint reaction forces in vivo during activities of daily living (ADL). There is also a pressing need for better elbow implant designs, as current total elbow arthroplasty (TEA) procedures face high complication rates, including aseptic loosening and periprosthetic fractures. The real-time data generated from this study will serve as a gold standard for

assessing implant durability, offering crucial evidence for the creation of more effective and durable elbow prostheses. Through these direct in vivo measurements, this research has the potential to revolutionise clinical practice and implant design, ultimately setting a new standard for elbow joint replacements and improving patient outcomes.

The health of bones and joints is significantly influenced by the forces they experience, and direct in vivo measurement is recognised as the most accurate means of assessing these forces over time and during activity. While musculoskeletal models are valuable for their flexibility and non-invasiveness, their inherent simplifications can lead to errors. For example, hip joint force models have been shown to significantly overestimate actual values (Heller et al., 2001; Li, 2021; Mellon et al., 2015). Although lower limb forces are well understood, the biomechanics of the elbow remain poorly characterised, leading to uncertainty in designing implants for longevity. Therefore, by generating real-time in vivo force data, this research will provide critical insights into the elbow joint mechanics, the distribution of stresses across bones and soft tissues, and how these forces are influenced by joint replacement.

Aseptic loosening continues to be a leading cause of failure in elbow arthroplasty. Previously published data on joint reaction forces have relied on mathematical calculations based on cadaveric muscle measurements, which can be prone to error due to strict boundary conditions. In our group's case series of the Discovery (LIMA Corporate S.p.A. Italy), elbow arthroplasty, we found (unpublished results) that failures of the humeral component were causally related to rotational malalignment of the ulnar component, possibly with insufficient humeral cementation, which induced sagittal torque on the humeral component thus

contributing to loosening. This is an issue detectable only through in vivo measurement.

The Discovery elbow implant which forms the basis for developing a modified instrumented version of its humeral implant stem in this project, is regarded as one of the more reliable designs currently in use. According to the UK National Joint Registry (NJR) 2025 data, the Discovery implant has a mean 5-year revision rate of approximately 7.76%, based on 1,244 procedures performed between 2012 and 2025. This places it among the better-performing implants, alongside the Coonrad-Morrey, which has a 5.9% mean 5-year revision rate from 2,307 procedures, and the Latitude implant, with a 7.22% revision rate based on 1,899 procedures over the same period. The GBS 111 shows a revision rate of 10.19% but is based on a much smaller cohort of 53 procedures recorded between 2012 and 2019, which limits the comparability of its data (National Joint Registry (NJR), 2025).

The Discovery system incorporates several design features aimed at reducing mechanical failure. The titanium humeral stem is engineered with an anterior flange, an articulating region-stem offset, and a sagittal curve that mimic the shape and orientation of the humeral intramedullary canal. The semi-constrained humero-ulnar linkage comprises large cobalt-chrome humeral hemispherical condylar surfaces connected by a central cylindrical bar linking with a compression-moulded ulnar polyethylene bearing having concave surfaces. Finite element analysis has shown that this “hour-glass” articulation produces lower von Mises stress than traditional cylindrical designs (Nishida et al., 2014). The anterior humeral flange is designed to lie against the anterior humerus without requiring interposed bone graft, thus resisting the sagittal bending moment that contributes to aseptic loosening.

A study from the Norwegian Joint Registry reported a 5-year survival rate of 95% among 190 Discovery TERs (Krukhaug et al., 2018), indicating that the anatomical features of the implant and condylar articulation mechanism have reduced the incidence of mechanical failure. Furthermore, this implant design is the preferred choice among the surgeons involved in this study, which supports its selection as the basis for the present project. By using this implant in our study, we aim to modify the humeral implant stem to accommodate implant instrumentation.

1.4. Significance and Impact

Currently, there is no published work on in vivo measurements of elbow joint reaction forces, and we are not aware of any ongoing research studies in this area. Existing literature primarily relies on mathematical modelling, which is subject to assumption bias and may not accurately reflect real-life conditions. Although there is interest in developing a short-stem, bone-conserving humeral implant, there is insufficient data to support iterative design improvements. Most advancements in implant design have been driven by lessons learned from clinical failures. This study will be the first to generate real-time in vivo force and moment data during activities of daily living, providing valuable insights to inform future implant design and enhance clinical practice.

The work in this thesis will lead to the development of an instrumented implant prototype that will allow in vivo elbow joint reaction force measurement. The data collected from these measurements will make it possible to understand the direction and magnitude of loading in an elbow replacement during typical ADL. The data and results will contribute to the evolution of a bone-conserving load-sharing implant which can safely resist the mechanical load generated at the

elbow and create a stress profile at the bone-implant interface that promotes osteointegration of an uncemented implant.

1.5. Future Directions for Clinical Study

This doctoral research forms part of a broader project aimed at developing a system for direct measurement of elbow joint forces. The work presented in this thesis focuses on the initial design concept, finite element analysis (FEA), development of implant instrumentation, and mechanical and biomechanical testing of a prototype humeral implant. At this stage, the implant remains an early prototype and will require further development, including design modifications, repeat testing, and validation of reproducibility, before it can be considered for use in a clinical setting. Subject to the successful completion of these steps, this work could support the production of a small batch of refined prototypes for future feasibility studies. These would be sterilised using ethylene oxide to ensure they are free from microbial contamination, which is critical for patient safety. As with all joint replacements, any future implantation would require long-term follow-up. In the initial year following surgery, in vivo joint forces would be measured during a range of everyday activities, using wearable motion capture devices and patient-reported outcome measures. Ethical and regulatory approval will be sought from the relevant institutional review boards and the Health Research Authority (HRA), and participants meeting defined inclusion criteria for total elbow replacement (TER) would be recruited into the study.

1.6. Thesis Structure

This thesis comprises seven chapters with a brief overview of each chapter provided below:

Chapter 1: Introduction

This chapter provides background context for the research, outlining the current state of knowledge in elbow joint biomechanics and the significance of measuring in vivo elbow joint forces. It clearly states the research aims and objectives along with insights into the next steps of this research work.

Chapter 2: Background and Literature Review

This chapter introduces the anatomy and movement of the human elbow joint. A concise history of elbow implant designs is introduced, highlighting the significance and importance of understanding the magnitude of elbow joint forces. It reports the current utilisation rates of elbow arthroplasty; the impact on the quality of life of patients undergoing elbow arthroplasty is outlined.

Chapters 3-6 detail the technical contributions of this thesis.

Chapter 3: Design, Development and Finite Element Analysis (FEA) of a Prototype Humeral Component

This chapter proposes a modified design of a customised humeral component prototype suitable to house the necessary telemetry instrumentation and strain gauges. In this chapter, the finite element modelling and analysis (FEA) used to determine the optimal locations for the strain gauges is described. Additionally, the chapter outlines the development stages of the implant instrumentation including a customised printed circuit board (PCB).

Chapter 4: Fatigue Test Evaluation of a Prototype Humeral Component for an Instrumented Total Elbow Prosthesis and Strain Validation Study

This chapter describes the mechanical assessment of the safety (durability and reliability) of the modified humeral component under peak anticipated loads using an experimental fatigue test study.

Chapter 5: Calibration of a Customised Humeral Component Prototype for an Instrumented Total Elbow Prosthesis

This chapter describes the development of a method for calibrating the instrumented elbow humeral stem across the six degrees of freedom for measurement of joint reaction forces using a single point axial load and a torque generating rig.

Chapter 6: In Vitro Measurement of Elbow Forces Using a Calibrated Prototype Implant – A Preliminary Biomechanical Study

This chapter describes an in vitro biomechanical study conducted to validate the functionality and performance of the instrumented humeral implant prototype in measuring forces and moments acting on the elbow joint during total elbow arthroplasty (TEA) on a synthetic bone model. The study focuses on two main objectives: (1) measuring the six degrees of freedom measured by the calibrated implant using strain gauge data under simulated physiological loading, and (2) validating the three forces and three moments during typical activities of daily living (ADL) against a simple free body ulnar component model and discussing possible reasons for any discrepancies. This work represents a key step in the iterative development and validation process of the implant prior to any in vivo applications.

Chapter 7: Discussion and Conclusion

This chapter summarises, discusses, critically evaluates the product of each chapter, and makes recommendations for future research directions.

Chapter 2: Background and Literature Review

2.1. Introduction

The elbow joint functions as an anatomical link between the upper extremity, connecting the shoulder and wrist. It has developed to allow for a wide range of motion, which is necessary for performing complex tasks. When its function is impaired, it can significantly interfere with the ability to carry out simple everyday activities and may even cause severe disability. Unlike restrictions in shoulder and wrist movement, limitations in elbow function can have a more significant impact an individual's overall quality of life. The distinct biomechanics of the elbow joint are essential in executing daily activities, which make its unrestricted movement particularly important in day-to-day living. Therefore, when assessing the impact of musculoskeletal problems, it is crucial to maintain optimal elbow functionality to ensure completion of daily tasks (Angst et al., 2005)

Flexion/extension and pronation/supination are two well-known degrees of freedom for the elbow joint. However, there is also a potential third degree of freedom called varus/valgus, which allows for a very small movement. Research has shown that most daily activities can be accomplished within a range of 30 to 130 degrees of flexion (Morrey et al., 1978). Similarly, in pronation/supination, a range of 100 degrees of rotation (50 degrees of pronation and 50 degrees of supination) is typically sufficient for most daily activities (Morrey et al., 1978). When the range of motion of the elbow becomes limited, a combination of medications and physiotherapy is often used to alleviate pain and improve mobility. However, if the range of motion falls below 100 degrees in flexion-extension, surgical intervention is often necessary. This is because a loss of 50% of elbow mobility corresponds to an 80% loss of upper limb function (Filho &

Galvão, 2010). In such cases, total elbow arthroplasty (TEA) is an appropriate treatment to relieve pain and improve range of motion.

Total Elbow Arthroplasty (TEA) is a versatile solution for patients experiencing significant loss of elbow function, in which part or the entire elbow joint is replaced with an implant in order to restore elbow function. While TEA provides satisfactory pain relief and restores elbow stability, there is a relatively high failure rate, with reported complications ranging between 11% and 38% (Welsink et al., 2017). The incidence of total elbow arthroplasty (TEA) has undoubtedly declined over the past 30 years, primarily due to advances in the medical management of rheumatoid arthritis and other inflammatory conditions, which have significantly reduced the need for surgical intervention. However, in the past 10 years, there has been a modest increase in the numbers of TEA procedures for cases of primary and secondary osteoarthritis including trauma as well as revision surgeries (National Joint Registry (NJR), 2025). The use of TEA appears to be increasing at a rate of 8% annually, driven by its growing popularity among younger patients with higher demands (Triplet et al., 2016).

The elbow joint, although not involved in weight-bearing, is still subjected to significant force during daily activities. These forces, which are primarily caused by muscle actions, are transmitted through a small surface area. The complex muscles surrounding the joint exert a substantial compressive force on it. It has been hypothesised in the literature that overloading the prosthesis during activities of daily living (ADL) can lead to the failure of TEA (Goldberg et al., 2008; Io & Lipman, 2009). Some studies have reported specific elbow load values that should not be exceeded after TEA in order to prevent failure. However, it is currently unknown how these findings impact clinical practice with TEA patients because the actual elbow loads experienced by patients during ADL are not well-

established. Daily tasks can result in high loads and stresses on the elbow, depending on the weight being lifted and the specific movement (King et al., 2019). Additionally, not all tasks involve external weight but still require load on the elbow, such as rising from a chair or steering a car.

To better understand the mechanics of the elbow, it is necessary to briefly explore the anatomy of the joint and its relevance to musculoskeletal treatment of the elbow.

2.2. Elbow Joint Anatomy

The human elbow serves as a fundamental joint in performing daily activities. It is responsible for hand positioning and transferring loads. Elbow injuries can severely hinder one's ability to carry out these simple tasks. In a healthy elbow, the function and range of motion are much more complex than what can be replicated in an elbow prosthesis as a fixed axis joint. Therefore, researchers must accurately measure the kinematics of the elbow which allows for six degrees of freedom.

The elbow joint permits motion and provides stability. It is composed of three primary bearing surfaces that are connected by multiple strong ligaments such as the ulnar collateral and radial collateral ligaments. The joint is operated by various intersecting muscles, including the biceps brachii, triceps brachii, and brachialis. All these structures coordinate to provide motion, transfer loads from the hand and forearm to the upper arm and maintain joint stability.

2.2.1. Bones

The elbow consists of three bones, as shown in Figure 2-1. These bones are the humerus, radius, and ulna. The humerus is the largest asymmetrical bone. It

connects to the shoulder blade at the proximal end and to the radius and ulna at the distal end. The ulna is the longer and larger of the two forearm bones. It extends from the elbow to the wrist on the side closest to the body (medial side). Finally, the radius is the shorter and slightly smaller bone of the forearm. It is positioned on the lateral side of the body extending from the elbow to the wrist.

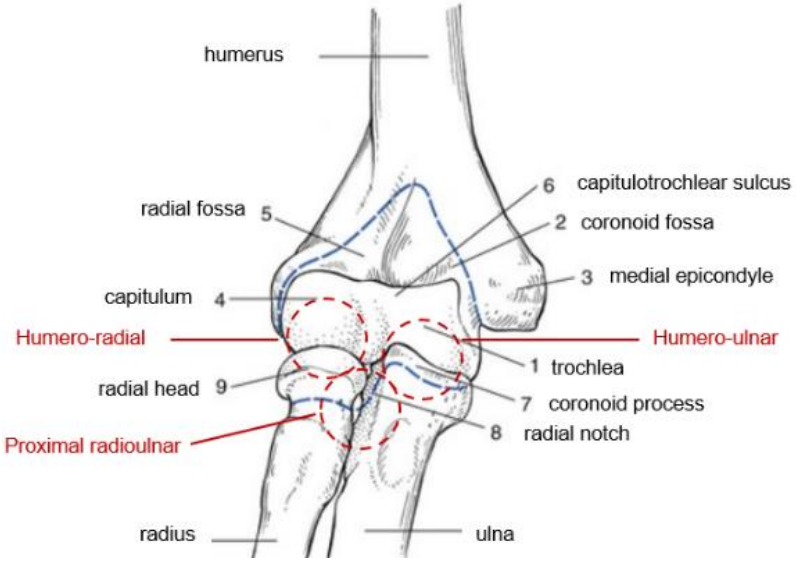

Figure 2-1: Anatomy of the elbow joint, illustrating the humero-ulnar and the humero-radial articulations (Key M, 2016).

2.2.2. Articulation

The elbow has three articulations (Figure 2-1). The first is the humero-ulna articulation, which connects the distal part of the humerus to the proximal part of the ulna. This articulation allows one degree of freedom, enabling flexion-extension movement of the elbow. Secondly, humero-radius articulation, it links the distal part of the humerus with the proximal head part of the radius. This articulation also allows for flexion-extension as well as movements of supination and pronation. The third articulation is the radius-ulna. It connects the two

proximal parts of the radial notch of the ulna and the radius, and it enables the movements of supination and pronation.

2.2.3. Joint Capsule

The joint capsule of the human elbow is a fibrous structure that encloses the elbow joint. It consists of strong, flexible connective tissue that provides stability to the joint. The capsule is composed of two layers: the outer fibrous layer and the inner synovial membrane. The outer layer is made up of dense, fibrous connective tissue. It provides structural support to the joint and helps maintain its integrity. The inner layer is a synovial membrane that produces synovial fluid. Synovial fluid lubricates the joint, reducing friction between articulating surfaces and nourishing the cartilage.

2.2.4. Ligaments

The elbow joint is held together by ligaments, which are bundles of strong, dense, and flexible connective tissue. These ligaments connect the articulating bones and help stabilize the elbow (Figure 2-2). The three ligaments of the elbow joint include the medial, lateral, and annular ligaments. The ulnar collateral ligament (UCL) is connected to the humerus bone, specifically the medial epicondyle, as well as to the medial coronoid process and olecranon on the ulna. It allows for flexion and extension movements but prevents any lateral movement of the elbow.

The radial collateral ligament (LCL) is made up of three parts; two of which extend from the lateral epicondyle of the humerus to the annular ligament, while the third part extends from the epicondyle to the lateral olecranon of the ulna. Like the UCL, it allows for flexion and extension movements but prevents any lateral movement of the elbow. The annular ligament stabilises the radius-ulnar

articulation. It is attached to the front and back of the ulna. This U-shaped ligament encircles the head of the radius to keep the radius in contact with the ulna.

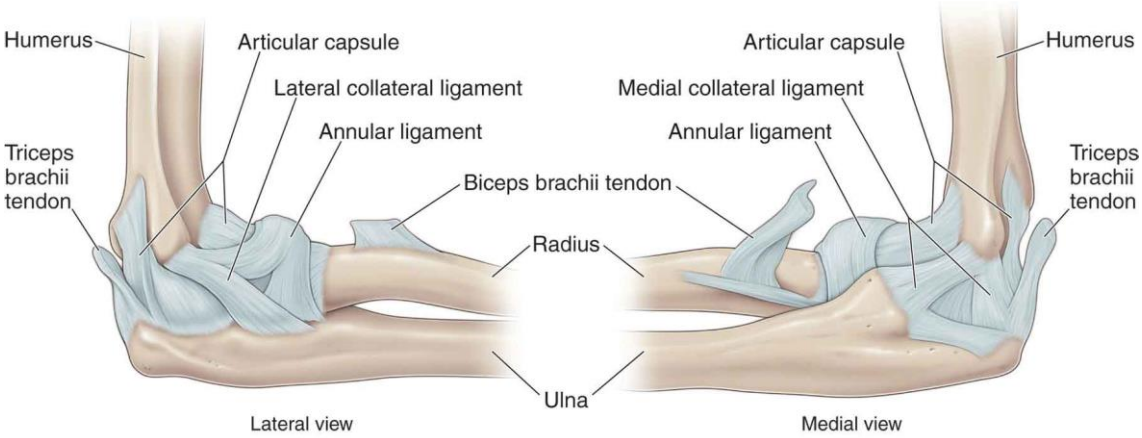

Figure 2-2: Elbow joint ligaments (Morton, 2011).

2.2.5. Muscles

The elbow joint relies on four main muscles for movement. First is the brachialis, known as the strongest elbow flexor and is located anteriorly to the arm. The biceps brachii is located superior to the brachialis, while the brachioradialis is found on the lateral side of the arm. The triceps brachii, which is the strongest elbow extensor is situated at the back of the joint (An et al., 1981) (
Table 2-1).

For movements of the radio-ulnar joint, two key pronator muscles are involved: the pronator teres which is positioned proximally to the joint, and the pronator quadratus, found at the distal end of the joint. These two muscles work along with the supinator muscle and the biceps brachii.

Table 2-1: Primary functions and movements of the elbow muscles (Fornalski, 2003).

Muscles	Primary Functions	Movements
Brachialis	Bends the forearm	Flexion
Biceps Brachii	Bi-articular muscle that helps control motion of the shoulder and elbow joint	Flexion and supination
Brachioradialis	Flexes the forearm during quick movements	Flexion and supination
Flexor Carpi Radialis	Facilitates bending and radial deviation of the wrist; weakly flexes the elbow	Flexion
Pronator Teres	Assists in flexion	Flexion and pronation
Triceps Brachii	Extends the elbow joint and stabilises it for fine movements, such as writing	Extension
Pronator Quadratus	Aids the pronator teres in pronation	Pronation
Supinator	Rotates the forearm palm upward	Supination
Biceps Brachii	Assists in controlling elbow movement	Flexion and supination

These muscles serve as both primary and secondary stabilisers for the elbow joint. The ulnohumeral joint provides bony stability, while the medial and lateral ligaments contribute to the overall stability of the elbow (Kaufmann et al., 2019).

The secondary elbow stabilisers are the flexor pronator muscles and the radiohumeral articulation Figure 2-3. These muscles stabilise the elbow dynamically while the radiohumeral articulation provides osseous constraint to valgus stress (Kaufmann et al., 2019). Finally, the elbow is also dynamically stabilised by muscles originating from the humerus Figure 2-3. The opposing forces generated by the biceps and brachialis with the triceps result in compression of the ulnohumeral joint, regardless of the weight being held or the position of the arm (Dunning et al., 2001).

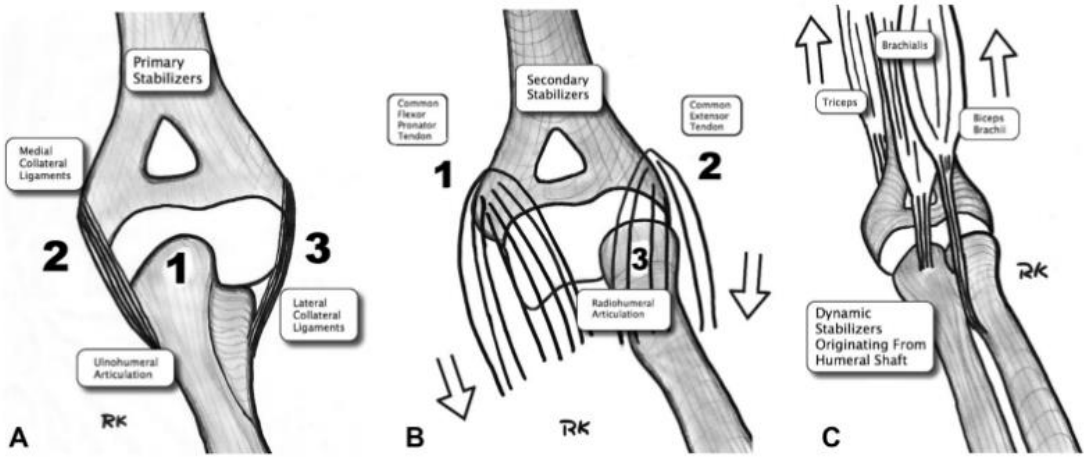

Figure 2-3: (A) Primary stabilisers of the elbow, (B) Secondary stabilisers of the elbow, (C) Dynamic stabilisers of the elbow (Kaufmann et al., 2019).

2.3. Elbow Joint Movement (Degree of Freedom)

The movement of the elbow involves two primary actions: flexion-extension and pronation-supination, along with a minor movement referred to as varus/valgus.

2.3.1. Flexion – Extension

This is the movement which consists of bending and straightening the arm. In extreme flexion, the radial head and coronoid process are in contact with the corresponding fossa of the humerus, flexing up to 150 degrees making the and

the angle between the arm and the forearm approximately 30° Figure 2-4. In extreme extension, the olecranon process is in contact with the corresponding fossa of the humerus; and the angle between the arm and the forearm is approximately 180°.

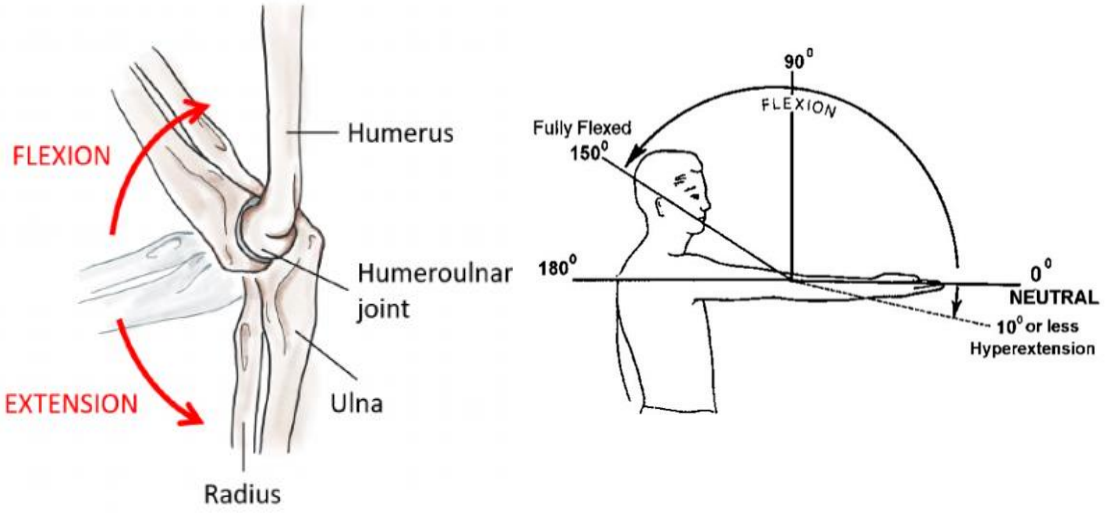

Figure 2-4: Flexion – Extension motion of the elbow joint (Morton, 2011).

2.3.2. Varus – Valgus

The elbow joint involves a very small movement known as valgus-varus. Although this movement is minor compared to others, it holds importance. Current prostheses do not accommodate for this movement.

Valgus generally means turned towards the outside Figure 2-5. In context, the movement of valgus corresponds to the movement of the forearm outwards from the plane of elbow flexion/extension. Conversely, Varus means turned towards the inside. For the elbow, the movement of varus corresponds to the forearm deviating inward from the plane of elbow flexion/extension.

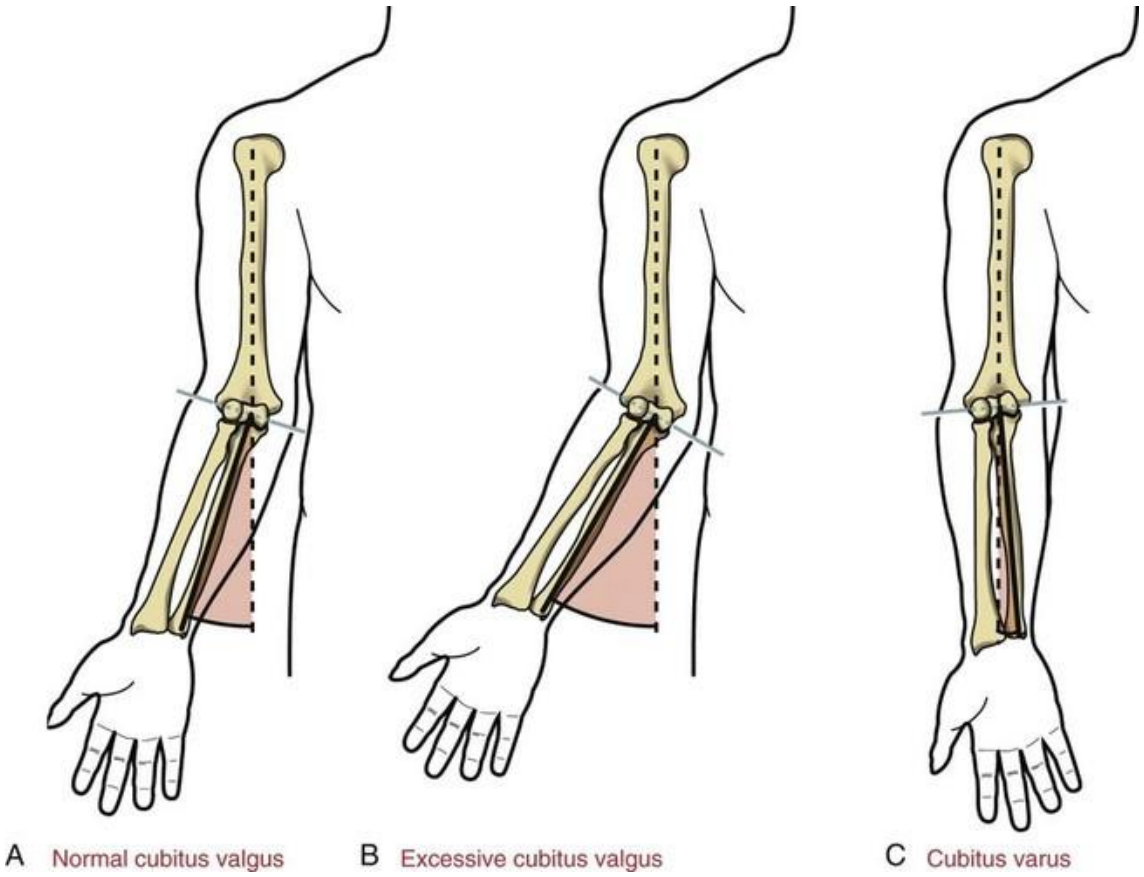

Figure 2-5: Varus – Valgus motion of the elbow joint (Neumann, 2016).

Elbow joint stability primarily relies on the collateral ligaments and the alignment of joint surfaces. These ligaments prevent excessive forearm adduction and abduction. The medial collateral ligament stabilises the joint during forearm movement away from the midline (valgus), while the radial collateral ligament ensures stability during forearm movement towards the midline (varus) (De Haan et al., 2011).

2.3.3. Pronation – Supination

This movement consists of rotating the forearm around its long axis (torsion). Pronation is the movement which makes the forearm rotate to the interior with the thumb at the interior Figure 2-6. The maximal angle of pronation is about 80°. Supination is the movement which makes the forearm rotate to the exterior with the thumb at the exterior. The maximal angle of supination is about 85°.

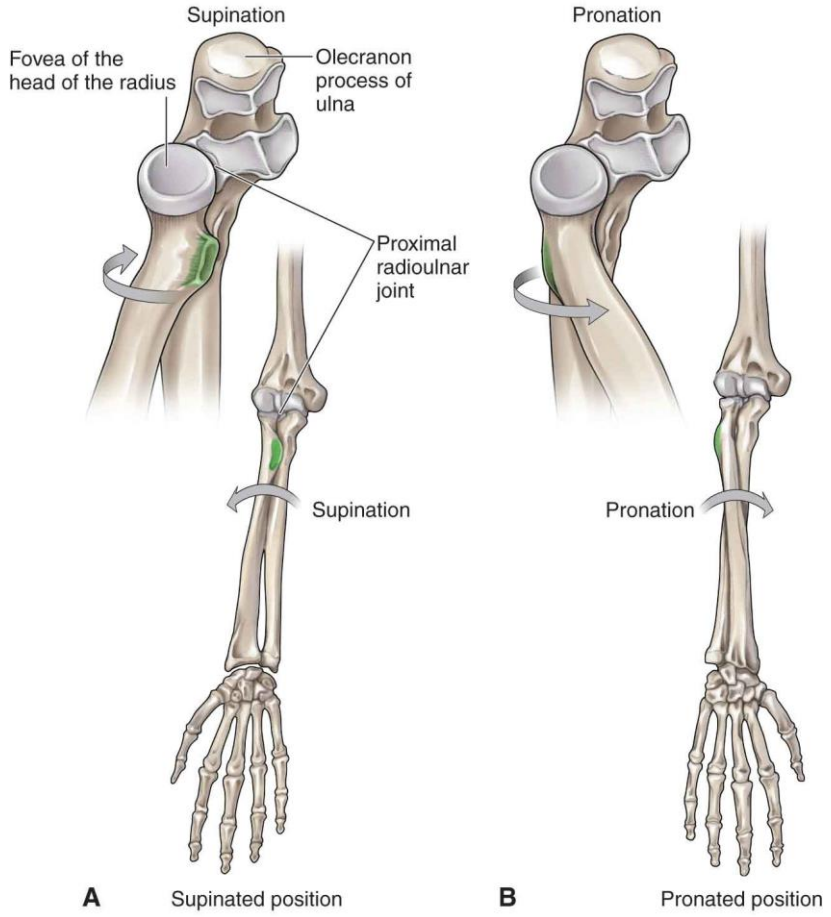

Figure 2-6: Pronation – Supination of the elbow joint (Morton, 2011).

2.4. Elbow Joint Pathology

The anatomical location of the elbow joint combined with its frequent use in various activities of daily living make the elbow joint prone to a range of acute injuries and joint diseases which often result in restricted elbow motion and pain. The most common elbow arthritis are rheumatoid arthritis, post-traumatic arthritis, instability, severe fracture, and osteoarthritis, which is classified as a degenerative joint disease characterised by the breakdown of articular cartilage and subchondral bone, typically due to mechanical wear and age-related changes (Jenkins et al., 2013).

Until the late 1990s, rheumatoid arthritis was the most predominantly diagnosed form of elbow arthritis. It is a joint disease that affects the synovium, if left

untreated, it can extend to affect the joint's articular surfaces because of the soft tissue and ligamentous damage surrounding the elbow joint and via instability and poor joint mechanics (Cameron et al., 2021). Elbow joint inflammation cause severe pain, cartilage loss and joint stiffness.

Since 2000 to date, the development of disease-modifying antirheumatic drugs (DMARDs) aimed at preventing damage at the synovitis effectively managed to reduce the need for surgical intervention for those suffering a rheumatoid elbow (Cameron et al., 2021). Nevertheless, other joint diseases have increasingly became problematic, leading to pain and disability. The most prevalent forms of arthritis are osteoarthritis and post-traumatic arthritis.

Osteoarthritis (OA) is a chronic degenerative disorder characterized by loss of articular cartilage and periarticular bone remodelling (Il et al., 2013). Osteoarthritis in the elbow involves the breakdown of the joint cartilage, followed by the formation of new bone spurs (osteophytes), which give rise to pain and stiffness. Over time, OA can cause inflammation of the synovial membrane, named synovitis, leading to pain, swelling, and limited movement of the joint (Liu-Bryan & Terkeltaub, 2015).

In cases of severe osteoarthritis (OA) or trauma where patients experience chronic pain that significantly impacts the function of the joint, Total Elbow Arthroplasty (TEA) is often performed. Elbow arthroplasty aims to relieve pain and restore joint function by replacing the damaged elbow joint with an artificial implant.

2.5. Total Elbow Arthroplasty (TEA)

2.5.1. Surgical Approach

The most common technique used for total elbow arthroplasty is the standard posteromedial approach (Bennett & Mehlhoff, 2009). The surgery involves making a straight longitudinal incision over the posterior part of the elbow. Once the subcutaneous flaps are lifted off, muscles are all placed gently on one side of the elbow. The ulnar nerve is identified in the upper arm and then protected. Then on the distal side of the humerus, dissection begins to release the lateral collateral ligament and then the medial collateral ligament from their distal humerus attachments. For the clear assessment of the humerus dimension, Humerus is rotated externally. To prepare the humerus, the midportion of the trochlea is resected as a rough cut using a bone saw (Bennett & Mehlhoff, 2009). The intramedullary canal of the humerus is exposed at the proximal base of the olecranon fossa and prepared with the starting rasp, followed by the small humeral rasp with light hammer taps. Finally, the humeral component of the prosthesis is carefully inserted into the humeral canal. To insert the Ulna component, the forearm is mobilised proximally where the mandibular canal is exposed (Prkic et al., 2017). The implants may be cemented using Polymethylmethacrylate (PMMA) cement to fix them to the bone and finally high molecular weight polyethylene is inserted between the components of the prosthesis (Kwaees et al., 2019).

2.5.2. Elbow Implant Fixation

During TEA, the humeral and ulna implants can be fixed in the bone using any of the following fixation techniques: Cemented fixation, cementless fixation, and hybrid fixation, where one component of the implant is cemented and the other

remains cementless. Modern elbow prostheses commonly utilise PMMA, relying on a stable interface between the cement and the implant component, as well as a strong mechanical bond between the bone and cement (Bates et al., 2020). In TEA, the cement mantal is considered thinner as compared to the hip and knee arthroplasties in which the cement mantle is between 2-5 mm (Ebramzadeh et al., 1994).

2.5.3. Types of Elbow Implants

Total elbow arthroplasty is the replacement of the humero-ulna joint articulation with an artificial joint that may or may not include the replacement of radio-capitellar and radio-ulnar joints. An elbow prosthesis consists of two components; the humeral stem and the ulna stem that articulate together to form the humero-ulna joint. Elbow prostheses can be grouped according to their basic design characteristics including the amount of constraint a prosthesis provides and the type of linkage between them. The humeral and the ulna stems can be linked or unlinked, the articulation between them can be either constrained, semi-constrained or unconstrained.

Linked elbow prostheses feature a physical connection between the humeral and ulna components, which prevents dislocation unless structural failure occurs. This type of linkage is exemplified by the Coonrad-Morrey prosthesis (Backman & Cil, 2017). In contrast, unlinked elbow prostheses do not have a physical connection between the humeral and ulnar components, such as the Souter-Strathclyde design (Valstar et al., 2002). The choice between linked and unlinked implants depends on the integrity of the collateral ligaments. When these ligaments are intact or can be reconstructed, an unlinked implant may be suitable. In the absence of these ligaments, the linked implant is favoured over the

unlinked one due to its inherent stability and ability to provide better support to the joint (Willing et al., 2014).

Table 2-2: Comparison of Advantages and Disadvantages of Linked and Unlinked Elbow Implants

Implant Type	Advantages	Disadvantages
Linked Implants	- Intrinsic stability; does not rely on soft tissue or ligament integrity	- Higher constraint can lead to increased stresses at the bone-cement interface
	- Suitable for patients with severe bone loss or ligament insufficiency	- Greater risk of aseptic loosening over time
	- Easier to implant in cases with poor soft tissue support	- Mechanical wear at the hinge mechanism can occur
		- Less physiological joint kinematics
Unlinked Implants	- More anatomical kinematics; allows more natural movement	- Requires intact soft tissue structures and good bone quality
	- Reduced stress transmission to the bone–cement interface	- Higher risk of instability or dislocation if soft tissues are insufficient
	- Lower long-term mechanical wear compared to linked designs	- Technically more demanding to implant and align

Constrained elbow prostheses have a rigid design that limits the range of motion to just flexion and extension. This design keeps the joint stable and controls dislocation by stopping excessive movement at the joint. On the other hand, semi-constrained elbow prostheses offer a balance between stability and movement. They allow for flexion – extension and some rotation, while still offering enough support to help avoid dislocation. Unconstrained elbow designs, in contrast,

permit full range of motion without major restrictions. They rely on the surrounding soft tissues, such as ligaments and muscles for stability.

Almost all elbow implants exhibit some amount of constraint due to the mated interaction between the ulnar and humeral components. Older generation of implants were designed as a simple hinge, where the interaction between the ulnar and humeral stems was fixed/ highly constraint, imposing high forces between the prosthesis and cement interface, eventually leading to aseptic loosening of the implant. Current designs are designed as a semi-constrained “sloppy” hinge, allowing some degrees of varus-valgus angulation (5^{o} or more).

The humeral and ulna stems can be long or short depending on the surgeon requirement. These stems can be fixed into the bones with or without Polymethyl Methacrylate (PMMA) bone cement, with cemented designs being more popular (Kwaees et al., 2019). Manufactured implants are coated with different materials such as titanium spray, porous beads, or plasma spray to improve fixation strength. The longevity and survivorship rates vary between different implants relative to their advantages and disadvantages.

The linked implants provide high stability when there is ligamentous insufficiency and better range of motion. Although they are prone to higher risk of mechanical loosening due to higher tension on the interface and often associated with complicated revision surgery. While the unlinked implants at are a lower risk of implant loosening and require less bone invasion, they have higher rates of joint dislocation and highly dependent on the intact ligament structure.

Currently, there are three basic elbow prosthesis subtypes: a resurfacing one (unlinked, semi-constrained, short stem), a loose hinge (linked and semi constrained), and hybrid (depending upon need can be changed from unlinked to linked (Zhang & Chen, 2019).

2.6. Brief History of Elbow Implants

Elbow arthroplasty had evolved over the years due to lessons learnt from previous failure. In the 16th century, Ambroise Pare performed the first salvage surgery of the elbow joint by surgically excising the infected soft tissue, distal humeral and ulnar bone to prevent amputation of the upper limb (Prkić et al., 2016). In the19th century, with the common use of anaesthesia, the surgery of creating pseudoarthrosis of the by resecting distal humerus and interposition arthroplasty with various soft tissue grafts emerged to become acceptable solutions for managing incapacitating elbow diseases (Prkić et al., 2016).

Building on the success of lower limb arthroplasty, the idea of replacing the elbow joint became acceptable, leading to the development of several prosthesis models. Elbow arthroplasty mainly evolved into two main streams. Anatomical arthroplasty where the prosthetic model was developed to mimic the native anatomical structures of the natural joint, and “functional” arthroplasty, which replaces the native joint with a hinge system without anatomically resembling the native joint.

In 1925, the first total elbow arthroplasty was carried out by Robineau using vulcanized rubber and metal anatomical prosthesis. In 1941, Boerema used a non-anatomical hinged prosthesis completely made of metal (Prkić et al., 2016). In 1952, Venable reported the use of a custom-made anatomical prosthesis used to treat distal humerus fracture (Venable, 1952). In 1954, Prevo developed a rigid hinged elbow prosthesis, but this was complicated by loosening due to high stress being transferred from the rigid hinge to the implant and poor fixation of implant to the bone (Prevo, 1954). Weiss (1970) and Dee (1972) developed fully constrained prostheses.

The Dee prosthesis only allowed motion in one plane, rotational and angular moments were believed to be transmitted to the interface between the implant and bone (Figure 2-7). Although the prosthesis reported improved range of motion, the over constraint implant resulted in increased incidence of implant loosening and subsequently triggered Dee to modify the design to a semi-constrained prosthesis with 15 degrees valgus-varus laxity. Clinical results were satisfactory but only for a short period of time (Dee & Sweetnam, 1970).

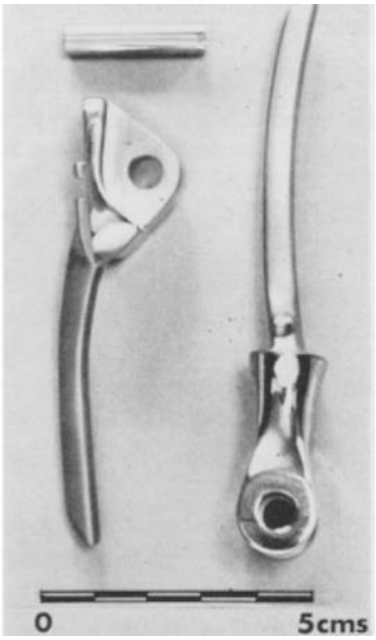

Figure 2-7: The Dee prothesis (Dee, 1972).

As the understanding of elbow biomechanics has advanced, older implants from the 1970s have undergone significant design modifications while keeping their original names. Newer prostheses presented some improved mechanical and anatomical features. To address the problem of implant aseptic loosening, several semi-constrained prostheses were developed. One of which is the Pritchard implant (Rosenfeld & Anzel, 1982) (Figure 2-8). This modified implant design aimed to reduce stresses at the bone-cement interface by relying on the native soft tissue for stability and absorb some of the load. The implant went through a series of modifications but ultimately failed due to excessive laxity and

malalignment. This in turn contributed to eccentric loading, increasing stress levels, resulting in polyethylene wear and loosening.

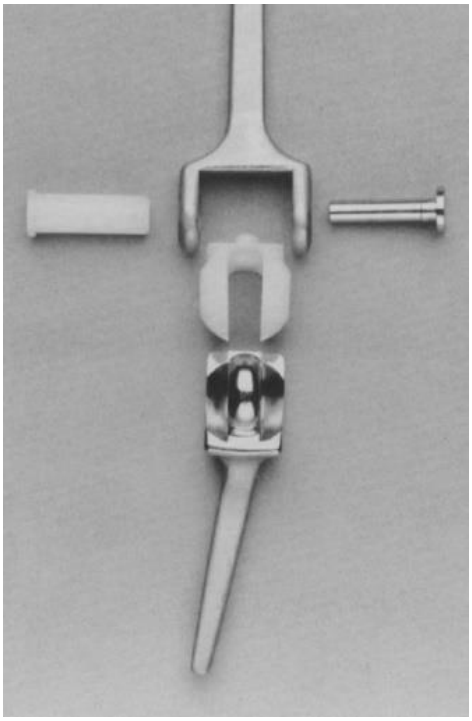

Figure 2-8: The Pritchard implant (Pritchard RW, 1983).

In 1971, the GSB I implant was introduced (Gschwend, Scheier, Baehler). It is a metal-on-metal rigid hinged implant (Gschwend & Scheier, 1974). The high loosening rate led to the development of GSB II in1976. The GSB II incorporated epicondylar flanges but did not have a sloppy hinge. Soon after, the GSB III prosthesis was created with sloppy hinge in 1978 and has been used since without major modifications (Figure 2-9). The laxity of this hinge mechanism allowed the collateral ligaments to absorb part of the stress.

Figure 2-9: The GSB III prosthesis (Schneeberger et al., 2000).

In 1973, the Souter-Strathclyde prosthesis was introduced as seen in Figure 2-10. This was a non-constrained implant with the humeral and ulnar components made of Vitallium and ultra-high molecular weight polyethylene (Malone et al., 2004). The design concept aimed to increase stability by relying on the collateral ligament and load-sharing. The design also incorporated a modified humeral component which can resist the internal rotation/torsional force during functional activities such as lifting a load between the palms of the hands. Flexion and extension loading during these daily activities introduced significant anterior tilting forces on the humeral stem. This effect was particularly evident in implants utilising the shorter 3 cm humeral stem, which failed to provide adequate resistance to bending moments generated during elbow movement. The anterior tilt contributed to micromotion and stress concentration at the bone–cement interface, thereby accelerating loosening.

To address this, a longer 7 cm humeral stem was introduced, which improved both axial and rotational stability. The extended stem length provided a larger surface area for load distribution within the humeral canal and offered greater

resistance to anterior-posterior tilting, particularly during flexion-extension cycles (Trail et al., 1999).

Despite these improvements, the overall increase in implant constraint meant to enhance joint stability, also led to greater load transfer to the humeral component. This unintended consequence contributed to a persistently high rate of loosening, especially when combined with other factors such as bone resorption and ligament deficiencies.

Another study compared 107 cases of rheumatoid arthritis that had the long-stem humeral component of the Souter-Strathclyde total elbow arthroplasty introduced as a primary procedure with a similar group of 202 cases that had the standard component. The study found no significant difference in overall survivorship between the standard and long-stem Souter-Strathclyde humeral implants when using revision as the endpoint. However, the causes of failure differed: the standard stem showed a high rate of humeral loosening (25 of 32 revisions), whereas the long stem had no cases of loosening, with most revisions due to instability (5 of 7). Based on these results, it was recommended that the long-stem humeral component as the preferred primary implant, noting that proper surgical technique and alignment are also critical for long-term success (Trail et al., 2002).

Figure 2-10: The Souter-Strathclyde prosthesis (Ikävalko et al., 2010).

In 1972, the first-generation Kudo prostheses (Type-1 and Type-2) were developed. This was a non-constraint implant where in some of the types, the humeral component was made of titanium alloy with a porous-coated stem (Kudo et al., 1994). The Kudo implant was further modified into Type-5 in which the humeral component was made of porous coated cobalt-chromium alloy with mechanical reinforcement of the critical portion of base of the stem to endure the stress concentration. The Kudo Type-5 showed satisfactory results in terms of improved range of movement (ROM) and less complication rates compared to other prostheses (Mori et al., 2006).

In 1973, the first Coonrad Morrey prosthesis was developed which later went through several modification stages. Early Coonrad designs (Type 1) were titanium implants with straight humeral stem without an anterior flange and a constrained high-density polyethylene hinge. Type II implant (1979 to 1981) was modified to have a floppy hinge giving varus/valgus laxity of 7°- 8° to overcome high loosening rates as a result of the constraint. Biomechanical evidence reported that loosening was the result of posterosuperior displacement of the implant due to the cyclic loads on the implant of nearly three times the body weight (Morrey et al., 1981). To address the loosening problem, Type III was developed with a loose hinge and a humeral stem with an anterior flange to resist posterosuperior displacement (Figure 2-11). The distal part of the humeral component and the proximal part of the ulnar component were coated with titanium plasma spray for better cement fixation. To improve rotational fixation and decrease stress at the bone-cement interface, a bone graft is used between the anterior cortex of the humerus and the flange. Although this implant has been in use since, up to date, loosening remains the main complication this implant suffers from (Dee & Sweetnam, 1970).

Figure 2-11: Coonrad-Morrey elbow prosthesis (Maheshwari et al., 2012)

Other prostheses were also developed such as the Latitude prosthesis. This prosthesis had undergone several modifications (Brownhill et al., 2019). The latest version is the Latitude EV (Wright Medical Technology (Arlington, TN, USA)). The general design concept is seen in Figure 2-12 below. The overall 10 years survival rate for the 1st and 2nd generation Latitude implants were 40% and 50% respectively whilst the 3rd generation (Latitude EV) only had 5 years follow up and the survival rate is nearly 90%.

Figure 2-12: The Latitude elbow implant (Meijering et al., 2022).

Dr. Hill Hasting, and Dr. Thomas J. Graham invented the Discovery Elbow System in the United States (LIMA Corporate S.p.A.), which incorporates a titanium humeral stem and ulnar stem linked via two hemispherical cobalt-chromium condylar bearings (Figure 2-13). The humeral stem features an anterior flange and has an anatomic bow to better mimic the intramedullary canal. The stem is laterally offset by 3mm, and it is also internally rotated 5 degrees to reproduce the axis of rotation. The semi-constrained Discover Elbow System allows for a varus–valgus laxity of 7°. The ulnar component also has a lateral bow, an anterior neck angle of 23 degrees and a lateral offset to reproduce the centre of rotation. The most successful feature of this system is the condylar bearing design that does not depend upon a hinge for stability. Finite element analysis has shown that this “hour - glass” articulation generates lower von Mises stress compared to the cylindrical articulation of the Coonrad Morrey system (Nishida et al., 2014).

Figure 2-13: The Discovery Elbow System (Morris et al., 2024).

The system has been designed to restore elbow joint biomechanics, improve anatomic stem design, decrease polyethylene-bushing wear, and produce a hinge that is easily revised. According to the Norwegian registry, only 19 elbow replacements required revision out of 190 cases recorded, resulting in a five-year survival rate of 95.4% (Huub et al., 2007). The Discovery humeral component was selected as the basis of the instrumented TEA because of its ability to offer effective pain relief, improved range of motion and long-term survivorship (Borton et al., 2021; Tiusanen et al., 2021).

2.7. Elbow Joint Forces

Joint reaction forces in the upper limb are generated by muscle actions and are crucial in enabling the limb to interact effectively with its environment during various activities. Therefore, it is essential to accurately assess the contribution of the individual muscles during the analysis of any activity. Dynamic stability of the joint is provided by the muscles that cross the elbow joint which also protect

the static constraints. Previous analyses have simplified all these muscle structures to just two or three muscles that primarily move the joint (Kojima, 1991; O'Daly et al., 2008), with each muscle that crosses the elbow applies a compressive load to the joint when contracted. In particular, the forearm muscles have been neglected, thus underestimating the forces at the elbow, and prediction of their acting in incorrect directions. The biceps, brachialis, and brachioradialis muscles flex the elbow, with the biceps also acting as the primary supinator of the forearm. The triceps is the main muscle responsible for elbow extension.

Understanding the magnitude of the forces that act on the elbow joint during activities of daily living (ADL) is fundamentally important for several reasons. Firstly, accurate measurements of joint forces directly influence the wear rates of elbow implant materials. A recent study aimed at developing a clinically relevant in vitro testing methodology that accurately replicates the mechanical damage seen in the articular complex of total elbow replacements (TERs) found that high magnitude and frequent joint loads significantly increase wear on the articulating surfaces of the prosthesis, particularly in the polyethylene components (Varadarajan & Kincaid, 2019). The study indicated that wear at the joint can begin to occur at joint loads corresponding to approximately 110 N weight in hand (WIH) and higher. This suggests that loads at or above this threshold are significant enough to induce wear and other forms of damage in the prosthetic components (Varadarajan & Kincaid, 2019).

Excessive joint forces can also lead to micromotion between the implant and surrounding bone, increasing the risk of implant aseptic loosening over time, which remains the leading cause of TER failure. Thus, in vivo force measurements can help develop ways to reduce this risk. In 2007, Cesar et al.

reported that loosening occurred more frequent on the humeral side in the GSB III prosthesis (Cesar et al., 2007). This loosening occurred due to increased forces at the posterior side (Cesar et al., 2007). Additionally, finite element analysis confirmed that stress concentrations occurred at the posterior side of the humeral component during flexion (Herren et al., 2004). Conversely, in the Kudo Type V prosthesis, loosening was less common due to better osseointegration of the titanium porous plasma-sprayed humeral stem. However, the ulnar component experienced high loads due to transfer of loosening forces from the humeral eventually leading to the failure of the ulnar component (Kodama et al., 2017). In unlinked prostheses, loosening often occurs due to multi-axial forces at the implant-cement and cement-bone interfaces (Morrey et al., 1993). For example, the Souter-Strathclyde TEA showed that failure of the ulnar component was due to differences in elasticity between the polyethylene and cement layers (Sjöden et al., 1995). In addition to the bone resorption caused by non-anatomical forces from ligament deficiencies and radial head resection increased the load on the hinges and contributed to stem loosening and arthroplasty failure. Finally, in resurfacing and semi-constrained TERs, high contact stress and rotational torque at the implant-bone and implant-cement interfaces were common causes of early aseptic loosening.

In vivo force measurements are crucial for realistic testing and regulatory approval of implants as laboratory tests often use standardised loads that may not accurately reflect physiological conditions. This is particularly important given the absence of internationally recognised test standards, such as ASTM or ISO, for assessing the durability of contemporary TER implants. Moreover, biomechanical models that simulate elbow joint loading require validation against in vivo data to ensure their accuracy. In vivo joint forces allow for validation of

these models, refining our understanding of elbow joint behaviour under various conditions.

Knowledge of in vivo elbow loading serves as the gold standard for understanding the loads applied to the elbow joint during various activities of daily living (ADL). These forces are particularly important in determining the longevity and functionality of elbow implants. This project aims to advance the development of the world's first in vivo elbow joint force measurement implant to enable direct, real-time measurements of joint forces. These insights will significantly improve our understanding of elbow biomechanics.

Force Magnitude

Publications on modelled elbow joint forces are very limited; however, most joint reaction forces have been predicted primarily for isometric actions under severe loading conditions. A study conducted by Amis A. predicted that the maximum forces during flexion reach up to 3 kN at both the humero-radial and humero-ulnar articulations. These forces were in relation to the prosthesis design (Amis et al., 1979).

The moments that act on the elbow during activities of daily living is thought to be substantial. Activities such as dressing and eating (light ADL) are predicted to create peak joint reaction forces of 300N, while during arm-assisted chair rises or pulling a large table, larger forces of 1700 to 1900 N were predicted (Nicol et al., 1977). Overall, the peak JRFs have been estimated to range from 350 N for light activities to 2094 N for extreme loading (Kincaid & An, 2013).

Force Vector

Every bone-on-bone force is compressive in nature due to the muscle activity that acts to compress the joint. No significant tensile loads are thought to be transmitted across the humeroulnar (HU) joint during normal elbow flexion or

extension with a force applied at the hand. This holds true even during pulling actions, like opening a door, which might intuitively seem to generate tensile forces. Based on theoretical joint loading algorithms, minimal forces are to be expected on the posterior aspect of the olecranon (Kincaid & An, 2013).

The force vector is posteriorly directed with most activities of daily living (ADLs) accomplished in the range of 30–130 degrees (Morrey et al., 2000). The force vector acts predominantly in-plane (sagittally) and any out of plane (z-axis) components that would result in mediolateral joint forces are thought to be negligible when compared to axial forces during pure flexion/ extension motion (Amis et al., 1980).

Joint Reaction Forces (JRFs) Due to Elbow Flexion

Previous analyses of elbow joint reaction forces during elbow flexion utilised computational inverse dynamic and distribution models. JRFs are maximal early in the flexion cycle when the arm is fully extended due to poor mechanical advantage of the prime flexors of the elbow (biceps, brachialis, and brachioradialis). When the flexion angle increases, muscle activities decrease and thus decrease the JRF (Amis et al., 1979a; Amis et al., 1979b; Amis et al., 1980).

A study carried out by Kincaid further confirmed that during elbow flexion, the maximum force that occurs in the elbow is generated in the first 30 degrees within the arc of flexion, whereby the assumed weight in hand (WIH) is multiplied by 15.7 (Kincaid & An, 2013).

EMG data showed significant activity in the major flexors of the elbow (biceps, brachialis, brachioradialis) during resisted flexion across all forearm and elbow joint positions while the muscles considered to be pure extensors showed relatively little electric activity (Funk et al., 1987). Biceps activity decreased in

flexion during forearm pronation and was greatest in neutral. Brachialis activity remained relatively constant in positions of both elbow flexion and forearm rotation. At 30° elbow flexion, electric activity in the brachioradialis was less in the pronated position than in other wrist positions, but this was not true at 90° and 130° of flexion. There was moderate activity in the extensor carpi ulnaris (ECU) and extensor carpi radialis (ECR) in all positions (Funk et al., 1987).

Joint Reaction Forces (JRFs) Due to Elbow Extension

Amis provided estimates of the JRFs during extension motion (Amis et al., 1979a; Amis et al., 1979b; Amis et al., 1980). The main extensor of the elbow is the triceps brachii. It has three heads (long, lateral, and medial) that work together to extend the forearm at the elbow. This reported data was further approximated using an equation where the joint reaction force multiplier was calculated, assuming a weight in hand (WIH) and as a function of elbow flexion angle (Kincaid & An, 2013). It has been concluded that maximal joint reaction force during extension occurs at the beginning of extension when the elbow is fully flexed approximately at 145 degrees of flexion. Conversely, the minimal JRFs occur near full extension of the forearm between 30-0 degrees flexion. This is due to the differences in the muscle moment arms and generating capacity of the prime movers involved in extension in comparison to the flexion motion. Likewise, initiating extension from a fully flexed position requires significant muscle activity because of the poor mechanical advantage of the triceps (TRI). It is also because of the differences in muscle recruitment, resulting net generating capacities and maximal strength in flexion as reported by (Askew et al., 1987).

Although the elbow is a non-weight bearing joint, significant JRFs can be transmitted across it. Joint Reaction forces in the upper limbs are typically caused by muscle actions, a large number of muscles cross the joint complex, applying

direct compression to the joint during both flexion and extension motions. The resulting JRFs are magnified when the motions are performed while grasping an object with some mass in the hand activating the forearm flexors. The extensor carpi ulnaris (ECU) was reported to present some activity during extension, however, the origin of the ECU lies along the axis of rotation therefore, it has little contribution during flexion or extension motions. The EMG data also reported no change in patterns in the extensor muscles when the forearm was rotated. Flexor muscles also showed no activity unless a high load was applied; in that case, a minor degree of activity resulted (Funk et al., 1987) .

Joint Reaction Forces (JRFs) Due to Varus/Valgus (VV) Motions

Valgus and varus moments are crucial to quantify because they affect the distribution of loads across the elbow joint. A proper understanding of these moments ensures that the implant stem can effectively withstand the forces encountered during daily activities, thereby preventing loosening or failure of the fixation. Additionally, knowledge of VV moments is essential for informing the design of the stem; it must be engineered to handle specific loading scenarios without compromising joint stability. There is limited information available regarding elbow forces and moments during rotary motion. During elbow flexion and extension, the forearm muscles that flex and extend the wrist exhibit some EMG activity. However, no substantial changes were recorded when the forearm was pronated or supinated (Funk et al., 1987). Previous experimental setups pin the forearm in neutral rotation, which makes it difficult to identify the contribution of forearm rotation, even though it likely influences elbow stability. Examination of explanted ultra-high molecular weight polyethylene (UHMWPE) bearings from semi- constrained TERs suggest in vivo loading is bi-axial due to the combination of compressive JRF and stresses resulting from varus/valgus motions (Day,

2016; Goldberg et al., 2008; Io & Lipman, 2009). Goldberg et al. reported that the mean ulnar stem varus or valgus malalignment relative to the humeral stem noted radiographically at the time of revision was approximately 4°. This exceeds the stated VV design limits of ±3.5°, generating a constant moment across the prosthesis even without an object in the hand (Goldberg et al., 2008). A Finite element analysis (FEA) study showed that extreme compressive JRFs (2000 N) alone were not enough to induce the creep and extrusion damage patterns associated with 16 retrieved CM ulnar bearings, VV moments were necessary in the analysis to induce stress patterns consistent with the damage observations (Io & Lipman, 2009). This study also concluded that a VV moment of 5 Nm was sufficient enough to exceed the theoretical yield strength of the UHMWPE material and cause plastic deformation greater than that found for the retrieved components (Io & Lipman, 2009).

Unlike flexion/extension loads which are produced as a result of active muscle contraction across the elbow joint, varus/Valgus (VV) motion is resisted by its geometry, joint capsule, collateral ligaments and dynamic forces.

Few available data report on the varus-valgus laxity of the joint. One such study compared the varus-valgus (VV) stability of a "loose hinged" modified Coonrad elbow prosthesis with an intact elbow using a system of pulleys to mimic muscle contraction and simulate flexion-extension motion (O'Driscoll et al., 1992). Joint kinematics were then measured via an electromagnetic tracking sensor revealing slightly higher prosthesis laxity than that of the intact cadaveric elbow joint. Both intact and reconstructed joints have displayed less VV laxity than their respective limits. It was suggested that the soft tissues of the joint absorb some of the forces and moments that would otherwise be transferred to the interface between the prosthesis and the bone in a reconstructed joint. Other reports have also revealed

similar results when testing and measuring prosthesis motion patterns and laxity, highlighting greater laxity observed in all elbow prostheses compared to intact elbows (An, 2005; De Vos et al., 2013; Schneeberger et al., 2000). The maximum VV rotation generated during most ADL in a healthy, intact joint is approximately ± 3-5°. An et al. also reported VV magnitudes of 0.25-2.75 Nm corresponding to a range of VV rotations of 1-3.5 degrees (An et al., 1986). The study by Funk et al. reported maximum external torques developed at the elbow in an isometric strength test to be an average of 17 Nm and 25 Nm in abduction (valgus) and adduction (varus), respectively (Funk et al., 1987). In this study, none of the muscles studied, except the anconeus (ANC), actively participated in resisting the VV stresses, as demonstrated by the EMG measurements. Therefore, it was concluded by the findings of Lo and Lipman that these simplified estimates of maximum VV moments are not likely realistic. EMG testing has shown that forearm forces can also resist varus forces such as the extensor carpi ulnaris (ECU), extensor carpi radialis longus and brevis (ECRL and ECRB) and anconeus. The forces that occur medially to resist a valgus moment may not be as substantial as those that resist a varus force (Buchanan et al., 1998). Although it is more physiological to apply repetitive loading on the prosthesis under below 5 Nm, the simplified varus moment estimate of 5 Nm may serve as an upper limit for prosthesis evaluation.

Joint Reaction Forces (JRFs) Due to Pronation/Supination (PS) Motions

The torques produced during pronation and supination significantly impact the stability of the implant stem. Understanding these forces is essential to ensure that the stem is designed to resist the rotational forces it experiences during various movements. Knowledge of these torques informs the design of elbow implant stems that can effectively handle the dynamic loads encountered during

daily activities. Pronation and supination (PS) motions are generated when the radius is rotated around the ulna. They are important movements in accomplishing common ADL such as turning keys, twisting doorknobs, or tightening screws. The is no information on studies that report on elbow JRFs during active PS loading. However, researchers have suggested that because of the relative size and moment arms of the muscle groups active in pronation/supination, as compared to flexion/extension or VV, PS JRFs and moments are much lower (Amis et al., 1979a), (Chadwick & Nicol, 2000; Morrey et al., 2000). A study reported the maximum torque strengths for women and men to be in the range of 4 Nm and 7 Nm in pronation and 4 Nm and 9 Nm in supination, respectively (Askew et al., 1987). Even higher values (13 Nm and 16 Nm) were reported by (O'Sullivan & Gallwey, 2002) .

Naito et al. and Gordon et al. both reported on the muscles active in supination such as the BIC, BRA and BRD were also active in pronation (Gordon et al., 2004; Naito et al., 1998). Additionally, ECRB was also reported to be responsible for both pronation and supination (O'Sullivan & Gallwey, 2002). Chadwick and Nicol reported PS loads of less than 2 Nm for occupational "pick and place" activities (Chadwick & Nicol, 2000). Similarly, Murray et al. found negligible PS forces during a study of ADL motions (Murray & Johnson, 2004). While PS loads would increase with more strenuous activities, they remain proportionally lower than VV loads due to the reduced moment arms.

2.8. Utilisation of TEA

Total elbow arthroplasties are less frequently performed compared to hip and knee replacements. Although the Swedish registry reports a decrease in the number of TEAs performed for rheumatoid arthritis (Weiss et al., 2008), the

number of TEA procedures for traumatic injuries has increased in recent years (Gay et al., 2012). The United states database shows that the utilisation of TEA more than doubled in the last 14 years with rates higher in females than males (Singh & Ramachandran, 2016). The utilisation rate of TEA was high in females, in particular, white females (74%) were much higher as compared to other race female patients (Zhou et al., 2016). The German database also shows an 84% increase in the number of TEA procedures between 2005 to 2014 associated with an increase and indications for trauma from 12% to 42% along with an increase in the number of revision cases (Klug et al., 2018). Data in the United States indicate that the number of TEA procedures has increased from 0.45 in every 100,000 in 1998 to 0.96/100,000 in 2011 (Singh & Ramachandran, 2016). A report by Day et al. showed a rise of 6.4 % annually in TEA procedures and a 7.6 % annual growth between 1993 and 2007 (Day et al., 2010).

Unlike hip and knee joint registries, there are a few registries for the elbow and therefore our knowledge about the current utilisation of the TEA is limited. The first national registries for the elbow and the shoulder were introduced in the early 2000s, with the oldest registry being the Finnish Arthroplasty, established in 1980, followed by Norway, New Zealand, Sweden, Australia, Denmark, and United Kingdom.

2.9. Revision TEA and Cost

While TEA is a versatile solution for patients experiencing significant destruction of the elbow joint secondary to inflammatory arthritis or trauma (Triplet et al., 2016), yet the survival rates of the elbow implants range from 70% to 81 % (Krukhaug et al., 2018). The low survival rates are often a result of problems associated with TEA, which lead to implant revision. Revision surgery is

associated with increased bone and soft tissue trauma, demanding complex solutions and therefore cost; it is often surgically challenging, and outcomes are worse compared to primary TEA. Mechanical failure remains one of the greatest problems in TEA leading to early failure of the implant or on later stages.

Therefore, understanding the cause of these problems and detecting them at early stage is necessary to avoid revision surgery. It's difficult to pinpoint the exact cost of TEA through the NHS, as detailed procedure costs are not publicly available. However, estimates based on typical UK private hospital pricing suggest that the hospital-related costs for TEA are around £15,600 (Hospital of St John & St Elizabeth, 2025). This usually covers the hospital stay and use of the operating theatre, but does not include fees for the surgeon, anaesthetist, or follow-up care like imaging or physiotherapy. While these figures do not directly reflect NHS costs, they offer a useful indication of the potential financial impact, particularly when considering the costs associated with revision surgeries or complications. In this context, innovations that aim to improve implant longevity could have meaningful cost-saving implications. Additionally, the average international check-up cost ranges between $135.20 ± $190.5 per visit, thus avoiding revision TEA reduces the cost for our hospitals as well as on the clinicians (Hendricks et al., 2018).

2.10. TEA Complications

The first report on the complications of TEA was published by Gschwend et al. in 1996 (Gschwend et al., 1996) in which a total complication rate of 43 % and a revision rate of 18 % was reported. The main complications included but not limited to ulnar nerve complications, aseptic loosening, dislocation, infection, instability, subluxation, intra-operative fracture, and fracture of the prosthesis.

Over the years, various surgical techniques and advancements in implant design have evolved with the aim to minimise this complication.

The design of stemmed TEA prostheses has developed as the indications for TEA have changed. The principle of preservation of bone architecture for ease of later revision has led to an evolution from fully constrained (in which inter-prosthetic stability and motion is determined by the shape and close 'fit' of the non-anatomic prosthetic articulation surfaces) to unconstrained prostheses (in which inter-prosthetic stability is conferred by the interaction of relatively anatomic prosthetic surfaces and periarticular ligaments).

Voloshin et al. reviewed the literature on the complication of TEA and found a reduction in the rate of complications of TEA as compared with the findings of Gschwend et al (Voloshin et al., 2011). The overall reduction rate was 18.7 ± 5.8 %. Although, the type of complications remains the same (loosening, instability, and deep infection), the reduction was attributed to advancements in prosthesis design and better surgical techniques.

A systematic review on TEA survival rates researched 3618 TEA cases and found that the most common complication rates related to biomechanical instability and loosening (9-14 %) with infection occurring in over 4 % of cases on average (Little et al., 2005). The analysis included complications from all types of arthroplasties covering constrained, semi-constrained, and un-constrained arthroplasty. Similarly, a review of 9308 implants was conducted, and a 13.5 % rate of revision cases were identified with a weighted mean follow-up of 81 months. This review also concluded that main reason for the revision was aseptic loosening (38 %) followed by deep infection (19%) (Prkic et al., 2017).

In a systematic review where a total of 9379 elbow implants were examined including both linked and unlinked prostheses, it was found that the rate of

complication had decreased (11% to 38%). Clinical loosening was common followed by deep infection (Welsink et al., 2017).

More recent literature support a gradual decline in complication rates associated with total elbow arthroplasty (TEA), although the procedure still carries notable risks. A systematic review reported by Davey et al. (2021) found complication rates of 12.9% for aseptic loosening, 3.3% for infection, 4.2% for implant dislocation, and 2.1% for nerve injury. The overall complication rate was 16.3%, with a revision rate of 14.6%. Despite these challenges, functional outcomes generally remained acceptable. These findings highlight that while improvements in implant design and surgical techniques have enhanced outcomes, aseptic loosening, infection, and other complications continue to present significant challenges to the long-term success of TEA (Davey et al., 2021).

2.11. Change in Quality of Life After TEA

The increase in the number of TEA procedures. It is likely to place a considerable financial strain on the health care system. In terms of quality of life and cost/utility ratio, few studies have been conducted and limited data is available regarding the efficacy of the treatment.

A study of 33 elbow arthroplasties performed between 2007 and 2013 aimed to quantify the improvements in the quality of life for patients undergoing TEA therapy reported a 91% rate of satisfactory outcome of the patients, with significant improvement in pre- and post-operative scores and an increased range of motion (Giannicola et al., 2013). Patient’s quality of life was mostly affected by pain reduction. The author also conducted a cost/utility ratio analysis, revealing that 70% of the patients showed satisfaction postoperatively.

Between 1984 to 1996, Angst et al studied 79 elbow arthroplasties to qualitatively assess the outcome after TEA. He reported a low pain level, good elbow stability, and overall, 82% were satisfied with the TEA while 8% of patients were not satisfied as the TEA did not meet their preoperative expectations.

Zhou et al. (2016) investigated 3146 patients and evaluated their hospital stay, cost, and rate of readmission within 30-days. He reported that the mean hospital stay was 4.2 ± 5 days, and the mean total hospital cost was 16.300 ± 4000 US dollars per case. The rate of re-admissions within 30 days was 4.4% (Zhou et al., 2016).

These findings highlight the importance of understanding the biomechanical function of the elbow joint to improve patient outcomes and the long-term efficacy of TEA. Developing an instrumented elbow implant capable of measuring all six degrees of freedom around the elbow hinge during real-life activities will provide vital biomechanical data. This data will provide us with a deeper understanding of elbow joint function to optimise rehabilitation programmes and promote patient independence.

The next chapter will focus on the conceptual design, computational modelling, and instrumentation development of a prototype customised humeral component, laying the foundation for its experimental validation and future refinement as part of an integrated instrumented elbow implant system.

Chapter 3: Design, Development and Finite Element Analysis (FEA) of a Prototype Humeral Component

3.1. Introduction

Over the past few decades, total elbow arthroplasty (TEA) has significantly evolved. Advances in the understanding of elbow biomechanics, implant design, and biomaterials have led to the development of implants with better mechanical and anatomical features. However, the unique anatomy and biomechanical properties of the elbow joint make complication rates for TEA about 20 to 45 % higher compared to the total hip or knee arthroplasty (Voloshin et al., 2011; Welsink et al., 2017).

Reported joint reaction forces estimated at the elbow have relied on musculoskeletal modelling using computational inverse dynamics, which are extremely useful due to their flexibility and nom-invasiveness. However, the simplifications and assumptions made in these models lead to inaccuracies. For example, models of the hip joint force have been shown to overestimate the measured values significantly (Heller et al., 2001; Li, 2021; Mellon et al., 2015). The true power of these models is when they are validated by in vivo measurement. Although the lower limb forces are now well understood, this is not the case for the elbow, and our limited knowledge of the elbow biomechanics is leading to uncertainty in designing elbow implants for longevity. To date, the elbow remains one of the few major joints in which in vivo joint forces have yet to be measured.

A solution is therefore needed to measure elbow joint reaction forces in vivo. One successful approach, which has been used in other joints, is embedding sensors in prostheses to measure force, kinematics, and temperature. Thus far, there has

not been an attempt to measure elbow joint reaction forces by embedding sensors in current elbow implants with minimal modification to their design. In other words, transforming the prosthesis into a "smart" or "instrumented" version. Bergmann et al. deigned an instrumented hip prosthesis, which incorporated strain gauges to measure force (Bergmann et al., 1993). Similarly, sensors were designed for the knee to measure the tibiofemoral compression force and shear forces. Smart instruments were also devised for the knee prosthesis to estimate their kinematics during different movements. Some instruments included self-powered force measuring capabilities (Arami et al., 2013; Khan et al., 2017).

To date, no instrumented prosthesis has been designed for TEA that can measure joint reaction forces during various activities of daily living. Consequently, the work in this chapter focuses on developing a customised humeral implant prototype for TEA, capable of reliably and safely housing instrumentation within it. This chapter aims to achieve the following specific objectives in developing such an instrumented humeral elbow prosthesis:

- To design and manufacture a 3D CAD elbow humeral component prototype with added geometrical modifications, suitable for housing implant instrumentation.
- To analyse the maximum von Mises stress experienced by the modified humeral component under peak physiological loads for performance analysis.
- To determine optimal strain gauge locations based on the strain distribution pattern on the implant.
- To strain gauge and develop the implant PCB circuit.

3.2. Materials and Methods

3.2.1. Prototype Mechanical Design

A brief history of previous elbow implants was presented in chapter 2 discussing the causes of failure. Advances in the understanding of elbow biomechanics, implant design, and biomaterials, some implants were developed with increased mechanical and anatomical features. Early fully constrained designs suffered high failure rates due to overconstraint and have consequently been replaced by semi-constrained and non-constrained designs (Siala et al., 2020; Zhang & Chen, 2019). Although nonconstrained implants experience a low incidence of loosening, they are at a higher risk of dislocation because of their dependence on the surrounding soft-tissue structures of the elbow. Subsequently, they add little value in cases of ligamentous insufficiency or poor bone stock and less favoured by many surgeons (Kaufmann et al., 2019). Modern semiconstrained elbow implants allow a degree of laxity at the hinge, mimicking the natural kinematics at the elbow. Many upper-limb activities occur with the shoulder abducted, which in turn generates a varus moment at the elbow. The laxity at the hinge allows load sharing between the prosthesis and soft tissues, minimising the force transmitted to the bone-cement interface and reducing the risk of loosening (Egidy et al., 2019; King et al., 2019). Thus, semiconstrained elbow implants provide stability and good functional outcomes and are consequently the most used implant type in modern practice (Egidy et al., 2019).

The Discovery Elbow System (LIMA Corporate S.p.A.) is a contemporary semiconstrained implant and one of the commonly used TEA prostheses in the United Kingdom, with 1,244 procedures performed between 2012 and 2025, both electively and in trauma cases (National Joint Registry (NJR), 2025). While

promising results in the short and medium term were reported by a recent systematic review and meta-analysis, there remains a paucity of long-term data available for the Discovery Elbow System (Welsink et al., 2017). The system has been designed to restore elbow joint biomechanics, improve anatomic stem design, decrease polyethylene-bushing wear, and produce a hinge that is easily revised. According to the Norwegian registry, only 19 elbow replacements required revision out of 190 cases recorded, resulting in a five-year survival rate of 95.4% (Huub et al., 2007). The current mean survival rate of the Discovery implant for surgeries performed between 2012 and 2025 is 99% at one year, 95.8% at three years, and 92.2% at five years postoperatively (National Joint Registry (NJR), 2025).

The most successful feature of this system is the condylar bearing design that does not depend upon a hinge for stability. Finite element analysis has shown that this “hour-glass” articulation generates lower von Mises stress compared to the cylindrical articulation of the Coonrad Morrey system (Nishida et al., 2014). Therefore, the Discovery humeral component was selected as the basis of the instrumented TEA because of its ability to offer effective pain relief, improved range of motion and long-term survivorship (Borton et al., 2021; Tiusanen et al., 2021).

The implant developed in this chapter is a prototype that, at this stage, is powered externally. Future iterations are planned to incorporate wireless power and data transfer via inductive coupling using a single pair of coils. In these future designs, the induction coil will be housed within a ceramic extension located at the tip of the titanium stem, and all internal components will be hermetically sealed through welding. This welding approach has demonstrated long-term viability in similar instrumented implants such as those used in hip, knee, and shoulder

replacements (Xie, 2013). A computer-aided 3D CAD design software (Solid-Works Corp.™, Dassault Systems, Concord, MA, USA) was used to create a geometrically modified 3D model of the Discovery humeral implant stem (LIMA Corporate S.p.A.) to accommodate for the implant instrumentation.

The material used in producing orthopaedic implants must withstand the corrosive effects when present in vivo environment (i.e. bodily fluids) and long-term cyclic mechanical loading over time. The Discovery humeral implant is made of titanium alloy (Ti-6Al-4V), one of the most biocompatible metals used in orthopaedic implants owing to its excellent mechanical properties (Quinn et al., 2020).

The Discovery humeral implant incorporates features such as a stem with a 5° valgus alignment and 5° internal rotation. The stem is offset medially and laterally offset by 3mm and has an anatomical bow to better mimic the intramedullary canal (Figure 3-1) while also featuring an anterior flange. Moreover, it features a cylindrical base geometry that has proven to improve load transfer to the metaphyseal bone (Goldberg et al., 1988) (Figure 3-1).

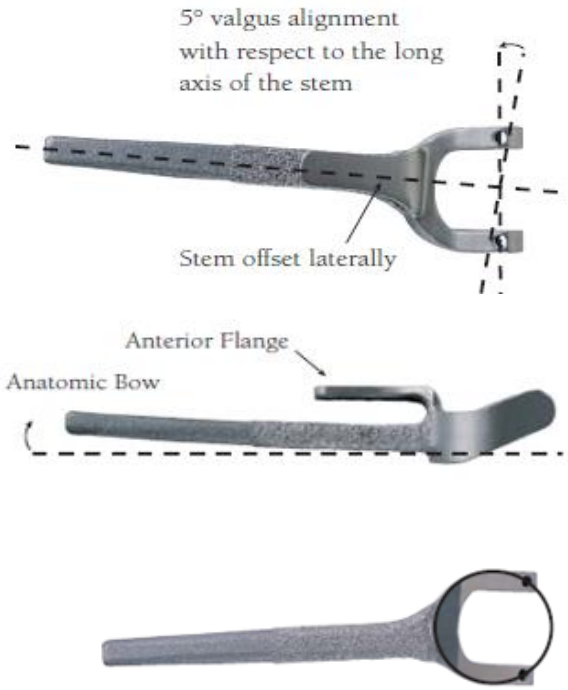

Figure 3-1: Discovery humeral component with 5° valgus angulation, anatomic bow and cylindrical base geometry.

The Discovery humeral component is connected to the ulna stem via two hemispherical cobalt-chromium condylar bearings. The standard length of the humeral implant is 100 mm, although longer stems measuring 150 mm are also available. However, the 100 mm implant length is mostly common than the longer 150mm stem which is occasionally used in cases of significant bone loss during primary replacement. The available geometrical description was utilised to guide the design iterations of the new customised humeral component, along with detailed dimensions that were directly measured from a physical Discovery humeral implant stem using a vernier calliper.

The newly modified component is a right-sided humeral body and stem and consisted of three primary regions (Figure 3-2): the humeral stem, humeral body (middle part between stem and forks), and two forks for mating with the condylar component (Figure 3-2)

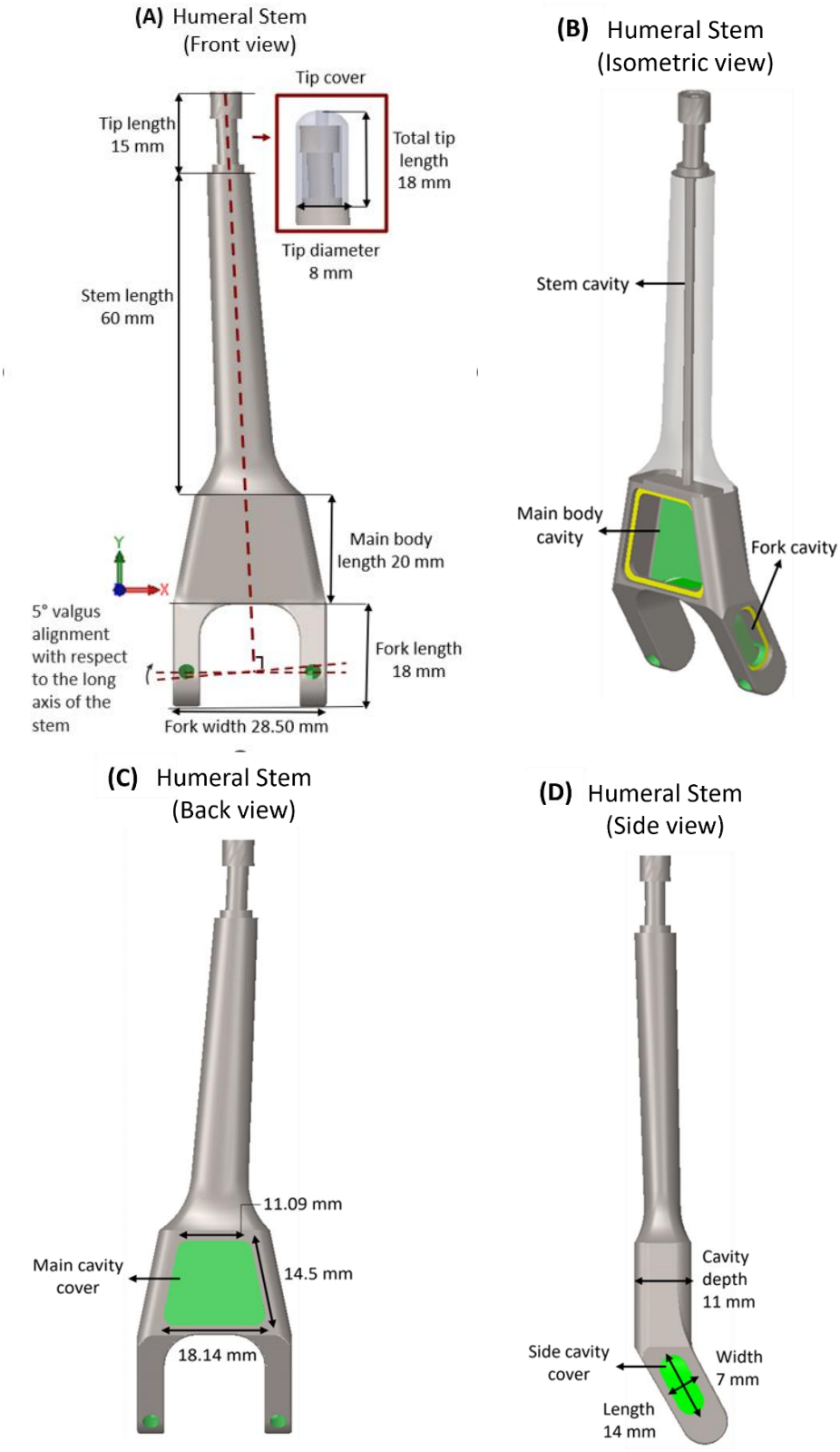

Figure 3-2: (A) Humeral Stem design and dimensions (B) Isometric view of implant with main body cavity and side cavity (C) Implant main body cavity dimensions (D) Implant side cavity dimensions.

The humeral body and forks contain 3 cavities accessible via welded covers which will accommodate the instrumentation for in vivo strain measurement. Overall, the modified humeral implant measured 116mm, placing it in the category of short-stemmed implants. This decision is supported by literature findings, indicating that using shorter stem lengths in reconstructions can result in bone structures that closely resemble their intact state (Austman et al., 2011; Reimeringer et al., 2013; Bieger et al., 2012; Munting et al., 1997; Arno et al., 2012; Shishani and Gobezie, 2017).

The humeral stem has a circular cross-section with a proximal tip diameter of 8 mm. The proximal end of the stem was specifically designed to accommodate future tip strain measurement instrumentation and implant coil assembly. This tip end is shielded by a dome-shaped cover to protect the mounted strain gauges. The humeral shaft length measures 75 mm and incorporates a hollow 2 mm axial hole for connection to the main cavity electronics. It maintained the 5° valgus alignment with respect to the long axis of the stem.

The main body of the implant prototype is somewhat larger than in the standard Discovery implant to provide space for housing the main instrumentation whilst not compromising the bone (Figure 3-3). It connects the distal end of the stem and to the proximal end of the forks. It is shaped like an isosceles trapezium with radiused edges to minimise stress concentration points. The main body has a height of 20 mm and an inner depth of 5.6 mm, and it is machined to create an internal cavity paired with a corresponding cover.

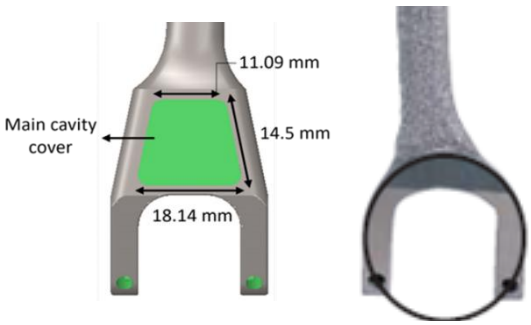

Figure 3-3: Modified and Discovery humeral implant base profiles.

The dimensions of the forks of the humeral implant prototype remained unchanged from the Discovery implant except for including cavities within them but maintaining their identical geometry for compatibility with the standard Discovery condylar bearings and ulna component.

The modified implant design did not include a flange due to the lack of evidence supporting its role in load transfer. A study by Craik et al. investigated the cortical strains in the distal humerus following total elbow arthroplasty and examined the biomechanical advantage of the anterior flange design. The study found no clear evidence of an advantage provided by the anterior flange during axial loading. Additionally, there were no significant changes in cortical strains when an antero-posterior (AP) bending load was applied with the anterior flange engaged (Craik et al., 2012). These findings are further supported by Quenneville et al., who used a cadaveric model to study the role of the anterior flange. Their research also found no significant differences in cortical strains with a 500-N axial load following engaging the anterior flange (Quenneville et al., 2008).

Table 3-1 summarises the design features included in the modified humeral implant in comparison to the standard Discovery humeral implant.

The Discovery Elbow System (DES) uses a spherical hinge bearing, comprising of two cobalt chromium (CoCr) hemispheres locked into the distal humeral component with medial and lateral Ti6Al4V screws (LIMA Corporate S.p.A. Italy). The two hemispheres are connected diametrically, producing an hourglass shape. It is hypothesised that this design minimises polyethylene wear (Hastings et al., 2014). For the purposes of fatigue testing and calibration, in the newly modified humeral implant, the hinge mechanism is simplified and represented by a cylindrical loading rod. The rod is designed with recesses that match those of the condylar bearings, where the forks of the humeral implant securely mate to the shape of the contact surfaces within it as seen in Figure 3-4. This design simplifies the representation of the hinge mechanism while ensuring consistent load distribution under controlled testing conditions. It minimises variables that could otherwise introduce complexity into fatigue analysis or affect the precision of calibration.

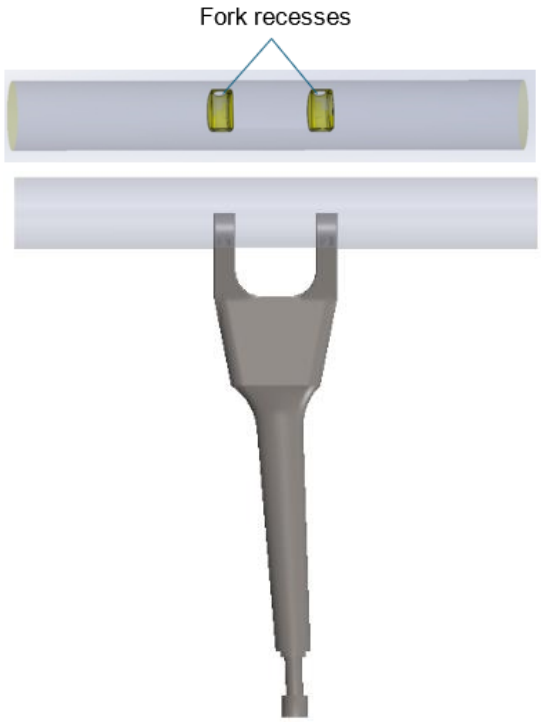

Figure 3-4: Cylindrical loading rod with fork recesses that match those of the condylar bearings.

Table 3-1: Comparison of design features between the standard Discovery humeral implant and modified humeral implant.

Design Features	Discovery Humeral	Modified Humeral
Stem 5° valgus alignment	Yes	Yes
Stem 5° internal rotation	Yes	No
Stem offset 3mm	Yes	Yes
Anatomical bow	Yes	No
Anterior Flange	Yes	No
Total humeral implant length	Standard: 100 mm	116 mm

3.2.2. Finite Element Analysis of Humeral Component Prototype

Before proceeding to the manufacturing stage described above, the newly modified humeral component model must undergo validation, verification, and prototyping processes. One such method of validation is through a Finite Element Analysis (FEA) study. This is to ensure that the geometrical modifications (i.e. creating cavities) made to the customised humeral component is reliable and safe and is capable of withstanding the stresses and strains it will encounter under physiological conditions without compromising its strength. Through FEA, potential design flaws can also be identified, and iterative improvements can be made to the customised humeral design.

3.2.2.1. FE Model Assembly

The individual SolidWorks part files (. sldprt) including the humeral implant stem, the loading rod and the cavity covers were then imported into “SolidWorks Assembly” to be assembled and prepared for FEA study. In practice, the covers will be joined to the cavities via Electron Beam Welding (EBW), which is one of the methods used to weld metal joints together. And so, in this assembly, a rigid mate contact was assigned between each corresponding cover and its cavity (main cavity and two fork cavities) on the humeral implant to mimic the same level of constraint in reality. The inner cavity walls of the rod were coincidentally mated with the humeral implant forks so that the forks snugly fit into the designated cavities in the loading rod. The centre point of the rod is machined to align with the centre point of the fork arc.

3.2.2.2. Material Properties

The results from the FE (Finite Element) model can vary significantly based on the input material properties assigned to each part involved in the simulation. Hence, it was ensured that the correct material properties of Titanium Grade 5 alloy (Ti-6Al-4V) were added from the datasheet and customised into the SolidWorks material library. Ti-6Al-4V has an Elastic Modulus (E) of 106-114 GPa, a yield strength (σy) of 1170 MPa, and a Poisson's ratio of 0.3. Titanium alloy (Ti-6Al-4V) was assigned to all the FE models in this study, which include the modified humeral implant stem, the corresponding weld caps, and the loading rod. The material properties of all parts were assumed to be elastic, linear, and homogeneous isotropic.

It is important to note that The FE model utilised a simplified version of the Discovery elbow humeral component. Specifically, two features present in the clinical implant were omitted: (1) the anterior flange, which contributes to resisting anterior translation and enhances fixation stability (Morrey et al., 2017), and (2) the 5° internal rotation of the stem relative to the anterior flange, which is intended to replicate the native humeral anatomy and improve alignment in total elbow arthroplasty (TEA) (van der Lugt et al., 2017). However, these geometric modifications were necessary for manufacturing constraints related to embedding the electronics and achieving experimental compatibility with the custom loading setup. While they do not substantially affect the axial compressive loading conditions investigated in this study, their potential influence on joint kinematics and localised stress distributions is acknowledged and further considered in the discussion.

3.2.2.3. Loading and Boundary Conditions

Bonded interactions were defined between all modelled components, including the contact between the humeral forks and the rod, as well as between each of the individual covers and the modified humeral component. The bonded contact between the covers and the humeral component ensured that the covers acted as if welded to the cavities. The total stem length of the humeral component was constrained (fixed), preventing all translational degrees of freedom (Figure 3-5). This setup represents the fixation of the humeral stem in a cemented total elbow replacement within the intramedullary canal of the bone. Axial point loads of different magnitudes (F) were applied at the centre of the rod of the humeral implant (Figure 3-5), causing a compressive force across the modified humeral component. The magnitude of F depended on the category of ADL being simulated. Although the elbow joint is not a weight-bearing joint, considerable forces from daily activities are transmitted through its small surface area, exerting a large compressive force on the joint especially the humeral ulna joint while performing flexion and extension.

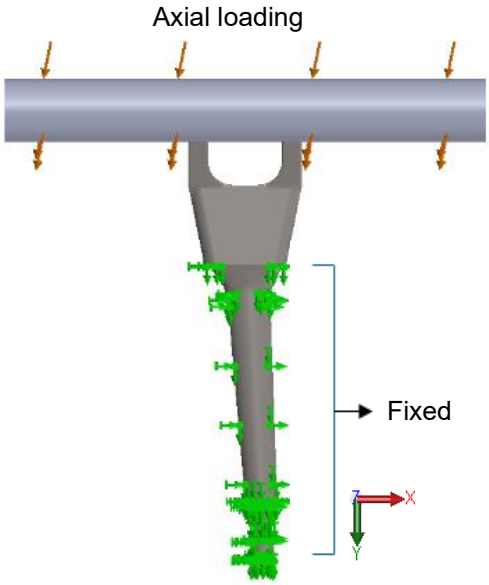

Figure 3-5: Stem fixation and axial loading of the modified humeral implant during FEA.

The elbow joint experiences a load of approximately one times body weight (1 x BW) during normal daily activities, and this can reach up to three times body weight (3 x BW) when lifting heavy objects and up to six times body weight (6 x BW) during pounding and throwing activities (Morrey & An, 1983). Nicol et al. (1977) reported modelled elbow joint forces in young, healthy male subjects engaged in various ADL (Nicol et al., 1977). It was reported that during normal activities of daily living (ADL), a maximum joint reaction force (JRF) of 300 was encountered, whereas during extreme ADL, the maximum JRF reached 2094 N (Nicol et al., 1977). JRFs for different activities of daily living (ADL) ranging from light (70-350 N), moderate (419-698 N), and strenuous (768-1396 N) duty to extreme (1466-2094 N) loading scenarios were reported by (Kincaid & An, 2013). The load scenario adopted here represented in vivo loading for the moderate activities of daily living (ADL) category, which is likely to prevail in the total elbow replacement (TER) patient cohort. However, strenuous and extreme levels were also simulated to determine if these forces would impose any potential failure in the modifications made to the custom humeral implant. Axial point loads (F) of 700 N, 1400 N, and 2100 N were applied, corresponding to moderate, strenuous, and extreme ADL, respectively.

3.2.2.4. Mesh Properties and Convergence

The modified humeral component model was meshed using free tetrahedral elements in SolidWorks (Solid-Works Corp.™, Dassault Systems, Concord, MA, USA). In order to ensure the accuracy of the results, the mesh quality was evaluated through a mesh convergence study. A total of 16 mesh densities were examined, maintaining approximately consistent element sizes throughout the humeral FE model. The specific element sizes across all mesh density levels

ranged from 3 mm to 0.14 mm. Von Mises stress is the failure criterion and solution to be converged in this FEA study. Von Mises stress evaluates the combined effect of the multiple types of stresses experienced by the modified humeral component. Unlike individual stress components measures that may not adequately represent the complex loading conditions at the elbow joint. Thus, this equivalent stress provides predictions of component failure with respect to its yield strength. The solution was regarded as converged when the change in results was < 5% (Pegg et al., 2013). Figure 3-6 shows that the results start stabilising with refined mesh densities and increased number of elements. The mesh was refined, and the solution was converged to 258801 elements, with an average element size of 0.9 mm.

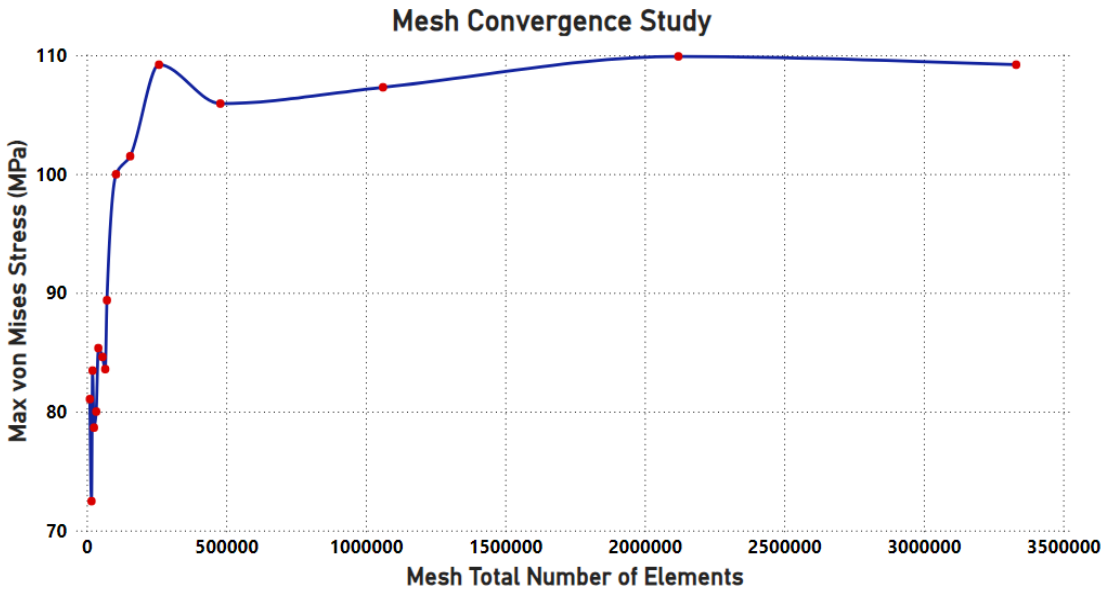

Figure 3-6: Mesh convergence study showing variations of max Von Mises Stress (MPa) with increasing mesh density.

3.2.3. Prototyping and Manufacturing

Prototyping was done using the 3D printing technology, also referred to as Additive Manufacturing (AM). AM is a modelling process by which physical objects are reconstructed from a digital 3D model by fusing materials together in a layer-by-layer fashion (Zhang et al., 2023). This technology has gained worldwide recognition in recent years in industries such as agriculture, aviation, robotics, aero-space and automotive, and healthcare (Ali et al., 2019). In the healthcare sector it is particularly prominent in the fields of plastic surgery, orthopaedics, and dentistry (Deshmukh et al., 2019). This prototyping method makes it possible to produce prototypes with precise complex shape geometry at a low cost. With this 3D technology, the humeral implant design dimensions can be evaluated, and the necessary refinements and improvements can be applied to the design to the required standard. This method significantly reduces costs and waiting times.

There are various 3D printing techniques with unique capabilities depending on the application. In this case, the Stereolithography (SLA) 3D printing technique was used to evaluate the dimensions of the humeral implant design and the proper fit of the covers on their respective cavities. The custom humeral component CAD file was transferred into a print preparation software (PreForm) to specify the settings and slice the 3D model, preparing it for printing. The component is then set to print. Once the humeral component has finished printing, it was cured using a UV laser to solidify the liquid photopolymer resin layer by layer, producing a physical prototype of the modified humeral component.

The humeral component prototype was then manufactured using Computer Numerical Control (CNC) machining. This manufacturing process uses

computerised controls to operate machinery and tools for shaping raw materials into precise components. It is widely used in industries that require high precision and repeatability, including the production of medical implants. This method ensured that complex features of the humeral component could be manufactured with reliable consistency. The cavity covers were attached using Electron Beam Welding (EBW), which is considered the safest and most precise welding technique for medical applications. EBW was chosen for its ability to produce a clean, controlled weld profile around the covers, guided by CNC to ensure consistent results. Test samples were developed and sectioned to verify weld depth and penetration. This technique is particularly effective for titanium due to its strength and biocompatibility.

3.2.4. Finite Element Study of Strain Distribution in Prototype Implant

To mount strain gauges onto the manufactured custom humeral component prototype and measure the strains experienced by the humeral implant during physiological conditions, optimal gauge locations need to be carefully identified via an FEA study. The objective of this FEA study is to find suitable strain gauge sites that provide adequate sensitivity to all degrees of freedom (d.o.f) around the elbow joint, each with unique sensitivity profiles and good selectivity.

The strain distribution pattern on the custom implant allows for predicting the areas that experience the most deformation and strain when subjected to the physiological loading likely to occur when performing various daily activities. Two important criteria for gauge site selection are sensitivity and selectivity. Each strain gauge location must be specifically sensitive to at least one degree of freedom load by assessing the areas experiencing the highest strains. This ensures that each d.o.f can be uniquely determined.

Selectivity of candidate gauge sites is important to be able to avoid ambiguity between degrees of freedom. Therefore, locations are selected where the strain output is predominantly due to the load of interest.

3.2.4.1. FE Model on COMSOL

This finite element analysis (FEA) study was performed on COMSOLTM, a commercially available simulation software package (COMSOL Multiphysics ®, Stockholm, Sweden).

3.2.4.2. Model Geometry and Material Properties

A minor geometrical modification was made to the humeral component model in this FE analysis. As shown in Figure 3-7 below, a modified loading bar was added between the humeral implant forks to simplify the hinge mechanism and reduce computational analysis time (Figure 3-7). The SolidWorks part file (. sldprt) of the modified humeral component was imported into COMSOL^{TM} software to perform the FEA study.

A continuous array of points was built on the outer wall surface of the U-shaped forks and main body cavities (Figure 3-7), representing potential candidate gauge sites where the strain is of interest in this analysis. These points were evenly spaced both vertically and horizontally and were placed on flat and curved surfaces extending from one fork cavity across the central base cavity and down to the other fork cavity. The same material properties of Titanium Grade 5 (Ti-6Al-4V) as in section 3.2.2.2. were assigned to the imported humeral model.

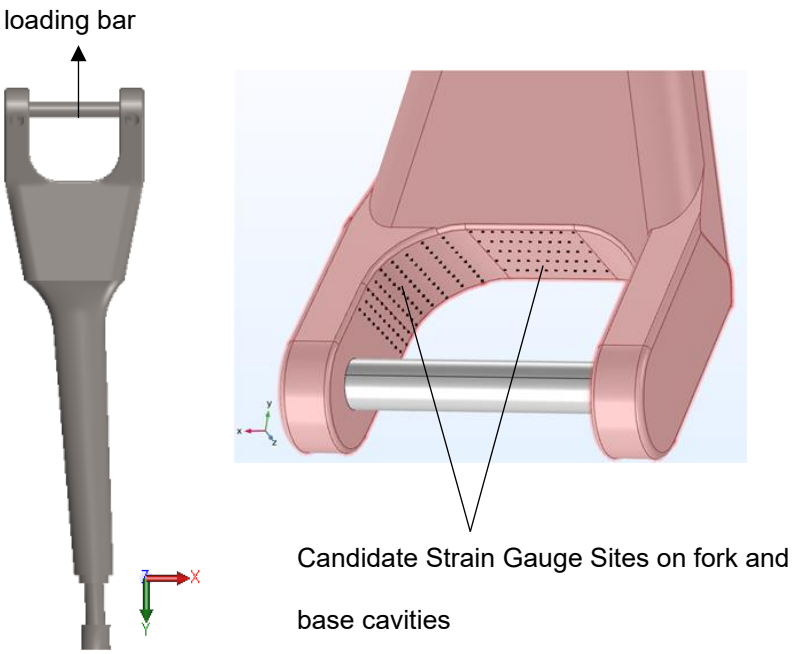

Figure 3-7: Modified loading bar attached to the humeral implant stem and the locations of candidate strain gauge sites during the FEA study in COMSOL.

3.2.4.3. Loading and Boundary Conditions

The coordinate system of the modified humeral implant model aligns with some anatomical references of the implant. In this system, the x-axis runs parallel to the loading bar (axle), the y-axis is axial and parallels the distal stem, and the z-axis is perpendicular to the axle at its centre (Figure 3-8).

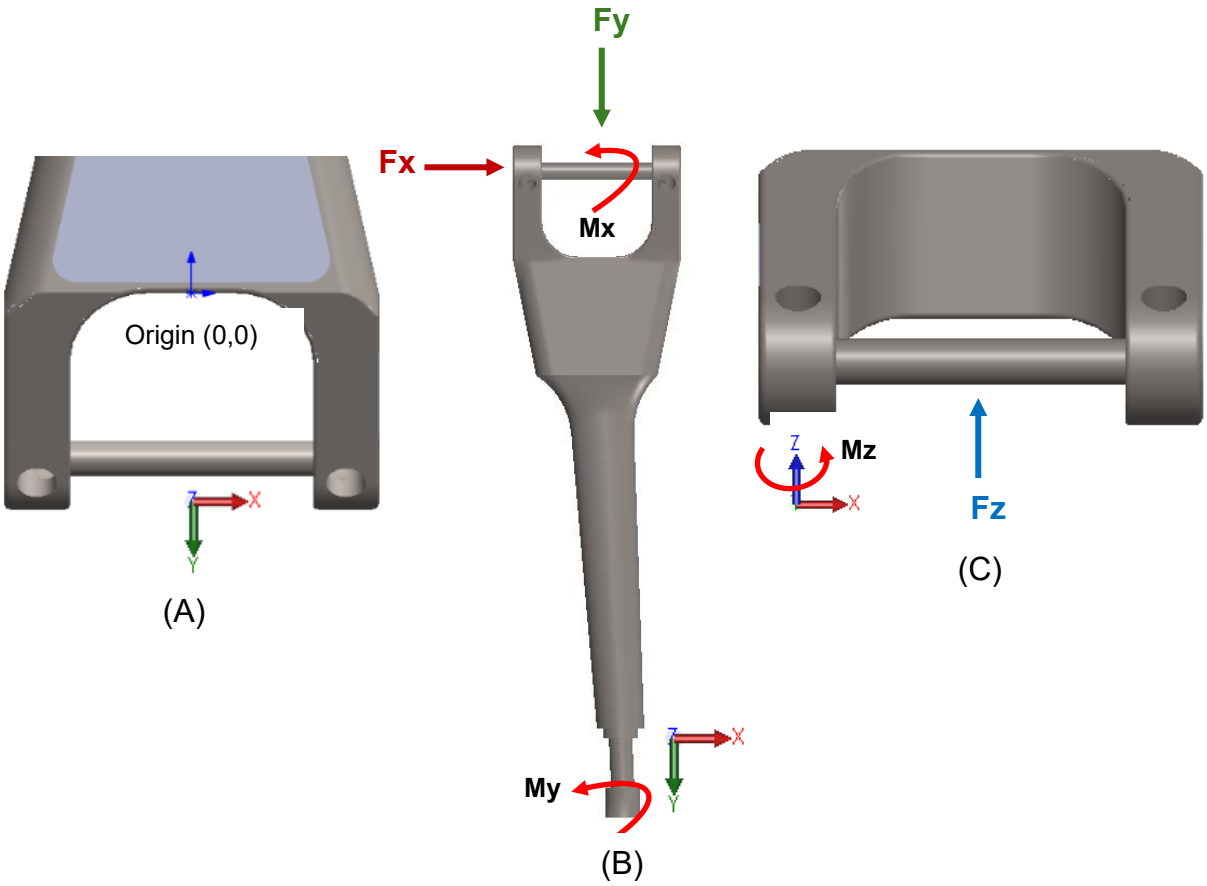

Figure 3-8: (A) Shows the zero coordinate point of the humeral implant, (B) Demonstrates the forces and moments applied in the direction of Fx, Fy, Mx and My, (C) The application of the Fz and Mz.

A fixed constraint was assigned to the humeral stem, preventing displacements in all directions. All six degrees of freedom loads were separately applied to the axle of the implant (Figure 3-8). These degrees of freedom consist of three forces (Fx, Fy, Fz) and three moments (Mx, My, Mz) acting at the elbow joint hinge. Each force had a magnitude of 100 N applied, while for each moment, 1 Nm was applied. A boundary load was applied corresponding to each case of force loading. Likewise, an applied moment was applied in each moment load case.

In order to assess the immunity of strains to variations in load distribution, the axle was divided into three equal segments as seen in Figure 3-9.

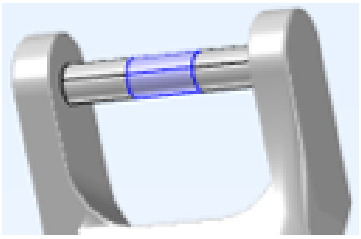

Figure 3-9: Illustrates the loading bar (axle) split into three equal sections.

All 6 degrees of freedom loads was then individually and separately applied to each segment to observe potential changes in strain output. This immunity test aims to determine whether altering the load distribution significantly affects the recorded strain profile. Any significant differences may lead to the elimination of certain gauge sites from further analysis.

3.2.4.4. Mesh Properties and Data Processing

The same mesh properties, specifically an element size of 0.9 mm as described in section 3.2.2.4., were used to mesh the modified humeral implant model in this study. The model was then computed, and the six independent components of the strain tensor, including normal and shear strains, were recorded at the specific points generated and exported in the form of an Excel® sheet for analysis. The normal strains were denoted as εxx (strain along the x-axis), εyy (strain along the y-axis), and εzz (strain along the z-axis), while the shear strains were denoted as εxy (shear strain on the xy plane), εyz (shear strain on the yz plane), and εzx (shear strain on the zx plane).

The raw strain data was further processed to essentially do the following:

1) Rotate direct strains to align them with the appropriate surfaces using Equation 1 below.

Equation 1: Strain transformation equation.

$$\varepsilon_{x'} = \left(\frac{\varepsilon_x + \varepsilon_y}{2}\right) + \left(\frac{\varepsilon_x - \varepsilon_y}{2}\right)\cos 2\theta + \frac{\gamma_{xy}}{2}\sin 2\theta$$

$$\varepsilon_{y'} = \left(\frac{\varepsilon_x + \varepsilon_y}{2}\right) - \left(\frac{\varepsilon_x - \varepsilon_y}{2}\right)\cos 2\theta - \frac{\gamma_{xy}}{2}\sin 2\theta$$

$$\gamma_{x'y'} = -\left(\frac{\varepsilon_x - \varepsilon_y}{2}\right)\sin 2\theta + \frac{\gamma_{xy}}{2}\cos 2\theta$$

2) Calculate the gauge strains using the transformed normal and shear strains using the equation below (Equation 2).

Equation 2: Strain transformation equation to find gauge strain.

$$\varepsilon_A = \varepsilon_{xx}\cos^2\alpha_A + \varepsilon_{yy}\sin^2\alpha_A + \gamma_{xy}\cos\alpha_A\sin\alpha_A$$

3) A few positions on each wall cavity experiencing high strain were guessed, then the “INDEX” and “SMALL” functions on Excel were used in combination to retrieve the coordinates of the points closest to those guessed positions.
4) A separation test was performed by calculating the linear distances between gauge positions to ensure that each gauge is sufficiently spaced.
5) Based on the positions identified a sensitivity matrix was constructed which compiled the strains associated with the identified positions corresponding to each individually applied load (Fx, Fy, Fz) and moment (Mx, My, Mz).
6) To determine the forces and moments that produced these strains, the sensitivity matrix was simply “inverted,” calculating the pseudoinverse matrix. The Moore-Penrose pseudoinverse is particularly useful in this

case as the sensitivity matrix is not square or singular, allowing for a solution to be found in least-squares terms. By applying the pseudoinverse, the system can be solved even when the matrix does not have a direct inverse, providing a way to calculate the forces and moments from the strain data accurately in an overdetermined or underdetermined system.

7) The inverted matrix was examined, using the ‘correl’ function in Excel, to compare each of the two sets of shear force and corresponding out-of-plane bending moment for all possible selectivities.
8) Retrieve the applied forces and moments and examine variations to added noise.

3.2.5. Strain Gauging of Humeral Component Prototype

Once the strain gauge locations were identified in the previous FEA study, the manufactured titanium humeral implant was prepared for internal strain gauging. However, prior to this, external strain gauging techniques were practiced on the 3D-printed resin prototypes. This step ensured precise and accurate strain gauge placement on the actual humeral component.

Strain gauge rosettes were mounted on the external walls of the three cavities. In this scenario, rosette strain gauges were better suited than individual strain gauges because they can measure strain in multiple directions and determine principal strains and their orientation as well as their compact design which made them more suitable for insertion into the small cavities where space was limited. This capability is crucial for capturing the complete strain profile and understanding the full strain state at the areas of interest. The humeral component resin prototype was instrumented with 350 Ω rectangular rosette (45°)

strain gauges (FRAB-2-350-23-1LJB-F, Tokyo Measuring Instruments Laboratory Co.™, Fukuoka, Japan) at two of the predefined locations. Each strain gauge rosette was placed centrally on the external wall of the left fork (C1) and right fork (C2) of the humeral implant as illustrated in Figure 3-10 below. The strain gauge rosettes were aligned 45° to the long axis of the local YZ plane of the humeral forks.

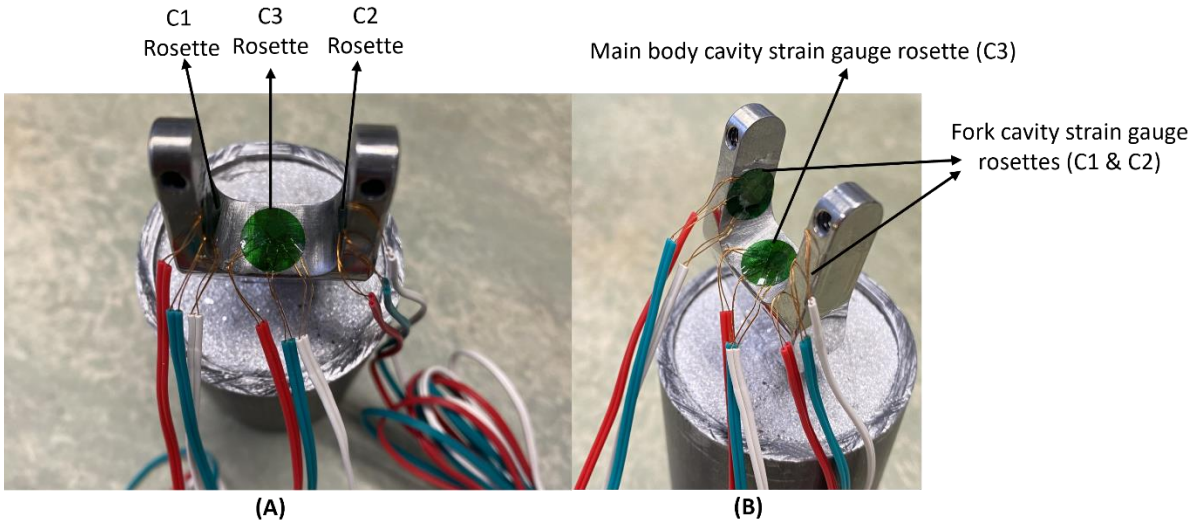

Figure 3-10: Gauge locations on the (A) Main cavity and (B) Fork cavities

The strain gauge bonding site was polished in a circular motion using sanding grits of medium (P220) and fine (P400, P600) grit sizes. This preparation step is necessary to make sure that the bonding site is smooth enough for good adhesion while also ensuring it picks up on the surface strains. Engineering Cleaning Wipes (ECW) were soaked in acetone and wiped across the bonding site in one direction to remove any dust created during the sanding process. The strain gauge rosette was bonded to the surface using instant adhesive (LOCTITE® 401). Afterward, a polyethylene sheet was placed over the area and pressed firmly with a finger for about one minute to ensure uniform stress

distribution. The polyethylene sheet was then disposed once the adhesive was cured, and the rosette was attached.

The titanium manufactured humeral implant was internally strain gauged with 350 Ω tri-axial 0°-45°-90° strain gauge rosettes (C5K-06-S5198-350-33F, Micro-Measurements, Vishay Precision Group, Inc. (VPG), North Carolina) following the same technique above (Table 3-2). In the left and right fork cavities, the rosette was placed centrally on the inner walls of the fork cavity, the wall opposite the weld cap, and the preattached cables were directed and led through the interconnecting hole (Figure 3-11) to directly connect to a customised printed circuit board (PCB), embedded in the main body cavity of the custom humeral implant. The fork strain gauge rosettes were located on the local YZ plane of the humeral forks with the middle gauge running parallel to the long axis (y-axis) of the gauge plane. In the centre cavity, the rosette was placed centrally on the bottom wall, with leads directed towards one side as seen in Figure 3-11 . The central rosette located on the local XZ plane of the humeral implant with the middle gauge parallel to the X axis.

Table 3-2: Strain Gauge Specifications.

Strain gauges	**Gauges length (mm)**	**Gauges factor**	**Gauge resistance (Ω)**
C5K-06-S5198-350-33F	0.36	-	350 ± 0.5
FRAB-2-350-23-1LJB-F	2	2.03±1.00	350 ± 1

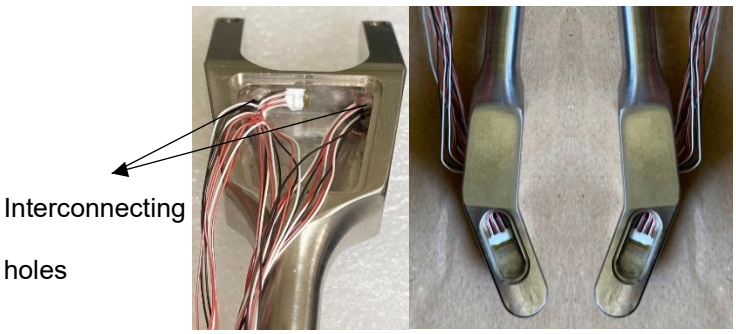

Figure 3-11: Illustrates the placement of the gauges on the inner walls of the main cavity and fork cavities with the wires directed through an interconnecting hole.

The output gauge strain readings (ε_A, ε_B and ε_C) correspond to Cartesian strain components (ε_{xx}, ε_{yy} and γ_{xy}) as shown in the Figure 3-12 below.

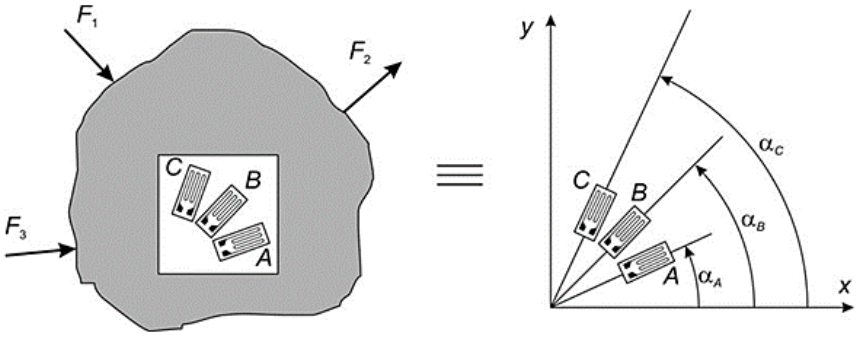

Figure 3-12: Strain gauge rosette orientation and force application.

These relationships are described by the following transformation equations (Equation 3):

Equation 3: Strain transformation equations to find rosette gauge strain

$$\boldsymbol{\varepsilon_A} = \varepsilon_{xx}\, cos^2\, \alpha_A + \varepsilon_{yy}\, sin^2\, \alpha_A + \gamma_{xy} \cos\, \alpha_A \sin\, \alpha_A$$

$$\boldsymbol{\varepsilon_B} = \varepsilon_{xx}\, cos^2\, \alpha_B + \varepsilon_{yy}\, sin^2\, \alpha_B + \gamma_{xy}\, cos\, \alpha_B\, sin\, \alpha_B$$

$$\boldsymbol{\varepsilon_C} = \varepsilon_{xx}\, cos^2\, \alpha_C + \varepsilon_{yy}\, sin^2\, \alpha_C + \gamma_{xy}\, cos\, \alpha_C\, sin\, \alpha_C$$

The calculated normal and shear strains were then used to determine the corresponding maximum and minimum principal strains and stresses. The

maximum principal strain ($\varepsilon 1$), minimum principal strain ($\varepsilon 2$), and principal directions (θ) can then be calculated using the following equations (Equation 4):

Equation 4: Equations to find principal strains and angle of principal directions.

$$\varepsilon_1 = \frac{\varepsilon_{xx} + \varepsilon_{yy}}{2} + \frac{1}{2}\sqrt{\left(\varepsilon_{xx} - \varepsilon_{yy}\right)^2 + {\gamma_{xy}}^2}$$

$$\varepsilon_2 = \frac{\varepsilon_{xx} + \varepsilon_{yy}}{2} - \frac{1}{2}\sqrt{\left(\varepsilon_{xx} - \varepsilon_{yy}\right)^2 + {\gamma_{xy}}^2}$$

$$tan2\theta = \frac{\gamma_{xy}}{\varepsilon_{xx} - \varepsilon_{yy}}$$

The principal strains were then used to calculate the maximum (σ_1), and minimum (σ_2), principal stresses as well as the von Mises stress value ($\sigma_{von\ Mises}$) through Equation 5 below.

Equation 5: Equations to find principal stresses and von Mises stress.

$$\sigma_1 = \frac{E}{1 - v^2}(\varepsilon_1 + v\varepsilon_2)$$

$$\sigma_2 = \frac{E}{1 - v^2}(\varepsilon_2 + v\varepsilon_1)$$

$$\sigma_{von\ Mises} = \left|\sqrt{{\sigma_1}^2 - \sigma_1\sigma_2 + {\sigma_2}^2}\right|$$

E is the Elastic Modulus of the titanium humeral component (E = 114 GPa), and v is the Poisson's Ratio (v = 0.33). The stress state was determined based on the measured strains. Since stress and strain are related through material properties, it is assumed that the stress predominantly acts in two directions in a Cartesian coordinate system, while the third direction (normal to the plane) experiences negligible stress. The material is assumed to have a very thin layer compared to its other dimensions, resulting in no stress variations through the material's

thickness. Therefore, the stress and strain in the third direction are considered to be effectively zero.

3.2.6. PCB Circuit Design

It was necessary to machine cavities in the humeral component to internally house the implant instrumentation. These cavities were a critical part in designing the implant's printed circuit board (PCB) because of the limited space available, their inaccessibility, and vulnerabilities. A customised electronic circuit had to be designed with the required small dimensions to be embedded into the main body cavity of the implant for telemetry.

The custom-designed PCB was therefore required to be small, robust, and reliable in terms of its operation over long periods of time. The shape and size of the PCB rigid base were designed based on the dimensions of the main body cavity where they would be integrated, as seen in Figure 3-13 below.

The electronic circuitry needed to be compact and flexible to fit inside the cavity directly and vertically. The custom-designed circuit is a rigid-flex PCB consisting of four rigid base layers connected by a flexi with a bend radius of 1.6mm. This flexible section allows the board to bend and fold, customising it to the desired shape and eliminates the need for many interconnections and cables. The total thickness of the PCB when flexed is 4.6 mm, which fits comfortably within the internal depth of the cavity, which is 5.8 mm Figure 3-13.

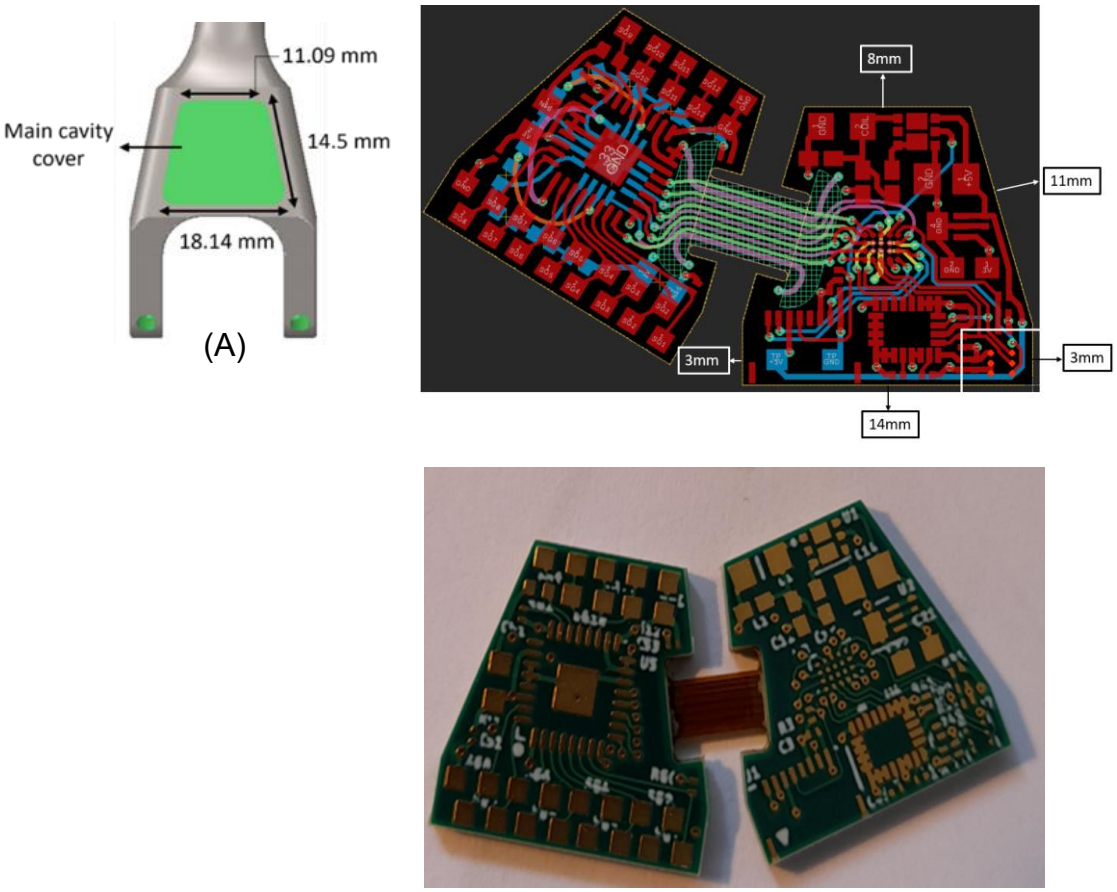

Figure 3-13: (A) Main body cavity dimensions, (B) Demonstrates the printed circuit board (PCB) design, dimensions and manufactured PCB.

The PCB was designed and fabricated by others, having 8 strain gauge channels for the fork and main cavity gauges, although a total of 9 gauges (as 3 rosettes) were mounted around the distal end of implant. This led to one of the gauges in the rosette mounted on the central base cavity not being wired to the electronic circuit. Specifically, the central gauge which was parallel to the hinge axle of the implant, was omitted, leaving the other two gauges (each positioned 45^{o} away) sensitive to X and Z loads. Another 4 strain gauge channels were designated on the PCB for the stem tip gauges, intended for a future study. Subsequently, the telemetry circuit was assembled and populated with all necessary components

for power supply and telemetry. The strain gauges were then wired onto the board to form a serial chain network of gauges with a supply voltage of 3V.

Following fabrication and assembly, the PCB was tested to ensure that it powers up correctly and that there are no short circuits present. The circuit was also tested for functionality to ensure that the strain gauges respond appropriately to input loads and that signals are processed correctly.

For the final complete in vivo telemetry, the instrumentation will be entirely housed inside the implant with the electronic circuitry, located in the main cavity of the implant wired up to a coil encapsulated within a pre-diffusion bonded ceramic endpiece at the tip of the stem. The internal coil is then inductively coupled with an external coil worn by the in-vivo subjects for wireless strain data transmission. However, at this development stage and following the testing, the PCB was placed directly inside the cavity and the tip of the stem was covered with a titanium cap to protect the tip strain gauges. The PCB incorporated a 24-bit analogue to digital converter (ADC) and the three PCB wires come out through a tiny hole in the cavity cover (Figure 3-14). The three wires were for power supply, ground connection and serial data telemetry. The serial data signal was then connected to a computer for data capturing and storage using a customised graphical user interface (GUI) on LabVIEW® software (2013, National Instruments™, Austin, Texas, USA).

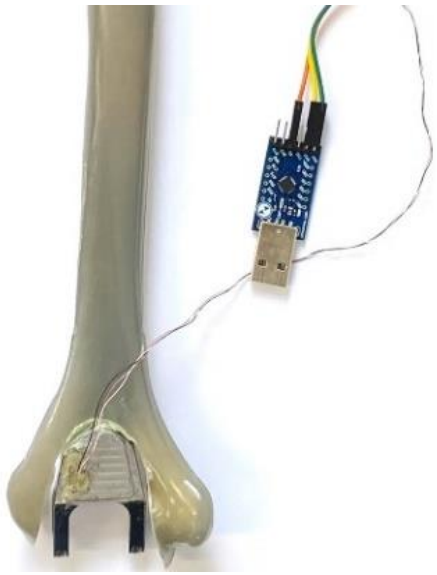

Figure 3-14: Shows the wires exiting the humeral component through a small hole in the cavity cover.

3.2.7. Welding

In vivo, all implanted instrumentation is housed within hermetically sealed cavities. To ensure the hermeticity of the electronic components, welds are required at the two fork cavities, the main cavity, and around the step tip. The electron beam welding process (EBW) was chosen for this weld. Electron Beam Welding (EBW) is a welding process where a high-velocity electron beam is used to join metals together (Węglowski et al., 2016). The kinetic energy of the electrons is converted into heat upon impact, melting the joints and forming a weld. This e-beam welding technique was suitable for welding the covers onto their respective cavities in the humeral component because it allows for precise control over the weld and produces minimal localised heat-affected zones, minimising material stress (Węglowski et al., 2016). Electron beam welding requires substantial equipment and is therefore unsuitable for execution in standard laboratory settings. Four manufactured humeral components (N = 4) and their covers, without the instrumentation inside them, were dispatched for

welding which will be used in the next fatigue testing stage of the modified humeral implants. Upon their return, the four components were thoroughly polished.

3.3. Results

The primary focus of this chapter was to develop a customised, instrumented humeral implant component for total elbow arthroplasty (TEA), capable of reliably and safely housing electronics within it. This was developed over several stages including structural design modifications, analysis and validation, manufacturing of the humeral component, allocation of sites for strain gauges, and the design and fabrication of the implant's PCB circuit.

3.3.1. Stress Analysis and Factor of Safety

The cavities created within the humeral implant prototype were designed to house the implant instrumentation without compromising the component's strength and to keep the maximum stress levels within the allowable limits for a specified factor of safety. The von Mises stress was assessed under worst case loading conditions.

The stress distribution on the humeral component revealed that the maximum von Mises stress on the implant was 96.6 MPa. This value corresponds to a simulated compressive load of 700 N (moderate ADL), as illustrated in Figure 3-15 below. Areas of high stress concentration, particularly around the modified parts of the implant, must be thoroughly accounted for to ensure optimum performance of the implant under physiological loads. Therefore, The stress distribution on the three added cavities was analysed. The stress was predominantly concentrated around the U-shaped forks of the humeral implant.

The outer surface of the medial and lateral forks exhibited similar patterns, with maximum surface von Mises stresses of 83.4 MPa and 64.1 MPa, respectively (Figure 3-16). However, the base surface of the main cavity experienced much lower stress of 18 MPa across the entire face (Figure 3-16). The cover of the main body cavity showed maximum Von Mises stresses of 60.6 MPa, which was similar to the medial fork cavity but lower compared to the lateral fork surface (Figure 3-16).

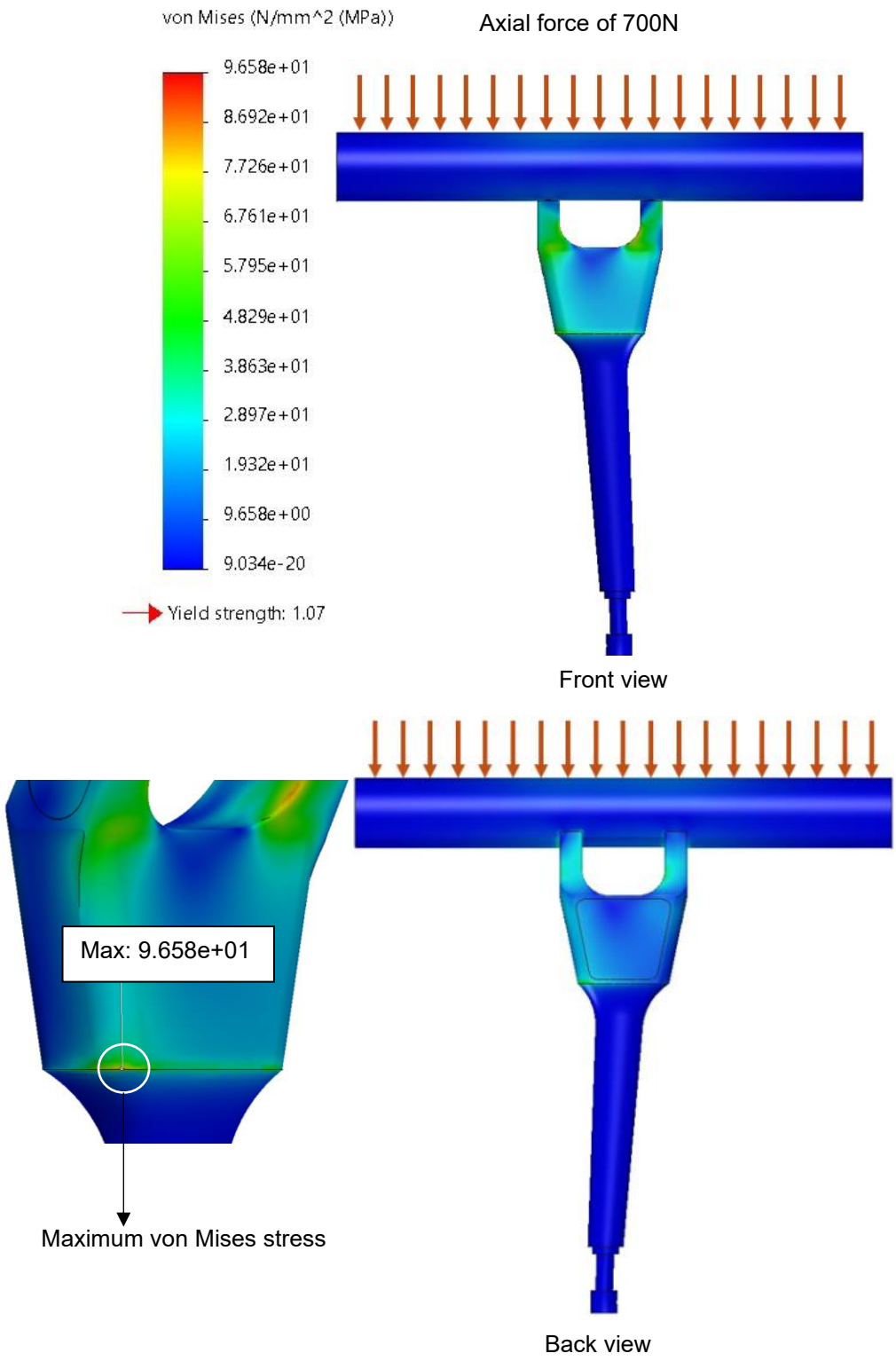

Figure 3-15: Finite Element Analysis (FEA) stress distribution of maximum von Mises stress on the humeral component under 700N axial load.

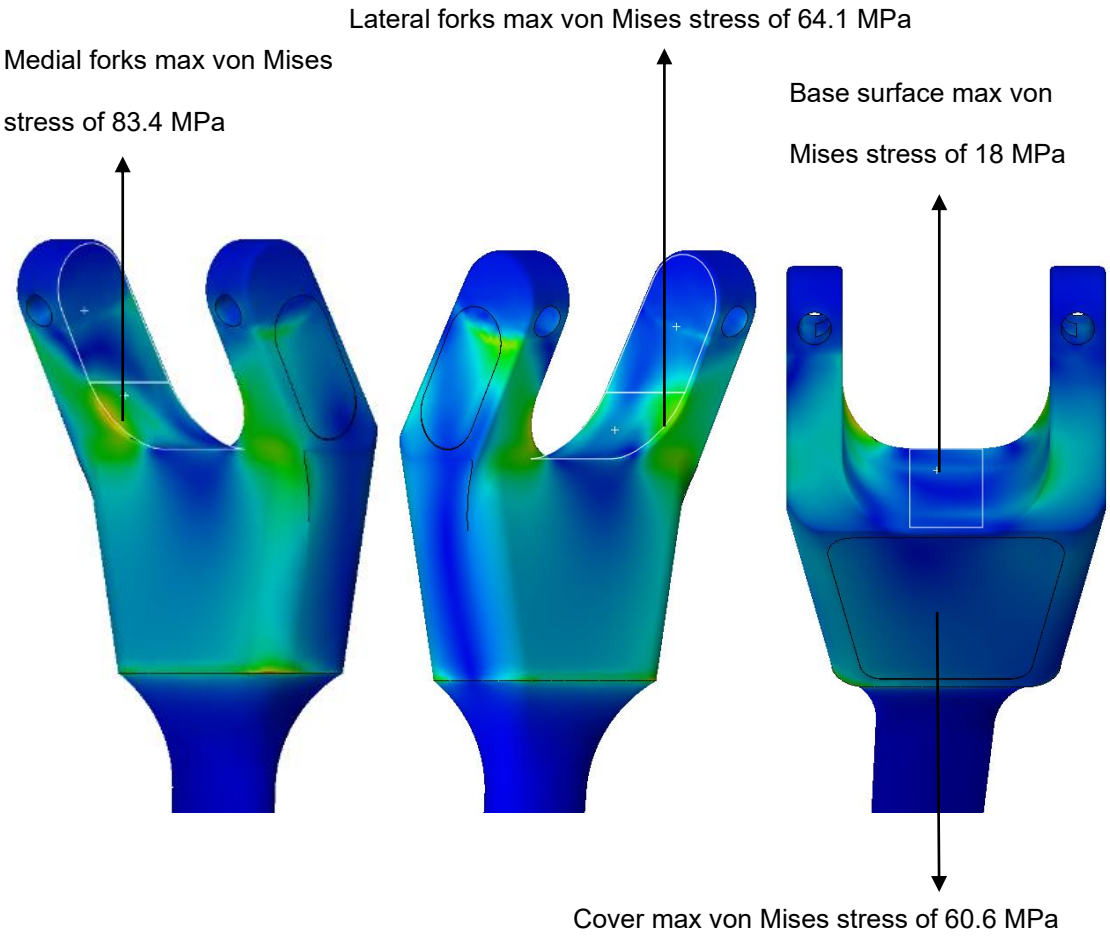

Figure 3-16: Finite Element Analysis (FEA) stress distribution of maximum von Mises stress on the outer surface of the U-shaped forks of the humeral implant under 700N axial load.

The maximum von mises stress was also reported for loads corresponding to different levels of daily activities (ADL). For the categories of light duty, moderate, strenuous, and extreme, the maximum Von Mises stresses were 48.3, 96.6, 193.1, and 288.4 MPa, respectively. Comparing the different types of ADL, the maximum Von Mises stress increased with increasing load, however, it consistently remained well below the yield (1070 MPa) strength of Titanium (Ti6Al4V).

The factor of safety (FOS) was calculated for each of the different ADL categories, as presented in Table 3-3 below. For the moderate activity level (700 N) category, the yield factor of safety (FOS) was 11.1, exceeding the minimum factor of safety of 2 accepted for orthopaedic implants (Khanoki and Pasini, 2013; Dowling, 2013; Browne, 1999). The calculated factor of safety was further validated by the FEA, which yielded a modelled factor of safety of 12.1, as shown in Figure 3-17 below. This value suggests that the modified humeral component is not expected to fail under both static and dynamic loading conditions within the specified load limits and therefore safe for manufacturing.

Table 3-3: Maximum von Mises stress, Yield FoS for all different activities of daily living categories (light duty, moderate, strenuous, extreme).

ADL Category	Peak JRF (N)	Max. von Mises Stress (MPa)	Yield FOS
Light duty	350	48.3	22.2
Moderate	700	96.6	11.1
Strenuous	1400	193.1	5.5
Extreme	2100	288.4	3.7

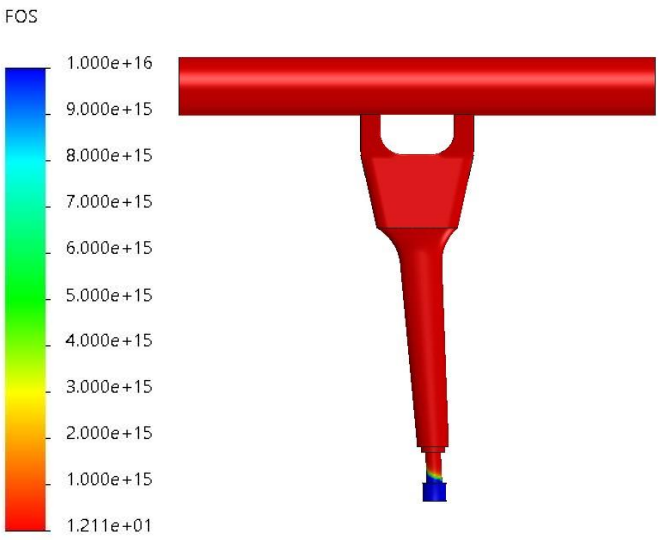

Figure 3-17: Modelled yield factor of safety (FOS).

Resin prototypes of the implant were printed to validate the dimensions. The prototypes were all accurate, and the covers fit perfectly on top of their respective cavities without any geometric mismatch. Subsequently, a total of 10 titanium humeral implant prototypes were manufactured via CNC machining.

3.3.2. Optimal Strain Gauge Sites

Due to the limited geometrical space available on the walls of the forks, points closest to the centre were considered (Figure 3-18). The coordinates of these points are shown in Table 3-4 below.

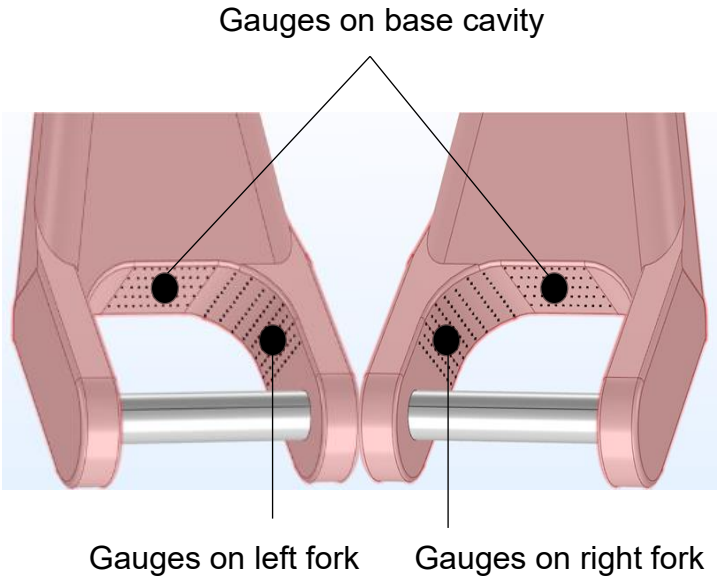

Figure 3-18: Locations of the candidate strain gauge sites on the right fork, left fork and base cavity surface.

Table 3-4: This table presents the coordinates (X, Y, and Z in mm) for 8 strain gauges positioned in the lateral cavity (left fork), base cavity, and medial cavity (right fork).

Strain Guage Location		X (mm)	Y (mm)	Z (mm)
Lateral Cavity (left fork)	Gauge 1	11.4	-8.1	-9.7
	Gauge 2	11.4	-8.1	-9.7
	Gauge 3	11.4	-8.1	-9.7
Base Cavity	Gauge 4	4.2	1.0	-6.3
	Gauge 5	4.2	1.0	-6.3
Medial Cavity (right fork)	Gauge 6	-11.4	-8.1	-9.7
	Gauge 7	-11.4	-8.1	-9.7
	Gauge 8	-11.4	-8.1	-9.7

In Table 3-5 is given a sample of the raw axial and shear strain data obtained from the finite element analysis for one of the strain gauge sites for each individually applied load. Relevant raw axial and shear direct strains were rotated along YZ plane for this particular site to align with the local gauge surface from which the gauge strain was calculated for each separate position using the previously described Equation 1.

Table 3-5: This table shows a sample of the raw axial and shear strain data for a single gauge site under applied loads of Fx, Fy, Fz, Mx, My and Mz.

	Raw Axial and Shear Strains at gauge site						
Load Applied	**EPYY**	**EPZZ**	**EPYZ**	**Rotated EPYY**	**Rotated EPYZ**	**Gauge Strain**	**Unit**
FX	-1.8E-06	-1.8E-05	2.3E-04	-1.8E-06	2.3E-04	-1.8E-05	μstrain/1000N
FY	-6.3E-04	4.2E-04	-1.3E-04	-6.3E-04	-1.3E-04	-6.3E-04	μstrain/1000N
FZ	3.7E-04	-5.1E-04	-1.7E-04	3.7E-04	-1.7E-04	3.7E-04	μstrain/1000N
MX	-2.1E-08	1.8E-08	-3.1E-08	-2.1E-08	-3.1E-08	-2.1E-08	μstrain/1Nm
MY	2.1E-06	-2.6E-06	-1.7E-06	2.1E-06	-1.7E-06	-2.6E-06	μstrain/1Nm
MZ	3.2E-06	-2.1E-06	5.5E-07	3.2E-06	5.5E-07	3.2E-06	μstrain/1Nm

The strain sensitivity matrix for these points is compiled in Table 3-6 below. The sensitivity matrix compiled eight different tensile (positive) and compressive (negative) strains at the 8 positions of interest. The smallest sensitivity measured was a compressive strain of -1.8E-09 microstrain per Newton (μstrain/N) due to Fx in the lateral cavity while the largest sensitivity observed was a compressive strain of -3.3E-06 μstrain/Nm due to Mz in the medial cavity (Table 3-6).

Table 3-6: Strain sensitivity matrix for all 8 positions located on lateral cavity, base cavity and medial cavity due to all 6 degrees of freedom applied.

Sensitivity matrix due to all 6 individual d.o.f							
Guage Location	**Gauge Angle (deg)**	**Fx**	**Fy**	**Fz**	**Mx**	**My**	**Mz**
Lateral Cavity (left fork)	0	-1.8E-08	4.2E-07	-5.1E-07	1.8E-08	-2.6E-06	-2.1E-06
	45	2.2E-07	-2.3E-07	-2.4E-07	-3.2E-08	-2.0E-06	1.1E-06
	90	-1.8E-09	-6.3E-07	3.7E-07	-2.1E-08	2.1E-06	3.2E-06
Base Cavity	0	-4.2E-08	1.2E-07	-5.4E-07	8.7E-09	3.3E-07	8.3E-08
	90	1.2E-07	3.6E-08	2.1E-07	-4.3E-08	-2.7E-07	2.7E-08
Medial Cavity (right fork)	0	-5.8E-08	3.6E-07	5.7E-07	2.8E-08	2.5E-06	2.0E-06
	45	-2.7E-07	-2.4E-07	-3.7E-07	-3.3E-08	2.3E-06	-1.0E-06
	90	-6.2E-09	-5.9E-07	4.5E-07	-4.2E-08	-2.1E-06	-3.3E-06
		μstrain/N	μstrain/N	μstrain/N	μstrain/Nm	μstrain/Nm	μstrain/Nm

The locations on both the medial and lateral fork surfaces experienced compressive strain when an axial force (FY) was applied. However, the lateral fork underwent slightly more compressive strain (-6.3e-07 μstrain/N) compared to the medial cavity (-5.9e-07 μstrain/N). In contrast, the points on the base cavity were less sensitive to the applied axial force, exhibiting a tensile strain of 3.6e-08 μstrain/N.

Applied FX resulted in less compressive strain on both the medial and lateral forks (less sensitive) compared to FY, with values of -6.2e-09 μstrain/N and -1.8e-08 μstrain/N, respectively. However, the points on the base cavity were more sensitive to this applied load, exhibiting a compressive strain of -4.2e-08 μstrain/N. Similarly, both forks were less sensitive to the load applied in FZ than FY, but more sensitive than the load applied in FX. The base cavity experienced

the highest tensile strain value of 2.1e-07 μstrain/N when FZ was applied, compared to FX and FY. Overall, Fy imposed the greatest compressive strain on the medial and lateral cavities and Fz imposed the greatest tensile strain on the base cavity of the humeral implant.

Both forks of the implant were highly responsive to the moment applied about the z-axis of the implant (Mz), producing the highest compressive strain of -3.3e-06 μstrain/Nm in the medial cavity and a tensile strain value of 3.2e-06 μstrain/Nm along the lateral fork cavity. In contrast, the base cavity experienced a lower sensitivity of 2.7e-08 μstrain/Nm.

Sensitivities due to My were higher than those due to Mx for the fork cavities but remained below the strains generated by Mz. The peak sensitivity for the base cavity was caused by moments about the y-axis of the implant (My), with a value of -2.7e-07 μstrain/Nm, followed by strains due to Mx (-4.3e-08 μstrain/Nm) and strains due to Mz. The matrix was inverted, as shown in Table 3-7 below, and examined to assess how independent each degree of freedom was from the others.

Table 3-7: Inverse strain sensitivity matrix due to all degrees of freedom applied.

Inverse Sensitivity matrix due to all 6 individual d.o.f							
Guage Location	**Gauge Angle (deg)**	**Fx**	**Fy**	**Fz**	**Mx**	**My**	**Mz**
Lateral Cavity (left fork)	0	-8.7E+06	1.2E+06	5.6E+05	-1.3E+07	-7.3E+05	5.2E+05
	45	-1.2E+06	2.1E+05	-1.3E+05	-7.9E+06	-2.1E+05	2.1E+05
	90	-4.9E+06	-1.7E+05	3.7E+05	-5.0E+06	-3.8E+05	4.0E+05
Base Cavity	0	3.3E+06	-4.6E+05	-7.2E+05	6.2E+06	2.8E+05	-2.0E+05
	90	9.3E+05	1.0E+06	1.9E+05	-1.5E+07	7.1E+04	-1.9E+04
Medial Cavity (right fork)	0	-3.9E+06	10.0E+05	7.9E+05	-7.5E+06	-2.4E+05	2.5E+05
	45	-3.3E+06	4.1E+05	-1.3E+05	-1.1E+07	-7.9E+04	1.1E+05
	90	-7.9E+05	-3.7E+05	4.5E+05	-2.6E+05	-8.4E+04	-7.2E+04
		μstrain/N	μstrain/N	μstrain/N	μstrain/Nm	μstrain/Nm	μstrain/Nm

The graph shown in Figure 3-19 displays the correlation coefficients between all 6 degrees of freedom. The correlation between the applied force FX and other degrees of freedom generally indicates low interdependence. The weakest correlation involving FX is with FZ, showing a coefficient of -0.17, suggesting a very weak inverse relationship. On the other hand, FX exhibits a stronger positive correlation with MY, with a coefficient of 0.70, indicating that increases in FX are associated with increases in MY. Moreover, FY appears largely independent of the other components, though it has a notable negative correlation with MX of -0.67. This suggests that increases in FY tend to correspond with decreases in MX. The most significant relationship observed is between MY and MZ which have a strong negative correlation coefficient of -0.79. This strong inverse relationship implies that increases in MY are strongly associated with decreases

in MZ. Conversely, the weakest correlations in the dataset are between FZ and MX, and FZ and MZ, both showing coefficients near zero (approximately ±0.07). These coefficients, despite their opposite signs, indicate that FZ has almost no linear relationship with MX and MZ. Overall, the correlation coefficients reveal that most degrees of freedom are highly independent of one another, with only a few pairs showing moderate to strong correlations.

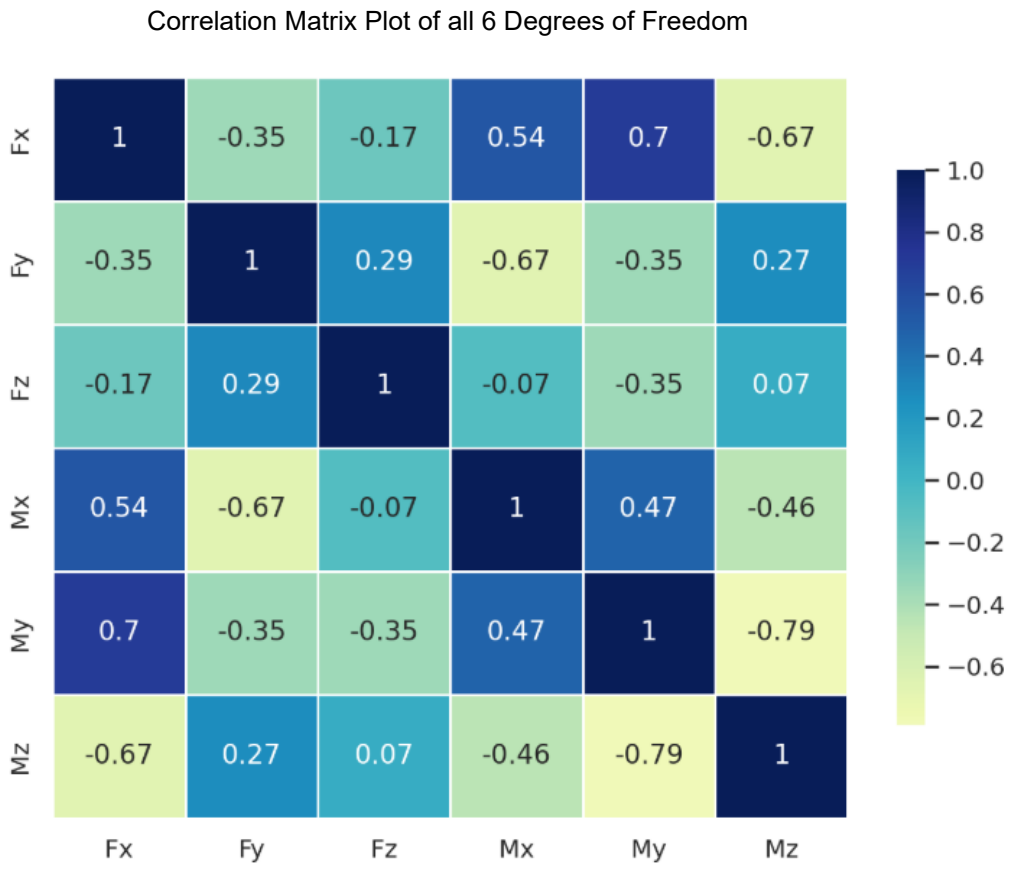

Figure 3-19: Correlation coefficients between all 6 degrees of freedom (Fx, Fy, Fz, Mx, My, Mz), displaying the correlation values between forces and moments. The colour scale represents the strength of the correlation, with dark blue indicating strong negative correlations, light green representing weak or no correlation, and dark green showing strong positive correlations.

A random noise of 1.0E-06 was introduced into the original matrix, and peak sensitivities were calculated for each individually applied load, as seen in Table 3-8. The gauge aligned at 90° on the base cavity surface was the most sensitive when either a force along the x-axis of the implant (FX) or a moment about the z-axis MZ was applied, with corresponding peak strain values of 4.3E-07 and 9.7E-07 μstrain/N, respectively. Peak sensitivities due to Fy and MZ occurred at the lateral fork cavity, specifically at the gauge aligned at 90°, with values of 6.3E-07 and 3.7E-06 μstrain/N, respectively. Lastly, the strain peaked on the surface of the medial fork cavity when either a force along the z-axis (FZ) or a moment of (My) was applied.

Table 3-8: Peak sensitivities for all degrees of freedom (Fx, Fy, Fz, Mx, My, Mz).

Peak Sensitivities					
Fx	Fy	Fz	Mx	My	Mz
4.3E-07	6.3E-07	5.7E-07	9.7E-07	2.9E-06	3.7E-06
μstrain/N			μstrain/Nm		

The inverse matrix was multiplied by the original sum of strains to retrieve the originally applied forces and moments through the relationship between the applied loads and moments (L). Loads and moments consist of the forces $L_1 = F_x$, $L_2 = F_y$, $L_3 = F_z$, $L_4 = M_x$, $L_5 = M_y$ and $L_6 = M_z$ in and around x, y and z directions and the strain gauge signals (S) output is expressed by the below matrix equation.

$$S = C \times L$$

Where **S** is the recorded strain gauge signals, **L** is the applied loads and moments, and **C** is the calibration matrix. The recorded signals were converted back into forces and moments by using the inverse of the calibration matrix as shown in the equation below where M is the inverse matrix (C^{-1}).

$$L = M \times S$$

The retrieved Fx was calculated to be 1002 N, showing a minimal error of 2 N compared to the originally applied load of 1000 N. Similarly, the calculated FY and FZ were 997 N and 998 N, respectively. These accurately reflected the original loads with low percentage errors of - 0.3% and -0.2%. However, the retrieved Mx was significantly different from the originally applied Mx (1 Nm) by 8 Nm as detailed in Table 3-9 below.

Table 3-9: This table displays the total sum of strains (in μstrain) for all 8 positions in response to 6 degrees of freedom loads applied. The retrieved loads and their associated errors are also presented.

Gauge Angle (deg)	**Fx**	**Fy**	**Fz**	**Mx**	**My**	**Mz**	**Sum of Strains**
0	-1.7E-05	4.2E-04	-5.1E-04	2.1E-07	-2.2E-06	-1.4E-06	-1.1E-04
45	2.2E-04	-2.3E-04	-2.4E-04	5.4E-07	-1.2E-06	1.6E-06	-2.5E-04
90	-1.3E-06	-6.3E-04	3.7E-04	-1.8E-08	2.9E-06	3.8E-06	-2.5E-04
0	-4.1E-05	1.2E-04	-5.4E-04	4.8E-07	3.4E-08	7.4E-08	-4.6E-04
90	4.3E-04	3.7E-05	-6.1E-05	3.4E-07	5.0E-07	6.1E-07	4.1E-04
0	-5.7E-05	3.6E-04	5.7E-04	5.7E-07	3.2E-06	2.3E-06	8.7E-04
45	-2.7E-04	-2.4E-04	-3.7E-04	8.1E-07	2.4E-06	-1.3E-06	-8.8E-04
90	-5.9E-06	-5.9E-04	4.5E-04	6.1E-07	-1.7E-06	-3.6E-06	-1.4E-04
Unit	μstrain	μstrain	μstrain	μstrain	μstrain	μstrain	μstrain
Applied loads	1000	1000	1000	1	1	1	
Retrieved loads	1002	997	998	9	1	1	
Error	2	-3	-2	8	0	0	
% Error	0.2	-0.3	-0.2	800	-	-	
Unit	N	N	N	Nm	Nm	Nm	

3.4. Discussion

This chapter focused on the development of a customised humeral implant component for TEA, designed to reliably and safely house instrumentation. The specific objectives achieved include included designing and manufacturing a modified version of an elbow humeral component, analysing the stress experienced by the modified humeral component under peak physiological loads, determining the optimal strain gauge locations based on the strain distribution pattern on the implant, and developing the implant PCB circuit and instrumentation.

3.4.1. Prototype Design

It is important to emphasise that the humeral implant described in this study is a prototype developed primarily for experimental validation and biomechanical analysis, rather than as a fully optimised clinical implant. With an overall stem length of 116 mm, it falls within the category of short-stemmed implants commonly used in clinical practice, providing a reasonable approximation of average humeral anatomy. However, this prototype is a fixed size and does not accommodate the anatomical variability found across different patients. Future iterations will need to address this by offering a range of implant sizes and geometries to ensure broader clinical applicability. Although the implant maintains essential geometric features and alignment consistent with the standard Discovery implant, modifications to house instrumentation have slightly increased its dimensions. These changes were carefully designed to minimise any adverse effects on bone preservation and mechanical integrity, yet further validation is required before clinical use. Therefore, while the prototype delivers valuable

biomechanical insights, additional development and testing are necessary before it can be translated into routine clinical practice.

3.4.2. Prototyping and Manufacturing

While the combination of Stereolithography (SLA) 3D printing and CNC machining allowed for the precise creation of the humeral implant prototype, it is important to recognise several limitations inherent to these manufacturing methods. The SLA 3D printing process, although quickly produced accurate physical models to assess design dimensions and fit, used photopolymer resin materials rather than the final titanium alloy. This means that the prototypes created during this stage do not fully replicate the mechanical strength, durability, or surface characteristics required for actual implant use. Therefore, any conclusions drawn from these resin models must be cautiously interpreted with regard to their real-world biomechanical performance.

CNC machining was used to manufacture the final titanium component, offering high precision and repeatability necessary for medical implants. However, this method has some constraints when it comes to producing highly complex internal geometries, which might limit the potential design freedom. This limitation could affect the ability to further optimise the implant shape or internal structure for improved biomechanical performance or integration with bone.

In terms of clinical impact, while Electron Beam Welding (EBW) provided a controlled and biocompatible means of joining the cavity covers to the implant, the welding process can introduce residual stresses and subtle changes in the microstructure of the titanium alloy. These factors might influence the long-term fatigue behaviour and corrosion resistance of the implant, although this would need to be confirmed through extensive mechanical testing and in vivo studies.

Overall, these manufacturing limitations highlight that this implant remains a prototype intended primarily for experimental validation rather than immediate clinical use. Future development will need to explore advanced manufacturing techniques such as more sophisticated additive manufacturing methods or hybrid approaches. This will better replicate complex anatomies, allow for patient-specific customisation and ensure the mechanical reliability required for safe, long-term implantation.

3.4.3. Prototype Instrumentation

The instrumented humeral implant prototype developed in this chapter marks an important advancement in elbow biomechanics. However, before translating this technology to human studies, several critical factors must be addressed. First, the instrumentation developed within this prototype requires thorough biocompatibility testing to ensure that all materials, including adhesives, sensors, and coatings, do not cause adverse biological reactions. Additionally, the implant must withstand standard sterilisation processes without compromising sensor accuracy or mechanical integrity.

Another important consideration is the long-term stability and reliability of the embedded electronics, particularly under the repeated loading conditions experienced in vivo. Wireless data transmission would also need to be integrated and validated, as tethered systems are not feasible for human use. Furthermore, regulatory requirements such as CE marking or FDA approval will necessitate extensive preclinical testing, potentially including animal models, to demonstrate safety, durability, and functionality over time.

Finally, it is important to acknowledge the potential limitations in sensor calibration, signal drift, and integration with the bone–implant interface in a live setting. These challenges highlight the need for further refinement of the implant and experimental protocol before clinical application can be considered. However, by identifying these areas early, this work lays the groundwork for future research focused on safe and effective translation to human use.

3.4.4. Stress Analysis and Factor of Safety

It was important that the strength of the humeral component remained uncompromised and that the maximum stress levels were kept within allowable limits for a specified factor of safety. The maximum von Mises stress on the implant was 96.6 MPa under a simulated compressive load of 700 N, which corresponds to moderate activities of daily living (ADL). This localised stress was found to be between the stem and the main body interface of the implant, as expected. This can be explained by the added cavity and altered geometry, which may have introduced such stress risers. However, the corners of the main body of the implant were designed with generous radii to minimise stress concentrations in the distal humerus, avoiding the risk of fractures in the previously intact medial or lateral epicondyles.

One important limitation of this study is the simplified geometry of the humeral implant used in the FE model. In particular, the anterior flange was not included. This design feature plays a key role in resisting anterior migration of the implant and in reducing stress on the cement mantle (Morrey et al., 2009; Brinkman et al., 2005), so its omission could lead to an underestimation of local stresses during elbow extension or posterior loading. Additionally, the original Discovery implant incorporates a 5° internal rotation of the humeral stem relative to the

flange to account for natural humeral retroversion and ensure proper alignment of the articular surfaces (van der Lugt et al., 2017; Sanchez-Sotelo, 2011). This rotational feature was also left out of the current model, which may have a minor effect on joint contact mechanics and alignment under non-axial loading. These simplifications were necessary to accommodate the internal instrumentation and are unlikely to impact results under pure axial loading. However, some caution is needed when applying these findings to more complex in vivo loading conditions. The stress was particularly distributed around the U-shaped forks of the implant with the outer surfaces of the medial and lateral forks exhibiting maximum von Mises stresses of 83.4 MPa and 64.1 MPa, respectively. The medial fork experienced greater stress because it is farther from the stem support and the load line of action followed by the lateral fork of the implant. The base surface of the main cavity, however, experienced much lower stress at 18 MPa. This can be explained by the fact that the greatest amount of force passes through the elbow articulation (distal end of the humeral component) at 0-30 degrees of flexion and in pronation (France et al., 2024; Islam et al., 2020). This aligns well with previous literature on the stress distribution around the elbow joint. A study used pressure sensitive transducers reported that the stress distribution was 57% across the radiocapellar and 43% across the ulnohumeral articulation (Halls & Travill, 1964). An et al. demonstrated that if the line of action of the contact pressure is in the middle of the articulation, the stress is almost equally distributed across the articular surface. Conversely, when the force is directed towards the margin of the articulation, the weight-bearing surface becomes smaller, the contact stresses become higher and the stress distribution becomes uneven (Morrey, 2017).

The yield factor of safety (FOS) was calculated based on the maximum stress concentration (96.6 MPa) on the humeral implant due to an applied load of 700N (moderate category) and was determined to be 11.1, as listed in Table 3-3. This value indicates that the humeral component is expected to perform safely under in vivo conditions during activities of daily living (ADL) without any risk of fracture for this applied load. The FOS was significantly greater than two (FOS = 11.1 > 2), which is the minimum factor of safety accepted for orthopaedic implants (Khanoki and Pasini, 2013; Dowling, 2013; Browne, 1999). Similarly, the FOS of the implant under a high compressive load of 2100 N, which corresponds to extreme activities of daily living, was marginally greater than three (FOS = 3.7 > 2), further providing the confidence that this implant is capable of handling the stresses experienced during such physiological conditions and therefore safe for manufacturing.

3.4.5. Optimal Locations for Strain Gauging

Initial analysis of strain gauge sites was based on available geometrical space rather than precise locations. The strain distribution was thoroughly investigated to ensure adequate sensitivity to all degrees of freedom applied. The strain distribution resulting from each individually applied load on the humeral component is shown in Table 3-5. Tensile stress at the local point resulted in positive strain while a negative strain value indicates compression due to compressive stress. The majority of strain concentrated around the distal part of the humeral component, particularly the medial and the lateral forks of the implant.

The medial cavity experienced the largest strain of -3.3E-06 μstrain/Nm due to a moment about the z-axis of the implant (MZ). This is expected, as moments

around the z-axis of the implant result in flexion/extension motions, which impose significant strain on the implant. The locations on both the medial and lateral fork surfaces experienced compressive strain when an axial force (FY) was applied. However, the lateral fork underwent slightly more compressive strain (-6.3e-07 μstrain/N) compared to the medial cavity (-5.9e-07 μstrain/N). Although this result may intuitively seem unexpected, it can be attributed to the irregular geometry of the implant. The complex shape and variations in the cross-sectional area could have led to an uneven distribution of strain across two forks of the implant. In contrast, the points on the base cavity were less responsive to the applied axial force, showing a tensile strain of 3.6e-08 μstrain/N. This observation aligns with the expectation that the majority of the applied forces are concentrated around the lower part of the humeral component, thereby causing less deformation in the base cavity compared to the forks of the implant.

Upon assessment of the correlation between all different degrees of freedom applied, FY appeared largely independent of the other components, though it has a notable negative correlation with MX (-0.67). This suggests that increases in FY tend to correspond with decreases in MX. This is because when the elbow joint experiences loading within the same plane, such as in varus or valgus loading, the applied shear forces (FY) influence the distribution of loads along the implant structure, which in turn affects the magnitude of the bending moment generated about the medial-lateral x-axis. Consequently, regions with significant shear force often show a corresponding effect on the bending moment magnitude, particularly near supports or points of fixation where the shear force is maximised. However, the correlation coefficients reveal that most degrees of freedom are highly independent of one another, with only a few pairs showing moderate to strong correlations.

A random noise of 1.0E-06 was incorporated into the sensitivity matrix model to assess how sensitive the system is to random noise and variations, thereby testing the strength of strain analysis. The percentage errors observed in the calculated forces and moments are attributed to this added noise, revealing differences as small as 0.2% for a difference of 2N between applied and calculated FX and FZ. The error between applied FY and calculated Fy was only 3N, suggesting insignificant variations and thus validating the stain analysis model used in analysing the strain at the desired sites. The calculated Mx was 9Nm compared to the applied 1Nm, showed a significant error of 8Nm. Further investigation into these inaccuracies is necessary to refine the strain sensitivity model. Confidence in the chosen gauge locations and orientations is primarily supported by the correlation coefficients, which ensure that each degree of freedom is accurately resolved. Based on the sensitivity analysis, the resolution for each degree of freedom was estimated using the strain resolution of the instrumentation, which is 1 μstrain. The calculated resolutions are as follows: 5.5e-08 N for FX, 2.8e-07 N for FY, 4.9e-06 N for FZ, 1.2e-08 Nm for MX, 3.8e-06 Nm for My and 3.8e-07 Nm for MZ.

These values represent the smallest forces and moments that the system can reliably detect. The sensitivity values, derived from the calibration matrix, confirm that the gauge locations are adequate for resolving the forces and moments of interest.

This chapter presented several limitations. One of which is that a single compressive load was applied for simplicity in the finite element (FE) study to assess the safety of the implant, without considering rotational movements such as pronation/supination or muscle and soft tissue forces. This may have limited our understanding the safe behaviour of the humeral implant under extreme

loading conditions. However, the moment arm for prono-supination is significantly smaller compared to flexion-extension (compressive load) (Amis et al., 1979; An et al., 2008; Chadwick and Nicol, 2000).

A limited range of positions was deliberately selected based on the available space in the fork cavities so by focusing on the strain behaviour of those representative regions, the strain response to applied axial and shear loads can be examined. While the FE study used to select strain gauge sites cannot accurately reproduce the in vivo strain behaviour and load transfer on the humeral component, it has been instrumental in understanding the strain sensitivity of the surface of interest to likely in vivo loads. This study highlighted the interdependence between each unique degree of freedom applied, which can be attributed to the irregular geometry of the humeral implant and the varying orientations of the surfaces to which the strain gauges were bonded. These greatly helped to discriminate between forces and moments acting along different axes, as the non-uniform surface orientations provide distinct strain patterns, thereby improving the sensitivity and accuracy of the strain measurement system.

Another limitation is that strain gauging was practised on resin prototypes before being applied to the actual titanium (Ti6Al4V) humeral implant. The surface preparation of resin differs from that of titanium, potentially affecting the adhesion and accuracy of the strain gauges. The titanium prototypes were carefully prepared to ensure accurate strain measurements in the subsequent chapters. Despite the placement of the gauges on the inner surfaces of the titanium prototypes and strain behaviour was studies on the outer surface, it was found that a 1mm wall thickness did not significantly alter the strain sensitivities. However, this may not hold true for larger wall thicknesses.

3.5. Conclusion

In this chapter, a customised instrumented humeral component prototype for Total Elbow Arthroplasty (TEA) has been developed for the first time to enable the measurement of joint reaction forces during activities of daily living in vivo. The work focused on designing and manufacturing a humeral component prototype with geometrical modifications capable of housing strain gauges and instrumentation while ensuring its structural integrity and performance under peak physiological loads. As an early-stage prototype, this design will serve as the foundation for future iterations, which will undergo further refinement and validation prior to clinical application.

The design is a geometrically modified version of the Discovery humeral implant stem, comprising three primary regions: the humeral stem, the humeral body (the middle part between the stem and forks), and two forks for mating with the condylar components. To accommodate the instrumentation for in vivo strain measurement, the humeral body and forks were modified to include three cavities accessible via welded covers.

Detailed finite element analysis (FEA) was performed to validate the design and determine optimal strain gauge locations. The results showed that the maximum von Mises stress experienced by the humeral implant was 96.6 MPa under a simulated compressive load of 700 N, representative of moderate activities of daily living (ADL). The yield factor of safety (FOS) was calculated for various ADL, ranging from light tasks (22.2) to moderate (11.1), strenuous (5.5), and extreme (3.7) activities. The FOS values remained well within acceptable limits, even under extreme loading conditions, where it exceeded the minimum required threshold of 2 for orthopaedic implants. These findings confirmed the robustness

and safety of the modified implant design, enabling its successful manufacture from titanium grade 5 (Ti-6Al-4V).

Strain distribution analysis identified the optimal strain gauge locations to ensure adequate sensitivity to all applied degrees of freedom. The study revealed that strain was predominantly concentrated around the medial and lateral forks of the implant, with the medial cavity experiencing the highest strain due to flexion/extension moments. Consequently, the titanium humeral implant was fitted with strain gauges at three key locations: the two fork cavities and the main body cavity. The pre-attached strain gauge cables were connected to a customised printed circuit board (PCB) embedded within the main body cavity of the implant.

Overall, this chapter presents the development of a functional and instrumented humeral component prototype designed with the aim of enabling in vivo strain measurement in the future, representing a promising step towards advancing TEA instrumentation for biomechanical studies.

Building on this foundation, the next chapter examines the performance and durability of this customised prototype through fatigue testing under simulated physiological loads. Furthermore, a strain validation study is conducted to compare the measured strains with the modelled strains predicted by finite element analysis (FEA). This investigation is essential for assessing the long-term reliability of the implant prototype.

Chapter 4: Fatigue Test Evaluation of a Prototype Humeral Component for an Instrumented Total Elbow Prosthesis and Strain Validation Study

4.1. Introduction

This chapter details the computational and experimental methods used to fatigue test a novel customised Ti6Al4V humeral component prototype for an instrumented Total Elbow Arthroplasty (TEA). Four Ti6Al4V humeral stems (N = 4), with modified geometry compared to the Discovery humeral stem, were designed, and manufactured for testing in this study. Finite Element (FE) models, including FE fatigue models, were validated, and used to evaluate the stress distribution on the humeral component and its safety. A brief review of currently available fatigue-tested humeral stem implants is also provided.

In comparison to the 10-year survival rates of 95% for total hip arthroplasty (THA) and 90% for total knee arthroplasty (TKA), the survival rate for TEA stands at a comparatively lower rate of 79.2% (Welsink et al., 2017). While TEA provides satisfactory pain relief and restores elbow stability, there is relatively high failure with the rate of reported complications ranging between 11% and 38% (Welsink et al., 2017). Infection, aseptic loosening, and periprosthetic fracture are the most common complications requiring revision surgery (Kwak et al., 2019). Revision surgery is associated with increased bone and soft tissue trauma, demanding complex solutions and therefore cost; it is often surgically challenging, and outcomes are worse compared to primary TEA. The use of TEA appears to be increasing at 8% annually, driven by its increasing use among younger patients with higher demands (Day et al., 2010; Triplet et al., 2016).

The design of stemmed TEA prostheses has developed as the indications for TEA have changed. The principle of preservation of bone architecture for ease of later revision has led to an evolution from fully constrained (in which inter-prosthetic stability and motion is determined by the shape and close ‘fit’ of the non-anatomic prosthetic articulation surfaces) to unconstrained (in which inter-prosthetic stability is conferred by the interaction of relatively anatomic prosthetic surfaces and periarticular ligaments) prostheses. The relative anatomicity of the unconstrained prostheses requires the preservation or restoration of the periarticular stabilising ligaments: this is difficult to achieve so all current TEA implants are designed as a semi-constrained articulation, providing relative inter-prosthetic stability with good functional outcomes. Consequently, this implant type is widely used in TEA (Egidy et al., 2019). However, the overall survival rates for all elbow arthroplasties stand lower than those observed for THA and TKA at 92% over 5 years, 81% over 10 years, 71% over 15 years, and 61% over 20 years (Welsink et al., 2017).

In the absence of periprosthetic infection and fracture, the most common reason for diminishing prosthetic survival remains aseptic loosening. It is axiomatic that this depends on the effective bonding of the humeral and ulnar implant-bone interfaces for load-sharing across the joint during normal activities of daily life (ADL). Such activities commonly involve load bearing prono-supination of the forearm, generating torque at the elbow. In intrinsically constrained elbow replacements, this torque is absorbed directly at the interface between the humeral implant and the bone. In the native elbow torque is distributed in the lateral and medial epicondylar regions, while in stemmed TEA without close implant-bone interface at the epicondylar region torque is transferred to the stem and tip of the humeral prosthesis. The actual torque generated in the native elbow

during ADL remains unknown: forces generated across the elbow have been calculated from basic biomechanical principles but hitherto not measured in vivo. Direct measurement of these forces acting on a joint or joint replacement is considered the gold standard for understanding bone-on-bone forces. For example, Bergmann et al. measured the resultant hip joint forces and their orientations during activities such as walking and running in two patients, using instrumented total hip prostheses to capture precise forces and moments directly at the joint (Bergmann et al., 1993; Graichen et al., 1999). Other studies have also measured the contact forces and moments directly at the shoulder (Westerhoff et al., 2009), as well as tibiofemoral forces in total knee arthroplasty using instrumented implants (Kirking et al., 2006).

There are no internationally recognised test standards (such as ASTM/ISO) for assessing the durability of contemporary TER implants, and methods for the preclinical evaluation of total elbow arthroplasties. The few available data on elbow prosthesis testing commonly report on varus-valgus laxity of the joint. One such study in 1992 compared the varus-valgus (VV) stability of a "loose hinged" modified Coonrad elbow prosthesis with an intact elbow using a system of pulleys to mimic muscle contraction and simulate flexion-extension motion (O'Driscoll et al., 1992). Joint kinematics were then measured via an electromagnetic tracking sensor revealing slightly higher prosthesis laxity than that of the intact cadaveric elbow joint. Both intact and reconstructed joints have displayed less VV laxity than their respective limits. It was suggested that the soft tissues of the joint absorb some of the forces and moments that would otherwise be transferred to the interface between the prosthesis and the bone in a reconstructed joint.

In 2000, Schneeberger et al. investigated the motion patterns and laxity of the Souter-Strathclyde prosthesis in eight cadaveric elbows. They used a pulley

mechanism to simulate elbow flexion, rotated the forearm by 90° to generate VV, and utilised an electromagnetic tracking sensor to measure kinematics. Their findings showed significant differences in the axis of rotation and motion patterns between the reconstructed and intact elbows. These differences were attributed to the articular geometry and the compression forces across the elbow resulting from muscle loading (Schneeberger et al., 2000).

In 2005, An developed a custom material testing machine to examine how the different designs of prosthesis influence joint stability. The testing protocol involved rotating the ulna in the varus-valgus (VV) direction with the humeral component fixed at 90° flexion and unconstrained in the z-translation, with the movement stopped at 15° of rotation. Axial loads of 10 N, 40 N, and 90 N were applied, and the maximum torque and corresponding displacement were recorded. Among the unhinged implants, the Souter and Kudo type 5 were the most constraint. An also assessed the laxity of the elbow prostheses, following the same methodology as King et al. (1994) (Ewald, 1995), and similar to O'Driscoll et al. (1992) and Schneeberger et al. (2000) (An, 2005). The study revealed that all elbow prostheses showed greater laxity than the intact elbow and that increasing the muscle load decreased VV laxity. This study confirmed that joint constraint depends on both the surrounding soft-tissues and the congruity of the articular geometry.

Recently, De Vos et al. (2013) measured the VV laxity of the modular Latitude total elbow prosthesis. They simulated active muscle contraction by applying axial forces of 20 N to the triceps, 10 N to the biceps, and 10 N to the brachial muscles. Motion tracking mechanism was also employed here. They found that linking the prosthesis resulted in increased valgus stability, which is an important indicator of clinical success. To better understand the causes of aseptic loosening, the

strain distribution on the bone surface post-elbow arthroplasty was also examined.

Completo et al. hypothesised that the nature and magnitude of cyclic loads on the elbow during daily activities generate stresses and strains exceeding the fatigue strength of bone and cement. In their study, they placed strain gauges on the medial, lateral, anterior, and posterior cortices of both the ulna and the humerus. Strain measurements were taken while applying joint reaction forces (JRF) of either 400 N or 700 N at three different angles: 60°, 90°, and 150°. These JRFs corresponded to 0.3 – 0.5 times the body weight, activities of daily living (An et al., 1984), more specifically occupational pick and place activities (Chadwick & Nicol, 2000), respectively. Clear changes in the biomechanical behaviour of both the humerus and ulna were found and correlated to possible fatigue failure by overload in the metaphyseal region and bone resorption by stress shielding at epiphyseal regions. These behaviours may indicate implant loosening.

Most total elbow arthroplasties involve fixation of both the humeral and ulnar components using polymethylmethacrylate (PMMA) bone cement (Morrey et al., 1998; Kamineni & Morrey, 2004). The effectiveness of this fixation is strongly influenced by the surgical technique. The introduction of cement restrictors has improved cement pressurisation, enabled better filling of the intramedullary canal and reduced distal cement extrusion (Trail & Nuttall, 2002). In parallel, advancements in surgical instrumentation have enhanced the accuracy of component placement, allowing for more consistent alignment and improved load transfer (King et al., 2006). These developments have contributed to improved implant stability, reduced micromotion at the bone–cement interface, and may

play a role in mitigating long-term aseptic loosening (Sabo et al., 2002; Schneeberger et al., 2000).

Possible prospective aseptic loosening can be investigated using torsion testing techniques. In 2010, van der Lugt et al. developed a testing rig that measured both torsional fatigue and torque to failure of the Souter-Strathclyde elbow prosthesis. The fatigue test applied cyclic axial torsion (0 – 4° internal rotation) for 200 cycles and torsional stiffness was calculated between the 10th and final cycle. Bone mineral density (BMD) measurements were recorded and found that it did not increase with humeral component size and that BMD was a much more important factor in the fixation of the implant.

Experimental reliability tests and computer simulated tests are two approaches for ensuring satisfactory performance of the implant under normal conditions. Computational models are widely accepted and used to evaluate the behaviour of different implant designs under physiologic loading (Maxian et al., 1996; Willing and Kim, 2009; Willing et al., 2014). To date, evaluating failure modes of TER has received scant attention in the research literature. Implant failure arising from overuse or bushing wear (Popoola et al., 2017; Wright and Hastings, 2005; Varadarajan and Kincaid, 2019) and the patterns of damage, different modes of wear, and the effect of implant design on stability of TER have been studied (Goldberg et al., 2008; Willing et al., 2014). Abnormal stresses in the bone and in the bone cement mantle which surpass the fatigue strength of the implant and cement, particularly in linked (constrained) prostheses can ultimately result in implant failure (Goel et al., 1989; Completo et al., 2011). There are few studies which specifically report the fatigue strength of humeral or ulna components (Kincaid et al., 2014; Varadarajan and Morrey, 2014).

We have developed a novel modified humeral component prototype of a TEA which can be instrumented, allowing the future generation of real-time in vivo 6 degree of freedom (d.o.f) force and moment data during ADL. To the best of our knowledge, this represents the first instrumented humeral elbow prosthesis prototype housing strain gauges to directly measure elbow joint forces in vivo. While this 6 d.o.f instrumented prosthesis lays the groundwork for validating existing theoretical musculoskeletal models, providing fundamental biomechanical data and informing implant redesign, it remains an early-stage prototype. Further design iterations, validation, and optimisation will be necessary before it can progress toward clinical application.

As a prerequisite to clinical application, the newly modified humeral implant prototype must undergo rigorous in vitro testing to evaluate its performance under physiological loading conditions. These tests aim to assess the structural integrity, safety, and reliability of the design modifications made to accommodate instrumentation. This chapter will:

1) Assess the safety of the modified humeral component with the peak anticipated loads from an experimental fatigue test
2) Report measured implant strains under such physiological loads during the test and validate them against modelled strains by finite element analysis (FEA), as spot validation
3) Use SolidWorks fatigue analysis to both give a lifetime prediction and usage factor

4.2. Methods

4.2.1. Experimental Approach

4.2.1.1. Implant Prototype Design and Fabrication

The proposed humeral component prototype in this study is a customised version of the Discovery humeral component (LIMA Corporate S.p.A.). The Discovery humeral component was selected as the basis of the instrumented TER because of its ability to offer effective pain relief, improved range of motion and long-term survivorship (Borton et al., 2021; Tiusanen et al., 2021). The customised humeral implant was developed using a computer-aided design software SolidWorks (Solid-Works Corp.™, Dassault Systems, Concord, MA, USA). The humeral component consisted of three primary regions (Figure 3-2): the humeral stem, humeral body, and two forks for mating with the condylar component (Figure 3-2). The humeral body and forks contain 3 cavities accessible via welded covers which will accommodate future instrumentation for in vivo strain measurement. For purposes of fatigue testing, these cavities were sealed with welded covers using electron beam welding (EBW) as per future instrumented implants.

The proximal end of the stem featured a circular geometry specifically designed to accommodate tip strain measurement instrumentation and implant coil assembly. A 2 mm axial hole connected this to the main cavity for the electronics. The main body of the implant is somewhat larger than in the standard Discovery implant to provide space for housing the instrumentation whilst not compromising the bone. The forks of the humeral implant remained unchanged from the Discovery implant except for including cavities within them but maintaining their identical geometry for compatibility with the standard Discovery ulna component (Figure 3-2). Overall, the modified humeral implant measures 116 mm in length.

This choice aligns with findings from the literature on hip, knee, wrist, and shoulder arthroplasty, which indicate that using shorter stem lengths in reconstructions can result in bone structures that closely resemble their intact state (Austman et al., 2011; Reimeringer et al., 2013; Bieger et al., 2012; Munting et al., 1997; Arno et al., 2012; Shishani and Gobezie, 2017). The humeral component has a valgus angulation and an internal rotation of 5 degrees relative to the long axis of the humeral shaft, as per the standard design.

4.2.1.2. Test Fixture Design

Test boundary conditions were set to simulate a worst-case loading scenario associated with moderate daily living activities (ADL) where the entire joint load is experienced by the component. This loading scenario was based on joint loads estimated using basic inverse dynamics analysis, which typically includes joint forces but does not account for detailed muscle contributions (Kincaid & An, 2013). A custom-designed test fixture was manufactured of stainless steel which assumed a rigid fixation of the stem within the bone. The test fixture consists of two parts: a circular fixture plate that connects to an adaptor plate on the machine (Figure 4-1A, B) and a rotating rod that mates with the fixture plate (Figure 4-1C). The rod was designed with cavities matching those of the condylar bearings for holding the forks of the humeral implant securely, whilst enabling various fixation angles of the humeral stem to be set. In the fatigue test, the rod was bolted to the fixture plate such that rotation could not occur.

(A) Test Fixture Plate

(B) Test Fixture Plate (Top View)

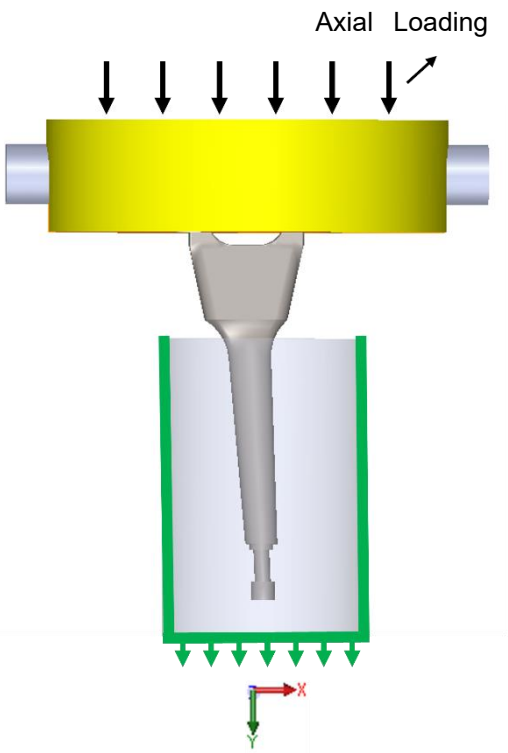

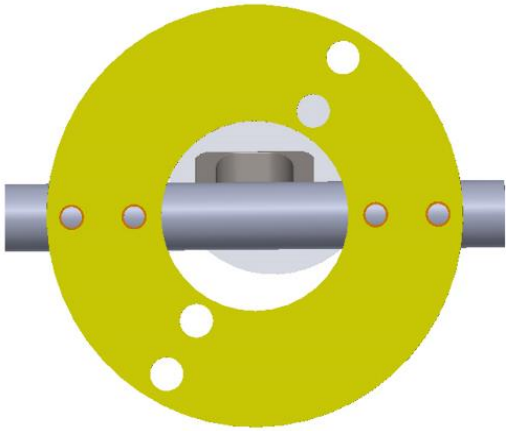

(C) Rotating Rod

(D) Implant in soft metal

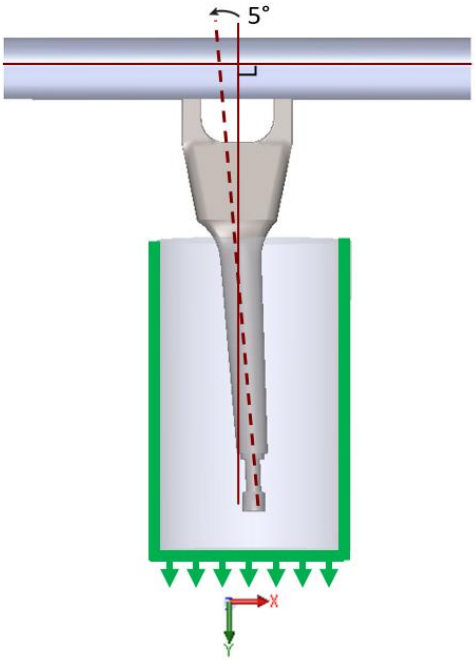

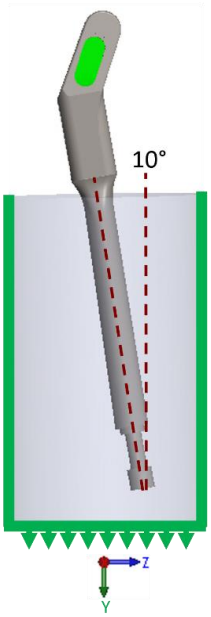

Figure 4-1: (A) Humeral Stem fixed at a 10° angle inside soft metal (B) Rotating rod placed on implant forks (C) Fixture plate placed on rotating rod (D) Fixture plate top view.

4.2.1.3. Implant Preparation and Strain Gauging

Four right sided humeral titanium (Ti-6Al-4V) components (N = 4) were manually polished to achieve a good surface finish. The humeral stem shaft was potted at 10° elbow flexion in the sagittal plane (Figure 4-1D) in a cylindrical steel pot ø50 x 80 mm filled with soft metal (Indium). One of the 4 humeral implants was instrumented with triaxial 350 Ω rectangular rosette (45°) strain gauges (FRAB-2-350-23-1LJB-F, TML Co.™, Fukuoka, Japan) at 3 specific locations (Figure 4-2).

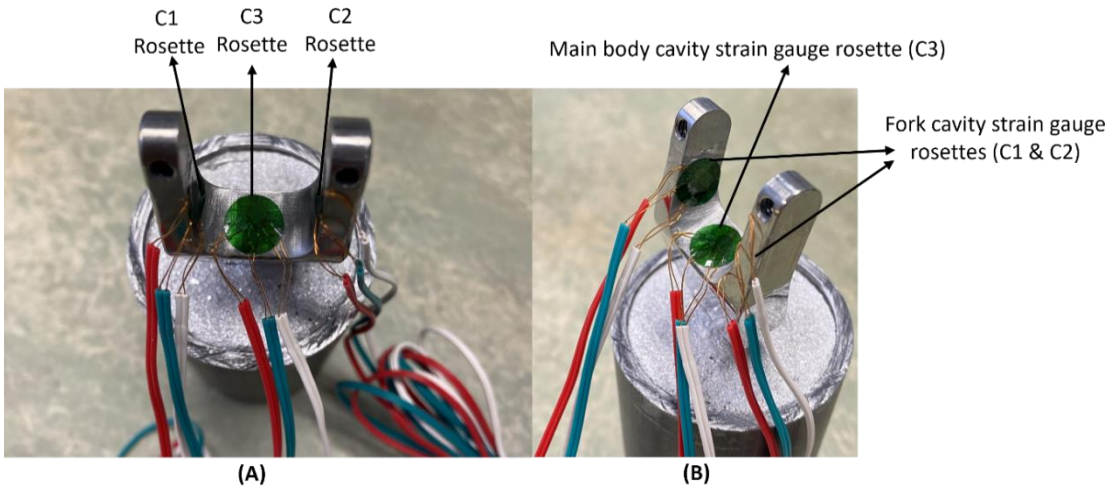

Figure 4-2: Gauge locations on the (A) Main cavity (C3 rosette) and (B) Fork cavities (C1 and C2 rosettes).

The locations of the rosette strain gauges were previously determined by a finite element analysis (FEA) study that predicted suitable internal regions for strain gauging the instrumented humeral component able to determine the 3 forces and 3 moments applied at the axle (Basiouny et al., 2022). The three locations are the external wall of the left fork (C1), right fork (C2) and main body cavities (C3) of the humeral implant. All the strain rosettes were connected to a data acquisition system consisting of a half bridge completion circuitry, preamplifier, 24-bit analog-

to-digital converters, and a serial data processor. Strain data were captured using LabVIEW software (2013, National Instruments, Austin, Texas, USA). The data were output in digital strain counts with a sensitivity of 545 counts per microstrain.

4.2.1.4. Loading and Measurements

The load scenario devised here was based on the data suggested as a benchmark for preclinical assessment of TER (Kincaid & An, 2013); here the maximum joint reaction force was reported for different activities of daily living (ADL) ranging from light, moderate, and strenuous duty to extreme loading scenarios with the peak joint reaction force (JRF) occurring approximately 10° anterior to the alignment of the humerus (y-axis in the sagittal plane) (Kincaid & An, 2013). Therefore, the modified humeral component was potted in soft metal (Indium) at an elbow flexion angle of 10°. The moderate duty ADL category was selected in this study with a JRF of 700 N applied to the humeral component (Kincaid & An, 2013).

The humeral implant was subjected only to compressive loads throughout the duration of the test as this better simulates the actual in vivo loading (Kincaid & An, 2013). Reported data concerning the frequency and speed of elbow flexion/extension movements are very limited. One study reported that rapid movement of the arm during typical ADL occurred at a rate of 5 Hz (Amis et al., 1980). It was estimated by Davis that nominal ADL entailed approximately 500,000 cycles per year (Kincaid and An, 2013; Davis, 1977). In this study, a total number of 5 million cycles (5Mc) were applied at 5 Hz, thus replicating 10 years of moderate patient activities.

4.2.1.5. Test Protocol

The test was conducted using an Instron ElectroPuls E3000 dynamic test machine paired with a 5 kN load cell (Instron Corporation™, Massachusetts, United States). A schematic of the test setup is shown in Figure 4-3. An illustration of the setup for the strain-gauged sample is provided in Figure A -1-1 in Appendix A-1.

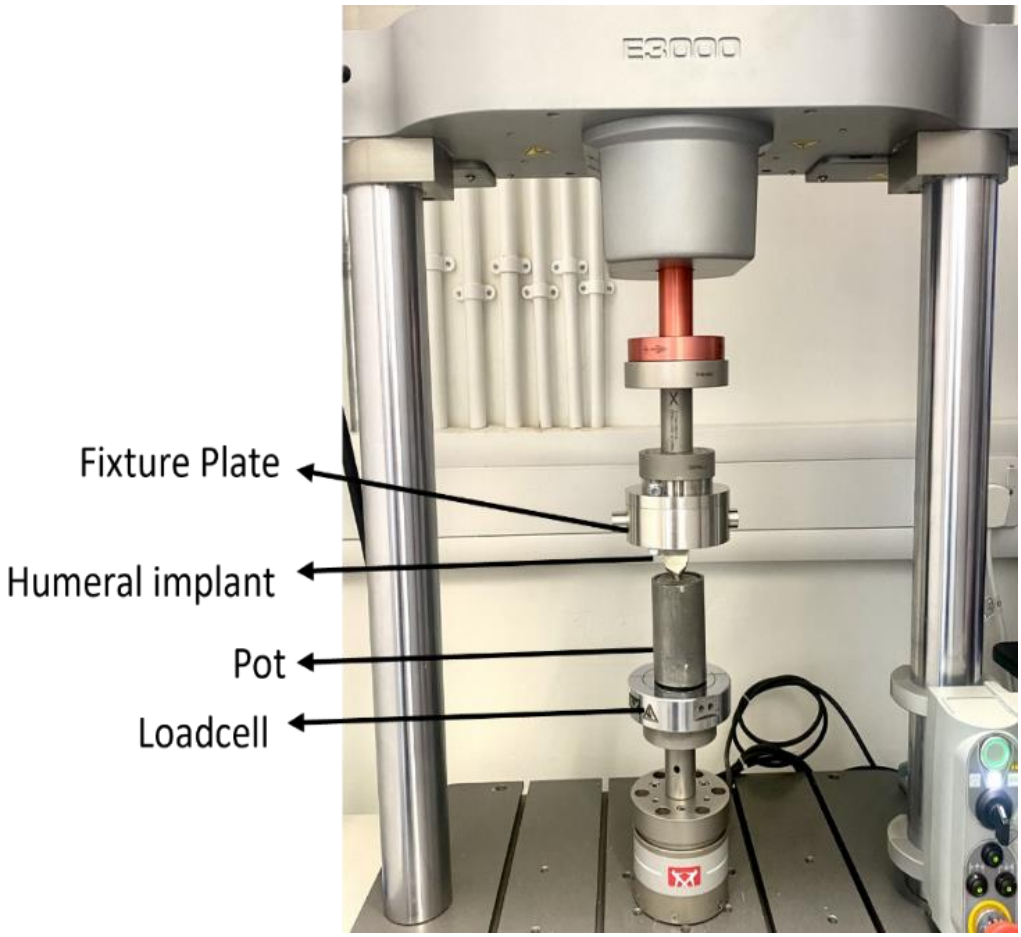

Figure 4-3: Illustration of fatigue test setup using the E3000 Instron machine.

The test fixture plate was attached to an adapter plate fixed to the machines actuator from the top and secured. The actuator operated in load control mode, applying the compressive JRF to the humeral implant. The forks of the potted humeral component were inserted into mating recesses within the loading rod and firmly locked in place with grub screws as per the normal condylar

component. The rod was then located in the fixture plate and secured. The sample was then carefully positioned under the load cell of the machine.

The test applied a sinusoidal waveform with a stress ratio (R) of 0.1, applying minimum (σ_{min}) and maximum (σ_{max}) compressive stresses corresponding to applied axial loading between 70 N and 700 N. The number of cycles involved in this test categorises it as a high-cycle fatigue (HCF) test, where the run-out duration (5Mc) was to be deemed successful for the load applied when there were no instances of deformation or fracture in the humeral implant, and there was no dissociation of the test specimens. Additionally, no damage should be observed in the weld used to attach the covers to the humeral component.

A total of 4 modified humeral implants were tested under these conditions. One specimen was strain gauged for the purpose of validating surface strains under physiological loading conditions. Before subjecting the implant to mechanical testing, strain counts were recorded at zero load. The test was then initiated, and strain counts experienced by the implant under loading were recorded for a duration of 60 seconds from the start. This duration was sufficient to capture the strain across one complete loading cycle. Due to the repetitive nature of the loading profile, only a sample of the strain data was required for recording. The test was set to conclude either upon the event of sample fracture or upon completing 5 million cycles.

4.2.2. Computation Modelling

In FE static modelling, the humeral component was statically loaded to predict the maximum von Mises stress on the implant under the same load applied in the experimental test (700 N). An FE fatigue analysis study was also conducted to predict the lifetime of the humeral component as well as the usage factor.

4.2.2.1. FE Static Modelling

The customised humeral implant prototype was generated using a computer-aided design software SolidWorks (Solid-Works Corp.™, Dassault Systemes, Concord, MA, United States). SolidWorks was also used to model the pot, a rotating rod that was fixed in place during FEA, and welded covers for the cavities of the implant. All parts were assembled on SolidWorks. Appropriate material properties were assigned to the modelled titanium (Ti-6Al-4V) humeral component, cavity covers and rotating rod (E = 110 GPa, V = 0.3), stainless steel pot (E = 200 GPa, V = 0.3), the soft metal (E = 10.8 GPa, V = 0.42). All components were meshed in SolidWorks with a free tetrahedral mesh with a mesh convergence study with 16 refined mesh densities and element sizes ranging from 6 mm to 0.5 mm. The solution was regarded as converged when the change in results was < 5% (Pegg et al., 2013), when a minimum element size of 0.5 mm was used at specific points of interest. A rigid contact condition was defined between all modelled components. This included the contact between the humeral forks - rotating rod, humeral stem- soft metal, as well as the soft metal - pot interfaces. The distal section of the modelled pot was assigned a fixed support to restrict displacement in all directions. In order to ensure comparability between the studies, the same loading conditions as were used in the experimental approach were applied in the FEA study to predict the maximum von Mises stress on the implant.

4.2.2.2. FE Fatigue Modelling

The same FE model developed above was used in the fatigue analysis study to predict the lifetime of the humeral component as well as the usage factor. Following the same protocol as the experimental fatigue test, a constant

amplitude loading event was applied with a stress ratio (R) of 0.1, ensuring maximum and minimum limits of 700 N and 70 N over 5 million cycles. This is a high-cycle fatigue (HCF) study and therefore the fatigue life of the implant will be assessed based on the S-N curve specific to HCF of Titanium (Ti-6Al-4V) (Peters et al., 2002).

To ensure the safety of the humeral implant stem, we assessed the local stresses to check that they did not exceed the material's yield stress (σ_y = 1100 MPa) for static loading (Boyer et al., 1994), together with endurance limit (σ_N = 460 MPa) for cyclic loading (Janeček et al., 2015). Yield factor of safety (FoS_{yield}) and fatigue factor of safety (FoSfatigue) were calculated using equations below. Generally, a FoS > 2 is required to ensure the safety of the humeral implant (Khanoki and Pasini, 2013; Dowling, 2013; Browne, 1999).

$$\mathbf{FoS_{yield}} = \frac{\text{Yield stress}}{\text{Maximum stress}}$$

$$\mathbf{FoS_{fatigue}} = \frac{\text{Endurance limit}}{\text{Maximum stress}}$$

The fatigue factor of safety was calculated using both the Goodman and (more conservative) Soderberg's formulae, commonly used to predict likelihood of fatigue failure, considering alternating stresses (σ_a) and mean stresses (σ_m) using the equations below with a stress ratio (R) of 0.1, applying minimum compressive stress (σ_{min}) at 70 N and maximum compressive stress (σ_{max}) at 700 N.

$$\sigma_m = \frac{(\sigma_{max} + \sigma_{min})}{2}$$

$$\sigma_a = \frac{(\sigma_{max} - \sigma_{min})}{2}$$

$$FoS_{Goodman} = \frac{1}{\frac{\sigma_a}{\sigma_N} + \frac{\sigma_m}{\sigma_{ut}}}$$

$$\mathrm{FoS}_{\,\mathrm{Soderberg}} = \frac{1}{\frac{\sigma_a}{\sigma_N} + \frac{\sigma_m}{\sigma_y}}$$

where the ultimate strength (σ_{ut}) of Ti-6Al-4V alloy is taken as 1170 MPa. If the FoS falls above the Goodman or Soderberg line, we can anticipate potential failure locations on the humeral implant. The equations do not consider the stress concentration factor of the local geometry which has the effect of reducing the endurance stress limit. Therefore, FE modelling was used to predict more accurate results for the specific implant geometry.

4.3. Results

4.3.1. Strain Gauge vs FEA Principal Strain Validation

The modelled and measured principal strains (PS1 and PS2) for strain gauges C1, C2, and C3 are presented in Figure 4-4 for a joint reaction force of 700N. The measured and modelled principal strains were found to be slightly higher at C2 (external wall of medial cavity). The measured and modelled minimum principal strain (PS2) at all three locations showed minor differences, with a 5% variation observed at C2 between the measured value (–2.20E+03) and the modelled value (–2.04E+03).

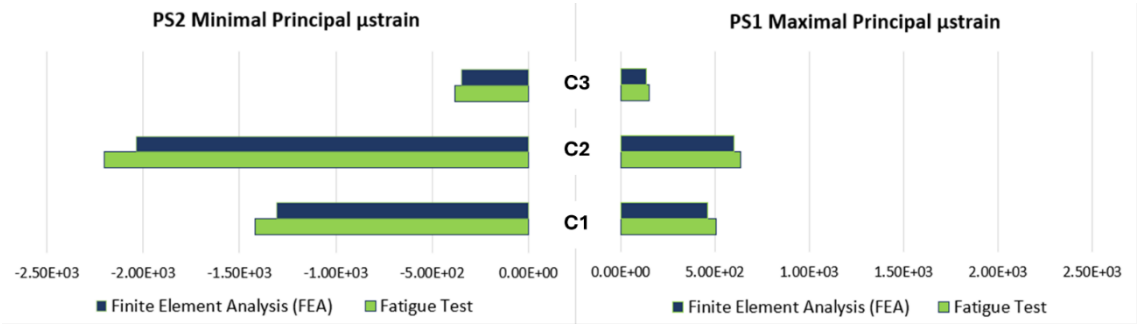

Figure 4-4: Average measured (Fatigue Test-300 cycles) principal strains (PS1 -maximal and PS2- minimal) Vs Modelled (FEA) principal strains for a joint reaction force of 700N.

For the C1 rosette (Figure 4-5), the maximum principal strain (PS1) angle relative to the YZ plane of the humeral implant was measured at –55° clockwise from the y-axis during the fatigue test and –47.5° in the FEA. At C2, the angle was +60° anticlockwise from the y-axis in the fatigue test and +65° in the FEA (Figure 4-5). For C3, the angle was +81° anticlockwise from the z-axis in the fatigue test and +69° in the FEA. Table 4-1 provides a summary of the principal strain directions at C1, C2, and C3.

Table 4-1: Fatigue test and FEA principal strain (PS) directions for each strain gauge rosette mounted on the humeral implant (Figure 4 5).

Gauge Location	Principal Strain (PS1) Angle		Direction w.r.t Humeral Implant
	Fatigue Test	FEA	
C1	-55°	-47.5°	Clockwise from humeral implant stem
C2	+60°	+65°	Anticlockwise from humeral implant stem
C3	+81°	+69°	Anticlockwise from the vertical Z axis

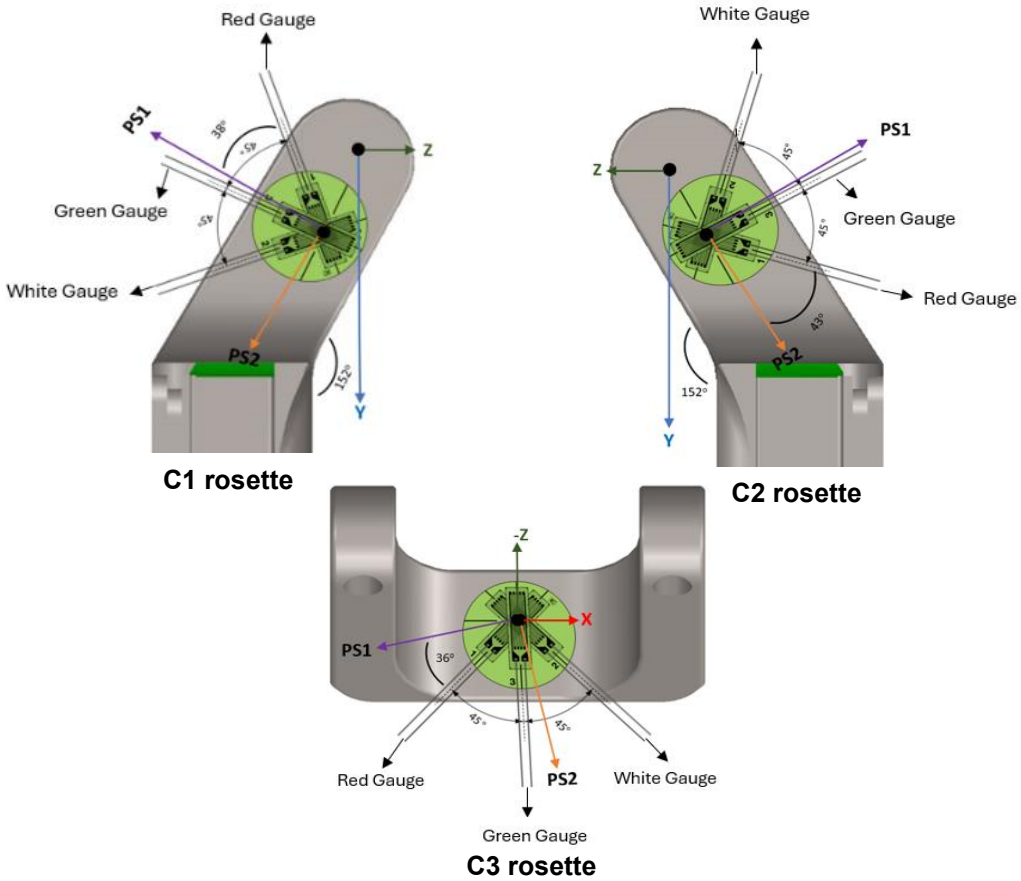

Figure 4-5: Gauge surface view showing the maximum principal strain (PS1) orientation (tensile) and minimum principal strain orientation (PS2) (compressive) of C1, C2 and C3 rosettes.

Figure 4-6 shows the dynamic strain profile of each gauge in each of the three rosettes, recorded over a period of 0.6 seconds corresponding to a total of three cycles. The peak principal strains of the mid-fork region C3 were much lower than those of the condylar forks C1 and C2.

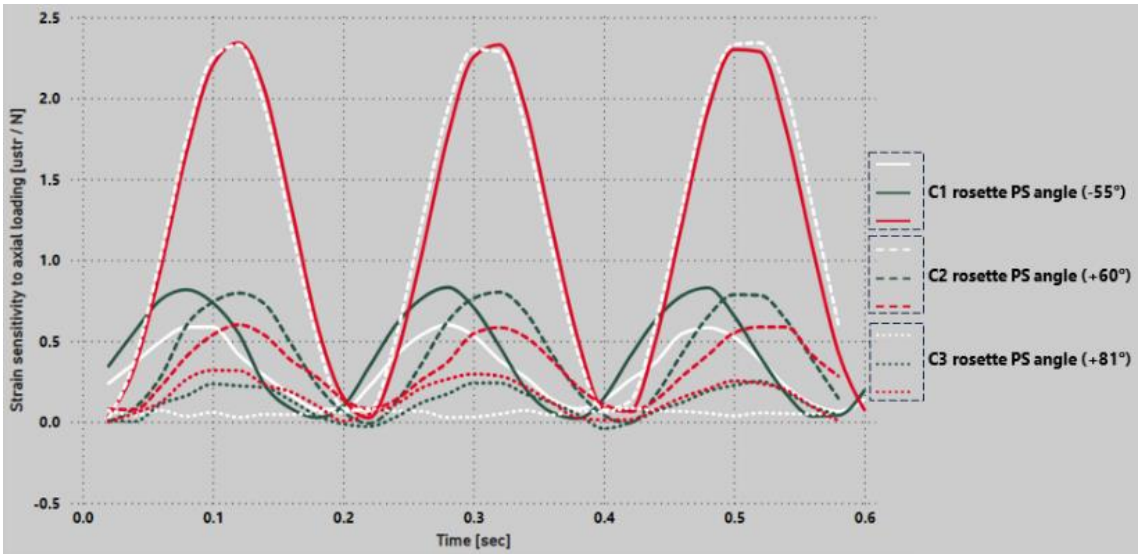

Figure 4-6: Dynamic strain profile for all 3 rosettes over a 0.6-second period (3 cycles) highlighting the maximum and minimum μstrain within a single cycle.

The principal strains measured from the fatigue test were compared with those obtained from FEA results using a Bland-Altman plot (Figure 4-7) to validate the modelled values against the experimental data. It is evident that the maximal and minimal principal strains from the experimental and FEA results at various strain gauge locations follow a similar pattern and are closely aligned. In the Bland-Altman plot, the dots represent the mean and difference (bias) between the principal strains (PS1, PS2) from the experimental fatigue test and the FEA study at each point of interest (C1, C2, C3).

The percentage difference between the experimental and modelled maximal principal strain (PS1) registered at C2 was 5%, which falls within the 95% confidence interval ranging from 128 to -199 μstrain.

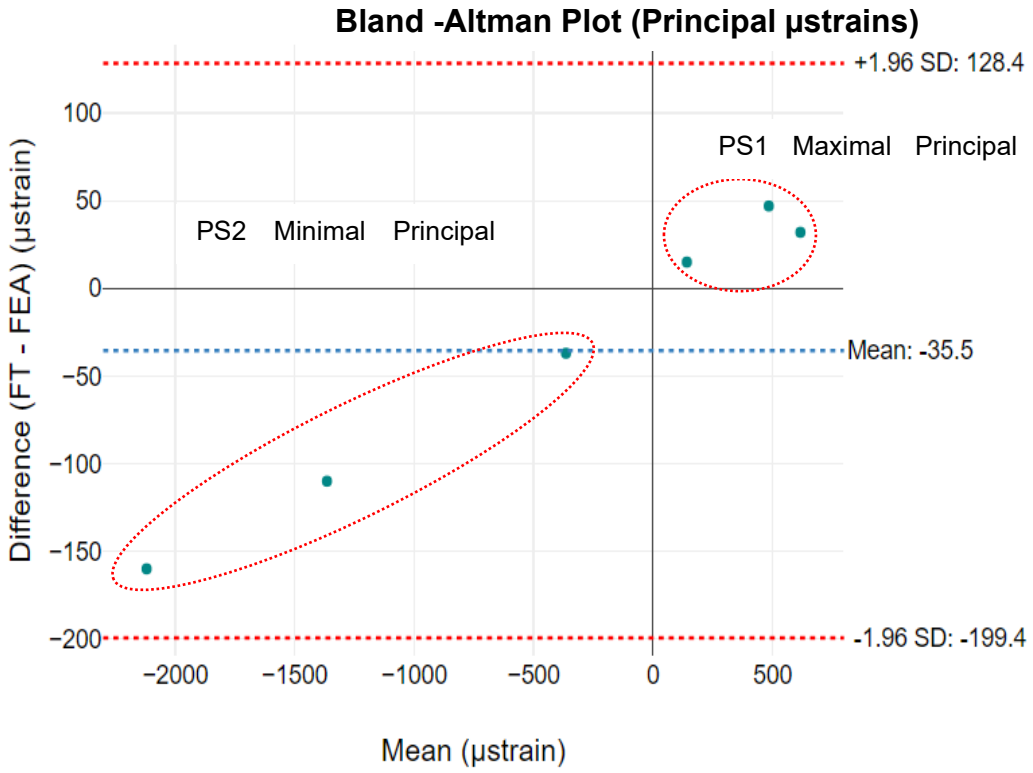

Figure 4-7: Bland-Altman plot comparing FEA and FT measurements for principal strains (µstrain). The plot shows the mean difference (-35.5 µstrain) and limits of agreement (±1.96 SD).

4.3.2. Fatigue Test Experimental Results

Each of the four humeral components (N = 4) successfully completed the applied loading regimen of 70 – 700 N for 5 million cycles. The tests were concluded at this point and the specimens were removed from the testing machine. Upon inspection of the specimens, it was visually noted that none of the tested samples exhibited any deformation on any part of the implant. No fractures or evidence of damage were detected on the welded caps of the humeral implants. The stress amplitude for all 4 samples remained relatively consistent throughout the test, which suggests that the implants likely maintained structural integrity under cyclic loading. Figure A -1-2 illustrates the stress amplitude profile for all four samples

over the 5 million cycles, highlighting initial fluctuations that stabilise within the first few thousand cycles.

4.3.3. FEA and Fatigue Analysis Results

In the FE analysis, the maximum von Mises stress on the implant prototype was identified at the tip of the right fork to be 127.0 MPa with peak alternating stress of 57.2 MPa. Upon completion of the FE fatigue modelling calculations, the software reported “Alternating Stresses everywhere in the model are below the minimum S-N Curve value resulting in no damage.”

The maximum von Mises stress of 127.0 MPa resulted in yield and fatigue FoS of 8.7 and 3.6, respectively, under static loading of the humeral component (Figure 4-8). Notably, similar maximum von Mises stresses of 115 MPa and 116 MPa were observed at the external wall of the left fork (C1) and right fork (C2), respectively.

The yield and fatigue FoS were 9.6 and 4 for C1 and 9.5 and 4 for C2. The external wall of the main body cavity experienced a significantly lower stress, 36 MPa. The welded cap joints also experienced an average von Mises stress of approximately 14.3 MPa. The overall maximum von Mises stress on the humeral component (127.0 MPa) remained well below the commonly accepted yield (1100 MPa) and fatigue (460 MPa) strengths of Titanium (Ti-6Al-4V).

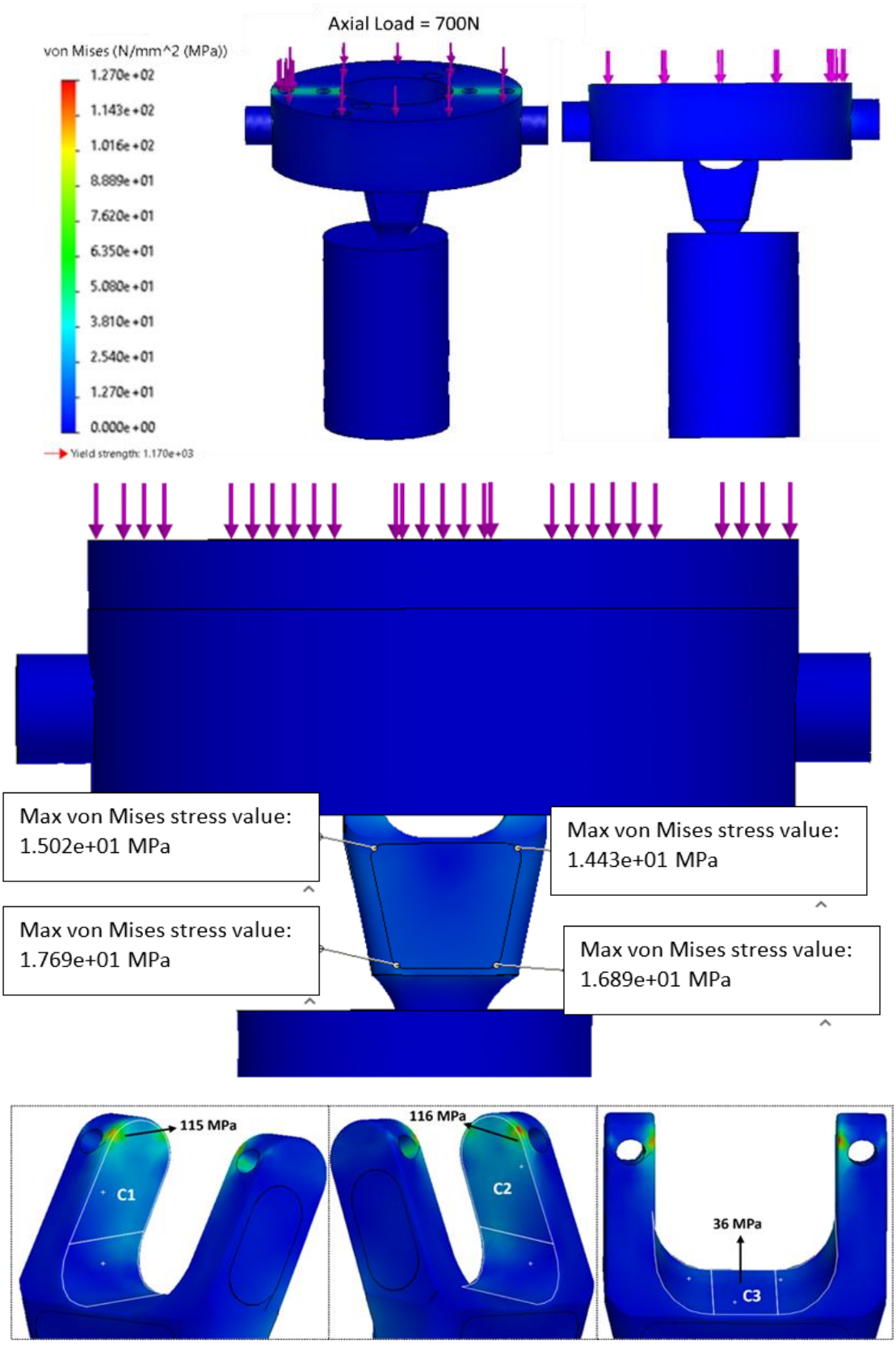

Figure 4-8: Finite Element Analysis (FEA) stress distribution of (A) Maximum von Mises stress on humeral component fixed in pot, (B) Maximum von Mises stress on weld cap joints (C) Maximum von Mises stress at the three strain gauge locations C1, C2, C3.

The fatigue factor of safety was also calculated during dynamic analysis according to the accepted theories of Goodman and Soderberg. For the humeral implant stem under moderate loading, the Goodman Factor of Safety (FoS) is 5.4, and the Soderberg FoS is 5.3, both of which are well above the threshold of 2. The Yield FoS, Fatigue FoS, Goodman FoS and Soderberg FoS were also calculated for different ADL categories including Light duty, moderate, strenuous and extreme and the results are presented in Table 4-2 below.

Table 4-2: Maximum von Mises stress, Yield factor of safety (FoS), Fatigue FoS, Goodman FoS and Soderberg FoS for all different activities of daily living categories (light duty, moderate, strenuous, extreme).

ADL Category	Peak JRF (N)	Max. von Mises Stress (MPa)	Yield FoS	Fatigue FoS	Goodman FoS	Soderberg FoS
Light duty	350	74.6	14.7	6.2	9.3	9.1
Moderate	700	127.0	8.7	3.6	5.4	5.3
Strenuous	1400	299.1	3.7	1.5	2.3	2.3
Extreme	2100	448.8	2.5	1.0	1.5	1.5

Under strenuous loading conditions, the stress increases to 299.1 MPa, reducing the Yield Factor of Safety (FoS) to 3.7, while the fatigue FoS drops to 1.5. Both the Goodman and Soderberg FoS values were near the critical threshold, standing at 2.3. Under extreme loading conditions, stress rises significantly to 448.8 MPa, bringing the Yield FoS down to 2.5, close to the minimum recommended limit. The fatigue FoS reaches a critical value of 1.0, and both Goodman and Soderberg FoS values fall to 1.5, dropping below the safe threshold of 2.

4.4. Discussion

This study evaluates the long-term durability and safety of the humeral component prototype under simulated physiological loading conditions. The implant tested here is a prototype designed specifically for standard total elbow arthroplasty (TEA) and is not a finalised clinical device. Due to this, the experimental setup was necessarily simplified and focused on assessing fundamental mechanical behaviour rather than replicating full physiological complexity.

The humeral implant strains, experienced under these loads, were also measured at 3 external locations and compared with model-predicted strains through a Finite Element Analysis (FEA). Having developed a prototype humeral component for a standard TEA, it was necessary to assess the implant using a loading profile for the activity level likely to prevail for this patient cohort.

All four humeral components (N = 4) demonstrated endurance beyond 5 million cycles, equivalent of predicted 10 years of moderate patient activities (Kincaid and An, 2013). This performance provides confidence that the long-term survival of this humeral component can be predicted under this loading profile. In the absence of an internationally recognised testing standard, such as ASTM/ISO, for assessing the durability of contemporary TEA, and of any in vivo force measurements to date, this study provides findings to support the development of a future instrumented humeral component for in vivo force measurement.

The fatigue model predicted that with the specific geometry used, the implant prototype would indeed survive as the experimental test confirmed. It was clear both from the simple theory and fatigue tests that a well radiused and polished implant would meet the fatigue criteria (at 700 N peak load and 5Mc), but the

machined pocket surfaces and welded joints, which were not specifically modelled, could have posed stress concentrations. There was no evidence from the fatigue test that these present any such risks, to the extent of the load applied and the length of test. This is further supported by the low von Mises stresses reported in the region of the welded joints as seen in Figure 4-8; also, electron beam welding is an established weld technique for implanted devices.

In the fatigue test, loads normally applied through the condylar bearing to the axle of the humeral implant were applied via a round rod with the same recesses as the condylar component, thus providing a representative interface, for load transmission along a fixed line of action. In a natural elbow joint, forces are distributed across both bone and surrounding soft tissues, which help absorb and distribute loads during daily activities. However, prosthetic joints like our modified humeral component bear these forces independently, relying only on its geometry and interaction with the bone. This modified design may expose the implant to different and sometimes greater stress concentrations than those found in a natural joint, particularly during everyday activities.

A point on the humeral stem will remain resistant to fatigue failure if both its alternating and mean stresses fall below the Goodman and Soderberg lines. The modelled alternating stress of 57.2 MPa lies well below the S-N curve, and the fatigue life was calculated to be 1.00e+7 cycles, suggesting that it can endure beyond the required number of cycles for the successful performance of this humeral implant. This peak alternating stress resulted from the maximum von Mises stress of 127.0 MPa, identified at the tip of the right fork. When the implant is fixed to the standard Discovery condylar bearing, the contact between the fork ends and the condylar bearings has far better conformity over a wider surface

area, reducing localised stresses compared to the simplified model. Therefore, this result represents a worst-case scenario.

Under moderate loading conditions, the Goodman Factor of Safety (FoS) and the Soderberg FoS were calculated were 5.4 and 5.3, respectively. These values indicate a strong safety margin, suggesting that the implant can reliably withstand moderate loading without significant risk of yielding or fatigue-related failure. In contrast, under strenuous loading, the Yield FoS remains within an acceptable range, but the reduced Fatigue FoS of 1.5 and the Goodman and Soderberg FoS values, both at 2.3, highlight that the implant is approaching its limits for long-term durability. This reduced margin suggests an increased risk of fatigue failure if strenuous loading occurs frequently. Under extreme loading conditions, the Yield FoS further declines to 2.5, suggesting that the implant is nearing its structural limit for static loads. The Goodman and Soderberg FoS values drop to 1.5, indicating a significant risk for failure due to cyclic loading stresses. These findings underline the importance of limiting exposure to extreme loads, as repetitive high stresses may push the implant beyond safe operational limits over time. In this case, the modified humeral implant is specifically designed for patients who are expected to engage in moderate daily activities. It is not intended for those undertaking strenuous or extreme physical tasks, and patients will be advised to avoid such activities.

The experimental fatigue test was found to agree well with the findings of the FE model, both for implant survival criteria and for strain magnitudes and directions at the 3 strain gauged sites, thus validating the model of the machined geometry. As the implant contains cavities for future electronics and strain gauges, a positive outcome of both an experimental and modelled fatigue analysis gives confidence as to the structural reliability in vivo over time. The stresses at the

edges of these weld covers were low, giving confidence that these welded joints were not structurally important.

The highest principal strains (PS1 and PS2) were observed at the medial fork cavity C2, due to its greater distance from the stem support, followed by a slightly lower strain magnitude at the lateral fork cavity C1 and a significantly lower strain seen at the central cavity C3. These measured strain values agreed, within a 10% variation, with the corresponding FE modelled strains as confirmed by the Bland-Altman pl which indicated that all the principal μstrain values lie within the 95% confidence interval of agreement. This shows that the strain magnitudes predicted by the FE model at these locations were sensitive enough to the loads applied during the fatigue test, with the capability to measure axial loads greater than 1 N.

This study had some limitations. The implant stems were embedded in soft metal to simulate bone fixation, and a single degree-of-freedom load was applied primarily along the flexion-extension axis. This loading was transmitted through a rod simulating the condylar bearing interface. The setup did not include pronation-supination movements or soft tissue contributions, which are known to affect elbow joint biomechanics but were excluded here to maintain experimental control. However, the moment arm for prono-supination is very small compared to valgus-varus or flexion-extension (Amis et al., 1979; An et al., 2008; Chadwick and Nicol, 2000).

The stem was potted in soft metal (Indium) to mimic the fixation of the stem within bone, lacking precise representation of the characteristics of cortical and cancellous bones. It is likely that the more elastic cortical and cancellous bone will absorb and share the stress with the implant, potentially reducing the risk for fatigue failure for the implant.

A single degree of freedom load was applied for simplicity, and the construct was over-constrained compared with an implant which has a rotating hinge axle. However, the effect of this would likely be to produce higher than normal stresses and therefore to give a worse-case scenario. The more than adequate FoS determined alleviated this simplification somewhat.

The use of strain gauges in specific locations accurately predicted the strain behaviour at those high stress local surfaces, validated against an FE static model. The experimental load cases were limited to one load case for simplicity, however the load scenario applied was representative of the major load in magnitude and direction acting on the implant during moderate activities of daily living (ADL).

Despite these simplifications and limitations, the experimental results validated the implant's fatigue resistance and strain measurement accuracy, providing a solid foundation for further development. Recognising these constraints is critical for contextualising the findings and planning future work that will incorporate more physiological loading scenarios and refined instrumentation.

4.5. Conclusion

This chapter assessed the long-term durability and safety of the customised Ti6Al4V humeral component prototype intended for instrumentation under simulated in vivo loading conditions through experimental fatigue testing and finite element (FE) static and fatigue analysis. The methodology and experimental setup demonstrated the safety and durability of the proposed customised humeral implant component for total elbow arthroplasty (TEA) during at least moderate daily activities.

The experimental results from fatigue testing indicated that all four humeral components (N = 4) successfully withstood a loading regimen of 70-700 N over 5 million cycles, simulating approximately 10 years of moderate daily activities. Inspections of the components after testing revealed no visible damage, deformation, or wear on any part of the implants, confirming their structural integrity and robustness.

Additionally, the measured strains experienced by the humeral implant under moderate physiological loading conditions validated the finite element (FE) study, adding confidence in the suitability of this implant for use in this population. The comparison of principal strains (PS1 and PS2) measured during fatigue testing with those predicted by FE analysis was conducted using a Bland-Altman plot, which demonstrated that the experimental strains closely aligned with the model predictions. The measured and modelled strains showed a high degree of agreement, with a maximum principal strain difference of only 5% at the external wall of the medial fork cavity (C2). This validation of the FEA model supports its ability in predicting strain behaviour and potential failure points under higher loads.

FEA results showed that the maximum von Mises stress on the humeral component remained significantly below the material's yield and fatigue strengths when loaded with a peak joint reaction force (JRF) of 700 N. The factors of safety were calculated for FoS_yield and FoS_fatigue during static analysis to be 8.7 and 3.6, respectively. Similarly, during dynamic loading of the humeral component, the FoS_Soderberg and FoS_Goodman were 5.3 and 5.4, respectively. The predicted fatigue life of the implant exceeded the required number of cycles, suggesting a potential for an extended service life.

The proposed modified humeral component for an instrumented TEA does not appear to pose any significant risk of fracture or deformation under the load applied during fatigue over a simulated 10-year life, and likely much longer. Despite certain limitations, such as the absence of rotational movements and simplified loading conditions, this test methodology provides valuable insights into the implant's performance. The experimental and modelled data are in agreement, confirming the implant's reliability for long-term use in total elbow replacements.

However, future research should include a wider range of load scenarios, particularly simulating loads corresponding to extreme activities of daily living (ADL), to enhance the predictive accuracy and ensure a comprehensive assessment of the implant's performance in reality.

Building on these findings, the next chapter focuses on the calibration of this prototype humeral component to ensure reliable in vivo measurements of joint reaction forces and moments. This involves refining the instrumentation and calibrating the strain gauge outputs. Such calibration is critical for translating the in vitro findings into meaningful in vivo data that can inform future biomechanical and clinical applications.

Chapter 5: Calibration of a Customised Humeral Component Prototype for an Instrumented Total Elbow Prosthesis

5.1. Introduction

This chapter outlines the calibration procedure and experimental testing undertaken for the newly developed instrumented Ti6Al4V humeral prototype designed for Total Elbow Arthroplasty (TEA). A single instrumented Ti6Al4V humeral stem (N = 1) was developed specifically for calibration in this study. A calibration method was designed to precisely measure the six forces and moments acting on the elbow joint during typical activities of daily living (ADL). This process establishes the relationship between known applied loads and the corresponding strain gauge voltage outputs to ensure interpretation of in vivo data.

The accuracy of instrumented implants is often constrained by their small size, the complexity of load transfer mechanisms, and the precision of their calibration. Various instrumented implants have undergone calibration using different loading setups and mathematical methods. One example is the technique used to calibrate the instrumented shoulder joint implant developed to measure contact forces and moments within the glenohumeral joint (Taylor et al., 1994, 2000, 2004). Other calibration techniques were also developed for other implants (Taylor et al., 1994, 2000; Taylor et al., 1997, 1998; Taylor & Walker, 2001). For accurate measurement, the calibration process must closely mimic in vivo conditions. Many instrumented implants, such as hip implants, have been calibrated using the well-established matrix method (Bergmann et al., 1982; Bergmann et al., 1988). In this method, multiple strain gauges are strategically placed to capture the combined response of forces and moments acting in

various directions. A calibration matrix is then generated to relate the applied loads and moments to the strain gauge outputs, enabling the isolation of individual degrees of freedom (d.o.f) through multiple linear regression. An alternative approach would be to use a single strain gauge or half bridge dedicated to each d.o.f. While this method simplifies the analysis by isolating specific responses, it assumes minimal mechanical interaction between directions and requires a highly regular geometry. Given the complex and irregular geometry of the humeral component, the matrix method is better suited, as it accounts for the interaction between forces and moments across all strain gauges. An instrumented hip implant was calibrated using a custom-built uniaxial test rig, where known loads and moments were applied. The calibration force was varied from zero to its maximum (Fx = 3.2 kN, Fy = 2 kN and Fz = 5 kN), while strain gauge readings were recorded. These readings are then used to calculate the 6x6 calibration matrix, which converts the strain gauge signals into load components (Damm et al., 2010). Using the same matrix method, an instrumented tibial tray was calibrated to measure six load components: three forces (medio-lateral, anteroposterior, and axial compressive) and three moments (flexion-extension, varus-valgus, and internal-external). A custom-built uniaxial mechanical testing rig was employed to apply known loads at specific points, generating various combinations of force and moment components. The strain gauge outputs from the prosthesis were then collected to build a calibration matrix (Heinlein et al., 2007).

Subsequently, the same calibration matrix method was applied to calibrate instrumented shoulder implants (Westerhoff et al., 2009). However, due to the shoulder joint's unique range of motion and loading conditions, a more complex setup was necessary. In this study, the shoulder implant was secured in a rigid

calibration frame using bone cement, mimicking in vivo conditions where the implant is firmly attached to the bone. Forces were applied using a specially designed calibration block attached to the head of the implant. The block featured multiple points strategically positioned to enable the application of different load offsets which generate different bending moments using the same load transfer mechanism. This design also accounts for the various orientations and directions the implant might encounter within the body (Westerhoff et al., 2009).

As forces and moments were applied, the strain gauges embedded within the implant recorded the resulting strains, and the relationship between the applied loads and strain gauge outputs was captured in a calibration matrix. The cross-sensitivities between strain gauges, which arise when a gauge responds to loads or moments outside its intended direction of measurement, were also accounted for during the calibration process.

Currently, there is no published studies detailing the calibration of elbow implants, largely because no attempts have been made to develop an instrumented elbow implant capable of measuring all six degrees of freedom around the joint. This chapter, therefore, focuses on outlining the calibration procedure specifically designed for our first-in-man developed instrumented humeral implant prototype.

The objectives of this chapter are:

1) Design suitable test setups to calibrate all six degrees of freedom of the instrumented humeral component as accurately as possible given the sever constraints.
2) Apply the matrix method to develop a calibration sensitivity matrix to measure the 3 forces and 3 moments acting on the elbow joint.

5.2. Materials and Methods

5.2.1. Preparation for the Calibration Setup

A custom-designed stainless steel loading plate was manufactured for the precise application of calibration forces and moments. The plate features twenty-three ball bearing holes, strategically arranged in a spiral pattern at predetermined offset distances to the centre point (0, 0) (Figure 5-1). Each hole is positioned at 45° increments around the plate. Hole 2 is located 10 mm above the central point along the positive x-axis with coordinates (10, 0) mm. Hole 21 is positioned to the right of the central point along the positive z-axis and has coordinates of (0, 10) mm. Hole 22 lies below the central point along the negative x-axis at coordinates (-10, 0) mm, and hole 23 is located 10 mm to the left of the central point along the negative z-axis with coordinates (0, -10) mm. All holes are chamfered with a 1 mm bevel to ensure good seating of the ball bearing during force application, providing secure and accurate contact point (Figure 5-1).

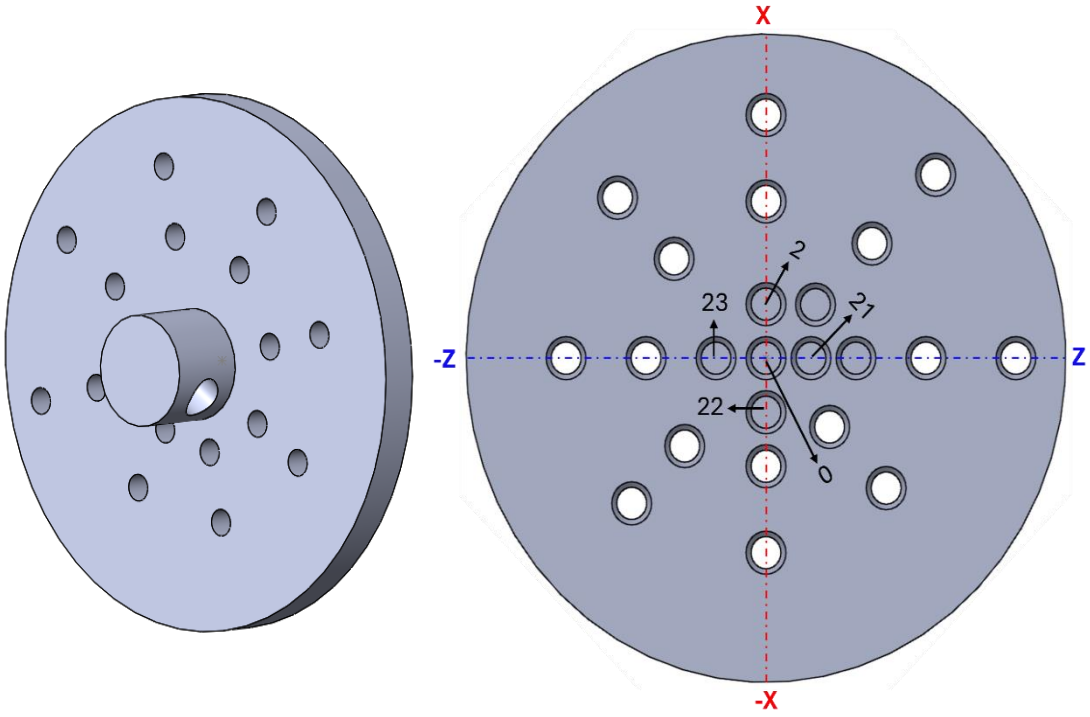

Figure 5-1: Calibration loading plate with twenty-three ball bearing holes, positioned around the central point (0, 0) of the plate. Holes 2 and 22 lie on the vertical positive and negative x-axis, while holes 21 and 23 are located on the positive and negative z-axis, respectively.

The instrumented humeral component prototype developed in Chapter 3, containing internal strain gauges and an integrated PCB containing all data acquisition circuitry within the main cavity, was used in this calibration procedure. The 3 wires used for power supply and telemetry were routed through a small opening in the cavity cover, which was securely glued rather than welded. This choice of gluing was made to allow easy access to the PCB in case of malfunction, as welding would make repairs impossible and could risk damage to the weld.

5.2.2. Application of Calibration Forces and Moments

To calibrate the six force and moment components of the instrumented elbow implant, it is essential to replicate physiological loading conditions that closely

resemble the in vivo forces and moments experienced by the elbow joint. The calibration was performed with respect to this implant-based coordinate system which was fixed in the middle of the main body of the instrumented humeral implant. The x-axis runs parallel to the loading bar and passes through its central axis. The y-axis is axial, aligned with the distal stem, and passes through the centre of the main body of the humeral implant. The z-axis is perpendicular to the loading bar at its midpoint, intersecting the centre of the main body of the implant. Calibrating all six degrees of freedom involved applying a combination of axial and shear loads, as well as bending and torque moments. Since it is not possible to apply each degree of freedom individually, the calibration process utilised multiple linear regression to isolate the sensitivities of each strain gauge for each pure degrees of freedom.

The load components ±Fx, ±Fy, ±Fz, ±Mx, and ±Mz were generated by applying force to specific ball bearing positions on the calibration plate. These loads were applied while the humeral stem was either fixed vertically in certain planes or inclined at specific angles in other planes. Three load cases were designed to calibrate these five degrees of freedom, each generating a combination of up to five different forces and moments simultaneously. The calibration of torque (±My) was conducted using a separate setup for two key reasons. Firstly, the coordinate system was centred about the hinge axis, allowing for a predictable application of pure My. Secondly, it was challenging to apply a significant magnitude of My during the main calibration due to the orientation of the jigs. By calibrating My separately, one degree of freedom was removed from the regression process, improving the overall calibration accuracy. These combined forces and moments simulate the complex biomechanical elbow movements, including

flexion/extension, varus/valgus, and pronation/supination. The loading scenarios and associated mechanical setups are detailed below:

5.2.2.1. Load Case 1 Setup (Stem vertical in YZ and XY planes):

In this setup, the humeral stem is secured vertically in both the YZ and XY planes, with compressive axial loads applied to the humeral component using a manually displacement-controlled Hounsfield loading machine fitted with a 10 kN load cell (Figure 5-2).

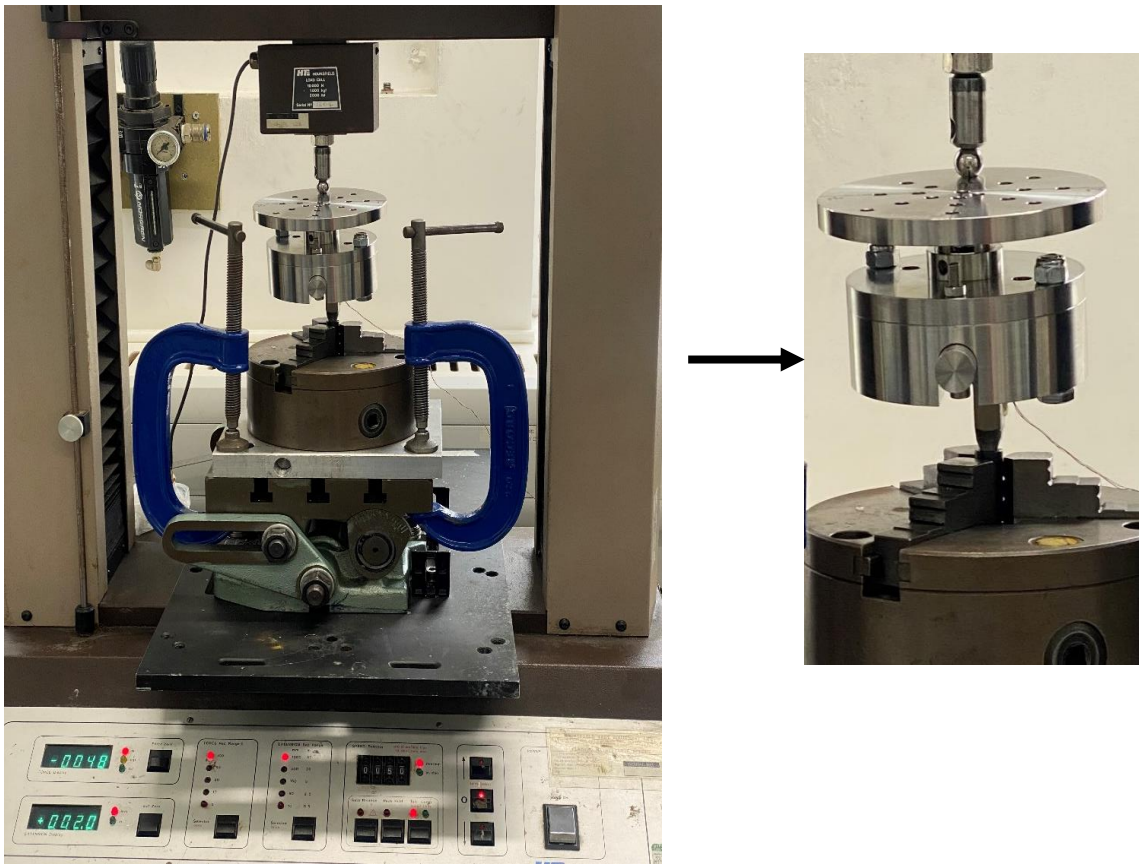

Figure 5-2: Setup configuration of Load Case 1. The humeral stem is vertical in both the YZ and XY planes with the implant rod is inclined 5° about the z-axis.

To prevent any movement or slippage during force application, two collets, each 8 mm in diameter, were placed around the circumference of the humeral stem. The stem, along with the collets, was then inserted into a 3-jaw metal chuck fixed

at the base of the machine. The chuck's jaws clamp down on the collets, firmly holding the stem in place (Figure 5-2).

The rod and circular test fixture plate from the fatigue test setup detailed in Chapter 4 (Figure 4-1) were also utilised in this calibration setup. The forks of the humeral component were inserted into pre-designed cavities within the rod and secured with posterior screws, similar to those used in the Discovery elbow system. The circular fixture plate was attached to the rod using nuts and bolts, serving as a mounting base for the calibration loading plate, which was also secured to the top of the fixture plate.

A ball bearing was positioned at various points of interest on the calibration plate (Figure 5-2). Axial loads were applied incrementally, varying from zero to a maximum at each specific load position. Table 5-1 below outlines the different hole positions used in load application and the calibration loads applied to each unique point in Load Case 1.

Table 5-1: Summary of applied forces (N) for Load Cases 1, 2 and 3 and positions of load application on the Plate. Positions correspond to holes 0 with coordinates (0,0), 23 (0, -10), 22 (-10, 0) and 21 (0, 10).

	Load Case 1	Load Case 2	Load Case 3
Postion of Load Application	Applied Force (N)	Applied Force (N)	Applied Force (N)
Hole 0 (Centre of Plate)	0	0	0
	114	114	100
	334	302	316
	528	520	504
Hole 23 (Located on -Z -axis)	0	0	0
	126	118	106
	330	328	320
	516	510	506
Hole 22 (Located on -X-axis)	0	0	0
	124	106	132
	310	318	334
	530	506	510
Hole 21 (Located on Z-axis)	0	0	0
	118	104	108
	332	316	308
	510	502	554
Hole 2 (Located on X-axis)	0	0	0
	122	114	126
	324	334	320
	512	530	516

The three wires of the PCB inside the humeral component designed for power supply, ground connection and serial data telemetry exited the implant through a small hole in the main cavity cover. The ADC was then linked to a computer for data capture and storage using a custom-designed graphical user interface (GUI) created in LabVIEW® software (2013, National Instruments™, Austin, Texas, USA). A specific set of forces and moments were applied using the Hounsfield loading machine, and the resulting strains were measured by the strain gauges embedded within the implant. These deformations caused changes in the

resistance of the strain gauges, which in turn altered the voltage output from the gauges. A total of 5 positions were axially loaded with strain gauge outputs monitored in real-time via the elbow GUI (Figure 5-3). The outputs were recorded

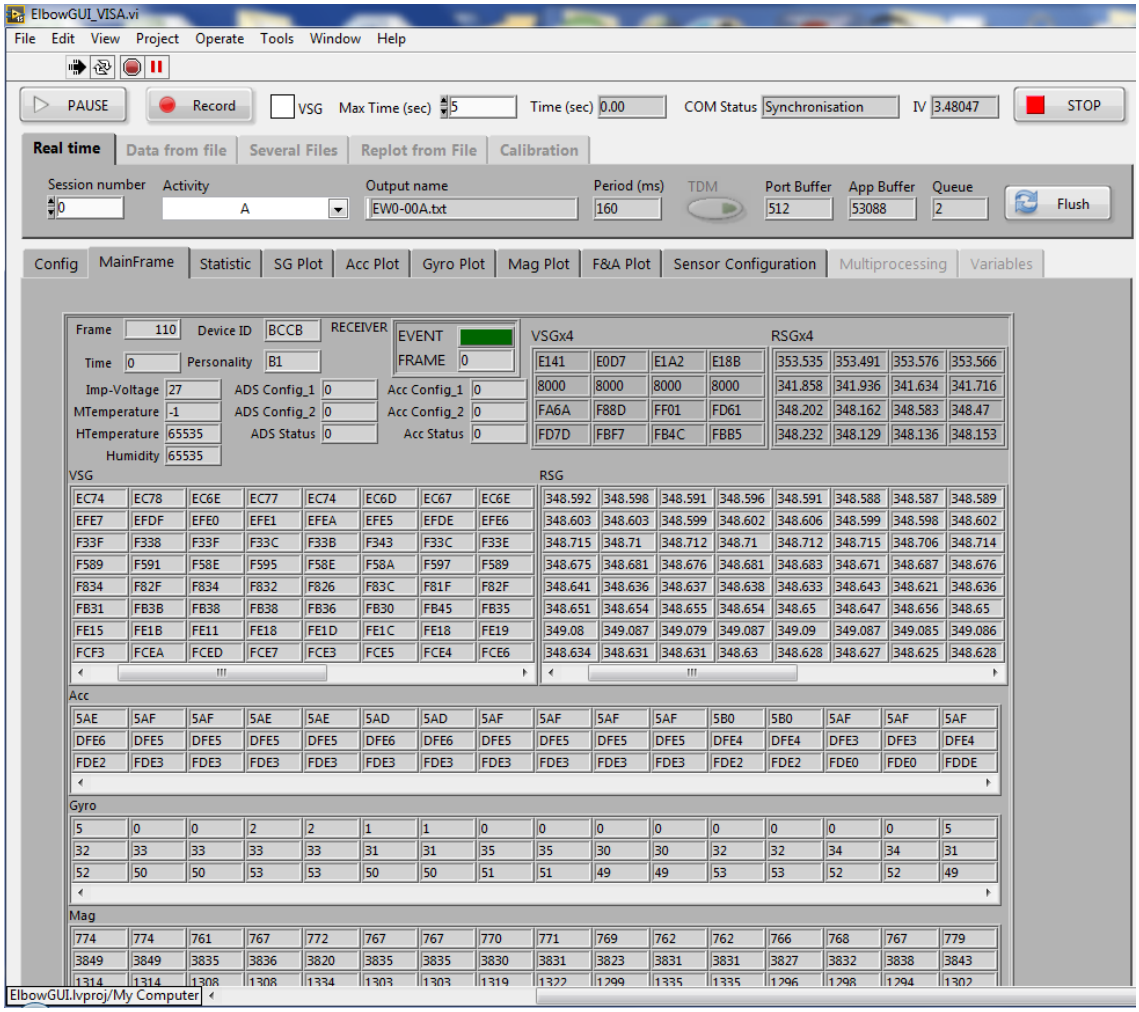

Figure 5-3: Custom-designed elbow graphical user interface (GUI) displaying real-time changes in the resistance of the 8 strain gauges positioned within the lateral, medial, and central cavities of the humeral implant.

initially in the unloaded state and then under the applied forces over a duration of 10 seconds.

5.2.2.2. Load Case 2 Setup (Angle plate inclined α deg in YZ plane):

In this loading scenario, the setup is identical to that in loading case 1, with the addition of an angle plate positioned underneath the chuck at the base of the

machine. This angle plate introduces an α angle of 10^{o} in the YZ plane while maintaining the same orientation in the XY plane (Figure 5-4). As a result, the stem rotated only in the YZ plane (Figure 5-4). The load was applied using the same procedure and at the exact same hole positions as in load case 1. Table 5-1details the hole positions used for load application and the specific calibration loads applied to each unique point in this load case. The strain gauge outputs were also recorded first in the unloaded state and then under the applied forces, for a duration of 10 seconds.

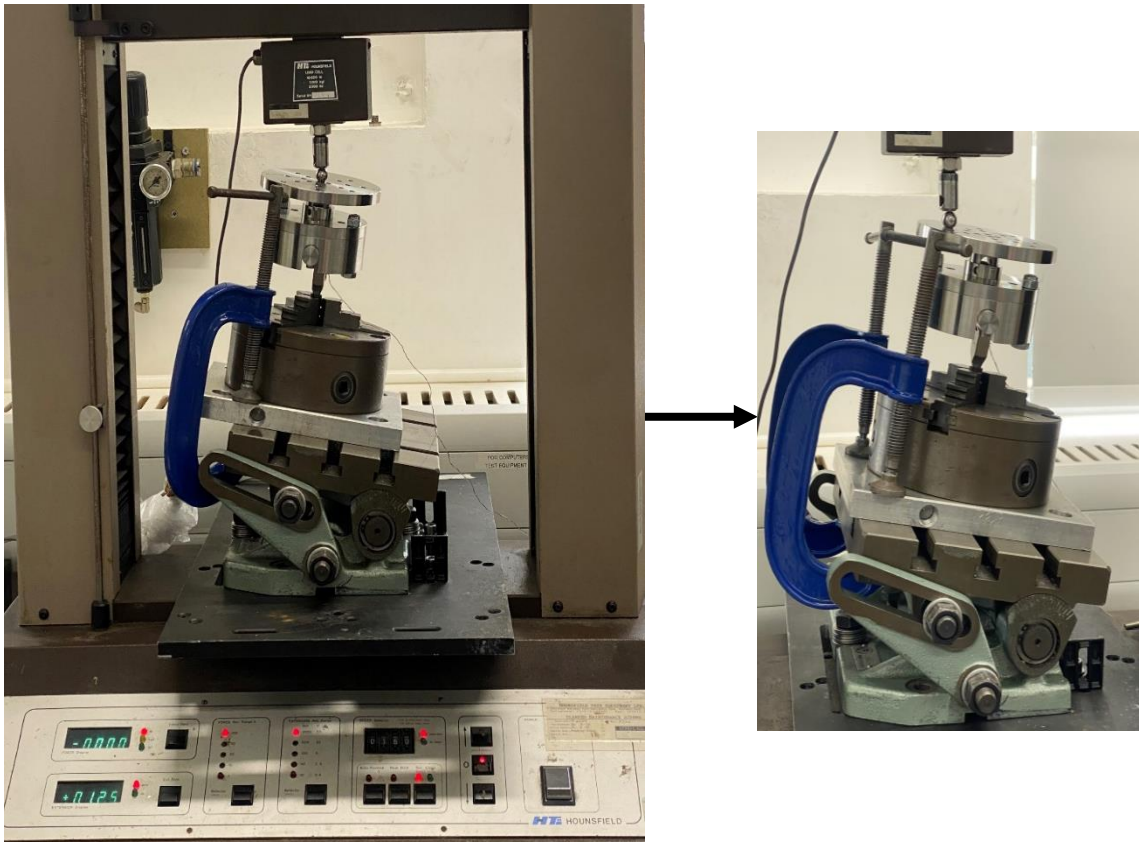

Figure 5-4: Setup configuration of Load Case 2. The humeral stem is inclined an α angle degree (10^{o}) in the YZ plane but remain vertical in the XY plane with the implant rod is inclined 5° about the z-axis.

5.2.2.3. Load Case 3 Setup (Angle plate inclined β deg in XY plane):

This loading setup is again identical to that in Load Cases 1 and 2, with the exception that this time the angle plate introduces a β angle of 10° in the XY plane while maintaining the same orientation in the YZ plane (Figure 5-5). As a result, the stem rotates exclusively within the XY plane (Figure 5-5). The load was applied using the same procedure and at the same hole positions as in Load Cases 1 and 2. Table 5-1 details the specific hole positions used for load application and the corresponding calibration loads applied to each unique point in this load case. As in Load Case 2, strain gauge outputs were recorded first in the unloaded state and then under the applied forces, for a duration of 10 seconds.

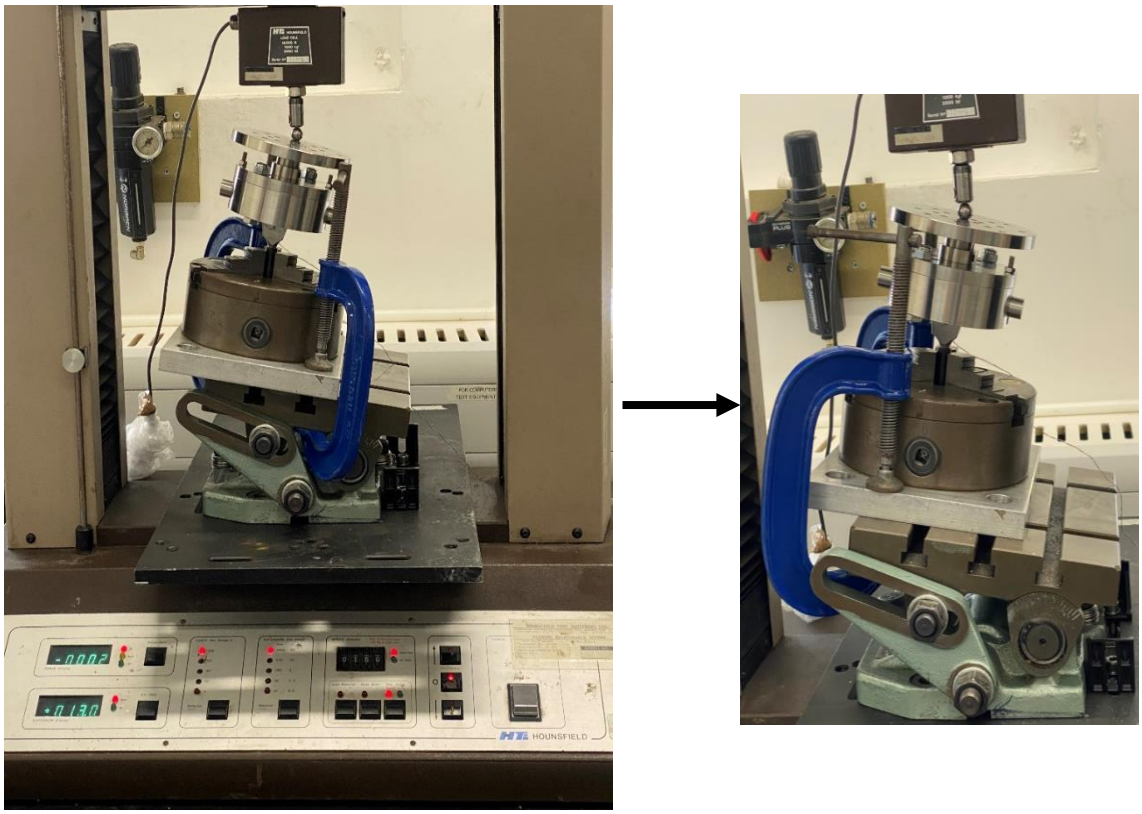

Figure 5-5: Setup configuration of Load Case 3. The humeral stem is vertical in the YZ plane but inclined a β angle of (10°) in the XY plane with the implant rod still inclined 5° about the z-axis.

5.2.2.4. Torque Calibration Setup (±My):

This torque setup is designed to generate a pure moment around the y-axis of the humeral implant stem. The humeral stem is securely fixed vertically in the same 3-jaw metal chuck used in the previous setups, with two 8 mm diameter collets around the stem to prevent movement or slippage. The custom-made humeral implant rod designed with cavities matching those of the condylar bearings for holding the forks of the humeral implant was securely attached on top.

Two rectangular metal brackets were bolted onto opposite sides of the base of the chuck. These brackets support a pulley system, which is mounted by drilling holes through the brackets and securing the pulley with a threaded rod. The central axis of the pulley is aligned vertically with the humeral implant rod. Weights were used to apply a calibration load via the pulley system. Boat yarns of 3 mm in diameter were secured with knots around the ends of the rod, with 16 mm shaft metal collars at both ends to prevent the rope from slipping. The boat yarn is then pulled horizontally over the pulley to hang the weights, applying a moment to humeral implant stem. The entire setup is clamped securely to the edge of a table, ensuring that the weights can hang freely without interfering with any other objects. Weights were evenly suspended at both ends of the two boat yarns on opposite sides. Simultaneously, the wires from the instrumented humeral component were connected to a data acquisition system linked to a computer. This setup allowed for real-time capture of strain as the implant was subjected to load. The table below details the weights used for loading the humeral component. Strain gauge outputs were recorded at each load level applied.

5.2.3. Data Collection and Processing

5.2.3.1. Resolving Calibration Forces and Moments

To construct an accurate sensitivity matrix for the instrumented elbow implant, it's essential to resolve the forces and moments into their three mutually perpendicular directions. In a real-world scenario, the elbow joint experiences forces and moments from various directions and magnitudes due to complex biomechanical movements. Each of these loads can be resolved into components along three orthogonal axes X, Y and Z. The concept of direction cosines was employed for the 3D analysis of the forces and moment. By resolving forces and moments into these components, the calibration process can be simplified and the relationship between strain gauge outputs and applied loads can be accurately determined.

Load Case 1:

The humeral implant stem is vertical in both the YZ and XY planes, but the implant rod is inclined 5° about the z-axis. This inclination results from the 5° valgus alignment of the humeral component, meaning the humeral component is tilted laterally by 5 degrees relative to the long axis of the stem (Figure 5-6).

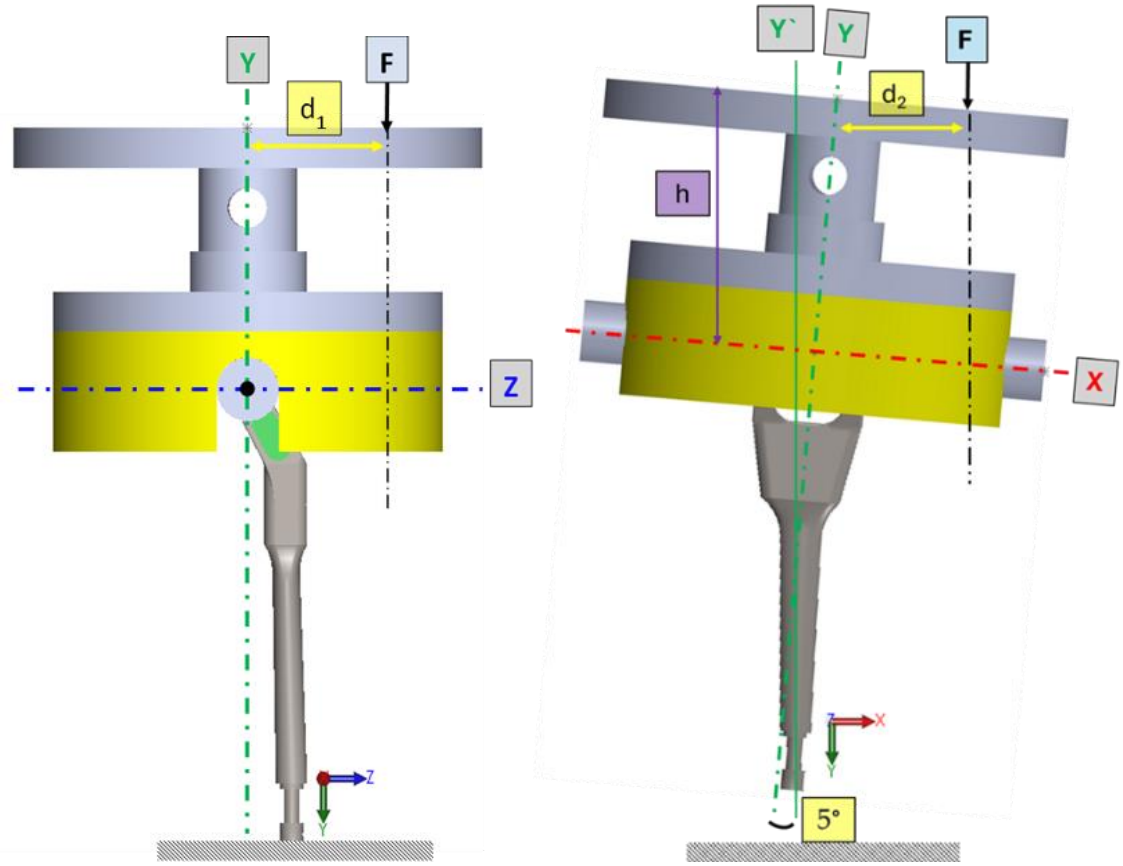

(A) (B)

Figure 5-6: Configuration of Load Case 1 setup showing the humeral stem aligned vertically in the YZ (A) and XY (B) planes, with the implant rod inclined at 5° about the z-axis.

In 3D analysis, forces and moments are typically represented as vectors with their components expressed as:

$$F = F_x i + F_y j + F_z k$$

where Fx, Fy, and Fz are the components of the force along the X, Y, and Z axes, respectively. Using the direction cousins of sin (5º), cos (5º), and cos (90º), the force components can be determined as:

$$F_x = F.\sin(5°)$$

$$F_y = F.\cos(5°)$$

$$F_z = F.\cos(90°)$$

The moment of a force about an axis is given by the cross product of the position vector (from the point of interest to the point of force application) and the force vector. The cross product inherently involves the direction cosines, as it depends on the angle between the vectors.

If r is the position vector: $\mathrm{r} = (\mathrm{r_x}, \mathrm{r_y}, \mathrm{r_z})$; and F is the force vector: $\mathrm{F} = (\mathrm{F_x}, \mathrm{F_y}, \mathrm{F_Z})$, the moment M is given by:

$$\mathrm{M} = \mathrm{r} \times \mathrm{F}$$

The cross product of the moment above can be written as the determinant of a matrix:

$$M = \begin{vmatrix} i & j & k \\ r_x & r_y & r_z \\ F_x & F_y & F_z \end{vmatrix}$$

Expanding the determinant:

$$\mathrm{M} = \left(\mathrm{r_y F_z} - \mathrm{r_z F_y}\right)\mathbf{i} + (\mathrm{r_z F_x} - \mathrm{r_x F_z})\mathbf{j} + \left(\mathrm{r_x F_y} - \mathrm{r_y F_x}\right)\mathbf{k}$$

To calculate the moment about an axis i, j and K can be replaced by the direction cousines of the unit vector and the determinant can be written as in this case:

$$M = \begin{vmatrix} x & y & z \\ d_2 & h & d_1 \\ \sin(5°) & \cos(5°) & \cos(90°) \end{vmatrix}$$

The moment components can then be determined as:

$$\mathrm{M_x} = -\mathrm{F}.\cos(5°).\ \mathrm{d_1}$$

$$\mathrm{M_y} = \mathrm{F}.\sin(5°).\ \mathrm{d_1}$$

$$\mathrm{M_z} = \mathrm{F}\ (\mathrm{d_2}.\cos(5°) - \mathrm{h}.\sin(5°))$$

Load Case 2:

In this scenario an angle plate was inclined an α degree in the YZ plane; the axle (implant rod) was inclined 5° about the z-axis as seen in Figure 5-7 below. The same concept above was used to work out the force and moment components.

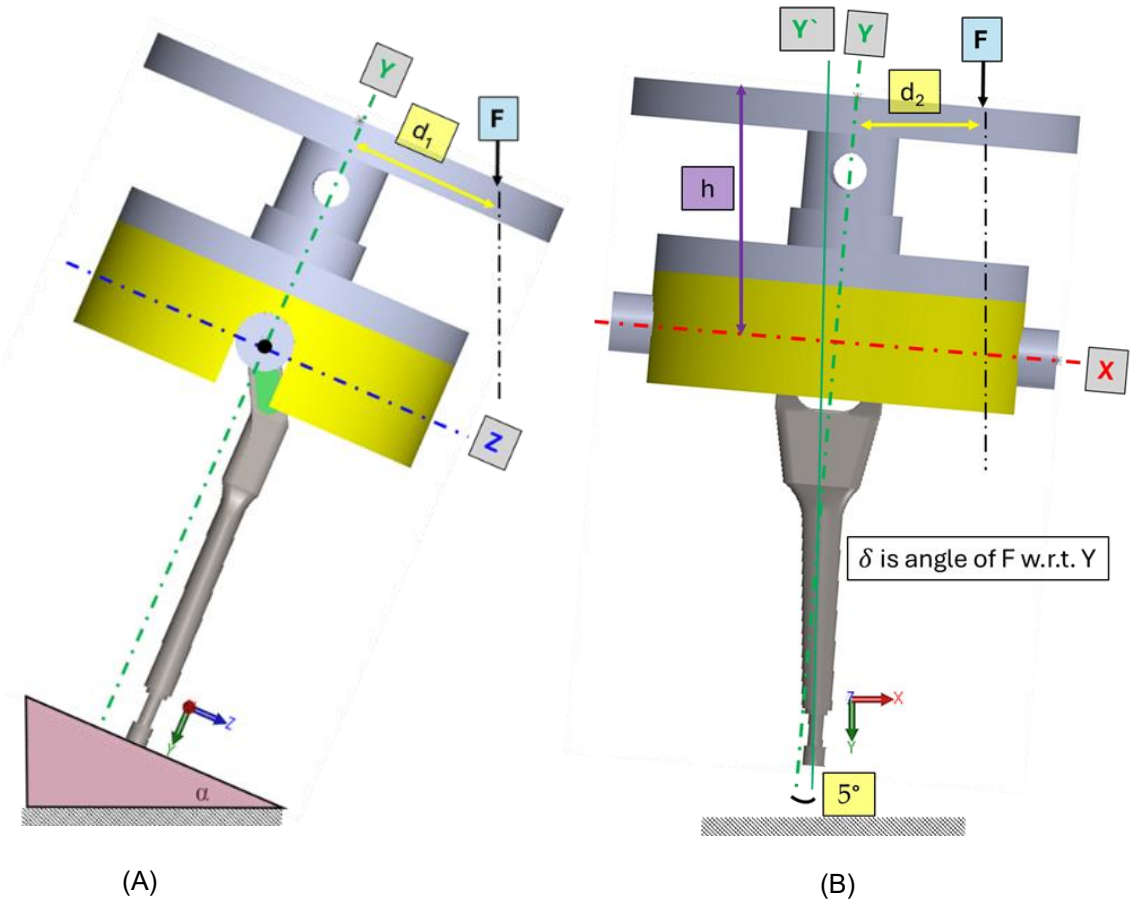

(A) (B)

Figure 5-7: Configuration of Load Case 2 setup showing the humeral stem inclined a α degree in the YZ plane (A) and aligned vertically in the XY plane with the implant rod inclined at 5° about the z-axis (B).

δ is the angle of the applied force F with respect to Y. To calculate δ, we use the cosine rule and the geometry of the system:

$$\delta = \text{acos}(\text{sqrt}(1 - \cos^2(85°) - \cos^2(90° - \alpha)))$$

This equation represents:

- cos (85°): This term represents the relationship between the X and Y components of the angle in the system.
- cos (90° - α): This term accounts for the inclination of the plate and its effect on the angle δ.
- (1 - cos² (85°) - cos² (90° - α)): This term combines the effects of both inclination angles (δ and 5°) on the direction of the applied force relative to the y-axis.

The expression inside the square root is calculated by combining the cosines of the angles, which is based on the geometry of the setup. The inverse cosine ($\cos^{-1}$) is used to solve for δ.

The determinant can be written as in this case:

$$M = \begin{vmatrix} x & y & z \\ d_2 & h & d_1 \\ \sin(5°) & \cos(\delta) & \sin(\alpha) \end{vmatrix}$$

The force and moment components can be determined by the following equations:

$$F_x = F.\sin(5°)$$

$$F_y = F.\cos(\delta)$$

$$F_z = F.\ \sin(\alpha)$$

$$M_x = F\ (\ h.\sin(\alpha) - d_1.\cos(\delta)\ )$$

$$M_y = F\ (\ d_1.\sin(5°) - d_2.\sin(\alpha)\ )$$

$$M_z = F\ (d_2.\cos(\delta) - \ h.\sin(5°)\ )$$

Load Case 3:

In this scenario an angle plate was inclined a β degree in the XY plane; the axle (implant rod) was inclined 5° about the z-axis as seen in Figure 5-8 below.

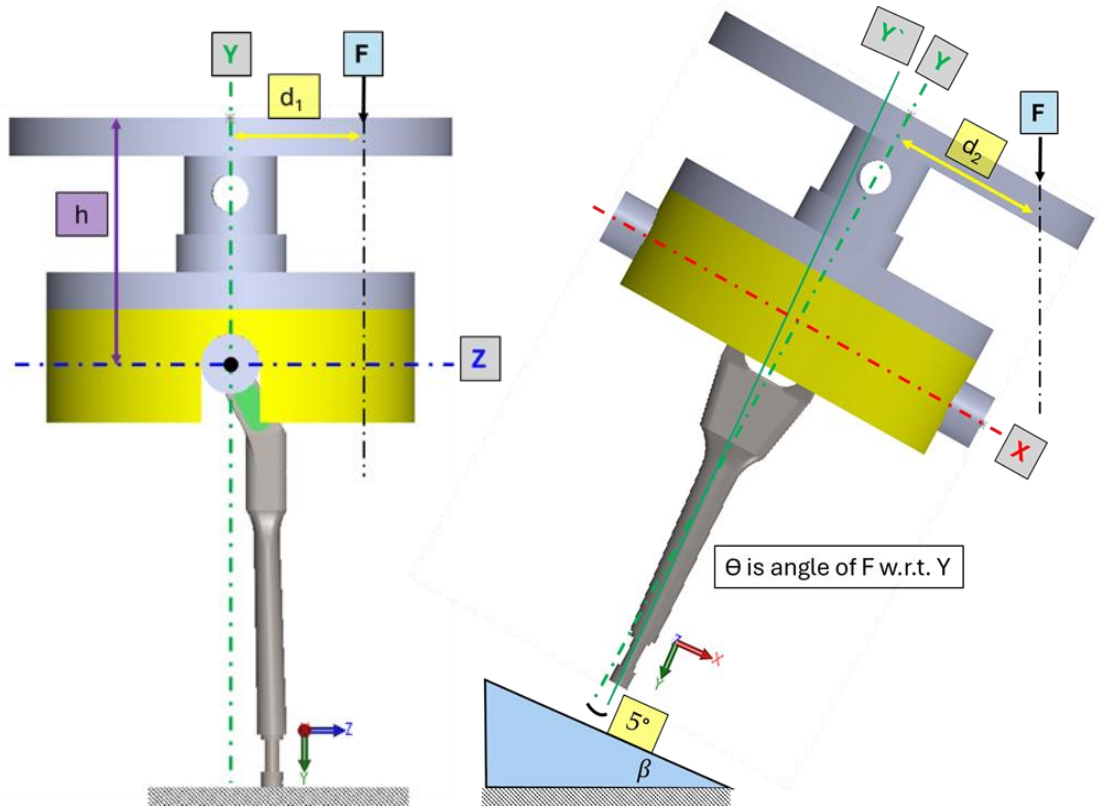

Figure 5-8: Configuration of Load Case 3 setup showing the humeral stem aligned vertically in the YZ plane (A) and inclined a β degree in the XY plane (B).

θ is the angle of the applied force F with respect to Y, therefore:

$$\theta = \mathrm{acos}(\mathrm{sqrt}(1 - \cos^2(85° - \beta) - \cos^2(90°)))$$

In this case, the determinant can be written as:

$$M = \begin{vmatrix} x & y & z \\ d_2 & h & d_1 \\ \sin(5° + \delta) & \cos(\theta) & \sin(90°) \end{vmatrix}$$

The force and moment components can be determined by the following equations:

$$F_x = F.\sin(5° + \beta)$$

$$F_y = F.\cos(\theta)$$

$$F_z = F.\cos(90°)$$

$$M_x = -F.d_1.\cos(\theta)$$

$$M_y = F\,(\,d_1.\sin(5° + \beta)\,)$$

$$M_z = F\,(d_2.\cos(\theta) - h.\sin(5° + \beta)\,)$$

5.2.3.2. Raw Strain Data Analysis

The raw strain gauge data were recorded and exported into an Excel® spreadsheet for analysis across all load cases. This dataset included the applied loads, the voltage outputs from the eight different strain gauges under various loads applied (VSG), and the corresponding resistance measurements of each strain gauge (RSG). To ensure data accuracy, the dataset was filtered to exclude potential signal errors and outliers.

After data cleaning, a linear regression was performed on the data to determine the relationship between the strain which was measured as gauge resistance in ohms (dependent variable) and the calibration applied forces in newtons (independent variable). To perform this, the Excel LINEST function was used which calculated the line of best fit using the equation of a straight line below.

$$Y = mx + b$$

Where:

Y is the strain gauge resistance in ohms (dependant variable)

X is the applied forces in newtons (N) (independent variable)

m is the slope of the line which represents the change in resistance per unit force (ohms/N)

b is the gauge resistance value when the applied force is zero

The LINEST function retuned the change in resistance per unit force (m) for each strain gauge resistance in ohms/N.

The ohms/N values are the relationship between the applied forces and the change in resistance,

Since strain sensitivity is typically measured in microstrain per newton (μstr/N), the ohms/N values were converted to μstr/N using the gauge factor of the strain gauge with the following equation:

$$\text{Microstrain/N (strain/N} * 1\text{e} - 6) = \frac{\text{change in resistance (m)} \left(\frac{\text{ohms}}{\text{N}}\right) * 1\text{e}6}{\text{Gauge factor} \times \text{Initial resistance (ohms)}}$$

This process was repeated for all the datasets collected corresponding to the different loading scenarios used in this setup.

5.2.3.3. Formation of the Calibration Sensitivity Matrix

To develop the calibration matrix, the known calibration forces are applied in various combinations at different points offset from the centre on the calibration plate. This method involves using eight strain gauges placed at pre-identified locations on the humeral implant to capture the complex forces and moments when the humeral implant is subjected to loads. Ideally, each strain gauge should only respond to a single load component, however this is not possible due to the compact size of the instrumented humeral implant stem and the cross-sensitivities between components.

Matrix calculations

The relationship between the applied loads and moments (L) which consist of the forces $\mathrm{L_1} = \mathrm{F_x}$, $\mathrm{L_2} = \mathrm{F_y}$, and $\mathrm{L_3} = \mathrm{F_z}$, in Newtons (N), and moments $\mathrm{L_4} = \mathrm{M_x}$, $\mathrm{L_5} = \mathrm{M_y}$ and $\mathrm{L_6} = \mathrm{M_z}$ measured in Newton-metres (Nm) along the x, y and z

directions, and the strain gauge signals (S) output is expressed by the below matrix equation:

$$\mathrm{S} = \mathrm{C} \times \mathrm{L}$$

Expanded equation:

$$\begin{pmatrix} C_{11} & C_{12} & \cdots & C_{16} \\ C_{21} & C_{22} & \cdots & C_{26} \\ \cdots & \cdots & \cdots & \cdots \\ C_{61} & C_{62} & \cdots & C_{66} \end{pmatrix} \begin{pmatrix} L_1 \\ L_2 \\ \cdots \\ L_6 \end{pmatrix} = \begin{pmatrix} S_1 \\ S_2 \\ \cdots \\ S_6 \end{pmatrix}$$

Where S is the recorded strain gauge signals (unitless), L consists of forces ($\mathrm{F_x}$, $\mathrm{F_y}$, $\mathrm{F_z}$) measured in Newtons (N) and moments ($\mathrm{M_x}$, $\mathrm{M_y}$, $\mathrm{M_z}$) measured in Newton-metres (Nm), and C is the calibration matrix that contains different coefficients for forces (N) and moments (Nm) which needs to be determined.

To convert the recorded signals back into forces and moments, the inverse of the calibration matrix is used as shown in the equation below.

$$\mathrm{L} = \mathrm{M} \times \mathrm{S}$$

M is the inverse matrix (C^{-1})

Compiling and inverting the calibration matrix

The calculated six force and moment components for each load applied in every scenario were compiled and arranged into columns, representing the independent variables in a new Excel® spreadsheet. The microstrain per newton values calculated for each load were similarly arranged in columns as the dependent variables. This table of columns formed the basis for performing regression analysis.

In the calibration setups described above, a separate setup was used for calibrating pure torque in the My direction, as previously described, which required adjustments to the data before conducting the regression analysis. Specifically, the true microstrain ('true μstr') values from the torque calibration

setup were subtracted from the microstrain values obtained from the other setup used to calibrate the remaining five degrees of freedom.

Regression analysis was then performed twice: once considering only the five degrees of freedom and again incorporating all six degrees of freedom. The R-squared value of the resulting regression was evaluated to determine the fit, while the P-value was assessed to gauge the statistical significance of the regression coefficients. The final regression coefficients were then compiled into a 6 x 8 calibration matrix. The inverse of this matrix will be calculated using the using the pseudoinverse method on Excel and will be used to determine the forces and moments acting on instrumented humeral component based on the measured strain gauge signals as a validation in this study and in the next stages of this project.

5.3. Results

The primary objectives of this chapter were to design and implement effective test setups for accurately calibrating the instrumented humeral component in all six degrees of freedom. This involved using the matrix method to construct a calibration sensitivity matrix, ensuring precise measurement of the three forces and three moments acting on the elbow joint.

5.3.1. Resolved Forces and Moments Applied

The resolved six force and moment components for the range of loads applied at each hole position are summarised in Table 5-2 for Load Case 1 , Table 5-3 for Load Case 2 , and Table 5-4 for Load Case 3. They were calculated using the set of equations described in the methodology for all the different load cases. An example illustrating how these forces were calculated and resolved is provided in

Appendix A-2. In all load cases Fy was the dominant force component followed by a smaller contribution from Fx. In Load Case 1, Mz was the only significant moment generated. The remaining three components had zero contributions. Fy remained the dominant force followed by some small Fx and no contribution from Fz when loads applied to holes 23 (located on - z-axis) and 21 (located on z-axis). In addition, moments were observed around Mx, My and Mz with Mx being the most significant moment followed by a smaller contribution from Mz and minor contribution from My. Similarly, in Load Case 3 where the inclination angle (β) lies in the XY plane, significant Mx were generated at holes 23 and 21. In Load Case 2, all six force and moment components had contributions, with Fy being the dominant force. Mx was the dominant moment at holes 23 and 2.

Table 5-2: Detailed decomposition of the 6 degrees of freedom (d.o.f.) results for Load Case 1 (Stem vertical in YZ and XY planes) .This table presents the resolved forces (Fx, Fy, Fz) in N and moments (Mx, My, Mz) in N.mm at five load application points. Each point corresponds to specific coordinates, including Hole 0 at (0, 0), Hole 23 at (0, -10), Hole 22 at (-10, 0), and Hole 21 at (0, 10).

X	Y	Z
sin(5)	cos(5)	cos(90)
0.0872	0.9962	0.0000

Stem Vertical in both planes				Force			Unit	Moment			Unit
Load Case 1	F(N)	1		Fx	Fy	Fz	N	Mx	My	Mz	N.mm
Hole 0 "centre of plate "				Hole 0 "centre of plate "							
d1	h	d2	mm								
0	56	0	mm								
Applied F (N)	Normalised F (N)	Angle (deg)	Cos (angle)								
0	0	1	0.9998	0	0	0	N	0	0	0	N.mm
114	1	1	0.9998	9.936	113.566	0	N	0	0	-556.402	N.mm
334	1	1	0.9998	29.110	332.729	0	N	0	0	-1630.161	N.mm
528	1	1	0.9998	46.018	525.991	0	N	0	0	-2577.021	N.mm
Hole 23 located on -Z				Hole 23 located on -Z							
d1	h	d2	mm								
-8.6	56	0	mm								
Applied F (N)	Normalised F (N)	Angle (deg)	Cos (angle)								
0	0	1.7	0.9996	0	0	0	N	0	0	0	N.mm
126	1	1.9	0.9995	10.982	125.521	0	N	1079.477	-94.442	-614.971	N.mm
330	1	1.9	0.9995	28.761	328.744	0	N	2827.201	-247.348	-1610.638	N.mm
516	1	2	0.9994	44.972	514.036	0	N	4420.714	-386.762	-2518.452	N.mm
Hole 22 located on -X				Hole 22 located on -X							
d1	h	d2	mm								
0	56	-10.1	mm								
Applied F (N)	Normalised F (N)	Angle (deg)	Cos (angle)								
0	0	1.2	0.9998	0	0	0	N	0	0	0	N.mm
124	1	1.6	0.9996	10.807	123.528	0	N	0	0	-1852.844	N.mm
310	1	1.6	0.9996	27.018	308.820	0	N	0	0	-4632.109	N.mm
530	1	1.7	0.9996	46.193	527.983	0	N	0	0	-7919.413	N.mm
Hole 21 located on Z				Hole 21 located on Z							
d1	h	d2	mm								
8.7	56	0	mm								
Applied F (N)	Normalised F (N)	Angle (deg)	Cos (angle)								
0	0	1.4	0.9997	0	0	0	N	0	0	0	N.mm
118	1	-0.6	0.9999	10.284	117.551	0	N	-1022.693	89.474	-575.925	N.mm
332	1	-0.6	0.9999	28.936	330.737	0	N	-2877.409	251.741	-1620.400	N.mm
510	1	-0.7	0.9999	44.449	508.059	0	N	-4420.116	386.710	-2489.168	N.mm
Hole 2 located on X				Hole 2 located on X							
d1	h	d2	mm								
0	56	10	mm								
Applied F (N)	Normalised F (N)	Angle (deg)	Cos (angle)								
0	0	1.4	0.9997	0	0	0	N	0	0	0	N.mm
122	1	-0.6	0.9999	10.633	121.536	0	N	0	0	619.909	N.mm
324	1	-0.6	0.9999	28.238	322.767	0	N	0	0	1646.317	N.mm
512	1	-0.7	0.9999	44.624	510.052	0	N	0	0	2601.587	N.mm

Table 5-3: Detailed decomposition of the 6 degrees of freedom (d.o.f.) results for Load Case 2 (Stem inclined an α degree in the YZ plane) .This table presents the resolved forces (Fx, Fy, Fz) in N and moments (Mx, My, Mz) in N.mm at five load application points. Each point corresponds to specific coordinates, including Hole 0 at (0, 0), Hole 23 at (0, -10), Hole 22 at (-10, 0), and Hole 21 at (0, 10).

X	Y	Z											
sin(5)	cos (δ)	sin(α)											
0.0872	0.9809	0.1736											
d1 variation	1.1027												
Stem Rotated only in YZ plane, angle, alpha					Force			Unit	Moment			Unit	
Loac Case 2	F(N)	1			Fx	Fy	Fz	N	Mx	My	Mz	N.mm	
Hole 0 "centre of plate "					Hole 0 "centre of plate "								
d1	h	d2	mm										
1.1027	56	0	mm										
Applied F (N)	Normalised F (N)	Angle (α) (deg)	sin(α)	cos (δ)									
0	0	8.6	0.1495	0.9848	0	0	0	N	0	0	0	N.mm	
114	0	8.7	0.1513	0.9846	9.936	111.828	19.796	N	985.262	10.956	-556.402	N.mm	
302	0	8.7	0.1513	0.9846	26.321	296.245	52.442	N	2610.079	29.023	-1473.978	N.mm	
520	0	8.7	0.1513	0.9846	45.321	510.091	90.297	N	4494.175	49.974	-2537.975	N.mm	
Hole 23 located on -Z					Hole 23 located on -Z								
d1	h	d2	mm										
-7.5	56	0	mm										
Applied F (N)	Normalised F (N)	Angle (α) (deg)	sin(α)	cos (δ)									
0	0	8.8	0.1530	0.9843	0	0	0	N	0	0	0	N.mm	
118	0	8.1	0.1409	0.9861	10.284	115.751	20.490	N	2015.294	-77.105	-575.925	N.mm	
328	0	8.1	0.1409	0.9861	28.587	321.749	56.957	N	5601.833	-214.327	-1600.877	N.mm	
510	0	8	0.1392	0.9864	44.449	500.281	88.561	N	8710.167	-333.252	-2489.168	N.mm	
Hole 22 located on -X					Hole 22 located on -X								
d1	h	d2	mm										
1.1	56	-10.1	mm										
Applied F (N)	Normalised F (N)	Angle (α) (deg)	sin(α)	cos (δ)									
0	0	8.4	0.1461	0.9853	0	0	0	N	0	0	0	N.mm	
106	0	8.4	0.1461	0.9853	9.239	103.980	18.407	N	916.120	196.095	-1567.555	N.mm	
318	0	8.4	0.1461	0.9853	27.716	311.940	55.220	N	2748.361	588.284	-4702.664	N.mm	
506	0	8.4	0.1461	0.9853	44.101	496.357	87.866	N	4373.178	936.075	-7482.855	N.mm	
Hole 21 located on Z					Hole 21 located on Z								
d1	h	d2	mm										
9.8	56	0	mm										
Applied F (N)	Normalised F (N)	Angle (α) (deg)	sin(α)	cos (δ)									
0	0	12.4	0.2147	0.9724	0	0	0	N	0	0	0	N.mm	
104	0	10.3	0.1788	0.9798	9.064	102.018	18.059	N	11.277	88.853	-507.595	N.mm	
316	0	9.9	0.1719	0.9811	27.541	309.978	54.873	N	34.266	269.977	-1542.308	N.mm	
502	0	9.7	0.1685	0.9817	43.752	492.434	87.171	N	54.435	428.888	-2450.122	N.mm	
Hole 2 located on X					Hole 2 located on X								
d1	h	d2	mm										
1.1	56	10	mm										
Applied F (N)	Normalised F (N)	Angle (α) (deg)	sin(α)	cos (δ)									
0	0	9	0.1564	0.9837	0	0	0	N	0	0	0	N.mm	
114	0	9	0.1564	0.9837	9.936	111.828	19.796	N	985.262	-187.003	561.873	N.mm	
334	0	9.1	0.1582	0.9835	29.110	327.635	57.998	N	2886.643	-547.886	1646.190	N.mm	
530	0	9.3	0.1616	0.9829	46.193	519.900	92.034	N	4580.602	-869.400	2612.218	N.mm	

Table 5-4: Detailed decomposition of the 6 degrees of freedom (d.o.f.) results for Load Case 3 (Stem inclined a β degree in the XY plane) .This table presents the resolved forces (Fx, Fy, Fz) in N and moments (Mx, My, Mz) in N.mm at five load application points. Each point corresponds to specific coordinates, including Hole 0 at (0, 0), Hole 23 at (0, -10), Hole 22 at (-10, 0), and Hole 21 at (0, 10).

X	Y	Z										
sin(5+β)	cos(θ)	cos(90)										
0.0872	1	0										
d2 variation	1.10											
Stem rotated only in XY plane, angle, beta					Force			Unit	Moment			Unit
Load Case 3	F(N)	1			Fx	Fy	Fz	N	Mx	My	Mz	N.mm
Hole 0 "centre of plate "					Hole 0 "centre of plate "							
d1	h	d2	mm									
0	56	1.1027	mm									
Applied F (N)	Normalised F (N)	Angle (β) (deg)	sin(5+β)	cos(θ)								
0	0	10	0.2588	0.9659	0	0	0	N	0	0	0	N.mm
100	1	10	0.2588	0.9659	25.882	96.593	0	N	0	0	-1342.877	N.mm
316	1	10	0.2588	0.9659	81.787	305.233	0	N	0	0	-4243.492	N.mm
504	1	10.1	0.2605	0.9655	131.294	486.598	0	N	0	0	-6815.924	N.mm
Hole 23 located on -Z					Hole 23 located on -Z							
d1	h	d2	mm									
-8.6	56	1.1027	mm									
Applied F (N)	Normalised F (N)	Angle (β) (deg)	sin(5+β)	cos(θ)								
0	0	10.4	0.0872	0.9962	0	0	0	N	0	0	0	N.mm
106	0	10.4	0.0872	0.9962	28.149	102.194	0	N	878.869	-242.081	-1463.655	N.mm
320	0	10.4	0.0872	0.9962	84.978	308.511	0	N	2653.191	-730.810	-4418.582	N.mm
506	0	10.5	0.0872	0.9962	135.223	487.597	0	N	4193.334	-1162.915	-7034.810	N.mm
Hole 22 located on -X					Hole 22 located on -X							
d1	h	d2	mm									
0	56	-8.9973	mm									
Applied F (N)	Normalised F (N)	Angle (β) (deg)	sin(5+β)	cos(θ)								
0	0	10.4	0.0872	0.9962	0	0	0	N	0	0	0	N.mm
132	0	10.4	0.0872	0.9962	35.053	127.261	0	N	0	0	-3107.997	N.mm
334	0	10.4	0.0872	0.9962	88.696	322.008	0	N	0	0	-7864.174	N.mm
510	0	10.5	0.0872	0.9962	136.292	491.452	0	N	0	0	-12054.082	N.mm
Hole 21 located on Z					Hole 21 located on Z							
d1	h	d2	mm									
8.7	56	1.1027	mm									
Applied F (N)	Normalised F (N)	Angle (β) (deg)	sin(5+β)	cos(θ)								
0	0	10.2	0.0872	0.9962	0	0	0	N	0	0	0	N.mm
108	0	10.2	0.0872	0.9962	28.316	104.222	0	N	-906.729	246.353	-1470.798	N.mm
308	0	10.2	0.0872	0.9962	80.754	297.225	0	N	-2585.858	702.562	-4194.499	N.mm
554	0	10.3	0.0872	0.9962	146.186	534.365	0	N	-4648.974	1271.815	-7597.172	N.mm
Hole 2 located on X					Hole 2 located on X							
d1	h	d2	mm									
0	56	11.1	mm									
Applied F (N)	Normalised F (N)	Angle (β) (deg)	sin(5+β)	cos(θ)								
0	0	11	0.0872	0.9962	0	0	0	N	0	0	0	N.mm
126	0	11	0.0872	0.9962	34.730	121.119	0	N	0	0	-600.154	N.mm
320	0	11.2	0.0872	0.9962	89.277	307.294	0	N	0	0	-1587.738	N.mm
516	0	11.4	0.0872	0.9962	145.688	495.006	0	N	0	0	-2662.652	N.mm

5.3.2. Raw Strain Data Analysis

The recorded raw strain gauge data included both the voltage outputs (VSG values) and the corresponding resistance measurements (RSG values) for each strain gauge. These values represent the raw readings captured by LabView during each individual loading case of the humeral component when subjected to the applied calibration forces.

The raw data were filtered to eliminate any errors or anomalies that could significantly impact the results. The relationship between the applied force and the resistance of each strain gauge is illustrated in Figure 5-9. Multiple samples at each load were obtained to filter the electrical noise to improve the accuracy of the calibration. A clear linear relationship was observed across all strain gauges between the applied calibration forces and their corresponding resistance changes in all load cases. Figure 5-9 highlights the varying responses of all eight strain gauges to the loads applied at hole 21 in Load Case 1. For some strain gauges, the resistance decreased as the force increased, while for others, resistance increased with the applied force. For instance, in Load Case 1 at loading hole 21, the resistance of Strain Gauge 8 (RSG8) decreased consistently with increasing force, as shown in Figure 5-10.

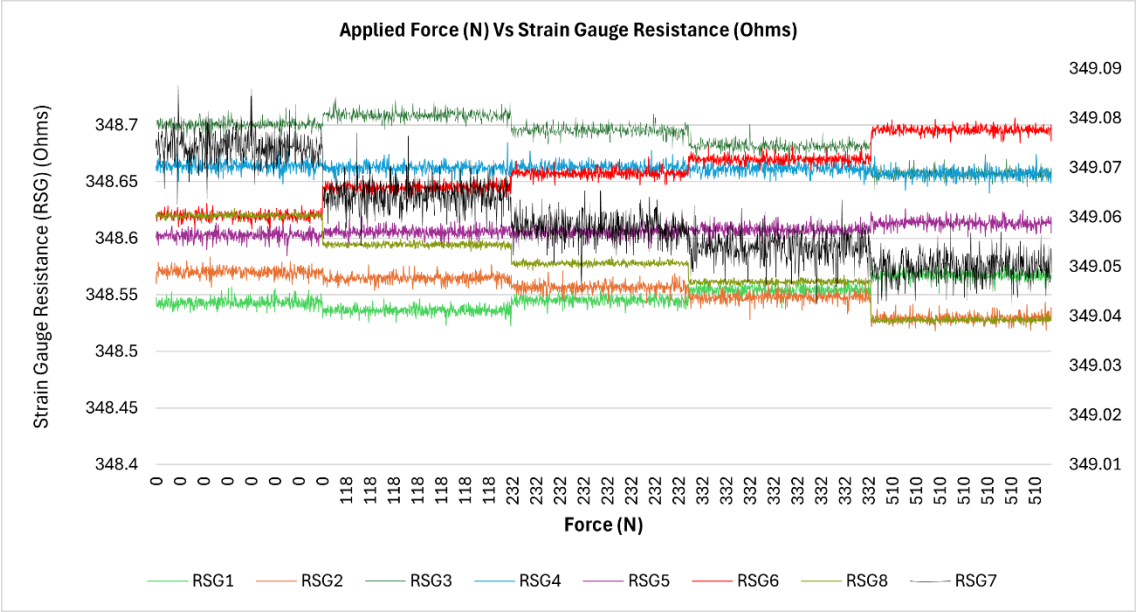

Figure 5-9: Relationship between applied force (N) at Hole 21 in Load Case 1 and the resistance of all 8 strain gauges measured in ohms. The graph illustrates distinct resistance changes corresponding to different applied force levels ranging from 0 – 510 N.

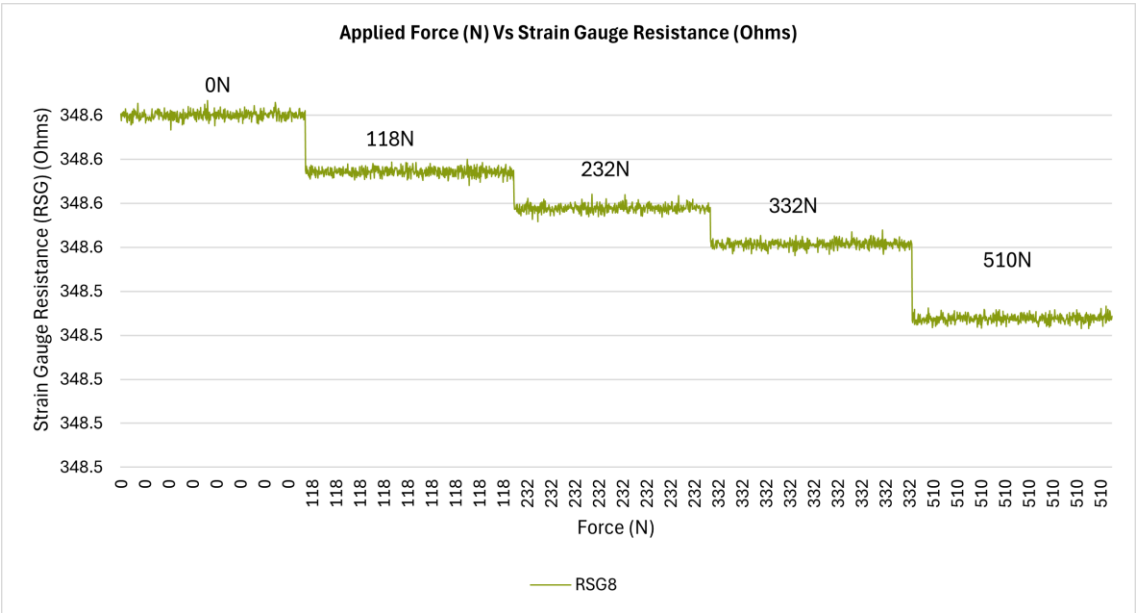

Figure 5-10: Relationship between applied force (N) at Hole 21 in Load Case 1 and the resistance of strain gauge 8 (RSG8) measured in ohms. The graph illustrates decreasing resistance with increasing applied force levels ranging from 0 – 510 N.

A linear regression analysis was conducted to establish the relationship between the measured strain gauge resistance (in ohms) as the dependent variable and the applied calibration forces (in newtons) as the independent variable. The LINEST function was utilised to perform this analysis, which returned the rate of change in resistance per unit force in Ohms/N which was then converted to μstr/N. Table 5-5 below summarises the rate of change in strain per unit force (μstr/N) for all the strain gauges across the multiple loading positions in each case.

Table 5-5: Summarises the rate of change in strain per unit force (μstr/N) for all 8 strain gauges across the 5 loading positions (Holes 0, 2, 21, 22, 23) in Load Case 1 (Stem vertical in both the YZ and XY planes), 2 (Stem inclined an α degree in the YZ plane) , 3 (Stem inclined a β degree in the XY plane), and 4 (Pure My applied).

Load Case 1									
Position	SG 1	SG 2	SG 3	SG 4	SG 5	SG 6	SG 7	SG 8	
Hole 0	8.59E-02	-8.07E-02	-1.48E-01	-5.61E-03	7.22E-03	1.93E-01	-4.61E-02	-2.80E-01	μstr/N
Hole 2	1.62E-01	-1.01E-01	-2.38E-01	1.63E-02	-1.46E-02	8.63E-02	-6.17E-02	-1.65E-01	μstr/N
Hole 21	7.54E-02	-1.10E-01	-1.32E-01	-1.62E-02	2.65E-02	1.94E-01	-6.35E-02	-2.40E-01	μstr/N
Hole 22	1.64E-03	-7.76E-02	-6.18E-02	-1.71E-02	2.69E-02	2.69E-01	-6.10E-02	-3.70E-01	μstr/N
Hole 23	7.47E-02	-7.59E-02	-1.55E-01	-6.94E-03	3.63E-03	1.86E-01	-3.59E-02	-2.91E-01	μstr/N
Load Case 2									
Position	SG 1	SG 2	SG 3	SG 4	SG 5	SG 6	SG 7	SG 8	
Hole 0	4.22E-02	-1.07E-01	-9.30E-02	-4.02E-03	2.46E-02	1.57E-01	-6.26E-02	-2.05E-01	μstr/N
Hole 2	1.54E-01	-1.24E-01	-2.28E-01	1.72E-02	-1.17E-02	6.44E-02	-4.76E-02	-1.25E-01	μstr/N
Hole 21	7.56E-02	-1.03E-01	-1.26E-01	-2.11E-02	4.39E-02	1.83E-01	-8.79E-02	-2.46E-01	μstr/N
Hole 22	1.23E-01	-8.15E-02	-2.05E-01	-1.97E-03	4.40E-03	1.86E-01	-4.43E-02	-2.89E-01	μstr/N
Hole 23	4.65E-02	-9.26E-02	-1.17E-01	4.88E-04	1.04E-02	1.34E-01	-4.87E-02	-2.25E-01	μstr/N
Load Case 3									
Position	SG 1	SG 2	SG 3	SG 4	SG 5	SG 6	SG 7	SG 8	
Hole 0	1.23E-01	-8.15E-02	-2.05E-01	-1.97E-03	4.40E-03	1.86E-01	-4.43E-02	-2.89E-01	μstr/N
Hole 2	1.35E-01	-1.27E-01	-2.11E-01	-1.59E-03	2.23E-04	1.35E-01	-2.92E-02	-2.13E-01	μstr/N
Hole 21	6.35E-02	-9.87E-02	-1.06E-01	-1.21E-02	1.64E-02	2.21E-01	-6.52E-02	-2.93E-01	μstr/N
Hole 22	7.00E-02	-5.23E-02	-1.37E-01	-2.89E-03	1.30E-02	2.21E-01	-7.45E-02	-3.32E-01	μstr/N
Hole 23	1.03E-01	-7.19E-02	-1.99E-01	-1.31E-03	1.17E-03	1.97E-01	-2.78E-02	-3.16E-01	μstr/N
Load Case 4 (Pure My)									
Strain	SG 1	SG 2	SG 3	SG 4	SG 5	SG 6	SG 7	SG 8	
	2.570088	-0.88247	-3.24407	0.740713	0.028622	-2.15702	0.48475	3.576263	μstr/N

The sensitivity of strain Gauge 8 (SG8) was the highest reaching 3.7E−01 μstr/N when the load was applied at Hole 22. Overall, Strain Gauge 8 showed the highest sensitivity across all positions loaded. However, when Hole 2 was loaded, the sensitivity of SG8 was very similar in magnitude but opposite in sign to that of strain gauge 1 (SG1), with sensitivities of -1.7E-01 μstr/N and 1.6E-01 μstr/N, respectively. Notably, the response of SG1 and SG8 with to the applied load followed essentially the same pattern in terms of their sensitivities but differed in sign and magnitudes. The strain gauge responses to applied loads were also found to be similar in pattern between SG3 and SG6, as well as between SG2 and SG7. Strain gauges 4 and 5 (SG4 and SG5) were the least sensitive gauges to the applied loads across all positions. The low sensitivities ranged from 1.7E-02 to 5.6E-03 μstr/N for SG4, and from 2.7E-02 to 3.6E-03 μstr/N for SG5.

The sensitivities of the strain gauges in the other load scenarios showed a similar response to the applied loads as in Load Case 1, with Strain Gauge 8 consistently being the most sensitive gauge across all load cases. However, In Load Case 2, its peak sensitivity reached 2.9E-01 μstr/N, which was slightly lower than the peak sensitivities observed in Load Cases 1 and 3.

5.3.3. Formulation of the Calibration Sensitivity Matrix

The calculated six force and moment components for each applied load in every scenario were organised into columns, with the corresponding microstrain per newton values representing the dependent variables (Table 5-6). The correlation between the three components of force (Fx, Fy, Fz) and the three components of moment (Mx, My, Mz) evaluated to assess the degree of independence between them under varying loading conditions. Certain pairs, such as Fx vs Fy and Fy vs Fz, exhibited periodic trends, indicating potential correlations. In contrast, others,

such as Fx vs My, appeared more irregular, suggesting weak or no correlation. The correlations between all the possible pairs are presented in Figure A -2-1 in Appendix A-2.

Table 5-6: The table shows the independent variables (Fx, Fy, Fz, Mx, Mz, My) representing the calculated forces (N) and moments (N.mm) applied in each scenario (Load Case 1, 2, 3) alongside the corresponding strain for RSG1 to RSG8 measured in microstrain (μstr).

Independent Variables (X)						Dependent Variable (Y)							
Force (N)			Moment			μstr							
Fx	Fy	Fz	Mx	Mz	My	RSG1	RSG2	RSG3	RSG4	RSG5	RSG6	RSG7	RSG8
9.94	113.57	0.00	0.00	-556.40	0.00	9.79	-9.20	-16.93	-0.64	0.82	21.98	-5.25	-31.92
29.11	332.73	0.00	0.00	-1630.16	0.00	28.68	-26.96	-49.59	-1.87	2.41	64.38	-15.38	-93.53
46.02	525.99	0.00	0.00	-2577.02	0.00	44.31	-41.65	-76.61	-2.89	3.72	99.47	-23.77	-144.50
10.98	125.52	0.00	1079.48	-614.97	-94.44	9.41	-9.56	-19.51	-0.87	0.46	23.44	-4.53	-36.69
28.76	328.74	0.00	2827.20	-1610.64	-247.35	24.65	-25.03	-51.10	-2.29	1.20	61.40	-11.85	-96.09
44.97	514.04	0.00	4420.71	-2518.45	-386.76	38.54	-39.14	-79.90	-3.58	1.88	96.00	-18.53	-150.25
10.81	123.53	0.00	0.00	-1852.84	0.00	0.20	-9.62	-7.66	-2.12	3.33	33.39	-7.57	-45.86
27.02	308.82	0.00	0.00	-4632.11	0.00	0.51	-24.04	-19.16	-5.31	8.33	83.48	-18.91	-114.65
46.19	527.98	0.00	0.00	-7919.41	0.00	0.87	-41.11	-32.75	-9.08	14.24	142.72	-32.34	-196.02
10.28	117.55	0.00	-1022.69	-575.93	89.47	8.90	-13.02	-15.52	-1.91	3.13	22.86	-7.49	-0.24
28.94	330.74	0.00	-2877.41	-1620.40	251.74	25.05	-36.63	-43.66	-5.36	8.81	64.31	-21.08	-79.75
44.45	508.06	0.00	-4420.12	-2489.17	386.71	38.48	-56.27	-67.07	-8.24	13.54	98.80	-32.38	-122.51
10.63	121.54	0.00	0.00	619.91	0.00	19.74	-12.34	-29.02	1.99	-1.78	10.53	-7.52	-20.17
28.24	322.77	0.00	0.00	1646.32	0.00	52.41	-32.78	-77.07	5.28	-4.73	27.97	-19.97	-53.57
44.62	510.05	0.00	0.00	2601.59	0.00	82.83	-51.79	-121.79	8.34	-7.47	44.19	-31.56	-84.66
9.94	111.83	19.80	985.26	-556.40	10.96	4.81	-12.23	-10.60	-0.46	2.80	17.88	-7.14	-23.40
26.32	296.24	52.44	2610.08	-1473.98	29.02	12.75	-32.41	-28.08	-1.21	7.42	47.36	-18.91	-61.99
45.32	510.09	90.30	4494.18	-2537.98	49.97	21.95	-55.81	-48.35	-2.09	12.77	81.55	-32.56	-106.74
10.28	115.75	20.49	2015.29	-575.93	-77.11	5.49	-10.93	-13.81	0.06	1.22	15.75	-5.75	-26.52
28.59	321.75	56.96	5601.83	-1600.88	-214.33	15.25	-30.37	-38.40	0.16	3.40	43.79	-15.98	-73.71
44.45	500.28	88.56	8710.17	-2489.17	-333.25	23.71	-47.22	-59.70	0.25	5.28	68.09	-24.85	-114.61
9.24	103.98	18.41	916.12	-1567.55	196.09	13.00	-8.64	-21.71	-0.21	0.47	19.71	-4.70	-30.59
27.72	311.94	55.22	2748.36	-4702.66	588.28	39.01	-25.92	-65.12	-0.63	1.40	59.12	-14.10	-91.78
44.10	496.36	87.87	4373.18	-7482.86	936.07	62.08	-41.25	-103.61	-1.00	2.23	94.07	-22.44	-146.04
9.06	102.02	18.06	11.28	-507.60	88.85	7.86	-10.67	-13.10	-2.19	4.57	18.99	-9.14	-25.59
27.54	309.98	54.87	34.27	-1542.31	269.98	23.87	-32.43	-39.79	-6.67	13.87	57.70	-27.76	-77.74
43.75	492.43	87.17	54.44	-2450.12	428.89	37.93	-51.52	-63.22	-10.59	22.04	91.67	-44.11	-123.51
9.94	111.83	19.80	985.26	561.87	-187.00	17.51	-14.11	-25.96	1.96	-1.33	7.34	-5.42	-14.28
29.11	327.64	58.00	2886.64	1646.19	-547.89	51.31	-41.34	-76.05	5.73	-3.90	21.51	-15.88	-41.83
46.19	519.90	92.03	4580.60	2612.22	-869.40	81.43	-65.60	-120.67	9.09	-6.19	34.13	-25.20	-66.38
25.88	96.59	0.00	0.00	-1342.88	0.00	12.27	-8.15	-20.48	-0.20	0.44	18.59	-4.43	-28.86
81.79	305.23	0.00	0.00	-4243.49	0.00	38.77	-25.76	-64.71	-0.62	1.39	58.75	-14.01	-91.20
131.29	486.60	0.00	0.00	-6815.92	0.00	61.83	-41.09	-103.20	-0.99	2.22	93.70	-22.35	-145.46
28.15	102.19	0.00	878.87	-1463.66	-242.08	10.95	-7.63	-21.07	-0.14	0.12	20.85	-2.95	-33.52
84.98	308.51	0.00	2653.19	-4418.58	-730.81	33.06	-23.02	-63.60	-0.42	0.37	62.94	-8.90	-101.18
135.22	487.60	0.00	4193.33	-7034.81	-1162.91	52.28	-36.41	-100.57	-0.66	0.59	99.53	-14.07	-159.99
35.05	127.26	0.00	0.00	-3108.00	0.00	9.25	-6.91	-18.13	-0.38	1.71	29.16	-9.83	-43.81
88.70	322.01	0.00	0.00	-7864.17	0.00	23.39	-17.48	-45.88	-0.96	4.33	73.77	-24.87	-110.85
136.29	491.45	0.00	0.00	-12054.08	0.00	35.72	-26.70	-70.06	-1.47	6.61	112.65	-37.98	-169.26
28.32	104.22	0.00	-906.73	-1470.80	246.35	-14.28	6.86	-10.66	-11.50	-1.31	1.77	23.92	-7.04
80.75	297.23	0.00	-2585.86	-4194.50	702.56	-40.72	19.56	-30.40	-32.79	-3.73	5.05	68.21	-20.08
146.19	534.36	0.00	-4648.97	-7597.17	1271.82	-73.25	35.18	-54.69	-58.98	-6.71	9.09	122.69	-36.12
34.73	121.12	0.00	0.00	-600.15	0.00	17.00	-15.98	-26.57	-0.20	0.03	17.07	-3.68	-26.78
89.28	307.29	0.00	0.00	-1587.74	0.00	43.18	-40.57	-67.47	-0.51	0.07	43.36	-9.35	-68.01
145.69	495.01	0.00	0.00	-2662.65	0.00	69.62	-65.43	-108.79	-0.82	0.11	69.91	-15.08	-109.66

Table 5-6 was then refined by removing the true strain for My ('true μstr') values, which were calibrated separately. The final data is presented in the table below.

Table 5-7: The table shows the independent variables (Fx, Fy, Fz, Mx, Mz, My) representing the calculated forces (N) and moments (N.mm) applied in each scenario (Load Case 1, 2, 3) alongside the corresponding strain for RSG1 to RSG8 measured in microstrain (μstr) after removing the true strain for My which was calibrated separately.

Independent Variables (X)						Dependent Variable (Y)							
Force (N)			Moment (Nmm)			μstr							
Fx	Fy	Fz	Mx	Mz	My	RSG1	RSG2	RSG3	RSG4	RSG5	RSG6	RSG7	RSG8
9.94	113.57	0.00	0.00	-556.40	0.00	9.79	-9.20	-16.93	-0.64	0.82	21.98	-5.25	-31.92
29.11	332.73	0.00	0.00	-1630.16	0.00	28.68	-26.96	-49.59	-1.87	2.41	64.38	-15.38	-93.53
46.02	525.99	0.00	0.00	-2577.02	0.00	44.31	-41.65	-76.61	-2.89	3.72	99.47	-23.77	-144.50
10.98	125.52	0.00	1079.48	-614.97	-94.44	7.24	-8.81	-16.78	-1.50	0.43	25.26	-4.93	-39.71
28.76	328.74	0.00	2827.20	-1610.64	-247.35	18.97	-23.08	-43.94	-3.93	1.14	66.16	-12.92	-103.99
44.97	514.04	0.00	4420.71	-2518.45	-386.76	29.67	-36.09	-68.70	-6.14	1.78	103.45	-20.21	-162.60
10.81	123.53	0.00	0.00	-1852.84	0.00	0.20	-9.62	-7.66	-2.12	3.33	33.39	-7.57	-45.86
27.02	308.82	0.00	0.00	-4632.11	0.00	0.51	-24.04	-19.16	-5.31	8.33	83.48	-18.91	-114.65
46.19	527.98	0.00	0.00	-7919.41	0.00	0.87	-41.11	-32.75	-9.08	14.24	142.72	-32.34	-196.02
10.28	117.55	0.00	-1022.69	-575.93	89.47	10.96	-13.72	-18.11	-1.31	3.16	21.14	-7.11	2.62
28.94	330.74	0.00	-2877.41	-1620.40	251.74	30.82	-38.61	-50.96	-3.70	8.88	59.47	-19.99	-71.71
44.45	508.06	0.00	-4420.12	-2489.17	386.71	47.35	-59.31	-78.28	-5.68	13.64	91.35	-30.71	-110.16
10.63	121.54	0.00	0.00	619.91	0.00	19.74	-12.34	-29.02	1.99	-1.78	10.53	-7.52	-20.17
28.24	322.77	0.00	0.00	1646.32	0.00	52.41	-32.78	-77.07	5.28	-4.73	27.97	-19.97	-53.57
44.62	510.05	0.00	0.00	2601.59	0.00	82.83	-51.79	-121.79	8.34	-7.47	44.19	-31.56	-84.66
9.94	111.83	19.80	985.26	-556.40	10.96	5.06	-12.32	-10.92	-0.39	2.80	17.67	-7.09	-23.05
26.32	296.24	52.44	2610.08	-1473.98	29.02	13.42	-32.64	-28.92	-1.02	7.42	46.80	-18.78	-61.07
45.32	510.09	90.30	4494.18	-2537.98	49.97	23.10	-56.20	-49.80	-1.76	12.78	80.59	-32.34	-105.15
10.28	115.75	20.49	2015.29	-575.93	-77.11	3.72	-10.32	-11.58	-0.45	1.20	17.24	-6.08	-28.98
28.59	321.75	56.96	5601.83	-1600.88	-214.33	10.33	-28.68	-32.19	-1.26	3.34	47.92	-16.91	-80.55
44.45	500.28	88.56	8710.17	-2489.17	-333.25	16.07	-44.59	-50.05	-1.96	5.20	74.51	-26.29	-125.25
9.24	103.98	18.41	916.12	-1567.55	196.09	17.50	-10.19	-27.39	1.09	0.52	15.93	-3.85	-24.33
27.72	311.94	55.22	2748.36	-4702.66	588.28	52.51	-30.56	-82.16	3.26	1.55	47.79	-11.55	-72.99
44.10	496.36	87.87	4373.18	-7482.86	936.07	83.56	-48.63	-130.73	5.19	2.47	76.04	-18.38	-116.15
9.06	102.02	18.06	11.28	-507.60	88.85	9.90	-11.37	-15.67	-1.61	4.59	17.28	-8.75	-22.75
27.54	309.98	54.87	34.27	-1542.31	269.98	30.07	-34.56	-47.61	-4.88	13.94	52.50	-26.60	-69.12
43.75	492.43	87.17	54.44	-2450.12	428.89	47.77	-54.90	-75.64	-7.75	22.15	83.41	-42.25	-109.81
9.94	111.83	19.80	985.26	561.87	-187.00	13.22	-12.64	-20.54	0.72	-1.38	10.94	-6.23	-20.25
29.11	327.64	58.00	2886.64	1646.19	-547.89	38.74	-37.02	-60.18	2.11	-4.04	32.06	-18.25	-59.33
46.19	519.90	92.03	4580.60	2612.22	-869.40	61.48	-58.75	-95.49	3.34	-6.42	50.87	-28.97	-94.14
25.88	96.59	0.00	0.00	-1342.88	0.00	12.27	-8.15	-20.48	-0.20	0.44	18.59	-4.43	-28.86
81.79	305.23	0.00	0.00	-4243.49	0.00	38.77	-25.76	-64.71	-0.62	1.39	58.75	-14.01	-91.20
131.29	486.60	0.00	0.00	-6815.92	0.00	61.83	-41.09	-103.20	-0.99	2.22	93.70	-22.35	-145.46
28.15	102.19	0.00	878.87	-1463.66	-242.08	5.40	-5.72	-14.06	-1.74	0.06	25.51	-4.00	-41.25
84.98	308.51	0.00	2653.19	-4418.58	-730.81	16.29	-17.26	-42.43	-5.25	0.19	77.02	-12.06	-124.52
135.22	487.60	0.00	4193.33	-7034.81	-1162.91	25.59	-27.24	-66.89	-8.35	0.29	121.92	-19.11	-197.12
35.05	127.26	0.00	0.00	-3108.00	0.00	9.25	-6.91	-18.13	-0.38	1.71	29.16	-9.83	-43.81
88.70	322.01	0.00	0.00	-7864.17	0.00	23.39	-17.48	-45.88	-0.96	4.33	73.77	-24.87	-110.85
136.29	491.45	0.00	0.00	-12054.08	0.00	35.72	-26.70	-70.06	-1.47	6.61	112.65	-37.98	-169.26
28.32	104.22	0.00	-906.73	-1470.80	246.35	-8.63	4.92	-17.80	-9.87	-1.25	-2.97	24.98	0.83
80.75	297.23	0.00	-2585.86	-4194.50	702.56	-24.60	14.02	-50.75	-28.15	-3.55	-8.48	71.25	2.35
146.19	534.36	0.00	-4648.97	-7597.17	1271.82	-44.07	25.16	-91.53	-50.57	-6.39	-15.40	128.19	4.49
34.73	121.12	0.00	0.00	-600.15	0.00	17.00	-15.98	-26.57	-0.20	0.03	17.07	-3.68	-26.78
89.28	307.29	0.00	0.00	-1587.74	0.00	43.18	-40.57	-67.47	-0.51	0.07	43.36	-9.35	-68.01
145.69	495.01	0.00	0.00	-2662.65	0.00	69.62	-65.43	-108.79	-0.82	0.11	69.91	-15.08	-109.66

Regression analysis was performed individually on each of the eight strain gauges. A sample of the regression results for strain gauge 3 is presented below in Table 5-8, where the R-squared value was determined to be 0.92, indicating a strong fit, and the Multiple R value was 0.96. The coefficients for all five degrees of freedom are also presented below, with the coefficient for the sixth degree of freedom added separately at a later stage.

Table 5-8: Regression results for Strain Gauge 3 (RSG3). The analysis shows an R-squared value of 0.92, indicating a strong fit. The Multiple R value of 0.96 reflects a high correlation between the independent variables (Fx, Fy, Fz, Mx, Mz) and strain response. The coefficients of all 5 degrees of freedom are also included.

RSG3								
SUMMARY OUTPUT								
Regression Statistics								
Multiple R	**0.96**							
R Square	**0.92**							
Adjusted R Square	0.89							
Standard Error	17.42							
Observations	45							
ANOVA								
	df	*SS*	*MS*	*F*	*Significance F*			
Regression	5	146108.87	29221.77	96.32	0.00			
Residual	40	12135.35	303.38					
Total	45	158244.23						
	Coefficients	*Standard Error*	*t Stat*	*P-value*	*Lower 95%*	*Upper 95%*	*Lower 95.0%*	*Upper 95.0%*
Intercept	0	#N/A	#N/A	#N/A	#N/A	#N/A	#N/A	#N/A
Fx	-0.30	0.11	-2.75	0.01	-0.53	-0.08	-0.53	-0.08
Fy	-0.13	0.02	-7.01	0.00	-0.17	-0.10	-0.17	-0.10
Fz	-0.17	0.12	-1.40	0.17	-0.42	0.08	-0.42	0.08
Mx	0.00	0.00	1.51	0.14	0.00	0.00	0.00	0.00
Mz	0.00	0.00	-2.57	0.01	-0.01	0.00	-0.01	0.00

Regression analysis was conducted a few times resulting in three different calibration metrics:

1) Considering the five degrees of freedom derived from applying eccentric loads without modifying My and the pure My added separately into the matrix
2) Considering the five degrees of freedom derived from applying eccentric loads with modifying My and the pure My added separately
3) Considering only all six degrees of freedom derived from applying eccentric loads without modifications to My

The final regression coefficients from each analysis were compiled into a 6 x 8 calibration matrix, as shown below in Table 5-9 for regression analysis 1, Table 5-10 for regression analysis 2, and Table 5-11 for Load Case 3.

Table 5-9: A 6 x 8 calibration matrix compiling the regression coefficients for (Fx, Fy, Fz, Mx, My, Mz) in the case of considering only the five degrees of freedom derived from applying eccentric loads without modifying My. The pure My was added separately into the last row of the matrix. Multiple R values are also displayed.

Multiple R	0.87	0.94	0.98	0.71	0.76	0.98	0.73	0.99	
Fx	-5.59E-01	4.11E-01	2.50E-01	-2.02E-01	1.41E-02	1.50E-01	4.36E-01	-2.87E-01	μstr/N
Fy	9.27E-02	-1.06E-01	-1.38E-01	3.23E-03	1.32E-02	1.96E-01	-8.33E-02	-2.74E-01	μstr/N
Fz	-1.07E-01	7.25E-03	5.57E-02	8.17E-02	-6.27E-02	-3.02E-01	5.41E-02	2.14E-01	μstr/N
Mx	3.17E-03	-1.76E-03	-2.04E-03	-7.72E-04	1.47E-03	1.70E-03	-1.87E-03	5.07E-04	μstr/Nmm
Mz	7.38E-03	-3.85E-03	-6.43E-03	1.73E-03	-9.55E-04	-4.93E-03	-1.61E-03	6.21E-03	μstr/Nmm
My	-2.66E-02	1.67E-02	3.10E-05	-6.59E-03	-4.16E-03	-4.79E-02	4.26E-02	6.68E-02	μstr/Nmm

Table 5-10: A 6 x 8 calibration matrix compiling the regression coefficients for (Fx, Fy, Fz, Mx, My, Mz) in the case of considering only the five degrees of freedom derived from applying eccentric loads with modifying My. The pure My was added separately into the last row of the matrix. Multiple R values are also displayed.

Multiple R	0.81	0.93	0.96	0.66	0.74	0.96	0.63	0.97	
Fx	5.80E-02	7.50E-02	-3.04E-01	-6.65E-02	-1.06E-01	-4.33E-01	3.56E-01	4.13E-01	µstr/N
Fy	8.89E-02	-1.04E-01	-1.35E-01	2.19E-03	1.29E-02	1.96E-01	-8.15E-02	-2.72E-01	µstr/N
Fz	3.20E-02	-5.51E-02	-1.70E-01	-5.82E-02	6.85E-02	-4.96E-01	1.87E-01	8.03E-01	µstr/N
Mx	8.12E-04	-7.40E-04	2.04E-03	1.76E-03	-8.48E-04	5.47E-03	-4.50E-03	-1.07E-02	µstr/Nmm
Mz	3.08E-03	-1.92E-03	-2.99E-03	5.51E-04	-1.23E-03	-5.49E-03	4.07E-04	6.39E-03	µstr/Nmm
My	-2.29E+04	7.88E+03	2.90E+04	-6.61E+03	-2.56E+02	1.93E+04	-4.33E+03	-3.19E+04	µstr/Nmm

Table 5-11: A 6 x 8 calibration matrix compiling the regression coefficients for (Fx, Fy, Fz, Mx, My, Mz) in the case of considering all six degrees of freedom derived from applying eccentric loads without modifications to My. Multiple R values are also displayed.

Multiple R	0.83	0.94	0.97	0.77	0.79	0.98	0.75	0.99	
Fx	-2.81E-01	2.34E-01	1.49E-01	-1.01E-01	5.90E-02	3.80E-01	1.20E-01	-5.48E-01	µstr/N
Fy	8.88E-02	-1.03E-01	-1.36E-01	1.80E-03	1.26E-02	1.93E-01	-7.89E-02	-2.71E-01	µstr/N
Fz	1.08E-01	-1.03E-02	-2.12E-01	7.50E-02	-8.97E-02	-3.37E-01	1.21E-01	2.12E-01	µstr/N
Mx	-5.57E-04	-1.43E-03	2.55E-03	-6.77E-04	1.92E-03	2.24E-03	-2.95E-03	5.83E-04	µstr/Nmm
Mz	2.98E-03	-1.06E-03	-4.81E-03	1.23E-04	-1.66E-03	-8.55E-03	3.36E-03	1.03E-02	µstr/Nmm
My	-2.47E-02	2.24E-02	-1.72E-03	-1.38E-02	-7.44E-03	-3.23E-02	4.55E-02	3.43E-02	µstr/Nmm

The inverse of these matrices as presented below (Table 5-14, Table 5-13, Table 5-12,) were calculated and used to test the accuracy of the calibration matrix in predicting the forces and moments in this study but also will be utilised in the next chapter in a biomechanical study to validate the measured forces and moments based on strain measurements in the instrumented humeral component.

Table 5-14: The inverse calibration matrix compiling the regression coefficients for (Fx, Fy, Fz, Mx, My, Mz) in the case of considering only the five degrees of freedom derived from applying eccentric loads without modifying My. The pure My was added separately into the last row of the matrix.

Multiple R	0.87	0.94	0.98	0.71	0.76	0.98	0.73	0.99	
Fx	1.67E+00	3.78E+00	-1.17E+00	-3.12E+00	3.71E+00	-4.89E+00	-6.29E-01	-3.47E+00	N/µstr
Fy	-5.80E+00	-7.26E+00	-3.74E+00	1.92E+00	-8.82E-01	2.34E+00	1.79E+00	1.81E-01	N/µstr
Fz	-3.10E+00	-7.75E-01	-1.83E+00	-3.81E+00	9.05E+00	-9.96E+00	-4.30E+00	-5.26E+00	N/µstr
Mx	-8.43E+01	2.31E+01	-1.14E+02	-4.35E+02	7.42E+02	-4.39E+02	-2.61E+02	-1.84E+02	Nmm/µstr
Mz	2.16E+02	2.50E+02	-6.54E+01	-7.14E+01	1.01E+01	-1.98E+02	2.16E+01	-1.39E+02	Nmm/µstr
My	-2.52E+01	-3.60E+01	-6.29E+00	1.62E+01	-2.30E+01	4.18E+01	1.99E+01	3.15E+01	Nmm/µstr

Table 5-13: The inverse calibration matrix compiling the regression coefficients for (Fx, Fy, Fz, Mx, My, Mz) in the case of considering all six degrees of freedom derived from applying eccentric loads without modifications to My.

Multiple R	0.83	0.94	0.97	0.77	0.79	0.98	0.75	0.99	
Fx	3.67E+00	1.06E+01	-4.35E+00	-5.69E-01	1.09E+01	1.73E-01	-2.11E+00	5.90E-01	N/µstr
Fy	-4.36E+00	-9.19E+00	-1.61E+00	-2.33E+00	-2.92E+00	-1.66E-01	2.06E+00	-1.68E+00	N/µstr
Fz	-6.43E+00	-1.90E+00	-3.14E+00	2.18E+00	8.52E+00	-9.06E+00	-3.37E+00	-4.87E+00	N/µstr
Mx	-3.04E+02	-5.79E+01	-2.22E+02	-9.13E+01	6.95E+02	-2.83E+02	-2.01E+02	-7.78E+01	Nmm/µstr
Mz	4.30E+02	6.50E+02	-2.38E+02	-1.13E+02	4.62E+02	2.40E+02	-5.01E+01	2.19E+02	Nmm/µstr
My	-5.57E+01	-8.66E+01	1.60E+01	-1.08E+01	-5.14E+01	-1.34E+01	2.29E+01	-1.20E+01	Nmm/µstr

Table 5-12: The inverse calibration matrix compiling the regression coefficients for (Fx, Fy, Fz, Mx, My, Mz) in the case of considering only the five degrees of freedom derived from applying eccentric loads with modifying My. The pure My was added separately into the last row of the matrix.

Multiple R	0.81	0.93	0.96	0.66	0.74	0.96	0.63	0.97	
Fx	-1.46E+00	9.15E-01	-1.72E+00	6.49E-01	1.26E+00	-3.30E+00	7.98E-01	-2.53E+00	N/µstr
Fy	-1.63E+00	-5.16E+00	-2.22E+00	-4.66E+00	3.02E-01	6.27E-01	4.01E-01	-8.29E-01	N/µstr
Fz	-5.40E+00	-1.10E+00	-3.10E+00	2.23E+00	9.60E+00	-7.81E+00	-3.06E+00	-4.04E+00	N/µstr
Mx	-2.38E+02	7.79E+01	-1.69E+02	3.03E+02	5.02E+02	-5.66E+02	-2.05E+02	-3.43E+02	Nmm/µstr
Mz	1.96E+02	-2.59E+02	2.10E+02	-2.77E+02	-5.71E+02	1.92E+02	2.80E+01	1.59E+02	Nmm/µstr
My	-2.55E-05	-4.93E-05	1.49E-05	-5.14E-05	-2.94E-05	-1.62E-05	1.67E-06	-1.08E-05	Nmm/µstr

5.4. Discussion

The primary focus of this chapter was to design and implement test setups capable of calibrating all degrees six degrees of freedom for the newly developed prototype stem. This calibration process ensures that the instrumented humeral component can reliably measure the complex forces and moments acting on the elbow joint.

To achieve this, two key objectives were addressed. Firstly, comprehensive experimental test setups were developed and executed to calibrate each degree of freedom independently (three forces and three moments). Secondly, the matrix method was applied to construct a calibration sensitivity matrix. This matrix is used for converting the raw strain gauge data into meaningful measurements of the three forces and three moments acting on the elbow joint during normal activities of daily living (ADL).

5.4.1. Resolved Components

In a real-world scenario, the elbow joint experiences forces and moments from various directions and magnitudes due to complex biomechanical movements. It was crucial to decompose the calibration force into its components (F_x, F_y, F_z, M_x, M_y, M_z) to better understand the behaviour of the measurement system. A more realistic analysis of the strain gauges response to the applied load becomes possible by identifying the specific contributions of each force and moment component. Ideally, applying a calibration load should generate a response in only one load component, as each strain gauge is designed to measure a specific force or a moment component aligned with its direction. However, the experimental results indicated that multiple load components were produced for the same calibration load applied.

For example, in Load case 1, a load vector of 114 N was applied to the central hole (Hole 0) on the calibration plate resulting in a total of three components acting simultaneously. These components were $\mathrm{F_x} = 9.9\ \mathrm{N}$, $\mathrm{F_y} = 113.6\ \mathrm{N}$ and $\mathrm{M_z} = -556.4\ \mathrm{Nmm}$. In other cases, up to five or six load components were observed. For instance, in Load scenario 2, when applying a force of 118 N to hole 23, located on the – z-axis, six components were generated: $\mathrm{F_x} = 10.3\ \mathrm{N}$, $\mathrm{F_y} = 115.8\ \mathrm{N}$, $\mathrm{F_z} = 20.5\ \mathrm{N}$, $\mathrm{M_x} = 2015.3\ \mathrm{Nmm}$, $\mathrm{M_y} = -77.1\ \mathrm{Nmm}$ and $\mathrm{M_z} = -575.9\ \mathrm{Nmm}$.

This phenomenon can be attributed to the inherent mechanical interaction between forces and moments in multiple directions due to the complex and irregular geometry of the humeral implant. Unlike standard six degrees-of-freedom (d.o.f) load cells, where strain gauges are arranged to isolate specific d.o.f measurements, the geometry of the humeral component results in all strain gauges contributing to the response in multiple degrees-of-freedom. As such, an applied load or moment in one direction generates strain signals across all gauges, with each gauge responding to a combination of forces and moments. This interaction was anticipated from the outset given the unusual configuration, and it underscores the necessity of applying calibration techniques, such as multiple linear regression, to isolate the contributions of each load and moment.

In Load Case 1, it was observed that applying force to the central hole (Hole 0), Hole 22 (on the – x-axis), and Hole 2 (on the x-axis) resulted in Fy being the dominant force component. The Fx component was much smaller, and Mz was the only significant moment generated. The remaining three components had zero contributions. Considering that in this scenario, the humeral implant stem was vertical in both the YZ and XY planes, the outcome is explained by the fact

that direction of the applied force primarily aligned with the y-axis. The small contribution of Fx is attributed to the 5° valgus alignment of the humeral component relative to the long axis of the stem.

Mz was the only moment generated because the z-axis acts as the axis of rotation for the YZ plane, therefore when a force is applied in this plane, it creates a lever arm relative to the z-axis. The length of this lever arm, combined with the magnitude of the force, generates a moment around the z-axis.

Applying calibration force on holes 23 (on - z-axis) and 21 (on z-axis), resulted in Fy again as the dominant force followed by some small Fx and no contribution from Fz. This is consistent with the alignment of the force application and the orientation of the holes relative to the coordinate axes. In addition, moments were observed around Mx, My and Mz with Mx being the most significant moment followed by a smaller contribution from Mz and minor contribution from My. The Mx can be attributed to the larger lever arms created by the positions of the holes relative to the x-axis. However, the contribution of My remained relatively low due to the smaller lever arms relative to the y-axis.

Similarly, in Load Case 3, the inclination angle (β) lies in the XY plane and the line of action of the force predominantly aligns with the y-axis. This alignment results in significant Mx contributions at holes 23 and 21, due to the larger lever arm created by the inclination angle.

In contrast, in Load Case 2, all six force and moment components had contributions, with Fy being the dominant force. Mx was the dominant moment at holes 23 and 2, driven by the larger lever arm relative to the x-axis, as the inclination angle in this case is within the YZ plane.

5.4.2. Raw Strain Data Analysis

During the calibration process, a series of known forces were systematically applied to the humeral component, and the corresponding changes in resistance were recorded for each strain gauge. The strain gauges consistently responded to the applied loads, demonstrating a predictable and reliable behaviour. Across all load cases, a clear linear relationship was observed between the applied forces and the resistance changes in all the strain gauges. In some cases, resistance decreased as the force increased, while in others, it increased. This linearity indicates that the strain gauges accurately reflect variations in load, consistently responding in the same way every time a load was applied. This consistency provides confidence that the actual mechanical forces acting on the humeral component are being accurately measured and represented.

The sensitivities of all the strain gauges were thoroughly assessed, Strain Gauge 8 (SG8) exhibited the highest sensitivity across all load cases reaching a peak of 3.7E−01 μstr/N in Load Case 1. This means that this strain gauge is well-placed on the medial fork of the implant where it experiences significant amount of strain under the applied load due to its greater distance from the point of load application. Therefore, it captured the significant strain changes, for every newton (N) of force applied, the strain gauge measured a change in strain of 0.37 microstrain (μstr).

Interestingly, when the load was applied at Hole 2 in Load Case 1, SG8 and Strain Gauge 1 (SG1) displayed nearly identical sensitivity magnitudes but with opposite signs. SG8 had a sensitivity of -1.7E-01 μstr/N, while SG1 measured 1.6E-01 μstr/N. This mirrored response suggests that the strain gauges are experiencing similar mechanical loads but in opposite directions. This is also likely due to their symmetrical positioning on the medial and lateral forks relative to the applied

load. The difference sign of strain sensitivity reflects the direction of the applied load relative to the orientation of strain gauge. The positive sensitivity value is because the strain gauge is experiencing tensile load, while negative strain indicates a compressive load.

The similar sensitivities observed between Strain Gauges 3 and 6 (SG3 and SG6), as well as between Strain Gauges 2 and 7 (SG2 and SG7) likely reflects their symmetrical positions on the humeral component. This consistency in response among these gauge pairs suggests that the measurement system is reliably capturing the strain distribution across the component, particularly in response to forces applied at different angles and positions.

On the other hand, Strain Gauges 4 and 5 (SG4 and SG5) showed the lowest sensitivities across all load positions in all setups. SG4 showed sensitivities ranging from 1.7E-02 to 5.6E-03 μstr/N, while SG5 ranged from 2.7E-02 to 3.6E-03 μstr/N. The lower sensitivity of these gauges is expected and attributed to their placement on the base cavity of the humeral component that experienced less strain under the applied loads.

5.4.3. Construction of the Calibration Matrix

The calibration sensitivity matrix was built by performing a separate regression analysis for each of the eight strain gauges to examine the relationship between the applied forces and the corresponding strain sensitivities.

The R-squared value for Strain Gauge 3 (SG3) was calculated to be 0.92, indicating that 92% of the variations in strain sensitivities can be explained by the model. This high R-squared value suggests that the regression model is a strong fit for the data, meaning that the model accurately reflects the relationship between the strain gauge responses to the applied forces. Additionally, the

Multiple R value for the same gauge was found to be 0.96 which indicates a high degree of correlation between the observed strain sensitivities and the predicted values from the model. In other words, the model has a high predictive accuracy, highlighting the strong linear relationship between the input calibration forces and the measured strains.

Overall, strain gauges 2, 3, 6, and 8 had Multiple R values of 0.93 or higher, indicating a strong correlation between observed and predicted strain responses. Conversely, strain gauges 1, 4, 5, and 7 recorded Multiple R values between 0.63 and 0.81, reflecting a moderate level of correlation. This variation indicates that some gauges demonstrate stronger predictive capabilities than others.

To evaluate how well the calibration matrix works, we used its inverse to calculate the forces and moments based on the measured strain sensitivities. The comparison between predicted and actual forces revealed an average error of 29.7 N for Fx, 26.9 N for Fy, and 25.5 N for Fz. The discrepancies in predicted versus actual applied moments were more pronounced. Despite the high Multiple R values, these differences suggest that the model, although showing strong correlation, may not fully account for other factors affecting strain responses, leading to prediction errors.

One possible explanation for these discrepancies is the application of pure My in the calibration matrix. While the five degrees of freedom (Fx, Fy, Fz, Mx, and Mz) were derived from applying eccentric loads to the humeral implant, My was introduced by applying a pure moment separately. The disadvantage of applying a pure moment, although they do not directly create friction, they can lead to additional stresses on the test fixtures, potentially increasing friction at contact points. This added friction can interfere with accurate strain measurements and misinterpreted as calibration errors. Pure moments also generate rotational

forces around the y-axis without a corresponding translational force. This often requires precise alignment of the strain gauges to measure sensitivities accurately. Furthermore, strain gauges are generally more sensitive to forces than to moments, as moments induce rotational strains that are harder to measure accurately with gauges designed primarily for linear strains.

In contrast, applying only eccentric forces and moments tends to yield better calibration results as previously concluded by Bergmann at al (Bergmann et al., 2008). Eccentric loading introduces a combination of normal and shear stresses along with moments, producing more distinct strain responses. This approach more accurately simulates real-world physiological loading conditions of the humeral implant stem, where forces are rarely applied centrally. Eccentric forces also help distribute loads more evenly across strain gauges, reducing the risk of localised measurement errors that can arise with pure moments.

Despite some discrepancies between the applied and predicted forces and moments, the inverse of the calibration matrix (constructed by considering the five degrees of freedom from eccentric loads, with the pure My component added separately) was chosen for the next phase of the validation study. This matrix will be used to measure forces and moments based on strain data in an upcoming biomechanical study.

Upon evaluating the different matrices compiled, the matrix constructed by considering the five degrees of freedom derived from applying eccentric loads, without modifying My and with the pure My added separately was found to be non-representative, as it accounted for My twice without appropriate adjustments. Similarly, the matrix that included all six degrees of freedom derived from applying eccentric loads without modifications to My was also deemed unsuitable, as the resulting My was insufficiently calibrated.

The most representative matrix was the one that considered the five degrees of freedom from eccentric loads, with My modified and the pure My added separately. In this matrix, the true strain ('true μstr') values from the separate torque calibration setup were removed, and My was appropriately adjusted, leading to a more accurate calibration. Therefore, the inverse of this matrix was selected to be used in the upcoming biomechanical validation study.

5.4.4. Limitations and Future Work

This experimental study had several limitations. One of which was the attachment method of the calibration loading plate to the humeral component, which involved using an additional intermediary plate. This added weight to the overall setup, restricting its ability to accommodate variations in alpha and beta angles in certain setups. As a result, the inclination angle was always kept to a minimum to avoid compromising the stability of the implant, even when clamped and secured properly. This constraint may have restricted the physiological relevance of the loading scenarios tested. In future studies, expanding the range of loading scenarios would improve the calibration process, allowing for a more comprehensive assessment of the humeral implant's behaviour under varied physiological conditions.

Another limitation was the inability to position the instrumented humeral implant at different flexion angles due to the design of the setup. The forks of the implant were constrained using posterior screws to the rotating rod, which restricted the ability to simulate the humeral component's behaviour under varying flexion angles. Understanding load distribution and mechanical response during flexion-extension movements of the elbow joint is crucial. Future work should incorporate a more adaptable setup that allows for flexion angle adjustments, enabling a more

comprehensive assessment of the humeral component's performance under conditions that more closely mimic actual physiological movements around the elbow joint.

The load case configurations did not generate sufficient My and hence the application of a pure moment around the y-axis. This approach had some possible negative impact on the accuracy of the calibration matrix. Pure moments do not replicate the complex loading conditions that the humeral implant would experience in a real-world scenario and can therefore introduce non-linearities and inaccuracies that compromise the reliability of the calibration procedure. In future studies, repeating this calibration process should be designed to entirely avoid the application of pure moments. This can be achieved by using a dedicated 6 d.o.f calibration rig, where multiple combinations of forces and moments are applied in sequence. This would help construct a more accurate and representative calibration matrix.

These limitations stem partly from the fact that this study was conducted using an early-stage prototype implant and a preliminary experimental setup designed primarily to validate fundamental mechanical behaviour and strain measurement feasibility rather than to reproduce comprehensive physiological loading.

These simplifications and constraints mean that the findings should be interpreted with caution when extrapolating to real-world implant performance under full physiological conditions. The restricted range of loading angles and absence of soft tissue effects may have led to underestimation or altered distribution of stresses and strains compared to in vivo behaviour.

5.5. Conclusion

This chapter detailed the procedure developed and implemented to calibrate the instrumented humeral component prototype. The process involved designing suitable test setups to calibrate all six degrees of freedom. Additionally, the matrix method was applied to develop a calibration sensitivity matrix to measure the three forces and three moments acting on the elbow joint, thereby enhancing the accuracy and reliability of the instrumented humeral component.

The coefficients yielded from the regression analysis represented the sensitivity of the strain gauges to the applied loads. Each coefficient indicated the change in the strain gauge output per unit of force or moment applied in a specific direction (x, y, or z). The coefficients of SG 2, 3, 6, and 8 consistently had Multiple R values of 0.93 or higher, indicating a strong correlation between observed and predicted strain responses. Conversely, strain gauges 1, 4, 5, and 7 recorded slightly lower Multiple R values between 0.63 and 0.87 in all the compiled matrices. This variation indicates that some gauges demonstrate stronger predictive capabilities than others.

Despite some discrepancies between the applied and predicted forces and moments, the inverse of the calibration matrix that considered the five degrees of freedom derived from eccentric loading, with My modified and the pure My added separately representing the sixth degree of freedom, was chosen for the next phase of the validation study. This matrix will be used to measure forces and moments based on strain data in an upcoming biomechanical study.

Building on this calibration framework, the next chapter focuses on applying the calibrated humeral implant prototype in an in vitro biomechanical study to measure elbow joint forces and moments under simulated physiological loading

conditions. This study will evaluate the ability of the implant to capture complex joint dynamics and provide insights into the mechanical behaviour of the elbow during activities of daily living. The findings will contribute to validating the implant's functionality and advancing its application in biomechanical and future clinical research.

Chapter 6: In Vitro Measurement of Elbow Forces Using a Calibrated Prototype Implant – A Preliminary Biomechanical Study

6.1. Introduction

This chapter details an experimental biomechanical study designed to measure all six degrees of freedom acting on the elbow joint during typical activities of daily living (ADL). This study uses a complete elbow implant, consisting of the previously calibrated instrumented humeral component prototype combined with the ulna and bearing parts from the Discovery Elbow System (DES). This implant was inserted into synthetic humeral and ulnar bones to simulate the biomechanics of a total elbow arthroplasty (TEA), focusing on the contribution of the brachialis muscle. Following this, an experimental biomechanical setup was used to measure and validate the three forces and three moments acting on the elbow joint during typical activities of daily living (ADL).

To date, the accurate measurement of forces and moments at the elbow joint has long been a challenge in biomechanics, with existing methods relying on indirect approaches or mathematical modelling. Historically, joint reaction forces in the elbow have been estimated through computational models, which often rely on assumptions and are limited by their inability to provide direct, real-world measurements. These models have predominantly focused on isometric actions under severe loading conditions. A few studies such as those by Amis et al. (1979) and Nicol (1977) provided estimates based computational inverse dynamics and distribution models. Amis et al. (1979) estimated that maximum forces during elbow flexion could reach up to 3 kN at both the humero-radial and

humero-ulnar articulations. This estimation was derived from cadaveric experiments in which controlled loads were applied to simulate elbow flexion. The study utilised cadaveric upper limbs, with weights and pulleys used to mimic muscle forces acting on the joint at different angles of elbow flexion and loading magnitudes (Amis et al., 1979a). Nicol et al. (1977) used a biomechanical model with data from motion capture, electromyography (EMG), and force transducers to estimate elbow joint forces in young, healthy male subjects performing various activities of daily living (ADL) (Nicol et al., 1977). Their study found that during light activities, such as dressing and eating, peak joint forces reached 300 N. In contrast, more strenuous ADL, such as arm-assisted chair rises and pulling a large table, resulted in peak joint forces of 1700 N and 1900 N, respectively (Nicol et al., 1977). These estimates have been corroborated and ranged from 350 N for light activities to 2094 N for extreme loading conditions (Kincaid & An, 2013).

While these computational models and inverse dynamics approaches have provided valuable estimates of elbow joint forces, they fall short of delivering direct, real-world measurements. Direct measurement of forces acting on the elbow joint enables quantitative in-vivo biomechanical assessments, which are considered the gold standard. Early instrumentation research predominantly centred on hip (Bergmann et al., 1993) and knee joints (Heinlein et al., 2007) (Kirking et al., 2006), as discussed in Chapter 5. These studies have yielded valuable force and moment data, validating previous modelling approaches that were found to overestimate the measured values significantly. Thus, the true power of these models is when they are validated by in vivo measurement.

Until now, direct measurement of elbow joint forces using implants has not been achieved. There have been no attempts to develop an instrumented elbow implant with embedded strain gauges specifically aimed at measuring forces and

moments around the axis of the elbow joint during normal activities of daily living (ADL). Therefore, this biomechanical study aims to conduct a preliminary validation of the instrumented humeral implant prototype, assessing its capability to measure elbow joint forces and moments during simulated activities of daily living (ADL), with the understanding that further design iterations and reproducibility studies are required before any progression towards human testing.

The specific objectives of this biomechanical study are:

1) To conduct an in vitro biomechanical study to validate the functionality and performance of the instrumented humeral implant prototype in measuring the forces and moments acting on the elbow joint, including the six degrees of freedom measured during calibration under simulated physiological loading conditions.
2) To quantify the three forces and three moments acting on the elbow joint during typical activities of daily living (ADL) and compare these measurements against modelled forces and moments to assess their validity.

6.2. Materials and Methods

6.2.1. Humerus and Ulna Bone Preparation

Total elbow arthroplasty (TEA) was carried out using synthetic humerus and ulna sawbones. For this study, large left-sided 4th generation humerus and ulna bone models (Models 3404 and 3426, Sawbones, Pacific Research Laboratories Inc.™, Vashon, USA) were used (Figure 6-1). The humerus had a total length of 365 mm with a canal distal diameter of 4 mm, while the ulna measured 270 mm in length. Both the humerus and ulna sawbones were constructed from short

fibre-reinforced epoxy which mimicked the material properties of cortical bone with a density of 1.64 g/mL. The cancellous bone properties were simulated using solid rigid polyurethane foam with a density of 0.27 g/mL. Previous studies have shown that these artificial humerus models exhibit biomechanical properties comparable to human femurs, making them suitable for in vitro research (Aziz et al., 2014; Dunlap et al., 2008).

Figure 6-1: Large left-sided 4th generation humerus and ulna bone model dimensions.

Distal Humeral Preparation

The procedure for preparing the humerus utilised the exact Discovery instrumentation kit used in real-life procedures with the Discovery elbow implant system and adhered to the Discovery standard surgical procedure (Discovery Elbow System Surgical Technique, 2024). The total elbow arthroplasty procedures were performed with clinical support from experienced surgical staff,

ensuring the accurate application of surgical techniques essential to this study. The anatomical axis of rotation and medial trochlea of the humerus were aligned using the fossa guide and a drill bit. A malleable retractor was placed on the anterior surface, and a hole was drilled through the guide. After removing the drill bit and fossa guide, a reamer was used to ream the humerus, defining the posterior proximal border of the 'U' shaped resection. Saw cuts were then made along the marked lines. Finally, the 'U' shaped cut was reamed to ensure a smooth surface finish (Figure 6-2).

The humerus sawbone already had a pre-drilled canal that was 4mm in its diameter. The pre-drilled canal was enlarged to the required size using incremental rasps of varied sizes. The rasp was inserted into the canal and tapped gently with a mallet to advance until a snug and secure fit for the instrumented humeral implant was achieved (Figure 6-2).

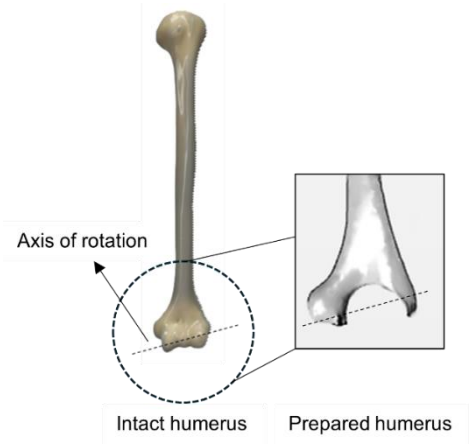

Figure 6-2: Intact and prepared humerus showing the axis of rotation.

Ulnar Preparation

To prepare the ulna, the tip of the olecranon along the posterior edge of the articulation was removed using an oscillating saw. The pre-drilled canal in the ulna sawbone was then refined with the smallest reamer, advancing until cortical contact was achieved. Ulnar rasps were subsequently used to further shape the

canal, aligning the rasp with the axis of rotation of the implant. Finally, a right sided ulnar component was trialled to confirm accurate placement and alignment (Figure 6-3).

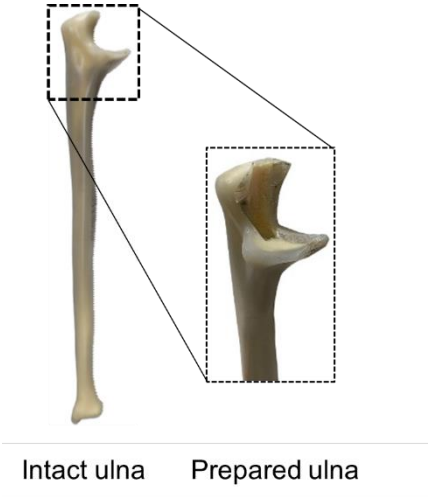

Figure 6-3: Intact and prepared ulna showing the drilled canal for the ulnar component.

Fixing of the Humeral and Ulna Components

Once the humeral and ulnar sawbones were prepared and a proper fit between the components and bones was achieved, the right-sided instrumented humeral component calibrated in chapter 5 was intentionally designed to be compatible with the standard Discovery condylar bearings and ulnar components. This calibrated humeral component was fixed into the humeral sawbone using polymethyl methacrylate (PMMA) bone cement. The bone cement was dispensed into the humerus up to the canal opening, and the humeral implant was carefully inserted, ensuring correct orientation. Once the component was fully seated in a satisfactory position, excess cement was thoroughly removed. Similarly, the ulnar implant was fixed by dispensing bone cement into the ulnar canal, then pressing the ulnar implant into place with attention to its orientation. The cement was allowed to cure and solidify for a few minutes as seen in Figure 6-4 below.

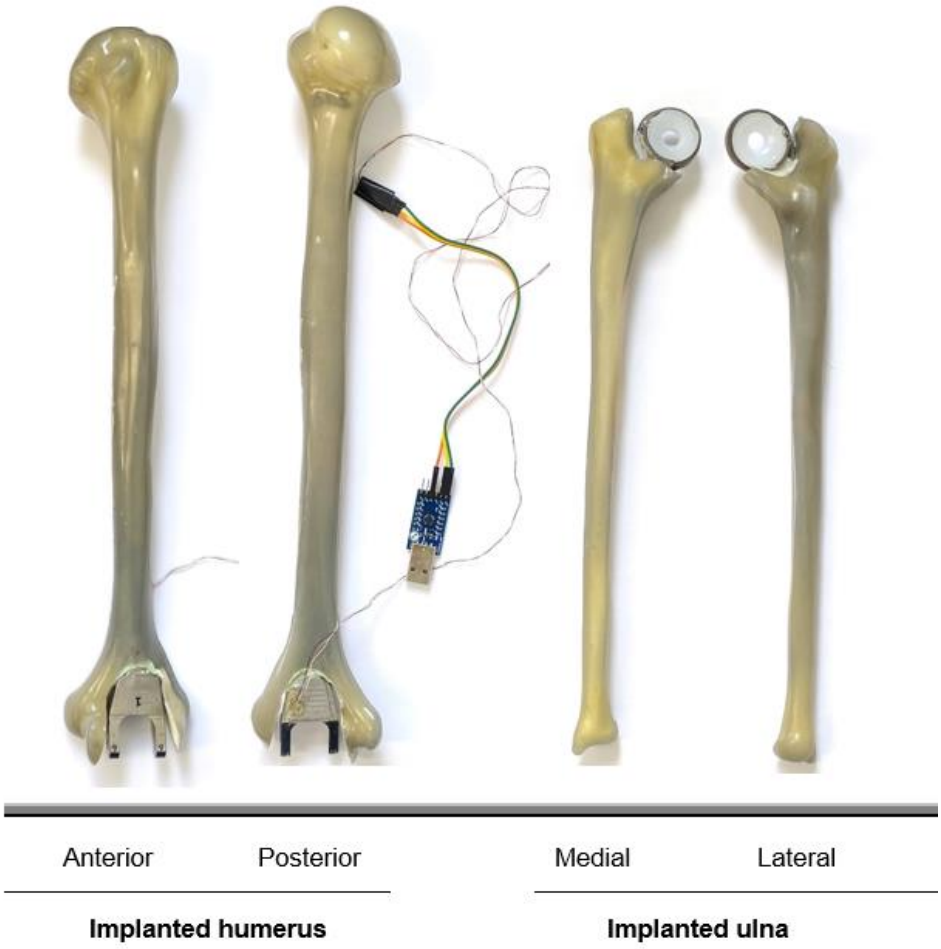

Figure 6-4: Anterior and posterior views of the implanted humerus (left) and medial and lateral views of the implanted ulna (right).

Model Assembly

After the cement had cured in both the humeral and ulnar sawbones, the components were joined as illustrated in Figure 6-5. The condyles were assembled onto the ulnar component, and the humeral component was then secured using the posterior locking screws.

Figure 6-5: Assembled elbow implant with the humeral and ulnar stems joined together via posterior locking screws.

6.2.2. Muscle Simulation

The experimental setup in this study was designed to approximate the in vivo biomechanical loading conditions on the elbow joint. To quantify the forces and moments acting on the joint during loading, it is essential to account for muscle forces, as they significantly influence joint stability and load distribution. The brachialis muscle which is the primary flexor of the elbow was attached to the assembled humerus and ulna sawbone model. Ideally, all muscle forces should be considered, however, the complexity of multiple muscle attachments and the issue of muscle redundancy in biomechanical modelling complicate the ability to accurately isolate and quantify the biomechanical contribution of each individual muscle to the distribution of forces across the joint. Therefore, only the brachialis was included in this setup to simplify the analysis and focus on its specific contribution.

In this biomechanical setup, a 0.3 mm diameter stainless-steel wire was used to simulate the forces exerted by the brachialis muscle on the elbow joint. This approach enabled consistent force application in a controlled environment when the muscle was tensioned. The attachment points in this setup mimicked its natural anatomical origin on the humerus and insertion on the ulna. And thus, the wire originated from the distal half of the anterior surface of the humerus, extending from the lower part of the shaft to just above the elbow joint, and was inserted into the tuberosity and coronoid process of the ulna. The wire was secured in position using stainless steel jubilee clips, which were wrapped around the diameter of the humerus and ulna shafts as shown in Figure 6-6. These clips provided a firm grip, ensuring that the wires remained securely in place during the application of controlled tension. The brachialis muscle acts to flex the elbow joint by pulling on the ulna, which makes it essential in elbow flexion, regardless of whether the forearm is pronated or supinated. Since the focus is on simulating the forces exerted by the brachialis muscle, which does not significantly affect the radius, the radius was excluded to simplify the experimental setup without significantly affecting the accuracy of the force measurements on the elbow joint.

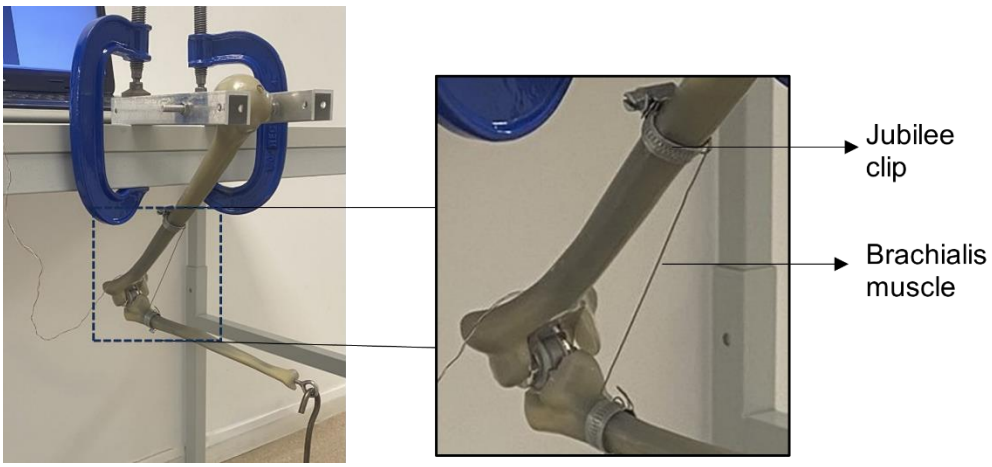

Figure 6-6: Biomechanical setup simulating brachialis muscle using a 0.3 mm stainless-steel wire secured with jubilee clips, mimicking its anatomical origin on the humerus and insertion on the ulna.

6.2.3. Experimental Setup

In this biomechanical setup, the arm was positioned in a dependent position to replicate the natural alignment of the forearm under the influence of gravity (Figure 6-7). This allowed for accurate simulation of the realistic loading conditions experienced during normal activities of daily living (ADL). To set up the swinging of the full arm in the sagittal plane with the elbow flexed, a 6 mm hole was drilled through the humeral head in the medial-lateral direction. A rod was then inserted through this hole, with the ends of the rod secured in brackets clamped to the edge of a table (Figure 6-7). This setup allowed the arm to hang freely and swing naturally. Dead weights were used to apply a hand-held load at the end of the ulna to simulate external loading. The elbow flexion angle was set by the brachialis muscle wire ass seen in Figure 6-7 below. The arm thus was free to swing with a humeral angle dependent on the external load.

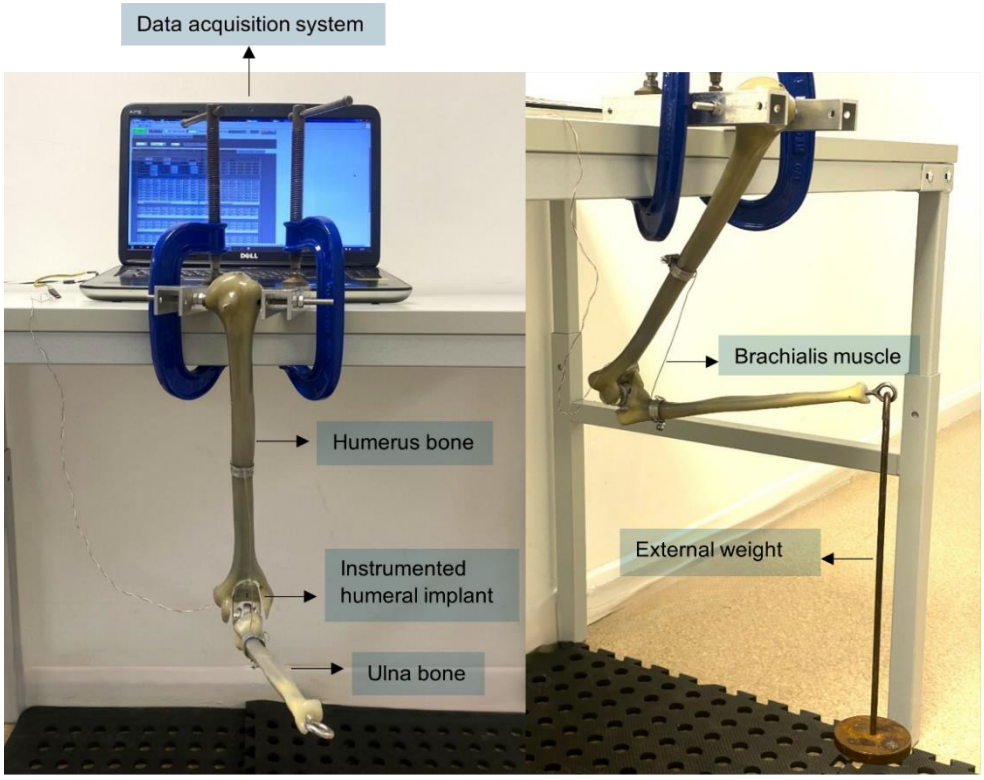

Figure 6-7: Biomechanical setup simulating arm loading during ADL, with the arm suspended by a rod through the humeral head, flexion set by the brachialis muscle, and external loads applied via dead weights.

6.2.4. Loading Scenarios

To fully simulate the six degrees of freedom at the elbow joint, three distinct loading scenarios were designed to replicate the full range of elbow joint movements: flexion-extension, varus-valgus, and pronation-supination (Figure 6-8). Each scenario focused on one of the primary axes of elbow motion to ensure a comprehensive evaluation of the response generated by the joint to the applied load.

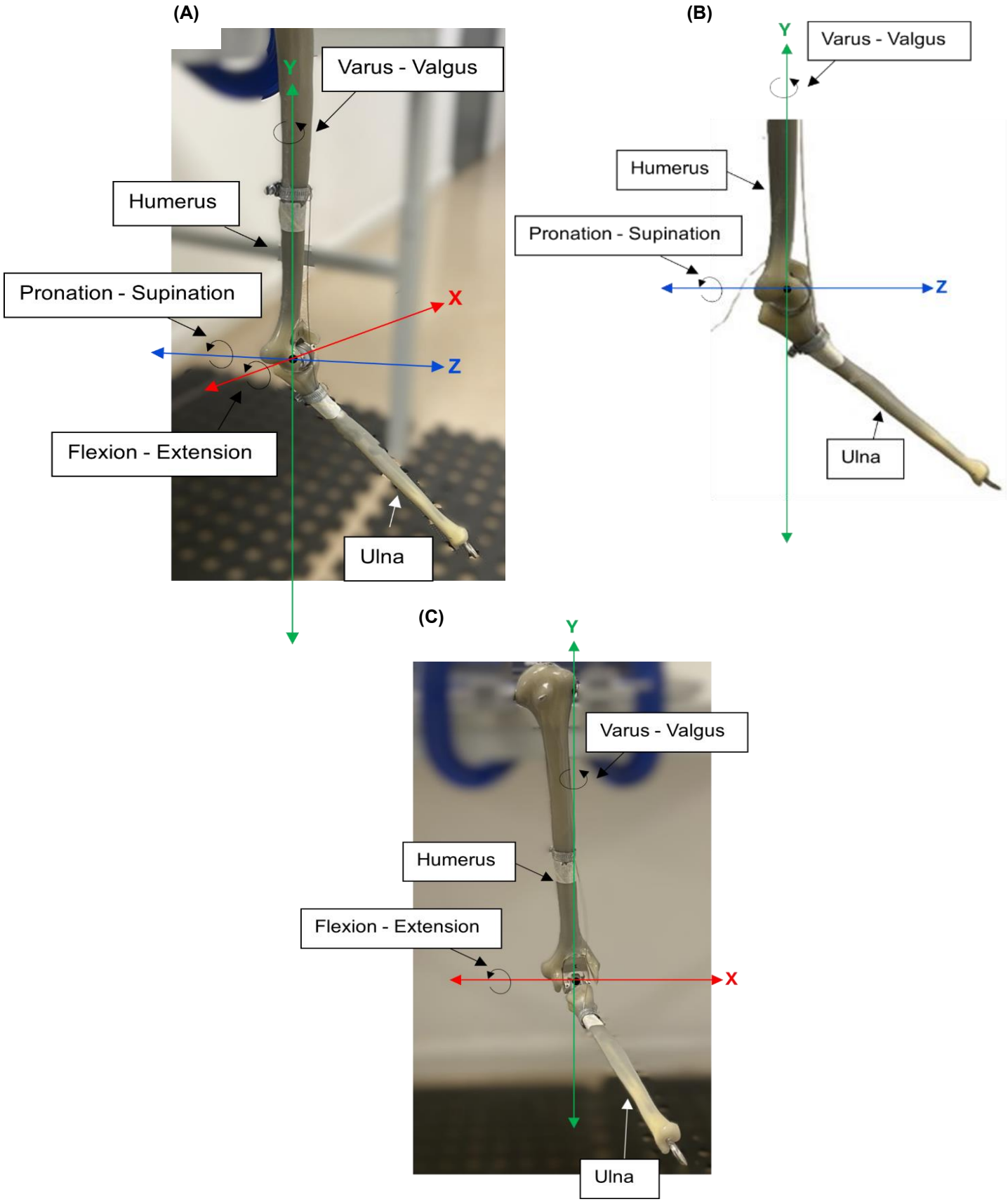

Figure 6-8: (A) Elbow motions and Coordinate System (XYZ) of setup with the forearm shown at 148° of elbow flexion, (B) Reference for Coordinate System in YZ only, and (C) Reference for Coordinate System in YX only with the forearm shown at 101° of elbow flexion .

6.2.4.1. Flexion - Extension

In this setup, the entire arm was suspended in the sagittal plane, with the brachialis muscle attached at flexion angles of 68°, 101°, and 148° as illustrated in Figure 6-9. At each angle, axial forces were sequentially applied using dead weights of 0.5 kg, 1.5 kg, 2.5 kg, 3.5 kg, 4.5 kg, and 5.5 kg. These weights generated moments about the x-axis, simulating the bending and straightening (flexion-extension) of the elbow joint.

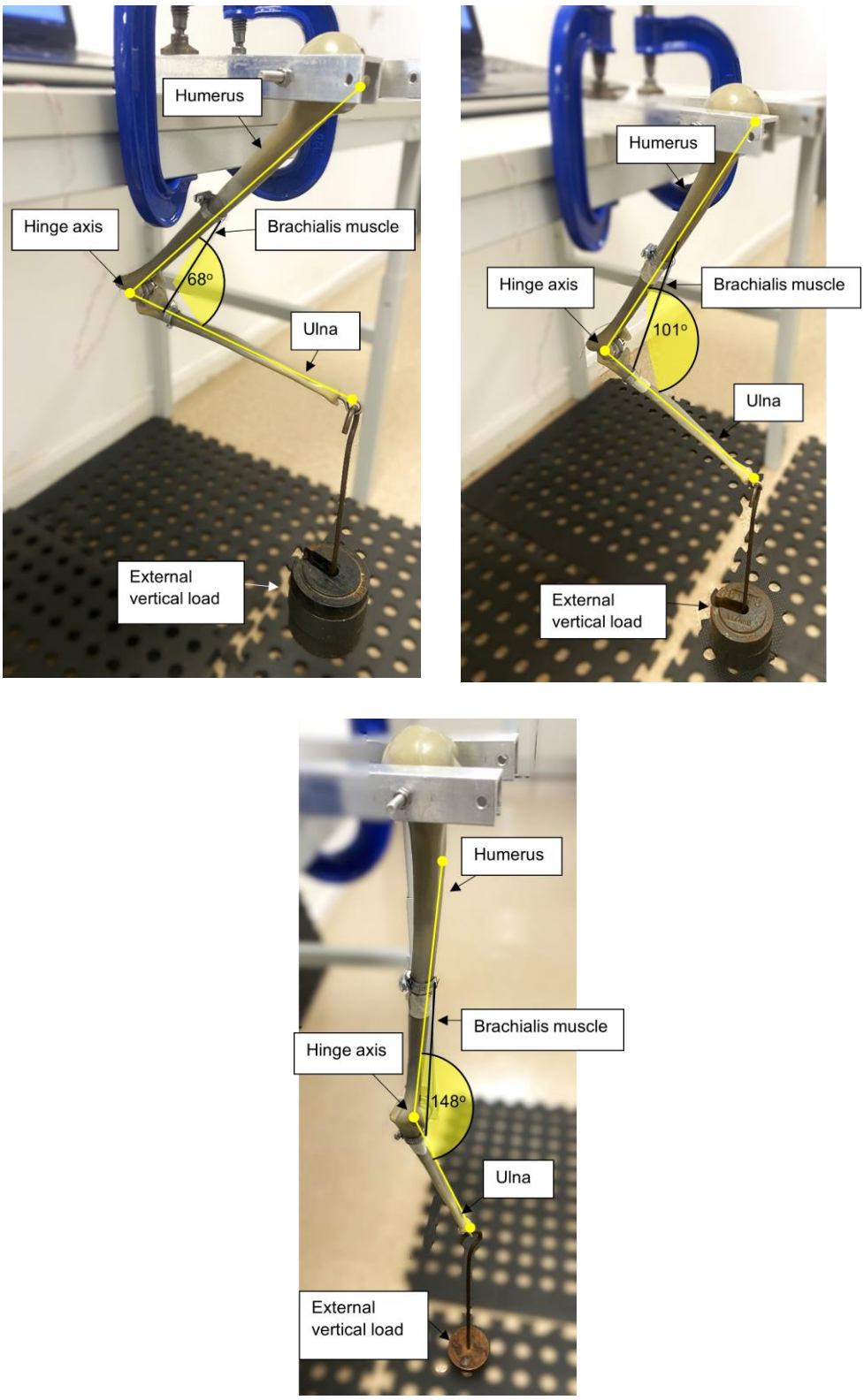

Figure 6-9: Experimental setup illustrating the arm suspended in the sagittal plane (YZ) with the brachialis muscle attached at flexion angles of 68°, 101°, and 148°. Axial forces were applied sequentially at each angle using dead weights (0.5 kg to 5.5 kg) to simulate elbow joint flexion-extension.

6.2.4.2. Varus - Valgus

The entire forearm was suspended with the elbow flexed at 68° in the YX plane. To simulate varus movement, a force was applied at an offset distance from the joint using a pulley system as seen in Figure 6-10. This setup creates rotary motion about the y-axis. A rig was used to attach the pulley system, with a rope secured to the end of the ulna sawbone and extended horizontally over the pulley in the varus direction. A dead weight of 0.5 kg was suspended at the end of the rope. Additionally, an axial force along the y-axis was applied to stabilise the setup. This axial force was provided by a jar filled with metal nuts, representing a total weight of 1 kg. The same setup was replicated for the valgus configuration, with the procedure adjusted to apply forces in the valgus direction.

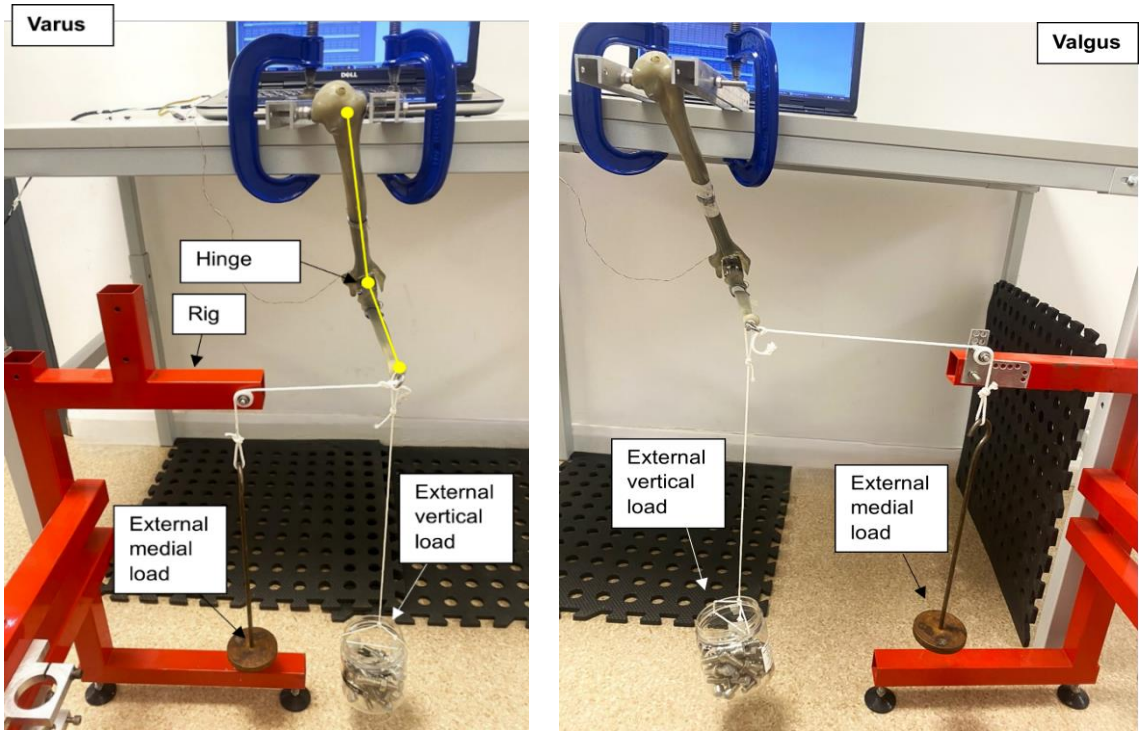

Figure 6-10: Experimental setup simulating varus-valgus motion of the arm with the brachialis muscle attached at 68° of elbow flexion. External medial force (0.5 kg) was applied in addition to an external vertical force (1 kg) to stabilise the setup.

6.2.4.3. Pronation - Supination

To simulate pronation movement of the arm, the arm was suspended with the elbow flexed at 68° as shown in Figure 6-11 below. Dead weights of 0.5 kg and 1.5 kg were positioned at a small offset from the end of the ulna sawbone to generate a moment around the z-axis of the elbow joint. This offset was achieved by inserting a small rod into the end of the ulna component, extruding medially only, from which the weights were suspended. The same setup was replicated for the supination configuration, with repositioning the rod in the supination direction.

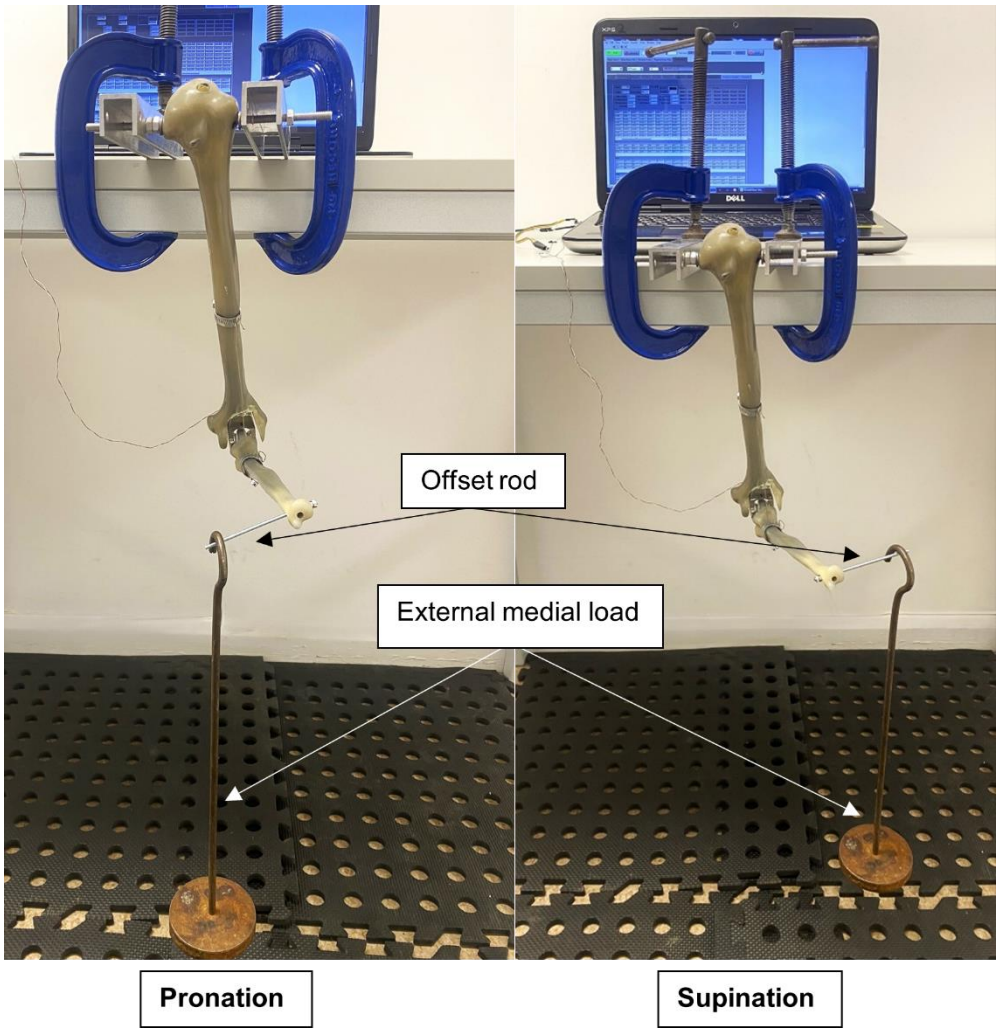

Figure 6-11: Experimental setup simulating pronation-supination motion of the arm with the brachialis muscle attached at 68° of elbow flexion. External medial force (0.5 kg) was applied at an offset distance from the hinge axis of the arm.

6.2.5. Data Collection and Analysis

The instrumented humeral component implanted into the humerus was connected to a computer via 3 wires that exited the implant through a small hole in the main cavity cover. The same custom-designed graphical user interface (GUI) was used as in the previous chapter. As dead weights were applied in each single loading scenario, the strain outputs were monitored in real time on the elbow GUI and recorded for each case for a duration of 10 seconds. The outputs were recorded initially in the unloaded state and then under the applied weights. The raw strain gauge data were exported to an Excel® spreadsheet for analysis. Each dataset included the applied weights for each scenario and the corresponding voltage (VSG) and resistance (RSG) outputs from the eight strain gauges. These values represent the unprocessed readings recorded by LabView during each individual loading case. To ensure accuracy, the data were filtered to remove potential signal errors and outliers.

After cleaning the data, a linear regression analysis was performed to determine the relationship between the measured resistance (in ohms) and the applied forces (in newtons). The LINEST function was used on excel to calculate the change in resistance per unit force (ohms/N). The ohms/N values represent the relationship between the applied forces and the change in resistance. Since strain is typically expressed in microstrain per newton (μstr/N), the ohms/N values were converted to μstr/N using the gauge factor of the strain gauge. This process was repeated for all datasets corresponding to the different loading scenarios in this biomechanical setup.

The resistance outputs from all eight strain gauges were converted to microstrain. These values were then multiplied by the inverse calibration matrix developed in the earlier calibration chapter. To convert the recorded strain signals back into

forces and moments, the inverse of the calibration matrix from chapter 5 shown later in Table 6-2 was applied, as shown in the equation below:

$$L = M \times S$$

Where M is the inverse matrix (C^{-1})

As a result, all the components of force (F_x, F_y, F_z) and moment (M_x, M_y, M_z) were determined. The LINEST function was then applied to the calculated forces and moments to determine the force magnification ratio (FMR). This magnification factor indicates how much the forces and moments measured in the biomechanical setup must be scaled to accurately represent the physiological forces experienced by the elbow joint under real in vivo conditions.

6.2.6. Theoretical Free-Body Diagram (FBD) Force Analysis

In order to validate the three forces and three moments measured in the biomechanical setup, a free-body diagram (FBD) model of the elbow setup was developed. The FBD allowed for the calculation of the theoretical forces and moments acting on the elbow joint based on the known external loads applied in each scenario, the geometries of the humerus and ulna sawbones, and the contribution of the brachialis muscle. A simplified Free-Body Diagram (FBD) of the arm setup was created, incorporating the humerus, ulna, and brachialis muscle. To calculate the three forces and three moments acting on the elbow joint, two orthogonal planes were used: the flexion-extension plane and the varus-valgus plane. Although, a complete 3D analysis using three orthogonal planes (sagittal, frontal, and transverse) would be ideal, this two-plane approach allowed for an approximation by capturing the most significant forces and moments that occur within those planes. This approach is supported by the absence of literature on joint reaction forces (JRFs) and contact stress in the elbow during active

pronation-supination (PS) loading. It has been proposed that because the muscle groups responsible for pronation and supination are relatively smaller and have shorter moment arms compared to those involved in other movements, such as flexion/extension, the JRFs and moments during PS motion are likely much lower than those encountered during flexion/extension and varus/valgus (Amis et al., 1979a; Amis et al., 1980; Chadwick & Nicol, 2000; Morrey et al., 2000).

The diagrams included external forces, such as the applied weights and the known lever arms, to replicate the loading conditions used in the experimental setup. Equilibrium equations derived from the FBD were then used to determine the unknown forces and moments at the elbow joint.

6.2.6.1. FBD Analysis in Flexion/Extension Plane (YZ Plane)

To ensure that the arm model is in static equilibrium, the sum of all forces in each of the three spatial directions must be zero, as well as the moments about each of the three axes (Figure 6-12). This balance guarantees that there is no net movement or rotation. Therefore, the following equilibrium equations were applied:

$\sum F_x = 0$, $\sum F_y = 0$, $\sum F_z = 0$, $\sum M_x = 0$, $\sum M_y = 0$, $\sum M_z = 0$

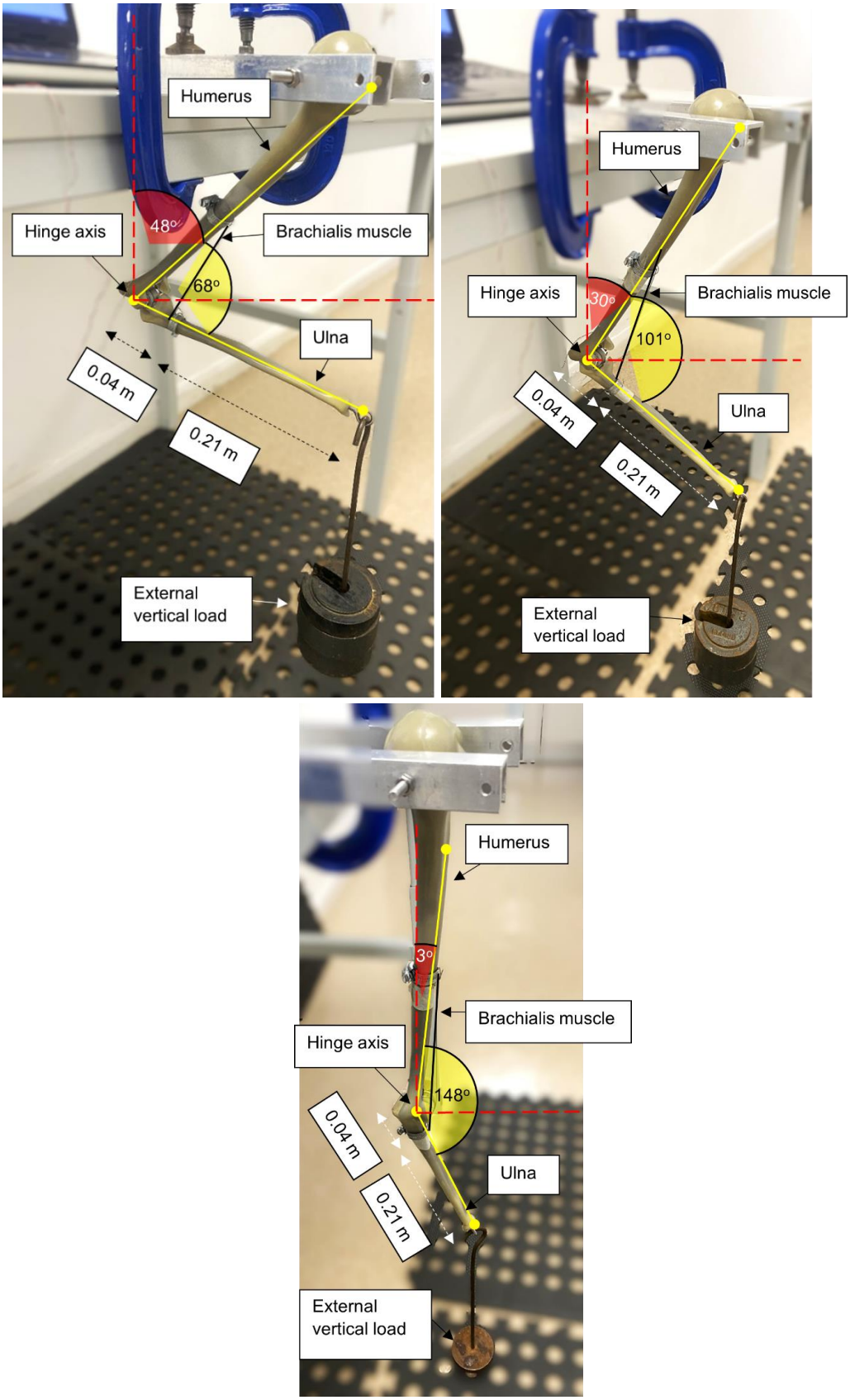

Figure 6-12: Free Body Diagram (FBD) force analysis in flexion-extension (YZ) plane at (A) 68° of elbow flexion, (B) 101° of elbow flexion, and (C) 148° of elbow flexion. The external force is applied in the vertical direction.

From the FBD in Figure 6-12 above, the following known forces and moment arms were set during the experimental setup for the case where the elbow was flexed at 68° and repeated for 101° and 148° of elbow flexion. The calculations for those cases are provided in Appendix A-3.

$\boldsymbol{\theta}$ = Elbow flexion angle = 68°

$\boldsymbol{\beta}$ = Brachialis angle relative to the horizontal plane = 80° anticlockwise

$\mathbf{F_E}$ = External weight force $= 4.5 \times 9.81 = 44.15$ N

$\mathbf{F_W}$ = Weight of the arm $= 0.15 \times 9.81 = 1.47$ N

$\mathbf{d_E}$ = Distance from external weight to hing axis $= 0.25 \times \cos(22°) = 0.23$ m

$\mathbf{d_B}$ = Distance from brachialis to hing axis $= 0.04 \times \cos(22°) = 0.04$ m

$\mathbf{d_W}$ = Distance from arm centre of mass (CoM)to hing axis $= 0.11 \times \cos(22°) = 0.10$ m

Using the equilibrium equations, the following values were determined for the case where the elbow was flexed at 68°, with clockwise directions considered positive and anticlockwise directions negative:

$$\sum M = (F_E . d_E) + (F_W . d_W) - (F_{B(y)} . d_B) = 0$$

$$\sum M = (44.15 \times 0.23) + (1.47 \times 0.10) - (F_{B(y)} .0.04) = 0$$

$F_{B(y)}$ = Brachialis force (vertical component) = 279.95 N

$F_{B\,(resultant)}$ = Resultant brachialis force

$$F_{B\,(resultant)} = \frac{F_{B(y)}}{\sin(\beta)} = \frac{279.95}{\sin(80°)} = 284.27 \text{ N}$$

$F_{B(z)}$ = Brachialis force (horizontal component)

$$F_{B(z)} = F_{B\,(resultant)} \times \cos(\beta) = 284.27 \times \cos(80°) = 49.36 \text{ N}$$

$F_{j(y)} = \text{Vertical joint reaction force}$

$$\sum F_y = F_E + F_W - F_{B(y)} + F_{j(y)} = 0$$

$$\sum F_y = 44.15 + 1.47 - 279.95 + F_{j(y)} = 0$$

$$F_{j(y)} = 234.34 \text{ N}$$

To account for the misalignment of the humerus relative to the vertical axis, a correction factor was applied, as the humerus may not always be perfectly vertical during the experimental setup. The cosine of the angle between the humerus axis and the vertical direction was used as the correction factor. This adjustment ensures that both the vertical force component (F_{jy}) and the external load F_E are aligned to act in the same direction.

$$F_{j(y)}(\text{corrected}) = F_{j(y)} \times \cos(48°) = 234.34 \times \cos(48°) = 156.80 \text{ N}$$

$F_{j(z)} = \text{Horizontal joint reaction force}$

$$\sum F_z = F_{j(z)} - F_{B(z)} = 0$$

$$F_{j(z)} = F_{B(z)} = 49.36 \text{ N}$$

$F_j = \text{Resultant joint reaction force}$

$$F_j = \sqrt{F_{j(y)(\text{corrected})}^2 + F_{j(z)}^2} = \sqrt{(156.80)^2 + (49.36)^2} = 164.39 \text{ N}$$

The Force Magnification Ratio (FMR) was calculated as the ratio of the joint reaction force to the external weight applied. This was then compared to the FMR derived from the biomechanical setup based on strain data. The FMR was determined using the following equation:

$$\text{FMR} = \frac{\text{vertical joint reaction force}}{\text{external load}} = \frac{F_{j(y)}(\text{corrected})}{F_E} = \frac{156.80}{44.15} = 3.6$$

The same calculation steps were repeated for the other loading scenarios with the elbow flexed at 101° and 148°.

6.2.6.2. FBD Analysis in Varus/Valgus Plane (XY)

The equilibrium equations were reapplied to determine the forces and moments acting within the varus-valgus plane with the elbow flexed at 68° to analyse the mechanical behaviour under these conditions (Figure 6-13).

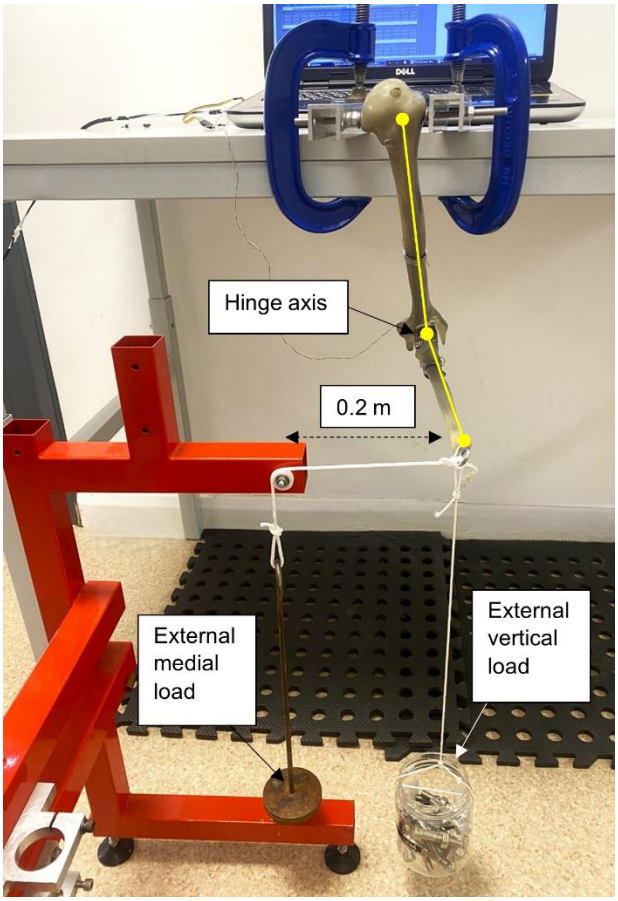

Figure 6-13: Free Body Diagram (FBD) force analysis in the varus-valgus (YX) plane at 68° of elbow flexion and an external force applied in the medial direction.

From the FBD in Figure 6-13 above, the following known forces and moment arms were set during the experimental setup for the case where the elbow was flexed at 68°:

θ = Elbow flexion angle = 68°

β = Brachialis angle relative to the horizontal plane = 122° anticlockwise

$F_{E(Y)}$ = External vertical weight = 44.15 N

F_M = External medial weight = $4.5 \times 9.81 = 44.15$ N

F_W = Weight of the arm = $0.15 \times 9.81 = 1.47$ N

$d_{E(Y)}$ = Distance from external vertical weight to hing axis = $0.25 \times \cos(22°) =$ 0.23 m

d_M = Distance from external medial weight to hing axis = 0.2 m

d_B = Distance from brachialis to hing axis = $0.04 \times \cos(22°) = 0.04$ m

d_W = Distance from arm centre of mass (CoM)to hing axis

$= 0.11 \times \cos(22°) = 0.10$ m

Using the equilibrium equations the following were determined:

$$\sum M = (F_{E(Y)} . d_{E(Y)}) + (F_W . d_W) - (F_{B(y)} . d_B) = 0$$

$$\sum M = (44.15 \times 0.23) + (1.47 \times 0.10) - (F_{B(y)} \times 0.04) = 0$$

$F_{B(y)}$ = Brachialis force (vertical component) = 279.95 N

$F_{B\,(resultant)}$ = Resultant brachialis force

$$F_{B\,(resultant)} = \frac{F_{B(y)}}{\sin(\beta)} = \frac{279.95}{\sin(122°)} = 330.11 \text{ N}$$

$F_{B(x)}$ = Brachialis force (horizontal component)

$F_{B(x)} = F_{B\,(resultant)} \times \cos(\beta) = 330.11 \times \cos(122°) = -174.93$ N

$F_{j(y)} = \text{Vertical joint reaction force}$

$$\sum F_y = F_{E(Y)} + F_W - F_{B(y)} + F_{j(y)} = 0$$

$$\sum F_y = 44.15 + 1.47 - 279.95 + F_{j(y)} = 0$$

$$F_{j(y)} = 234.34 \text{ N}$$

After applying the correction factor to $F_{j(y)}$, it becomes:

$$F_{j(y)}(\text{corrected}) = F_{j(y)} \times \cos(48°) = 234.34 \times \cos(48°) = 156.80 \text{ N}$$

$F_{j(x)} = \text{Horizontal joint reaction force}$

$$\sum F_x = F_{B(x)} + F_M - F_{j(x)} = 0$$

$$F_{j(x)} = -174.93 + 44.15 = -130.79 \text{ N}$$

$F_j = \text{Resultant joint reaction force}$

$$F_j = \sqrt{F_{j(y)(\text{corrected})}^2 + F_{j(x)}^2} = \sqrt{(156.80)^2 + (-130.79)^2} = 204.19 \text{ N}$$

The Force Magnification Ratio (FMR) was also calculated and compared to that obtained from the strain data.

6.2.6.3. Overall Elbow Joint Reaction Force (JRF)

To calculate the overall biomechanical joint reaction force (JRF) acting on the elbow, the forces along each of the two planes were combined vectorially using the below equation.

$$\text{JRF} = \sqrt{F_x^2 + F_y^2 + F_z^2} = \sqrt{(-130.79)^2 + (313.60)^2 + (49.36)^2} = 343.35 \text{ N}$$

6.3. Results

The primary objectives of this study were to perform total elbow arthroplasty (TEA) on a synthetic bone model and thus validate a simple free body model of the setup to demonstrate the functionality and performance of the instrumented humeral implant prototype. An in vitro biomechanical study was conducted to validate the six degrees of freedom measured by the calibrated instrumented prototype implant using strain gauge data under simulated physiological loading conditions. Additionally, the three forces and three moments acting on the elbow joint during typical activities of daily living (ADL) were measured and compared with modelled forces and moments from mathematical models to assess their accuracy and validity.

6.3.1. Forces in Flexion/Extension Plane (YZ)

Table 6-1 below presents a sample of the raw strain gauge output data recorded during elbow flexion at 68°. This includes voltage outputs (VSG values) and corresponding resistance measurements (RSG values) from each strain gauge. These values were captured by LabView and reflect the strain gauge responses to different external loads applied to the humeral component. The raw data was filtered to eliminate any errors or anomalies that could impact the results.

Table 6-1: Sample of raw strain gauge output data recorded during elbow flexion of 68°, including voltage outputs (VSG values) and corresponding resistance measurements (RSG values) for each strain gauge.

Load [N]	Load [kg]	MFrame	VSG1	VSG2	VSG3	VSG4	VSG5	VSG6	VSG7	VSG8	RSG1	RSG2	RSG3	RSG4	RSG5	RSG6	RSG7	RSG8
0	0	185	-5239	-4208	-3349	-2785	-2088	-1312	-512	-797	348.4816	348.5532	348.6758	348.6205	348.5877	348.5777	349.029	348.579
0	0	185	-5240	-4212	-3350	-2782	-2094	-1319	-517	-800	348.4827	348.5517	348.674	348.6241	348.5879	348.5767	349.028	348.5775
0	0	185	-5241	-4210	-3349	-2787	-2092	-1317	-517	-798	348.4812	348.5519	348.6763	348.6209	348.5877	348.5773	349.0269	348.5781
0	0	185	-5244	-4214	-3348	-2784	-2087	-1314	-515	-797	348.481	348.5492	348.6748	348.6195	348.5879	348.5771	349.0267	348.5779
0	0	185	-5243	-4213	-3349	-2781	-2089	-1317	-516	-797	348.4812	348.5502	348.6734	348.6218	348.5885	348.5765	349.0265	348.5781
0	0	185	-5239	-4210	-3345	-2782	-2090	-1314	-516	-797	348.4825	348.5507	348.6763	348.6226	348.5877	348.5785	349.0273	348.579
0	0	185	-5243	-4207	-3346	-2782	-2088	-1317	-512	-803	348.4787	348.5515	348.675	348.6209	348.5889	348.5748	349.0306	348.5756
0	0	185	-5240	-4215	-3351	-2780	-2086	-1312	-519	-802	348.4839	348.5509	348.6727	348.6216	348.5883	348.5804	349.028	348.5767
0	0	185	-5239	-4219	-3345	-2784	-2088	-1318	-514	-793	348.4862	348.5469	348.6771	348.6209	348.5902	348.576	349.0265	348.5806
0	0	185	-5246	-4216	-3346	-2783	-2093	-1317	-515	-796	348.4806	348.5471	348.6748	348.622	348.5862	348.5754	349.0259	348.5779
4.905	0.5	31	-5230	-4215	-3366	-2778	-2081	-1305	-503	-797	348.4901	348.5592	348.6677	348.6224	348.5895	348.5787	349.0346	348.5808
4.905	0.5	31	-5240	-4219	-3362	-2776	-2082	-1309	-502	-795	348.4856	348.5538	348.6665	348.6216	348.5887	348.5746	349.0321	348.5796
4.905	0.5	31	-5233	-4221	-3356	-2776	-2077	-1307	-502	-797	348.4908	348.5519	348.6704	348.6209	348.5914	348.5768	349.0344	348.5802
4.905	0.5	31	-5239	-4218	-3361	-2783	-2079	-1303	-502	-795	348.4858	348.554	348.67	348.6176	348.5877	348.5773	349.0323	348.5798
4.905	0.5	31	-5236	-4215	-3361	-2774	-2078	-1310	-501	-796	348.4864	348.5559	348.6669	348.6216	348.5916	348.5746	349.0338	348.58
4.905	0.5	31	-5235	-4223	-3363	-2778	-2081	-1307	-503	-794	348.4904	348.5536	348.6679	348.6214	348.5893	348.5768	349.0323	348.581
4.905	0.5	31	-5236	-4221	-3363	-2784	-2079	-1310	-503	-798	348.4889	348.5542	348.6702	348.6178	348.5912	348.5754	349.0338	348.5791
4.905	0.5	31	-5235	-4219	-3367	-2781	-2080	-1310	-501	-796	348.4887	348.5569	348.6675	348.6197	348.591	348.5748	349.034	348.5802
4.905	0.5	31	-5232	-4219	-3358	-2780	-2083	-1308	-501	-797	348.4905	348.5538	348.6715	348.622	348.5895	348.5762	349.035	348.5804
4.905	0.5	31	-5236	-4214	-3363	-2787	-2081	-1308	-493	-798	348.486	348.5571	348.6715	348.6174	348.5895	348.5721	349.0379	348.5791

Linear regression analysis was conducted to determine the relationship between the measured resistance (in ohms) and the applied dead weights (in newtons) in each loading scenario. The analysis yielded the rate of change in resistance per unit force in Ohms/N which was subsequently converted to μstr/N. The resistance outputs from all eight strain gauges were converted to microstrain. These microstrain values were then multiplied by the inverse calibration matrix (Table 6-2) to determine the corresponding components of force (F_x, F_y, F_z) and moment (M_x, M_y, M_z).

Table 6-2: The inverse calibration matrix derived in chapter 5 compiling the regression coefficients for (Fx, Fy, Fz, Mx, My, Mz).

Multiple R	0.81	0.93	0.96	0.66	0.74	0.96	0.63	0.97	
Fx	-1.46E+00	9.15E-01	-1.72E+00	6.49E-01	1.26E+00	-3.30E+00	7.98E-01	-2.53E+00	N/μstr
Fy	-1.63E+00	-5.16E+00	-2.22E+00	-4.66E+00	3.02E-01	6.27E-01	4.01E-01	-8.29E-01	N/μstr
Fz	-5.40E+00	-1.10E+00	-3.10E+00	2.23E+00	9.60E+00	-7.81E+00	-3.06E+00	-4.04E+00	N/μstr
Mx	-2.38E+02	7.79E+01	-1.69E+02	3.03E+02	5.02E+02	-5.66E+02	-2.05E+02	-3.43E+02	Nmm/μstr
Mz	1.96E+02	-2.59E+02	2.10E+02	-2.77E+02	-5.71E+02	1.92E+02	2.80E+01	1.59E+02	Nmm/μstr
My	-2.55E-05	-4.93E-05	1.49E-05	-5.14E-05	-2.94E-05	-1.62E-05	1.67E-06	-1.08E-05	Nmm/μstr

During elbow flexion at 68°, 101°and 148°, the results indicate that overall, the predominant force component was F_y, directed along the y-axis. Significant moments (M_z) were also observed around the z- axis with the highest magnitude compared to other components. It is evident that other force and moment components were also present but were less pronounced. A sample of the calculated force and moment components is presented below in Table 6-3.

Table 6-3: This table presents a sample of the three forces (N) and three moments (N.mm) calculated based on the strain measurements during elbow flexion of 68°.

Force (N)			**Moment (N.mm)**		
Fx	Fy	Fz	Mx	Mz	My
-1.339	37.072	4.7195	-782.545	1953.279	525.348
-4.587	-30.354	-14.103	-914.886	-507.640	-444.537
-13.380	-50.631	13.733	-3376.311	3179.372	261.119
-21.715	-49.078	-24.797	-2576.525	795.346	-321.977
-2.943	9.241	0.882	86.008	-568.867	-12.155
28.059	-48.930	-17.509	508.545	-5536.599	-1039.982
-0.040	-103.032	-71.792	-4158.785	-3074.286	-1367.218
-18.642	23.305	-8.085	602.006	-3236.137	-675.593
-4.261	-63.632	-21.328	-3264.601	-1108.157	-767.086
-2.967	-81.002	-4.439	-4827.608	806.398	-369.352

Table 6-4 below summarises the forces calculated from the free body diagram (FBD), including the resultant brachialis muscle force (F_B), the vertical joint reaction force ($F_{j(y)}$), and the horizontal joint reaction force ($F_{j(z)}$) at each flexion angle (Table 6-4).

Table 6-4: Summary of the resultant brachialis muscle force (F_B), the vertical joint reaction force ($F_{j(y)}$), and the horizontal joint reaction force ($F_{j(z)}$) during flexion-extension simulation of the arm at 68°, 101°and 148° of elbow flexion.

Flexion Angle (°)	**Resultant Brachialis Muscle Force** (F_B)**, (N)**	**Vertical Joint Reaction Force** ($F_{j(y)}$)**, (N)**	**Horizontal Joint Reaction Force** ($F_{j(z)}$)**, (N)**
68	284.3	156.8	49.4
101	301.9	202.9	-113.1
148	280.1	234.0	9.8

The measured and calculated Force Magnification Ratio (FMR) under different flexion angles are summarised in the Table 6-5 below. At 68° Flexion, the measured FMR was 14.1, while the calculated FMR from the FBD analysis was 3.6, showing a large difference between the two values. However, at 101° flexion, the measured and calculated FMR values were 6.6 and 4.6, respectively. The difference between these values is smaller compared to 68° flexion. Finally, at 148° flexion, the measured and calculated FMR were 5.3 and 2.7, respectively. There is still a noticeable difference between the two measurements, although both values are lower overall. In general, as flexion angle increases from 68° to 148°, both measured and calculated FMR values decrease.

Table 6-5: Table presents the measured and calculated Force Magnification Ratio (FMR) during elbow flexion at angles 68°, 101°and 148°.

Flexion Angle (°)	Measured FMR	Calculated FMR
68	14.1	3.6
101	6.6	4.6
148	5.3	2.7

6.3.2. Forces in Varus/Valgus Plane (XY)

The same data processing steps were followed to experimentally calculate the forces and moments in the varus plane. Table 6-6 below presents the forces calculated from the free body diagram (FBD), including the brachialis muscle force ($\mathrm{F_B}$), the vertical joint reaction forces ($\mathrm{F_{j(y)}}$), and the horizontal joint reaction force ($F_{j(x)}$) for elbow flexion angle of 68° (Table 6-6).

Table 6-6: Summary of the resultant brachialis muscle force ($\mathrm{F_B}$), the vertical joint reaction force ($\mathrm{F_{j(y)}}$), and the horizontal joint reaction force ($\mathrm{F_{j(z)}}$) during varus-valgus simulation of the arm at 68°of elbow flexion.

Flexion Angle (°)	Resultant Brachialis Muscle Force (F_B), (N)	Vertical Joint Reaction Force ($F_{j(y)}$), (N)	Horizontal Joint Reaction Force ($F_{j(x)}$),(N)
68	330.1	156.8	-130.8

The measured Force Magnification Ratio (FMR) in this plane was 49.0, while the FMR calculated from the FBD was 3.6, representing a significant difference between the two values.

6.3.3. Overall Joint Reaction Force (JRF)

Similar force components from both the flexion-extension and varus-valgus planes were combined first and used to calculate the overall joint reaction force (JRF) on the elbow, resulting in a value of 343.35 N. This JRF corresponds to an external load of approximately 4.5 kg held at 68° of elbow flexion and representative of moderate activities such as opening a door or lifting a small bag or a gallon of milk (Kincaid & An, 2013).

Kincaid and An (2013) developed an equation to estimate the Joint Reaction Force Multiplier (JRFM) per unit Weight in Hand (WIH) as a function of the elbow flexion angle (α) in degrees, which can then be used to calculate the Joint Reaction Force (JRF). Following their approach, the JRFM was calculated in our study using this established equation (Kincaid & An, 2013):

$$JRFM=15.13+(1.32\times10^{-1})\,\alpha-(8.52\times10^{-3})\,\alpha^2+(9.46\times10^{-5})\,\alpha^3-(3.21\times10^{-7})\,\alpha^4$$

By substituting α as 68° and by multiplying the resulting JRFM by the Weight in Hand (WIH) of 4.5 kg, the Joint Reaction Force (JRF) on the elbow was estimated to be 335.06 N. This estimated JRF reasonably aligns with the JRF of 343.35 N calculated through the Free Body Diagram (FBD) model.

6.4. Discussion

In this study, the newly modified instrumented humeral prototype was implanted into a humeral sawbone to test its capability in measuring the forces and moments acting at the hinge of a semi-constrained elbow joint. The accuracy of the six degrees of freedom measured by the calibrated instrumented humeral implant was validated through an in vitro biomechanical study where the six

degrees of freedom around the joint were measured based on strain gauge data during typical activities of daily living (ADL).

In the flexion-extension loading scenarios, a vertical external weight was applied along the y-axis, leading to F_Y being the largest force component across all loading conditions regardless of the flexion angle. This outcome is expected, as during elbow flexion, the arm moves primarily within the sagittal plane, and the load applied aligned with the y-axis. As a result, the elbow joint predominantly experiences forces along this axis, making F_Y the dominant force component. Although, it was expected that only forces and moments aligned with this direction (F_Y) would be observed, the results revealed unexpected force and moment components in other directions. For example, there were noticeable degree of lateral and rotational responses (F_X) and (F_Z), respectively. This can be attributed to the cross-sensitivity nature of the strain gauges embedded within the humeral component, where often a force applied in one direction can inadvertently induce responses in other directions. Another possibility is that, in real-life scenarios, the loading conditions might not be perfectly simple or isolated. For instance, the application of a downward force can interact with other forces or moments present in the biomechanical system, resulting in the detection of additional components.

Among the experimentally calculated moments, M_Z stood out as the most significant with the highest moment magnitude. This observation is likely linked to the use of a right instrumented humeral component implanted into a left humeral sawbone. The design of the right humeral component is tailored for a particular anatomical orientation specific to the right arm. When implanted into a left-sided humerus, the natural alignment is disrupted and in turn can introduce unintended mechanical effects such as additional rotational effects. Those

moments around the z-axis (M_Z) reflect pronation - supination motion of the elbow joint. This misalignment complicated the way the humeral component interacted with the sawbone under load. In real-life biomechanical conditions, deviations in anatomical alignment can create off-axis forces and moments that cause the joint to experience additional forces that are not typically expected with a correctly aligned implant, leading to unexpected components detected in the strain data.

Although this misalignment might initially be perceived as a limitation, it highlights the robustness of the implant in detecting a wide range of mechanical responses. This demonstrates that the instrumented humeral component is capable of measuring the forces and moments acting on the joint, even under non-ideal conditions, further validating its performance.

It was important to calculate the vertical force magnification ratio (FMR) from the biomechanical setup based on the strain data and compare it to the theoretical FMR in each scenario. This is because the forces applied in the biomechanical experiment such as the dead weights do not perfectly replicate the complex real-world forces acting on the joint.

In the flexion-extension plane with the elbow flexed at 68°, the calculated FMR was 3.6. This means that those measured forces and moments need to be adjusted by a factor of 3.6 to match the actual forces and moments experienced by the elbow joint in a real-life situation. However, the measured FMR during the experiment was found to be significantly higher, at 14.1. Significant differences between the measured and calculated FMR values were also observed at flexion angles of 101° and 148°, with the closest alignment between FMR values occurring at 90°. This can be explained by the underlying elbow biomechanics itself. The elbow is a complex joint, not a simple hinge, and its motion involves

rotational and translational components as it moves through flexion (Morrey et al., 1998; An et al., 1983). As the angle of flexion changes, so do the moment arms of the muscles acting across the joint, particularly the brachialis and biceps, which alters how effectively they generate joint forces (An et al., 1981). Around mid-range flexion angles like 101°, these muscles often operate with greater mechanical advantage. This could lead to an increase in joint reaction forces relative to the applied load and therefore a higher FMR. At more extended or more flexed positions (e.g., 68° or 148°), the changes in muscle leverage and joint contact mechanics may reduce this amplification effect. Additionally, slight variations in the positioning of the implanted component, especially since it does not perfectly replicate the natural joint axis, may introduce off-axis forces and moments that further influence the measured FMR. Taken together, these biomechanical factors provide a more comprehensive explanation for the variation in FMR values.

This difference may also be partly attributed to the complexity of the calibration setup. The mechanical configuration during the calibration stage of the instrumented implant was complicated, as calibrating such a humeral component with irregular geometry in six degrees of freedom poses significant challenges. In the future, developing a purpose-built calibration rig that can apply forces and moments directly to each axis of the humeral component would improve accuracy. Such a rig would enable precise control over force application, ensuring that each degree of freedom is accurately calibrated to reflect the real-life conditions the implant would experience.

Several other factors may have contributed to the discrepancy in the measured FMR. One possibility is the use of basic formulae to calculate the sensitivity matrix, which was based on the applied forces, offset distances, and angles.

While these formulae are useful, they may not account for all the complexities of the system. Additionally, for optimal strain gauge placement, the gauges should be positioned as far as possible from the load application points to minimise the impact of end effects, which could pick up localised forces that don't reflect the overall strain experienced by the component. Another factor that likely influenced the results is the imperfect bonding between the humeral and ulna stems inside the sawbones. Any misalignment or imperfect bonding would disrupt the transfer of forces, leading to inaccurate force measurements and affecting the overall joint reaction force calculations. These issues highlight the need for improved calibration setup to replicate real-world conditions more accurately.

The overall JRF on the elbow was calculated and modelled from the FBD to be 382.2 N which corresponds to an external load of approximately 4.5 kg held at 68° of elbow flexion. The JRF was also calculated through an equation established in the literature to be 335.12 N. The two values reasonably align. However, the observed differences in JRF estimates may stem from several factors. One of which is that the equation from Kincaid and An (2013) is based on generalised conditions and assumptions that may not perfectly reflect the specific setup and loading conditions in this study. Simplifications in our FBD model also may not fully represent real-world biomechanics.

Although the brachialis muscle force stayed fairly consistent across the three tested flexion angles, ranging from 280.1 N to 301.9 N, the joint reaction forces (JRFs) showed significant variation. This is likely due to how the elbow flexion angle affects the muscle's line of action and its moment arm. Even small changes in muscle force can have a much bigger impact on the joint because of shifts in mechanical advantage and joint geometry. For example, at 101° elbow flexion, the horizontal joint reaction force actually changed direction despite a slight

increase in brachialis force. This suggests that joint loading depends not just on how much force the muscle produces, but also on the position of the limb. This underscores the importance of accounting for joint biomechanics when interpreting JRF data across flexion-extension movements.

This study faced several limitations. The instrumented humeral component was implanted into artificial humeral and ulna sawbones, constructed from short fibre-reinforced epoxy resin which mimics cortical bone and rigid polyurethane foam simulating cancellous bone. Although these materials are considered advanced alternatives to cadaveric bones, they may not entirely capture the complex properties of natural bone.

The experimental biomechanical model only simulated the brachialis muscle. Although, this allowed for isolated analysis of the specific force contributed by the brachialis muscle, the absence of other muscles (such as the biceps brachii, triceps, or brachioradialis) limits the ability to fully replicate physiological loading conditions. The brachialis muscle was also represented by a stainless-steel wire attached to the humerus and ulna sawbones at its anatomical insertion points. This approach was chosen to approximate the muscle's natural line of action and force direction during elbow flexion as closely as possible within the practical limits of the experimental model. However, modelling the brachialis as a single wire does have some important limitations. The brachialis is a complex, three-dimensional muscle with a broad origin and insertion, but the wire simplifies this to a single line of force, overlooking the muscle's shape, volume, and the way it wraps around bones and tissues. These are factors that affect force direction and magnitude. Additionally, this model does not capture changes in muscle tension during dynamic movement, nor does it consider the role of other muscles that work together with the brachialis. For these reasons, while the wire model offers

a useful approximation, it does not fully represent the true biomechanical behaviour of the brachialis in vivo.

The calibration matrix was developed based on a single flexion angle (10°). This may have resulted in varying sensitivities at different flexion angles. In the current biomechanical setup, larger flexion angles were tested, potentially introducing discrepancies in force and moment measurements. To improve accuracy, future experiments should either test at lower flexion angles consistent with the calibration or recalibrate the system to better match the larger flexion angles used in the setup. Another important aspect of this study is the use of a right instrumented humeral component implanted into a left humerus sawbone. While this introduces a potential limitation due to anatomical misalignment, it also presents a unique advantage in demonstrating the robustness and versatility of the implant. In the future, it would be ideal to implant this instrumented humeral component into a right-sided biomechanical model or to develop a left-sided instrumented humeral component.

Due to the significant costs associated with developing a fully instrumented implant and the time required for its calibration, this validation study utilised only a single instrumented humeral component (N = 1) prototype. As a result, all measurements and findings were based on this single specimen, which may not fully capture the variability and performance of the implant across different samples. To gain a more accurate understanding of the performance of the instrumented humeral, it would be ideal to test multiple specimens to validate the reliability and consistency in different conditions.

6.5. Conclusion

This chapter focused on assessing and validating the performance of the instrumented humeral elbow prototype implant in measuring the six forces and moments acting on the elbow joint under physiological conditions. This evaluation involved performing a total elbow arthroplasty (TEA) on synthetic humeral and ulnar bone models and conducting an in vitro biomechanical study to verify the six degrees of freedom captured by the calibrated instrumented humeral implant. The joint reaction forces measured using the biomechanical setup developed in this study showed significant differences compared to those predicted by theoretical Free Body Diagram (FBD) modelling. This variation can largely be attributed to the complex biomechanics of the elbow, including changes in muscle moment arms with flexion angle. Additionally, slight misalignments of the prototype implant may introduce off-axis forces, further affecting joint loading measurements. Nevertheless, the instrumented humeral implant was functional and measured the forces and moments it experienced under various loading conditions.

The experimental setup was deliberately designed to deviate from ideal anatomical alignment to evaluate the performance of the prototype implant under non-ideal and variable loading conditions. This approach demonstrated that the implant can still provide reliable strain measurements despite minor misalignments. While these initial results are promising and highlight the potential of the prototype, further design iterations and reproducibility studies will be necessary to improve accuracy and support future clinical translation.

The next chapter summarises the key contributions of this thesis, discusses the implications of the research findings, and reflects on the study's limitations. It

concludes by outlining future directions for advancing the development of the instrumented humeral implant, with a focus on refining the prototype through further design iterations, improving reproducibility, and addressing the challenges identified throughout this work to support its eventual application in biomechanical and clinical research.

Chapter 7: Discussion and Conclusion

7.1. Summary of Key Findings

This chapter outlines the research problem and highlights key findings from the chapters of this thesis and concludes with a review of the overall study limitations and future directions.

Total elbow arthroplasty (TEA) has seen significant clinical advancements over the years. The first elbow replacements were introduced in the 1970s, and since then, there have been continuous efforts to improve implant design and reduce the failure rates, particularly in patients with degenerative conditions like rheumatoid arthritis or traumatic injuries. In recent years, there has been an increase in TEA procedures performed on younger patients at an annual rate of 8% among more active individuals (Triplet et al., 2016). This raises concerns about the long-term durability of the implants, as well as the potential need for revision surgery. The average survival rate of elbow implants typically ranges from 70% to 81% at 10 to 15 years post-operation, depending on factors like implant type, surgical technique, and patient activity levels (Krukhaug et al., 2018). More recent data report a 5-year implant survival rate of approximately 95.3% for trauma-related total elbow arthroplasty (TEA) and 92.6% for elective TEA procedures (National Joint Registry (NJR), 2023). These figures suggest a modest improvement in short- to mid-term survivorship in recent years, likely due to advances in implant design, surgical techniques, and perioperative care. However, long-term outcomes beyond the 5-year mark remain limited and relatively low compared to the higher survival rates seen in hip and knee replacements (Evans et al., 2019).

Despite the clinical success of TEA and the growing use of the procedure, issues such as aseptic loosening, infection, instability, and periprosthetic fractures continue to present significant challenge (Huub et al., 2007; Kim et al., 2018; Kim et al., 2011; Klug et al., 2018; Park et al., 2013; Toulemonde et al., 2016). The survival rate of TEA is significantly longer in patients with inflammatory arthritis compared to those with trauma-related conditions (Amirfeyz & Blewitt, 2009; Hildebrand et al., 2000). Additionally, the risk of complications increases in patients with young age, obesity, smoking, and high comorbidity (Celli & Morrey, 2009; Prkic et al., 2017; Schoch et al., 2017). To overcome these complications, many modifications have subsequently been proposed, and new implants have been created for the purpose of improving implant survivorship (Cross et al., 2010). In 1972, Dee introduced the first total elbow arthroplasty (TEA) prosthesis, which was a rigid hinged design with a high degree of constraint at the humeral and ulnar articulations (Dee, 1972). This initial implant was found to have rates of component loosening as high as 50% (Cross et al., 2010; Dee, 1972). Because of the absence of any laxity to the implant, all forces were transferred to the implant-cement-bone interface, resulting in loosening, fractures to the stem or bone, and broken hinges (Kaufmann et al., 2019). This has led to the emergence of unlinked implants which transmit less force to the implant-cement-bone interface as compared to fully linked implant designs.

It is important to emphasise that current clinical literature does not support a clear superiority of either linked or unlinked total elbow prostheses in terms of clinical outcome, complication rate, or survivorship. A retrospective study of 167 TEAs found no clinically significant differences in Oxford Elbow Score, Mayo Elbow Performance Score, or range of motion between linked and unlinked designs at 10.5-year follow-up (Plaschke et al., 2015). Similarly, a comparative series of 26

patients reported no meaningful functional differences between semiconstrained (linked) and unconstrained (unlinked) prostheses over 2-6 years (Wright et al., 2000). A systematic review confirmed good long-term outcomes for both linked and unlinked TEA designs and highlighted the absence of randomised prospective trials comparing them (Davey et al., 2021).

However, it is important to acknowledge that the available evidence is limited to retrospective and observational studies, which may be influenced by confounding factors such as surgeon selection, preoperative elbow stability, and patient pathology. Thus, while implant choice should be informed by patient-specific anatomy, stability, and surgical expertise, clinicians should be cautious about assuming outcome differences based solely on implant design. The lack of randomised prospective trials highlights an important gap in the evidence and limits definitive conclusions.

Modern prostheses were then developed with a sloppy hinge mechanism which allow for up to 7°-10° of laxity. These modern designs allow for some degree of varus-valgus movement, while still providing stability to axial rotation. These implants were found to decrease mechanical stresses on the implant-cement-bone interfaces and instead forces are transmitted to the surrounding soft tissues improving longevity (Dee, 1972; Kaufmann et al., 2019; Leclerc and King, 2011; Little et al., 2005).

With these recent technical advancements, the survivorship of modern total elbow arthroplasty (TEA) has improved (Prkić et al., 2016). A recent systematic review of 9308 TEA procedures reported a revision rate of 13.5% (Prkic et al., 2017). However, another review of 5957 surgeries showed slightly less favourable outcomes with a mean survival rate of 79.2% at 11.1 years (Welsink et al., 2017). While these outcomes represent progress, there remains significant

scope for further improvement, as TEA continues to have poorer surgical outcomes compared to other modern joint arthroplasties (Cross et al., 2010; Labek et al., 2011; Prkic et al., 2017; Sanchez-Sotelo, 2017). This stems largely from our limited understanding of elbow biomechanics, particularly the forces at play which leads to challenges in designing more durable implants.

To date, reported joint reaction forces in the elbow have primarily relied on musculoskeletal modelling, which involves simplifications and assumptions that can lead to inaccuracies. As a result, the elbow remains one of the few major joints where in vivo forces have yet to be accurately measured. Direct measurement of these forces acting on and distributed through the prosthesis is regarded as the gold standard for obtaining reliable in vivo data on the mechanical changes that contribute to the failure of the implant. Direct measurements of joint forces have been successfully achieved in larger joints such as the hip and knee using instrumented implants (Arami et al., 2013; Bergmann et al., 1993). However, to date, no instrumented prosthesis has been designed for total elbow arthroplasty (TEA) to measure joint forces during various activities of daily living.

Therefore, the aim of this doctoral thesis was to design and develop a customised prototype instrumented humeral component for a total elbow prosthesis capable of measuring six degrees of freedom of elbow joint reaction forces. The project progressed through several key stages: finite element analysis (FEA) and experimental testing of the implant, evaluation of the modified humeral stem's safety through fatigue testing, and the development of a calibration method for all six degrees of freedom.

Finally, the functionality and performance of the prototype were evaluated under simulated physiological loading conditions in an in vitro biomechanical study.

This doctoral thesis developed the first prototype of an instrumented humeral implant stem capable of providing direct physiological data that has not previously been measured in vivo. While these findings are promising, the implant remains at a developmental stage, requiring further design iterations, testing for reproducibility, and refinement before any clinical application. Nonetheless, the data obtained lays the groundwork for validating theoretical musculoskeletal models of elbow biomechanics, improving understanding of elbow joint function, informing rehabilitation programmes, and guiding the future design of elbow implants to improve long-term outcomes.

To address this gap, Chapter 3 focuses on the successful design, manufacture, and development of a prototype humeral component, modified to accommodate strain gauges and instrumentation while maintaining structural integrity. The humeral design is a geometrically adapted version of the Discovery humeral implant stem (LIMA Corporate S.p.A.), selected to integrate the instrumentation. The Discovery humeral component was chosen due to its proven ability to provide effective pain relief, improved range of motion, and long-term durability (Borton et al., 2021; Tiusanen et al., 2021). The prototype component is right-sided and comprises three primary regions: the humeral stem, the humeral body (middle part between stem and fork), and two forks designed to mate with the condylar components. The humeral body and forks contain 3 cavities accessible via welded covers which accommodated the instrumentation for strain measurement. The integrity of the customised humeral implant design was evaluated through finite element analysis (FEA), which provided critical insights into the stress distribution under various loading conditions. The maximum von Mises stress of 96.6 MPa, observed under a simulated compressive load of 700 N (moderate ADL), is well below the yield strength of titanium grade 5 (Ti-6Al-4V), which is

approximately 1070 MPa. This significant margin indicates that the implant can withstand moderate activities of daily living (ADL) without risk of material failure. The yield factor of safety (FOS) was calculated based on the loads applied during various activities of daily living (ADL), ranging from light tasks (22.2) to moderate (11.1), strenuous (5.5), and extreme (3.7) activities. The FOS values demonstrated that the implant consistently exceeds the minimum FOS threshold of 2 for orthopaedic implants (Khanoki and Pasini, 2013; Dowling, 2013; Browne, 1999). This suggests that the humeral implant design is structurally robust and capable of withstanding even the highest expected loads during extreme activities.

The distribution of von Mises stresses across the implant was concentrated in areas subjected to bending and compression, particularly near the humeral body and forks. However, the stress levels in these regions remained well within acceptable limits, supporting the initial geometric modifications made to accommodate the instrumentation. While these findings confirm that the current design maintains structural integrity, further testing and design refinements will be necessary to ensure consistent long-term performance and reliability in vivo.

The positioning of strain gauges on the prototype humeral implant was determined through a strain analysis study aimed at identifying sites with optimal sensitivity and selectivity for measuring forces and moments. Strain distribution was thoroughly investigated to ensure that the gauges could capture the applied degrees of freedom (DOFs) effectively. The strain analysis revealed that the medial and lateral forks of the implant experienced the highest strain concentrations, particularly in the medial cavity, which recorded a strain sensitivity of -3.3E-06 μstrain/Nm due to flexion/extension moments. This high sensitivity to strain in the fork cavities ensured detection of bending and torsional loads. In

contrast, strain around the base surface of the main cavity was lower, reflecting reduced force transmission in the more proximal regions of the implant. This uneven strain distribution aligns with findings from previous studies, which noted that the greatest forces pass through the distal end of the humeral component (France et al., 2024; Islam et al., 2020).

The implant's complex geometry limited strain gauge placement, requiring careful consideration to balance accessibility, sensitivity, and structural integrity. A sensitivity matrix was developed to correlate strain readings with applied forces and moments across the DOFs. This analysis provided valuable insights into the relative contributions of each gauge location, enabling us to identify the positions with the least redundancy and highest selectivity.

The calculated percentage error between the applied and measured forces and moments remained minimal at 0.2%, this has further confirmed the robustness of the predictive model used. Strain sensitivities for each DOF varied significantly; for instance, gauges in the fork cavities exhibited higher sensitivity to bending moments, while those in the main body cavity were more responsive to axial loads.

The final configuration included strain gauges in three primary locations: the two fork cavities and the main body cavity. The positions were finally determined based on the available geometric space with this particular arrangement to optimise sensitivity while maintaining structural integrity and minimising interference with the functionality of the implant. Pre-attached strain gauge cables were connected to a customised printed circuit board (PCB) embedded within the main body cavity of the implant, ensuring seamless integration of the measurement system.

The long-term durability and safety of the customised humeral implant, following its development, was evaluated through an experimental fatigue test study, as detailed in Chapter 4. This assessment employed a loading profile representative of the activity levels expected for the targeted patient cohort. Four right-sided titanium (Ti-6Al-4V) humeral component prototypes (N = 4) underwent fatigue testing, each subjected to a compressive load of 700 N for 5 million cycles at a frequency of 5 Hz. The results demonstrated that all humeral prototypes successfully withstood the 5 million cycles, equating to approximately 10 years of moderate activity. Importantly, no damage or structural failure was observed. These results provide encouraging preliminary evidence supporting the implant's mechanical durability. However, further testing and refinement will be necessary to fully establish its suitability for clinical use in instrumented total elbow arthroplasty (TEA).

Both experimental fatigue testing and Finite Element Analysis (FEA) validated the implant's structural reliability under the predefined loading conditions. The fatigue model predicted that the implant, with its specific modified geometry, would survive the applied loads, a result corroborated by the experimental tests. The modelled alternating stress of 57.2 MPa was significantly below the S-N curve, with a calculated fatigue life of 10 million cycles, suggesting that the implant could endure well beyond the required number of cycles for optimal performance. Additionally, the Goodman and Soderberg Factors of Safety (FoS) were calculated under moderate loading conditions as 5.4 and 5.3, respectively, indicating a robust safety margin.

Under strenuous and extreme loading scenarios, the structural limits of the implant were approached. For strenuous loading, the Fatigue FoS decreased to 1.5, highlighting an increased risk of fatigue failure with frequent exposure to such

conditions. Similarly, under extreme loads, the Goodman and Soderberg FoS values reduced to 1.5, underscoring the importance of advising patients to avoid excessive physical tasks that could jeopardise implant longevity. Despite these findings, the implant prototype is tailored to patients engaging in moderate daily activities, ensuring safe and reliable performance within these parameters.

The fatigue test also highlighted the importance of design features such as smooth radii and polished surfaces in reducing stress concentrations, particularly at the machined pockets and welded joints. Electron beam welding, an established technique for implanted devices, further contributed to the structural integrity. The low von Mises stresses observed in the vicinity of the welded joints and edges of the weld covers provided additional confidence in the durability of the implant prototype.

Strain analysis revealed that the highest principal strains (PS1 and PS2) were concentrated at the medial fork cavity (C2), which exhibited greater strain than the lateral fork cavity (C1) and significantly more than the central cavity (C3). These findings were consistent with the FE model, with measured strains agreeing within a 10% variation. This validated the ability of the model to predict strain magnitudes and directions at key locations.

In the absence of an internationally recognised testing standard, such as ASTM or ISO, for evaluating contemporary TEA implants, this study provides important preliminary findings supporting the development of a prototype instrumented humeral component for in vivo force measurement. The results validate the modified implant design and establish a foundation for future work focused on improving implant reliability and advancing the understanding of elbow joint biomechanics through direct physiological measurements.

Building on these findings, Chapter 5 primarily focused on the design and implementation of test setups for calibrating the six degrees of freedom of the prototype instrumented humeral implant stem. This calibration process is crucial for ensuring that the implant can measure the complex forces and moments acting on the elbow joint during daily activities.

This study addressed two key objectives: first, to develop experimental setups that calibrate each degree of freedom independently (three forces and three moments); and second, to apply the matrix method to construct a calibration sensitivity matrix. This matrix facilitates the conversion of raw strain gauge data into meaningful measurements of the forces and moments acting on the elbow joint, allowing for a more realistic analysis of the sensitivities of each strain gauge to the applied load.

The results of the calibration process demonstrated cross-sensitivities between the various components being measured. This means that when a force was applied to measure one degree of freedom, it simultaneously generated responses in other directions, suggesting that the alignment of the strain gauges might have contributed to unintended interactions. For example, when a load vector was applied to a calibration hole, significant force component of Fy was observed, along with smaller contributions from other forces and moments. This highlighted the complex biomechanical behaviour of the elbow joint and the need for a thorough understanding of these interactions to achieve accurate measurements.

The calibration process of the humeral component revealed that systematically applied known forces elicited consistent and predictable changes in resistance across all strain gauges. A clear linear relationship was established between the applied forces and the resistance changes, confirming that the strain gauges

accurately reflect variations in load. This consistency provides confidence in the measurement system's ability to accurately represent the mechanical forces acting on the humeral component.

A distinct linear relationship was identified between the applied known forces and the resulting changes in resistance of the strain gauges. This confirmed that the strain gauges effectively reflected variations in load. Strain Gauge 8 (SG8) consistently exhibited the highest sensitivity peaking to 3.7E−01 μstr/N in Load Case 1. This high sensitivity is attributed to its optimal placement on the medial fork of the implant which experiences significant strain due to its distance from the point of load application. This reliability gives us assurance that the calibrated system can accurately capture the mechanical forces acting on the humeral component.

A calibration sensitivity matrix was constructed and evaluated, which plays a critical role in accurately correlating the strain gauge responses to applied forces. For instance, the high R-squared value of 0.92 for Strain Gauge 3 indicated a strong relationship between the applied loads and strain measurements, meaning that the calibration model effectively captured the behaviour of humeral component under loads. However, discrepancies between predicted and actual forces were found as presented in chapter 5. This highlighted potential limitations in the calibration process, particularly the importance of using eccentric loads rather than pure moments for better calibration outcomes.

The development and validation of the calibration sensitivity matrix are essential for measuring mechanical forces and moments in the prototype instrumented humeral implant. This chapter not only enhances our understanding of elbow joint biomechanics but also lays the groundwork for subsequent chapters that validate the performance of the implant. By addressing current limitations in the calibration

process and demonstrating the implant's capability to provide reliable real-time data, this work contributes significantly to the thesis's overall goal of developing a dependable instrumented elbow implant prototype for in vivo force measurements in elbow replacements.

Following on, the objectives of Chapter 6 were to conduct a biomechanical study to validate the functionality and performance of the calibrated prototype in measuring the forces and moments acting on the elbow joint. Firstly, total elbow arthroplasty (TEA) was performed on synthetic bone models. Secondly, an in vitro biomechanical study was conducted to validate the six degrees of freedom measured by the calibrated implant, using strain gauge data under simulated physiological loading conditions. Finally, the study aimed to measure the three forces and three moments acting on the elbow joint during typical activities of daily living (ADL) and compare these measurements with modelled forces and moments to evaluate their validity.

In the flexion-extension plane, the measurements revealed that the dominant force component was F_Y along the y-axis, which is expected during elbow flexion and corresponds to the primary bending motion of the joint. However, there were also noticeable forces and moments in other directions. While some of these secondary forces may arise from the cross-sensitivity of the strain gauges and interactions of multiple forces during real-world conditions, it is important to recognise that the elbow is not a simple hinge joint. Instead, it is a compound joint allowing multiple degrees of freedom such as slight varus/valgus and rotational movements. Moreover, anatomical variations and the positioning of the implanted humeral component, which does not replicate a perfect hinge mechanism, contribute to these varus/valgus and rotational force components. Moreover, anatomical variations play a role in these forces. The positioning of the implanted

humeral component, which does not replicate a perfect hinge mechanism, also contributes to the varus/valgus and rotational force components. Therefore, these forces likely represent realistic physiological loading conditions. They are not unexpected and cannot be attributed solely to measurement artefacts or implant misalignment. This interpretation is supported by previous biomechanical studies, which have shown that the elbow experiences complex, multi-directional loading during flexion rather than simple uniaxial bending. For example, Morrey et al. (1998) described how the elbow undergoes varus and valgus stresses as well as torsional forces during normal daily activities, due to its anatomical structure and the interaction of muscles and ligaments. Similarly, An et al. (1983) showed that the kinematics of the elbow involve coupled rotations and translations that result in non-negligible forces and moments across multiple axes. These findings support the notion that the secondary varus/valgus and rotational forces measured in this study are consistent with the physiological function of the elbow rather than artefacts or abnormalities.

The most significant moment observed was M_Z, associated with the rotational forces from pronation-supination motion, which was likely influenced by the anatomical misalignment of the right humeral component implanted into a left humeral sawbone. Despite this misalignment, the implant prototype demonstrated its ability to measure a range of mechanical responses, highlighting its robustness.

The measured Force Magnification Ratio (FMR) was higher than the values calculated from the free body diagram (FBD), reflecting discrepancies likely due to several factors. These include the inherent complexity of elbow biomechanics, where rotational and translational motions alter force transmission, the challenges in calibrating the implant, the constraints on strain gauge placement,

and imperfect bonding of the stems to the bones in the experimental setup. Despite these discrepancies, the joint reaction force (JRF) calculated from the FBD was 343.35 N, which closely aligned with the JRF estimated using an established equation in previous literature (335.06 N), which further validates the performance of the implant prototype under non ideal conditions (Kincaid and An, 2013).

7.2. Study Limitations

This study acknowledged several important limitations. First, the use of artificial bone substitutes and a simplified biomechanical model incorporating only the brachialis muscle limit the physiological accuracy of the setup. More critically, the complex mechanical setup, combined with constraints in strain gauge placement and imperfect bonding of the implant stems, resulted in a non-ideal calibration matrix. This impacted the ability to fully replicate physiological loading conditions and may have contributed to measurement discrepancies observed across different flexion angles. Furthermore, the calibration matrix was developed based on a single flexion angle (10°), potentially introducing inaccuracies when the implant was tested at higher flexion positions.

This prototype implant is still at an early stage and requires multiple design iterations and testing cycles to improve calibration reliability, reproducibility, and overall performance. Future work should focus on developing a purpose-built calibration rig, testing across multiple specimens, refining the experimental setup to better mimic in vivo conditions, and expanding calibration across a range of flexion angles.

Despite these limitations, the study successfully demonstrates the feasibility of using an instrumented humeral implant prototype to measure six degrees of

freedom of elbow joint forces and moments. Even under non-ideal conditions, the implant prototype provides valuable biomechanical data that can enhance understanding of elbow joint function during activities of daily living. These promising results support the ongoing development of the implant towards a reliable tool for in vivo biomechanical and clinical research.

7.3. Future Work

Future work building on this doctoral thesis should address several key areas to enhance reproducibility, applicability, and clinical relevance. Due to cost and time constraints, only a single instrumented humeral implant prototype (N = 1) was developed and tested, limiting the ability to conduct experiments across multiple samples. Testing multiple implants would enhance the robustness and reliability of the findings by providing a larger, more statistically meaningful dataset. This expanded testing would offer deeper insights into implant performance under varying loading conditions and help identify any variability in behaviour between different prototypes. Ultimately, increasing the sample size will strengthen the conclusions and provide a more solid foundation for future implant design improvements and clinical applications.

The fatigue tests conducted in Chapter 4 were limited to testing the four humeral implant samples (N = 4) up to 5 million cycles due to time constraints. This cycle count simulated roughly 10 years of moderate patient activity. Future studies could extend testing beyond 5 million cycles to better understand the long-term durability and reliability of the prototype design under real-life conditions. By evaluating samples to the point of failure, data can be reported on the mechanisms of fatigue failure, identifying potential weak points, and reveal wear patterns. This testing enables more accurate predictions of the implant lifespan

across diverse patient profiles, ultimately guiding the design of safer, longer-lasting implants for clinical applications.

Chapter 5 presented one of the most significant challenges in this thesis which was the mechanical configuration used to calibrate the instrumented prototype and was constrained by the cost and availability of advanced testing equipment. Calibrating a humeral component with irregular geometry across six degrees of freedom is inherently complex. The calibration setup lacked flexibility for adjusting inclination angles during loading, which was necessary to maintain implant stability. As a result, pure moments were applied which does not fully represent the complex, real-world loading conditions the implant would experience, potentially introducing non-linearities and inaccuracies into the calibration matrix. To address these limitations, future studies should aim to develop a purpose-built calibration rig capable of applying forces and moments directly to each axis of the humeral component. Such a rig would allow precise control over force application, ensuring each degree of freedom is calibrated with greater accuracy and alignment with real-life conditions. This improvement would enhance the reliability and applicability of the calibration matrix for biomechanical assessments.

In Chapter 6, sawbone models were used in the biomechanical setup as a substitute for cadaveric bone. Although, sawbones is commonly used in experimental setups due to their consistency and ease of handling, they lack the natural variation in density and composition between cortical and cancellous bone, which plays a crucial role in how the bone responds to loads and stresses. For future studies, using cadaveric bone with intact cortical and cancellous structures would provide a more accurate representation of the biomechanical behaviour of the humeral bone under physiological load. Additionally, this

approach would allow for a more detailed examination of the interface between the implant and the bone and offering insights into the long-term performance of the implant.

7.3.1. Future Design Benefits

This research presents the development and initial validation of a prototype instrumented humeral implant capable of directly measuring elbow joint reaction forces and moments under controlled physiological loading. The integration of strain gauges and signal-processing circuitry into a structurally modified humeral stem is an early but significant step towards enabling direct measurement of in vivo elbow biomechanics, an area that has remained largely unexplored to date. Currently, the development of total elbow arthroplasty (TEA) implants relies heavily on musculoskeletal simulations. While these offer useful insights, they are often based on assumptions that may not reflect the complex and variable loads experienced in daily life. This prototype implant offers a potential route to overcome such limitations by enabling future collection of real loading data that can be used to refine implant geometries, particularly regarding stress distribution, joint constraint, and load transfer across the bone-cement-implant interface. With further development, such data could support more tailored designs for specific patient groups, anatomical variations, or activity levels, ultimately aiming to reduce risks such as mechanical failure and aseptic loosening.

The strain measurements obtained in this study also provide a foundation for the development and validation of higher-fidelity computational models. These models may be particularly useful in simulating rare or extreme loading scenarios, which are often difficult to recreate experimentally. Over time, this could

contribute to more efficient, bone-preserving implant designs by reducing reliance on overengineered components that contribute to stress shielding.

In terms of material performance, the titanium-based prototype was shown to tolerate physiological levels of static and cyclic loading. While this is encouraging, further work is required to explore long-term durability and the feasibility of alternative materials such as composites or additively manufactured alloys, which may offer improved biomechanical compatibility.

Additionally, the strain gauge configuration tested here, particularly in regions such as the forks of the humeral component showed high sensitivity to bending moments and low prediction error (0.2%), highlighting their potential value in future smart implants. These insights could be transferable to other joints, such as the shoulder or ankle, where there is a similar lack of in vivo force data.

Importantly, while these findings are promising, the device remains at the prototype stage, and further validation under broader loading conditions, as well as long-term mechanical and biocompatibility studies, are necessary before clinical translation can be considered. Nevertheless, this work provides an early proof-of-concept that may inform future strategies for implant instrumentation and evidence-based TEA design.

Although preliminary, this study offers meaningful insights that could support the development of the next generation of data-informed elbow implants, advancing design, material selection, real-time monitoring potential, and patient-specific treatment approaches.

7.3.2. Vision for Clinical Translation and Future Development

The long-term goal of this research is to translate the instrumented humeral implant into clinical use, where it could be implanted during total elbow

arthroplasty (TEA) procedures to measure joint forces and moments in vivo. These measurements could provide meaningful insight into how the joint behaves during everyday activities, helping to improve implant design, rehabilitation protocols, and patient outcomes. While instrumented implants have been successfully used in the hip and knee, the elbow remains largely underexplored. This project aims to bridge that gap by laying the groundwork for the first smart elbow implant designed for real-time, in vivo load measurement.

Sterilisation and Implantation Conditions

One of the key challenges in moving towards clinical translation is ensuring the implant can withstand surgical conditions, particularly sterilisation and fixation with PMMA bone cement.

Before implantation, the humeral implant must be sterilised, a process that could impact both the electronic components and the mechanical integrity of the implant housing. Common sterilisation methods like autoclaving, ethylene oxide gas, and hydrogen peroxide plasma each come with their own heat and chemical effects. It's important to ensure that these processes do not compromise the sensors or any adhesive bonds inside the implant.

PMMA bone cement also presents a challenge. During curing, the cement can reach high temperatures (often exceeding 80–90 °C), which may affect the sensors or the surrounding materials. It's essential to test the implant's performance under these conditions to ensure signal stability and structural durability. These factors should be investigated further in benchtop and potentially pre-clinical testing as part of the transition to clinical readiness.

Prototype Refinements Needed for Clinical Use

While the current prototype has performed well in controlled laboratory settings, several areas need refinement before the implant is suitable for patient use.

- **Power Supply and Data Collection**

  For clinical use, the implant will be powered wirelessly through inductive coupling, a method widely used in instrumented hip and knee implants. Inductive coupling works by transferring energy between two coils via a magnetic field. An external coil outside the body generates an alternating magnetic field, which induces a current in a coil inside the implant. This means the implant does not require an internal battery, reducing the risk of surgical replacements. In this design prototype, a coil will be integrated at the tip of the humeral stem, allowing efficient wireless power transfer through the surrounding tissue. This approach has been successfully applied in smart hip implants such as those developed by Taylor et al. (2004) and knee implants described by Taylor et al. (2011), demonstrating its reliability and safety for in vivo use.

  The patient will wear an external set of electronics that communicates with the implant via inductive coupling. This external unit powers the implant wirelessly and also receives strain measurement data collected by sensors inside the implant during the patient's everyday activities. Similar to instrumented hip and knee implants, this setup allows continuous monitoring of joint forces and moments in real-life conditions without restricting the patient's movement. The external device acts as both the power source and data receiver, ensuring that valuable biomechanical information is captured securely and reliably for clinical analysis.

- **Waterproofing and Durability**

  The implant will be exposed to moisture, varying temperatures, and repetitive loading. This means the electronics must be fully sealed within a biocompatible, waterproof enclosure that can withstand long-term

implantation. Mechanical durability under physiological conditions will need to be validated through extended testing.

- **Post-Sterilisation and Cementing Validation**

  The system must remain accurate and functional after sterilisation and cement embedding. Calibration drift, adhesive degradation, or insulation failure could all impact data reliability. A robust protocol will be needed to verify performance after surgical preparation.

- **Patient Compliance and Ethical Considerations**

  For patients, the implant should be entirely passive, requiring no maintenance or behavioural changes post-surgery. Once implanted, the device should operate quietly in the background, collecting data without disrupting daily life.

  That said, ethical considerations remain essential. Patients must be fully informed about what data is being collected, how it will be used, and who will have access to it. Data security and patient privacy must be prioritised, particularly if data is transmitted wirelessly or stored over long periods. Informed consent processes will need to be thorough and transparent, especially in early clinical trials.

Schematic Overview

The instrumented elbow implant is designed to measure joint forces and moments in real time during human trials, building on the success of similar systems already used in hip and knee implants. To help explain this, a schematic adapted from established hip implant designs as seen in Figure 7-1 (Taylor et al., 2004) shows how the external data collection system works.

The prototype humeral implant includes a coil that’s wirelessly connected to a set of electronics worn by the patient. This external unit powers the implant and

collects data from sensors inside the implant. The information is then sent to a computer, giving clinicians easy access to joint load measurements for monitoring and analysis.

Right now, the design is still at an early prototype stage. Future work will focus on improving the efficiency and reliability of the wireless power supply to reduce reliance on internal batteries, making data transmission more robust for continuous monitoring, and developing user-friendly interfaces with reminders to help patients stay engaged and compliant.

These improvements will help make the system practical for long-term use in clinical trials, supporting safer rehab protocols and allowing early detection of any implant issues

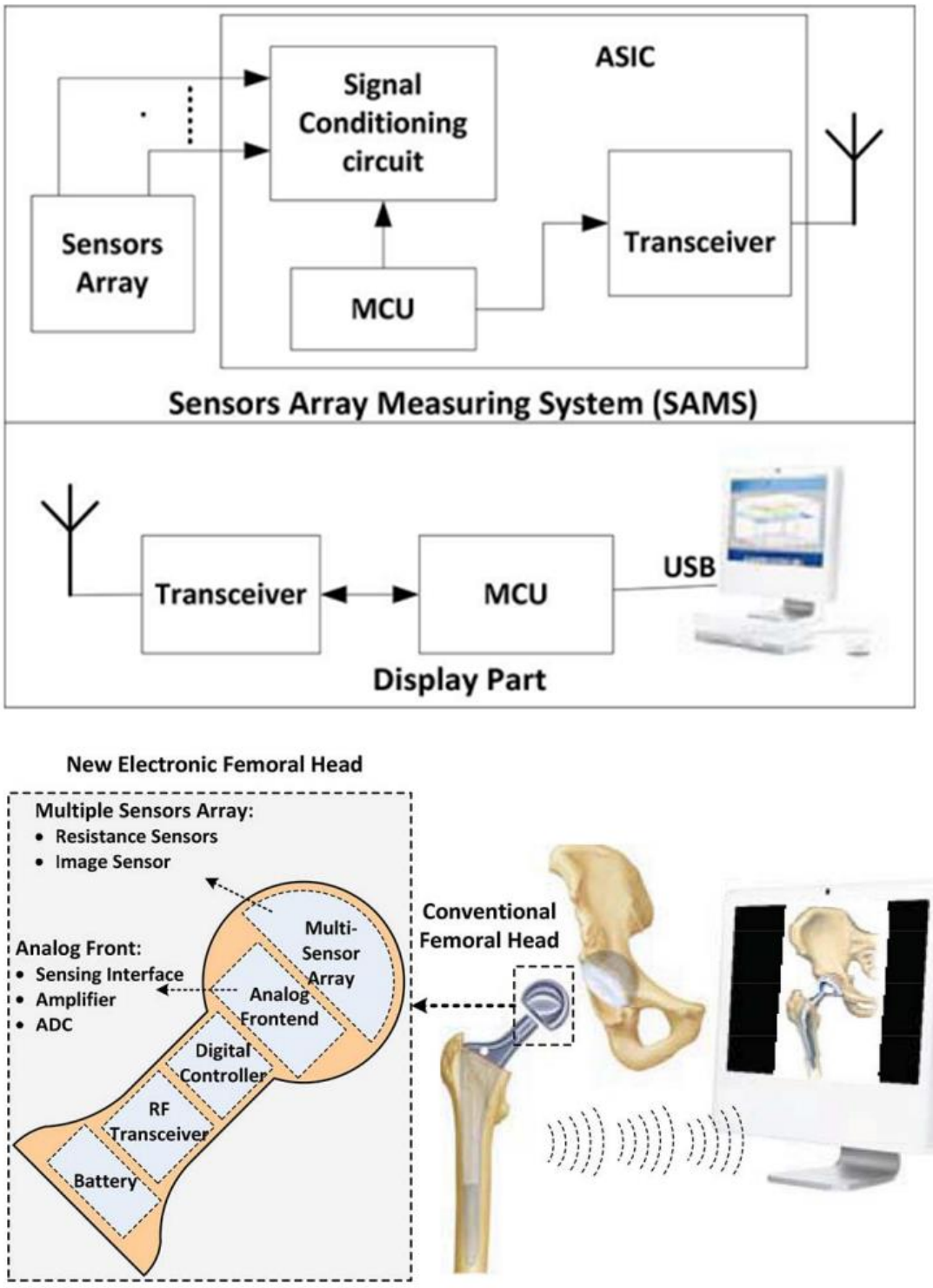

Figure 7-1: Block diagram and architecture of the instrumented hip implant system (Wang et al., 2024).

7.4. Long-Term Outlook and Clinical Readiness

This doctoral work sits within a larger research programme aimed at developing a smart elbow implant for first-in-human studies. The focus here has been on the core building blocks, prototype design, finite element analysis (FEA), instrumentation of the humeral component, and initial mechanical and biomechanical testing. These efforts have created a foundation on which clinical translation can begin.

The next phase will involve producing a small batch of implants for clinical evaluation. However, before any in vivo studies can begin, additional in vitro testing and design refinement will be necessary to address the limitations discussed earlier in the thesis. These improvements will help ensure the system is robust, reliable, and safe under real surgical and post-operative conditions.

Once implants are manufactured and surgically implanted, they will need to be monitored over several months to evaluate their long-term stability and data performance. This extended testing will be critical for understanding how the implant behaves in a living joint over time and will help inform future regulatory approval and wider clinical use.

Appendix A

A-1: Supplementary Material for Chapter 4

In Chapter 4, Figure 4-3 shows one humeral implant sample undergoing fatigue testing. Out of the four samples, one is instrumented with three triaxial 350 Ω rectangular rosette (45°) strain gauges. Figure A -1-1 below illustrates the setup on this sample during testing on the E3000 Instron Fatigue Testing Machine.

Figure A -1-1: Illustration of fatigue test setup for the strain gauged sample using the E3000 Instron machine.

Each of the four humeral components successfully endured the applied loading regimen of 70–700 N for 5 million cycles. The stress amplitude remained relatively consistent throughout the test, with only small variations, which suggests that the implant likely maintained structural integrity under cyclic loading. This performance demonstrates the reliability and safety of the humeral implants for long-term use, particularly in replicating moderate daily activities. Figure A -1-2 illustrates the stress amplitude profile for all four samples over the 5 million cycles, highlighting initial fluctuations that stabilise within the first few thousand cycles.

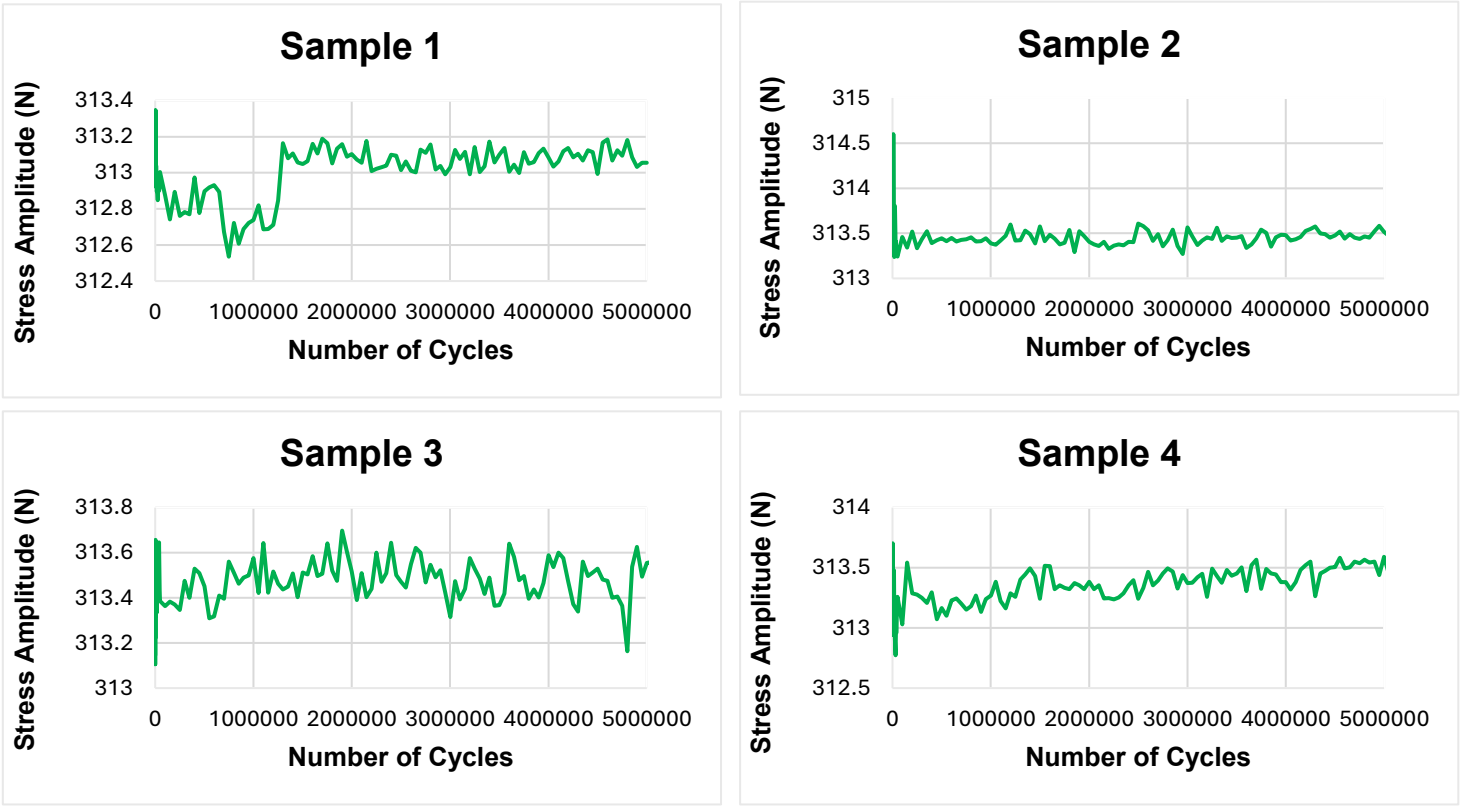

Figure A -1-2: Stress amplitude profile for all four humeral implant samples over 5 million cycles. Initial fluctuations are observed during the first few thousand cycles, followed by stabilisation, with the stress amplitude remaining relatively consistent throughout the test.

A-2: Supplementary Material for Chapter 5

Example calculations of the resolved forces presented in Table 5-2 for load case 1

In 3D analysis, forces and moments are typically represented as vectors with their components expressed as:

$$\mathrm{F} = \mathrm{F_x i} + \mathrm{F_y j} + \mathrm{F_z k}$$

From Figure 5-6, we use the direction cousins of $\sin(5°)$, $\cos(5°)$, and $\cos(90°)$, along with the applied force of 114 N, to calculate the force components:

$$\mathrm{F_x} = 114 \times \sin(5°) = 9.936\ \mathrm{N}$$

$$\mathrm{F_y} = 114 \times \cos(5°) = 113.566\ \mathrm{N}$$

$$\mathrm{F_z} = 114 \times \cos(90°) = 0\ \mathrm{N}$$

The moment of a force about an axis is given by the cross product of the position vector. From Figure 5-6, let $\mathrm{d_1} = 0\ \mathrm{mm}$, $\mathrm{d_2} = 0\ \mathrm{mm}$ and $\mathrm{h} = 56\ \mathrm{mm}$. The moment components can be calculated as follows:

$$\mathrm{M_x} = -114 \times \cos(5°) \times 0 = 0\ \mathrm{N.mm}$$

$$\mathrm{M_y} = 114 \times \sin(5°) \times 0 = 0\ \mathrm{N.mm}$$

$$\mathrm{M_z} = 114\ (0 \times \cos(5°) - 56 \times \sin(5°)) = -556.402\ N.mm$$

The remaining resolved force and moment components presented in Table 5-2 are calculated using the same methodology, accounting for variations in the applied force, $\mathrm{d_1}$ and $\mathrm{d_2}$.

Example calculations of the resolved forces presented in Table 5-3 for load case 2

In Figure 5-7, the angle plate was inclined a $10°$ in the YZ plane.

$$\delta = acos\left(sqrt\left(1 - \ cos^2(85°) - \ cos^2(90° - 10°)\right)\right) = 11.2°$$

From Figure 5-7, let the applied force be 114 N, $\mathrm{d_1} = 1.1\ \mathrm{mm}$, $\mathrm{d_2} = 0\ \mathrm{mm}$ and $\mathrm{h} = 56\ \mathrm{mm}$.The force and moment components are calculated as follows:

$\mathrm{F_x} = 114\ \times\ \sin(5°) = 9.936\ \mathrm{N}$

$\mathrm{F_y} = 114\ \times\ \cos(11.2°) = 111.828\ \mathrm{N}$

$\mathrm{F_z} = 114\ \times\ \sin(10°) = 19.796\ \mathrm{N}$

$\mathrm{M_x} = 114\ (\ 56.\sin(10°) - 1.1\ \times \cos(11.2°)\ ) = 985.262\ \mathrm{N.mm}$

$\mathrm{M_y} = 114\ (\ 1.1\ \times\ \sin(5°) - 0\ \times \sin(10°)\ ) = 10.956\ \mathrm{N.mm}$

$\mathrm{M_z} = 114\ (0\ \times\ \cos(11.2°) -\ 56\ \times\ \sin(5°)\ ) =\ -556.402\ \mathrm{N.mm}$

The remaining resolved force and moment components presented in Table 5-3 are calculated using the same methodology, accounting for variations in the applied force, $\mathrm{d_1}$ and $\mathrm{d_2}$.

Example calculations of the resolved forces presented in Table 5-4 for load case 3

In Figure 5-8, the angle plate was inclined a β degree in the XY plane.

θ is the angle of the applied force F with respect to Y, therefore:

$$\theta = \mathrm{acos}\left(\mathrm{sqrt}\left(1 - \cos^2(85° - 10°) - \cos^2(90°)\right)\right) = 15°$$

From Figure 5-8, let the applied force be 100 N, $d_1 = 0\ \mathrm{mm}$, $d_2 = 1.1\ \mathrm{mm}$ and $h = 56\ \mathrm{mm}$.The force and moment components are calculated as follows:

$$F_x = 100 \times \sin(5° + 10°) = 25.882\ \mathrm{N}$$

$$F_y = 100 \times \cos(15°) = 96.593\ \mathrm{N}$$

$$F_z = 100 \times \cos(90°) = 0\ \mathrm{N}$$

$$M_x = -100 \times 0 \times \cos(15°) = 0\ \mathrm{N.mm}$$

$$M_y = 100\ (\ 0 \times \sin(5° + 10°)\ ) = 0\ \mathrm{N.mm}$$

$$M_z = 100\ (1.1 \times \cos(15°) - 56 \times \sin(5° + 10°)\ ) = -1342.877\ \mathrm{N.mm}$$

The remaining resolved force and moment components presented in Table 5-4 are calculated using the same methodology, accounting for variations in the applied force, d_1 and d_2.

Correlation Analysis of Force and Moment Components

Figure A -2-1 presents a series of plots demonstrating the correlation between the three components of force (Fx, Fy, Fz) and the three components of moment (Mx, My, Mz) for each applied load scenario, as detailed in Table 5-6. Each plot provides a visual representation of how one variable varies with respect to another.

Certain pairs, such as Fx vs Fy and Fy vs Fz, exhibit periodic trends, indicating potential correlations. In contrast, others, such as Fx vs My, appear more irregular, suggesting weak or no correlation. This analysis is crucial for assessing the degree of independence between the force and moment components under varying loading conditions. Correlated variables suggest a dependency, where changes in one component may predictably influence another. Conversely, weak or no correlation, as seen in pairs like Fx vs My, indicate greater independence, meaning these components may behave more autonomously. This assessment of dependence of forces and moments ensures that each variable contributes uniquely to the overall loading scenario.

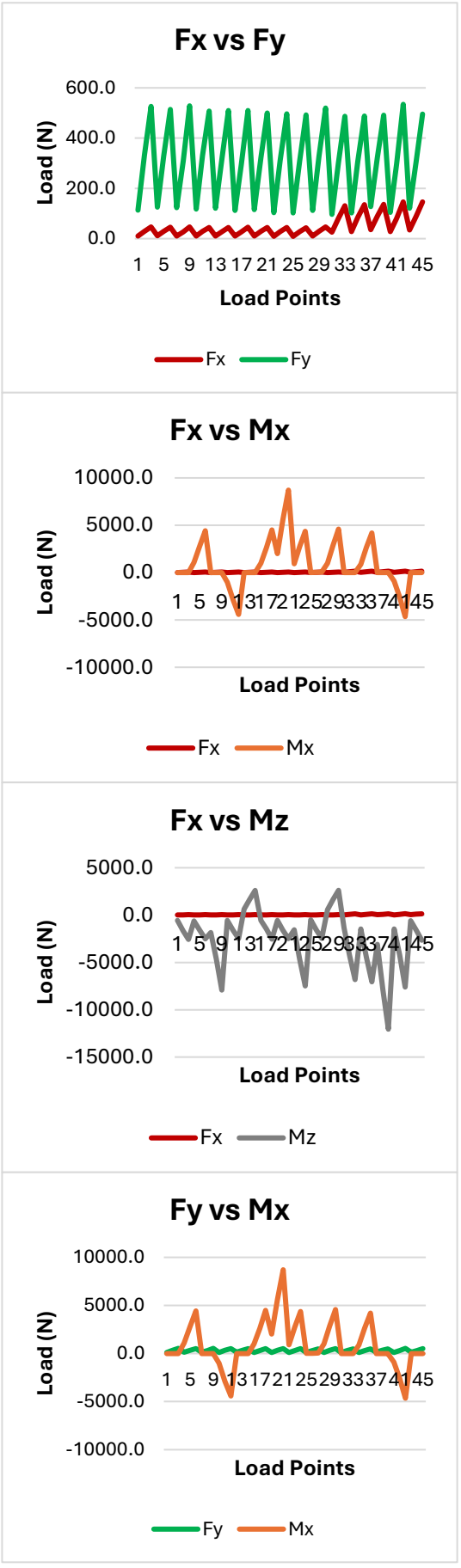
Fx vs Fy
600.0
400.0
200.0
0.0
Load (N)
1 5 9 13 17 21 25 29 33 37 41 45
Load Points
Fx
Fy
Fx vs Fz
200.0
150.0
100.0
50.0
0.0
Load (N)
1 5 9 13 17 21 25 29 33 37 41 45
Load Points
Fx
Fz
Fx vs Mx
10000.0
5000.0
0.0
-5000.0
-10000.0
Load (N)
1 5 9 13 17 21 25 29 33 37 41 45
Load Points
Fx
Mx
Fx vs My
2000.0
1000.0
0.0
-1000.0
-2000.0
Load (N)
1 5 9 13 17 21 25 29 33 37 41 45
Load Points
Fx
My
Fx vs Mz
5000.0
0.0
-5000.0
-10000.0
-15000.0
Load (N)
1 5 9 13 17 21 25 29 33 37 41 45
Load Points
Fx
Mz
Fy vs Fz
600.0
400.0
200.0
0.0
Load (N)
1 5 9 13 17 21 25 29 33 37 41 45
Load Points
Fy
Fz
Fy vs Mx
10000.0
5000.0
0.0
-5000.0
-10000.0
Load (N)
1 5 9 13 17 21 25 29 33 37 41 45
Load Points
Fy
Mx
Fy vs My
2000.0
1000.0
0.0
-1000.0
-2000.0
Load (N)
1 5 9 13 17 21 25 29 33 37 41 45
Load Points
Fy
My

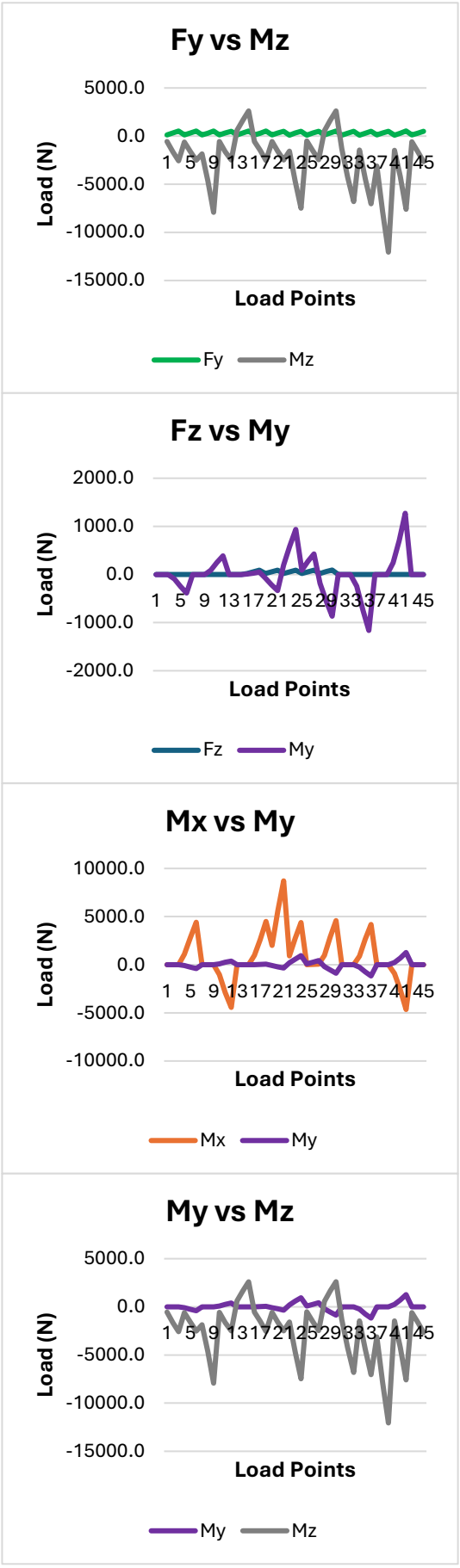
Fy vs Mz
5000.0
0.0
-5000.0
-10000.0
-15000.0
Load (N)
1 5 9 13 17 21 25 29 33 37 41 45
Load Points
Fy
Mz
Fz vs Mx
10000.0
5000.0
0.0
-5000.0
-10000.0
Load (N)
1 5 9 13 17 21 25 29 33 37 41 45
Load Points
Fz
Mx
Fz vs My
2000.0
1000.0
0.0
-1000.0
-2000.0
Load (N)
1 5 9 13 17 21 25 29 33 37 41 45
Load Points
Fz
My
Fz vs Mz
5000.0
0.0
-5000.0
-10000.0
-15000.0
Load (N)
1 5 9 13 17 21 25 29 33 37 41 45
Load Points
Fz
Mz
Mx vs My
10000.0
5000.0
0.0
-5000.0
-10000.0
Load (N)
1 5 9 13 17 21 25 29 33 37 41 45
Load Points
Mx
My
Mx vs Mz
10000.0
5000.0
0.0
-5000.0
-10000.0
-15000.0
Load (N)
1 5 9 13 17 21 25 29 33 37 41 45
Load Points
Mx
Mz
My vs Mz
5000.0
0.0
-5000.0
-10000.0
-15000.0
Load (N)
1 5 9 13 17 21 25 29 33 37 41 45
Load Points
My
Mz

Figure A -2-1: Correlation plots between Forces (Fx, Fy, Fz) and Moments (Mx, My, Mz) for each applied load scenario in calibration, as detailed in Table 5-6. Periodic trends are observed in some pairs, such as Fx vs Fy and Fy vs Fz, suggesting potential correlations, while others, such as Fx vs My, exhibit irregular patterns, indicating weak or no correlation.

A-3: Supplementary Material for Chapter 6

Calculations for the Free Body Diagram (FBD) analysis at 101° elbow flexion

From the FBD in Figure 6-12, the following known forces and moment arms were set during the experimental setup:

$\boldsymbol{\theta}$ = Elbow flexion angle = $101°$

$\boldsymbol{\beta}$ = Brachialis angle relative to the horizontal plane = $112°$ anticlockwise

$\mathbf{F_E}$ = External weight force $= 4.5 \times 9.81 = 44.15$ N

$\mathbf{F_W}$ = Weight of the arm $= 0.15 \times 9.81 = 1.47$ N

$\mathbf{d_E}$ = Distance from external weight to hing axis $= 0.25 \times \cos(11°) = 0.25$ m

$\mathbf{d_B}$ = Distance from brachialis to hing axis $= 0.04 \times \cos(11°) = 0.04$ m

$\mathbf{d_W}$ = Distance from arm centre of mass (CoM)to hing axis $= 0.11 \times \cos(11°) = 0.11$ m

Using the equilibrium equations with clockwise directions considered positive and anticlockwise directions negative:

$$\sum M = (F_E . d_E) + (F_W . d_W) - (F_{B(y)} . d_B) = 0$$

$$\sum M = (44.15 \times 0.25) + (1.47 \times 0.11) - (F_{B(y)} .0.04) = 0$$

$F_{B(y)}$ = Brachialis force (vertical component) = 279.95 N

$F_{B\,(resultant)}$ = Resultant brachialis force

$$F_{B\,(resultant)} = \frac{F_{B(y)}}{\sin(\beta)} = \frac{279.95}{\sin(112°)} = 301.94 \text{ N}$$

$F_{B(z)}$ = Brachialis force (horizontal component)

$$F_{B(z)} = F_{B\,(resultant)} \times \cos(\beta) = 301.94 \times \cos(112°) = -113.11 \text{ N}$$

$F_{j(y)}$ = Vertical joint reaction force

$$\sum F_y = F_E + F_W - F_{B(y)} + F_{j(y)} = 0$$

$$\sum F_y = 44.15 + 1.47 - 279.95 + F_{j(y)} = 0$$

$$F_{j(y)} = 234.34 \text{ N}$$

$$F_{j(y)}(\text{corrected}) = F_{j(y)} \times \cos(30°) = 234.34 \times \cos(30°) = 202.94 \text{ N}$$

$F_{j(z)}$ = Horizontal joint reaction force

$$\sum F_z = F_{j(z)} - F_{B(z)} = 0$$

$$F_{j(z)} = F_{B(z)} = -113.11 \text{ N}$$

F_j = Resultant joint reaction force

$$F_j = \sqrt{F_{j(y)(\text{corrected})}^2 + F_{j(z)}^2} = \sqrt{(202.94)^2 + (-113.11)^2} = 232.33 \text{ N}$$

$$\text{FMR} = \frac{\text{vertical joint reaction force}}{\text{external load}} = \frac{F_{j(y)}(\text{corrected})}{F_E} = \frac{202.94}{44.15} = 4.6$$

Calculations for the Free Body Diagram (FBD) analysis at 148° elbow flexion

From the FBD in Figure 6-12, the following known forces and moment arms were set during the experimental setup:

$\boldsymbol{\theta}$ = Elbow flexion angle = 148°

$\boldsymbol{\beta}$ = Brachialis angle relative to the horizontal plane = 88° anticlockwise

$\mathbf{F_E}$ = External weight force = $4.5 \times 9.81 = 44.15$ N

$\mathbf{F_W}$ = Weight of the arm = $0.15 \times 9.81 = 1.47$ N

$\mathbf{d_E}$ = Distance from external weight to hing axis = $0.25 \times \cos(58°) = 0.13$ m

$\mathbf{d_B}$ = Distance from brachialis to hing axis = $0.04 \times \cos(58°) = 0.02$ m

$\mathbf{d_W}$ = Distance from arm centre of mass (CoM)to hing axis = $0.11 \times \cos(58°) =$ 0.06 m

Using the equilibrium equations with clockwise directions considered positive and anticlockwise directions negative:

$$\sum M = (F_E . d_E) + (F_W . d_W) - (F_{B(y)} . d_B) = 0$$

$$\sum M = (44.15 \times 0.13) + (1.47 \times 0.06) - (F_{B(y)} .0.02) = 0$$

$F_{B(y)}$ = Brachialis force (vertical component) = 279.95 N

$F_{B\ (resultant)}$ = Resultant brachialis force

$$F_{B\ (resultant)} = \frac{F_{B(y)}}{\sin(\beta)} = \frac{279.95}{\sin(88°)} = 280.12 \text{ N}$$

$F_{B(z)}$ = Brachialis force (horizontal component)

$$F_{B(z)} = F_{B\ (resultant)} \times \cos(\beta) = 280.12 \times \cos(88°) = 9.78 \text{ N}$$

$F_{j(y)}$ = Vertical joint reaction force

$$\sum F_y = F_E + F_W - F_{B(y)} + F_{j(y)} = 0$$

$$\sum F_y = 44.15 + 1.47 - 279.95 + F_{j(y)} = 0$$

$$F_{j(y)} = 234.34 \text{ N}$$

$$F_{j(y)}(\text{corrected}) = F_{j(y)} \times \cos(3°) = 234.34 \times \cos(3°) = 234.02 \text{ N}$$

$F_{j(z)}$ = Horizontal joint reaction force

$$\sum F_z = F_{j(z)} - F_{B(z)} = 0$$

$$F_{j(z)} = F_{B(z)} = 9.78 \text{ N}$$

F_j = Resultant joint reaction force

$$F_j = \sqrt{F_{j(y)(\text{corrected})}^{\,2} + F_{j(z)}^{\,2}} = \sqrt{(234.02)^2 + (9.78)^2} = 234.22 \text{ N}$$

$$\text{FMR} = \frac{\text{vertical joint reaction force}}{\text{external load}} = \frac{F_{j(y)}(\text{corrected})}{F_E} = \frac{234.02}{44.15} = 6.3$$

References

Ali, M. H., Batai, S., & Sarbassov, D. (2019). 3D printing: a critical review of current development and future prospects. Rapid Prototyping Journal, 25(6), 1108–1126.

Amirfeyz, R., & Blewitt, N. (2009). Mid-term outcome of GSB-III total elbow arthroplasty in patients with rheumatoid arthritis and patients with post-traumatic arthritis. Archives of Orthopaedic and Trauma Surgery, 129(11), 1505–1510.

Amis, A. A., Dowson, D., & Wright, V. (1979a). Muscle strengths and musculo-skeletal geometry of the upper limb. Engineering in Medicine, 8(1), 41–48.

Amis, A. A., Dowson, D., & Wright, V. (1979b). Muscle strengths and musculo-skeletal geometry of the upper limb. Engineering in Medicine, 8(1), 41–48.

Amis, A. A., Dowson, D., Wright, V., & Miller, J. H. (1979). The derivation of elbow joint forces, and their relation to prosthesis design. Journal of Medical Engineering & Technology, 3(5), 229–234.

Amis, A. A., Dowson, D., & Wrights, V. (1980). Analysis of Elbow Forces Due to High-speed Forearm Movements. Journal of Biomechanics , 13, 825–831.

Amis, A. A., Dowson, D., & Wrights, V. (1980). Elbow Joint Force Predictions for Some Strenuous Isometric Actions. 13, 765–775.

An, K. N. (2005). Kinematics and constraint of total elbow arthroplasty. Journal of Shoulder and Elbow Surgery, 14(1), S168–S173.

An, K. N., Hui, F. C., Morrey, B. F., Linscheid, R. L., & Chao, E. Y. (1981). Muscles across the elbow joint: A biomechanical analysis. Journal of Biomechanics, 14(10), 659–669.

An, K. N., Morrey, B. F., Chao, E. Y. S., & Linscheid, R. L. (1983). Kinematics of the elbow. Clinical Orthopaedics and Related Research, 177, 131–140.

An, K. N., Kwak, B. M., Chao, E. Y., & Morrey, B. F. (1984). Determination of muscle and joint forces: a new technique to solve the indeterminate problem. Journal of Biomechanical Engineering, 106(4), 364–367.

An, K. N., Morrey, B. F., & Chao, E. Y. (1986). The Effect of Partial Removal of Proximal Ulna on Elbow Constraint. Clinical Orthopaedics and Related Research , 209, 270–279.

Angst, F., John, M., Pap, G., Mannion, A. F., Herren, D. B., Flury, M., Aeschlimann, A., Schwyzer, H. K., & Simmen, B. R. (2005). Comprehensive assessment of clinical outcome and quality of life after total elbow arthroplasty. Arthritis Care and Research, 53(1), 73–82.

Arami, A., Simoncini, M., Atasoy, O., Ali, S., Hasenkamp, W., Bertsch, A., Meurville, E., Tanner, S., Renaud, P., Dehollain, C., Farine, P. A., Jolles, B. M., Aminian, K., & Ryser, P. (2013). Instrumented knee prosthesis for force and kinematics measurements. IEEE Transactions on Automation Science and Engineering, 10(3), 615–624.

Arno, S., Fetto, J., Nguyen, N. Q., Kinariwala, N., Takemoto, R., Oh, C., & Walker, P. S. (2012). Evaluation of femoral strains with cementless proximal-fill femoral implants of varied stem length. Clinical Biomechanics, 27(7), 680–685.

Askew, L. J., An, K. N., Morrey, B. F., & Chao, E. Y. S. (1987). Isometric elbow strength in normal individuals. Clinical Orthopaedics and Related Research, 222, 261–266.

Austman, R. L., King, G. J. W., & Dunning, C. E. (2011). Bone stresses before and after insertion of two commercially available distal ulnar implants using finite element analysis. Journal of Orthopaedic Research, 29(9), 1418–1423.

Aziz, M. S. R., Nicayenzi, B., Crookshank, M. C., Bougherara, H., Schemitsch, E. H., & Zdero, R. (2014). Biomechanical measurements of stiffness and strength for five types of whole human and artificial humeri. Journal of Biomechanical Engineering, 136(5), 051006.

Backman Daniel, & Cil Akin. (2017). Current concepts in elbow arthroplasty. EFORT Open Reviews , 2, 83–88.

Basiouny, M., Lambert, S., Kuenfoo, C., & Taylor, S. (2022). Towards the Measurement of Elbow Joint Forces in Man: A Finite Element Study. 27th Congress of the European Society of Biomechanics Abstract Book.

Bates, T. J., Fergason, J. R., & Pierrie, S. N. (2020). Technological Advances in Prosthesis Design and Rehabilitation Following Upper Extremity Limb Loss. Current Reviews in Musculoskeletal Medicine, 13(4), 485.

Bennett, J. B., & Mehlhoff, T. L. (2009). Total Elbow Arthroplasty: Surgical Technique. Journal of Hand Surgery, 34(5), 933–939.

Bergmann, G., Graichen, F., & Rohlmann, A. (1993). Hip Joint Loading During Walking and Running, Measured in Two Patients. Journal of Biomechanics, 26(8), 969-990.

Bergmann, G., Graichen, F., Rohlmann, A., Westerhoff, P., Heinlein, B., Bender, A., & Ehrig, R. (2008). Design and calibration of load sensing orthopaedic implants. Journal of Biomechanical Engineering, 130(2), 021009.

Bergmann, G., Graichen, F., Siraky, J., Jendrzynski, H., & Rohlmann, A. (1988). Multichannel Strain Gauge Telemetry for Orthopaedic Implants. Journal of Biomechanics, 21(2), 169-176.

Bergmann, G., Siraky, J., Rohlmann, A., & Koelbel, R. (1982). Measurement of spatial forces by the “Matrix”-method. V/VI 9th World Congress IMEKO, 395–404.

Bieger, R., Ignatius, A., Decking, R., Claes, L., Reichel, H., & Dürselen, L. (2012). Primary stability and strain distribution of cementless hip stems as a function of implant design. Clinical Biomechanics, 27(2), 158–164.

Borton, Z. M., Prasad, G., Konstantopoulos, G., Morgan, M. L., Cresswell, T., Espag, M. P., Tambe, A. A., & Clark, D. I. (2021). Mid- to long-term survivorship of the cemented, semiconstrained Discovery total elbow arthroplasty. Journal of Shoulder and Elbow Surgery, 30(7), 1662–1669.

Boyer, R. R., Welsch, G., & Collings, E. W. (1994). Materials Properties Handbook: Titanium Alloys (Vol. 1).

Brinkman, J. M., de Vos, M. J., Eygendaal, D., & van der Werken, C. (2005). Failure of the Coonrad-Morrey total elbow prosthesis: Complications in 25 elbows after 8–12 years. Acta Orthopaedica Belgica, 71(5), 530–535.

Browne M, Langley RS, Gregson PJM. (1999). Reliability theory for load bearing biomedical implants. Biomaterials , 20(14), 1285–1292.

Brownhill, J. R., Pollock, J. W., Ferreira, L. M., Johnson, J. A., & King, G. J. W. (2019). The effect of implant linking and ligament integrity on humeral loading of a convertible total elbow arthroplasty. Shoulder & Elbow, 11(1), 45.

Buchanan, T. S., Delp, S. L., & Solbeck, J. A. (1998). Muscular Resistance to Varus and Valgus Loads at the Elbow. Transactions of the ASME , 120, 634–639.

Cameron, D., Kuen, C., & Jon, C. (2021). Inflammatory arthritis and the elbow surgeon. Journal of Clinical Orthopaedics and Trauma, 20, 101492.

Celli, A., & Morrey, B. F. (disorders). Total elbow arthroplasty in patients forty years of age or less. The Journal of Bone and Joint Surgery, 91(6), 1414–1418.

Cesar, M., Roussanne, Y., Bonnel, F., & Canovas, F. (2007). GSB III total elbow replacement in rheumatoid arthritis. The Journal of Bone and Joint Surgery, 89(3), 330–334.

Chadwick, E. K. J., & Nicol, A. C. (2000a). Elbow and wrist joint contact forces during occupational pick and place activities. Journal of Biomechanics, 33, 591–600.

Completo, A., Pereira, J., Fonseca, F., Ramos, A., Relvas, C., & Simões, J. (2011). Biomechanical analysis of total elbow replacement with unlinked iBP prosthesis: An in vitro and finite element analysis. Clinical Biomechanics, 26(10), 990–997.

Craik, J. D., Hl Laffer, C., Richards, S. W., Walsh, S. P., & Evans, S. L. (2012). Distal humerus cortical strains following total elbow arthroplasty. Journal of Engineering in Medicine , 227(2), 120–128.

Cross, M. B., Sherman, S. L., Kepler, C. K., Neviaser, A. S., & Weiland, A. J. (2010). The evolution of elbow arthroplasty: innovative solutions to complex clinical problems. The Journal of Bone and Joint Surgery, 92(2), 98–104.

Damm, P., Graichen, F., Rohlmann, A., Bender, A., & Bergmann, G. (2010). Total hip joint prosthesis for in vivo measurement of forces and moments. Medical Engineering and Physics, 32(1), 95–100.

Davey, M. S., Hurley, E. T., Gaafar, M., Molony, D., Mullett, H., & Pauzenberger, L. (2021). Long-term outcomes of total elbow arthroplasty: A systematic review of studies at 10-year follow-up. Journal of Shoulder and Elbow Surgery, 30(6), 1423–1430.

Davis, P. R. (1977). Some significant aspects of normal upper limb. Conference on Joint Replacement of the Upper Extremity. London, Institute of Mechanical Engineers.

Day, J. S. (2016). 12 - The Clinical Performance of UHMWPE in Elbow Replacements (Steven M. Kurtz, Ed.; third). Elsevier/Academic Press.

Day, J. S., Lau, E., Ong, K. L., Williams, G. R., Ramsey, M. L., & Kurtz, S. M. (2010). Prevalence and projections of total shoulder and elbow arthroplasty in the United States to 2015. Journal of Shoulder and Elbow Surgery, 19(8), 1115–1120.

De Haan, J., Schep, N. W. L., Eygendaal, D., Kleinrensink, G.-J., Tuinebreijer, W. E., & Den Hartog, D. (2011). Stability of the Elbow Joint: Relevant Anatomy and Clinical Implications of In Vitro Biomechanical Studies. The Open Orthopaedics Journal, 5(1), 168.

De Vos, M. J., Wagener, M. L., Hendriks, J. C. M., Eygendaal, D., & Verdonschot, N. (2013). Linking of total elbow prosthesis during surgery; A biomechanical analysis. Journal of Shoulder and Elbow Surgery, 22(9), 1236–1241.

Dee, R. (1972). Total replacement arthroplasty of the elbow for rheumatoid arthritis. The Journal of Bone and Joint Surgery, 54(1), 88–95.

Dee R, & Sweetnam, D. (1970). Total Replacement Arthroplasty of the Elbow Joint for Rheumatoid Arthritis: Two Cases. Proceedings of the Royal Society of Medicine, 63(7), 653–655.

Deshmukh, K., Houkan, M. T., AlMaadeed, M. A. A., & Sadasivunid, K. K. (2019). Introduction to 3D and 4D printing technology: State of the art and recent trends. 3D and 4D Printing of Polymer Nanocomposite Materials, 1–24.

Discovery Elbow System Surgical Technique. (2024). In Limacorporate S.p.A. www.limacorporate.com

Dowling, Norman E. (2013). Mechanical behavior of materials: Engineering methods for deformation, fracture, and fatigue. In (4th Edition, pp. 1–977). Angshuman Chakraborty.

Dunlap, J. T., Chong, A. C. M., Lucas, G. L., & Cooke, F. W. (2008). Structural properties of a novel design of composite analogue humeri models. Annals of Biomedical Engineering, 36(11), 1922–1926.

Dunning, C. E., Zarzour, Z. D. S., Patterson, S. D., Johnson, J. A., & King, G. J. W. (2001). Muscle forces and pronation stabilize the lateral ligament deficient elbow. Clinical Orthopaedics and Related Research, 388, 118–124.

Ebramzadeh, E., Sarmiento, A., McKellop, H. A., Llinas, A., & Gogan, W. (1994). The cement mantle in total hip arthroplasty. Analysis of long-term radiographic results. The Journal of Bone and Joint Surgery, 76(1), 77–87.

Egidy, C. C., Cross, M. B., Nam, D., Figgie, M. P., & Jost, B. (2019). Total elbow arthroplasty: Outcomes driving the evolution of implant design. JBJS Reviews, 7(5).

Ewald, F. C. (1995). Motion and laxity of the capitellocondylar total elbow prosthesis. The Journal of Bone and Joint Surgery, 77(9), 1462–1463.

Filho, G. M., & Galvão, M. V. (2010). POST-TRAUMATIC STIFFNESS OF THE ELBOW. Rev Bras Ortop, 45(4), 347–356.

Fornalski, S., Gupta, R., & Lee, T. Q. (2003). Anatomy and Biomechanics of the Elbow Joint. Techniques in Hand and Upper Extremity Surgery, 7(4), 168–178.

France, T., Lockwood, W., Gu, S., Tucker, N., Baldini, T., Lauder, A., & Catalano, L. W. (2024). Radiocapitellar and Ulnotrochlear Pressures Increase in a Radial Head Fracture Model: A Cadaveric Biomechanical Analysis. Journal of Bone and Joint Surgery, 106(7), 600–607.

Funk, D. A., An, K. N., Morrey, B. F., & Daube, J. R. (1987). Electromyographic analysis of muscles across the elbow joint. Journal of Orthopaedic Research, 5(4), 529–538.

Gay, D. M., Lyman, S., Do, H., Hotchkiss, R. N., Marx, R. G., & Daluiski, A. (2012). Indications and reoperation rates for total elbow arthroplasty: An analysis of trends in New York State. Journal of Bone and Joint Surgery, 94(2), 110–117.

Giannicola, G., Bullitta, G., Sacchetti, F. M., Scacchi, M., Polimanti, D., Citoni, G., & Cinotti, G. (2013). Change in quality of life and cost/utility analysis in open stage-related surgical treatment of elbow stiffness. Orthopedics, 36(7), e923-30.

Goel, V. K., Lee, I.-K., & Blair, W. F. (1989). Effect of the Coonrad elbow prosthesis on stresses in the humerus. Clinical Biomechanics, 4, 1–6.

Goldberg, S. H., Urban, R. M., Jacobs, J. J., King, G. J. W., O'Driscoll, S. W., & Cohen, M. S. (2008). Modes of wear after semiconstrained total elbow arthroplasty. Journal of Bone and Joint Surgery, 90(3), 609–619.

Goldberg, V. M., Figgie Iii, H. E., Inglis, A. E., Figgie, M. P., & York, N. (1988). Current Concepts Review Total Elbow Arthroplasty. The Journal of Bone and Joint Surgery, 70(5), 778–783.

Gordon, K. D., Pardo, R. D., Johnson, J. A., King, G. J. W., & Miller, T. A. (2004). Electromyographic activity and strength during maximum isometric pronation and supination efforts in healthy adults. Journal of Orthopaedic Research, 22(1), 208–213.

Graichen, F., Bergmann, G., & Rohlmann, A. (1999). Hip endoprosthesis for in vivo measurement of joint force and temperature. Journal of Biomechanics, 32, 1113–1117.

Gschwend, N., & Scheier, H. (1974). Elbow-Arthroplasty with the New Gsb-Prosthesis. Scandinavian Journal of Rheumatology, 3(4), 177–182.

Gschwend, N., Simmen, B. R., & Matejovsky, Z. (1996). Late complications in elbow arthroplasty. Journal of Shoulder and Elbow Surgery, 5(2), 86–96.

Halls, A. A., & Travill, A. (1964). Transmission of pressures across the elbow joint. The Anatomical Record, 150(3), 243–247.

Hastings, H., Lee, D. H., & Pietrzak, W. S. (2014). A prospective multicenter clinical study of the Discovery elbow. Journal of Shoulder and Elbow Surgery, 23(5), 95–107.

Heinlein, B., Graichen, F., Bender, A., Rohlmann, A., & Bergmann, G. (2007). Design, calibration and pre-clinical testing of an instrumented tibial tray. Journal of Biomechanics, 40(1), S4–S10.

Heller, M. O., Bergmann, G., Deuretzbacher, G., Dürselen, L., Pohl, M., Claes, L., Haas, N. P., & Duda, G. N. (2001). Musculo-skeletal loading conditions at the hip during walking and stair climbing. Journal of Biomechanics, 34(7), 883–893.

Hendricks, T. J., Chong, A. C. M., & Cusick, R. P. (2018). The Cost of Routine Follow-Up in Total Joint Arthroplasty and the Influence of These Visits on Treatment Plans. KANSAS JOURNAL of MEDICINE, 11(3), 59–66.

Herren, D. B., Ploeg, H., Hertig, D., & Klabunde, R. (2004). Modeling and Finite Element Analysis of a New Revision Implant for the Elbow. Clinical Orthopaedics and Related Research, 420, 292–297.

Hildebrand, K. A., Patterson, S. D., Regan, W. D., MacDermid, J. C., & King, G. J. W. (2000). Functional outcome of semiconstrained total elbow arthroplasty. The Journal of Bone and Joint Surgery, 82(10), 1379–1386.

Hospital of St John & St Elizabeth. (2025). Total Elbow Replacement Surgery.

Huub, J. L., Van Der Heide, M. J., De Vos, J.-M., Brinkman, D., & Eygendaal, F. H. J. (2007). Survivorship of the KUDO total elbow prosthesis-comparative study

of cemented and uncemented ulnar components: 89 cases followed for an average of 6 years. Acta Orthopaedica, 78(2), 258–262.

II, J. F., Miller, L. E., & Block, J. E. (2013). Quality of Life in Patients with Knee Osteoarthritis: A Commentary on Nonsurgical and Surgical Treatments. The Open Orthopaedics Journal, 7, 619–623.

Ikävalko, M., Tiihonen, R., Skyttä, E. T., & Belt, E. A. (2010). Long-term survival of the Souter-Strathclyde total elbow replacement in patients with rheumatoid arthritis. Journal of Bone and Joint Surgery - Series B, 92(5), 656–660.

Islam, S. U., Glover, A., MacFarlane, R. J., Mehta, N., & Waseem, M. (2020). The Anatomy and Biomechanics of the Elbow. The Open Orthopaedics Journal, 14(1), 95–99.

Janeček, M., Nový, F., Harcuba, P., Stráský, J., Trško, L., Mhaede, M., & Wagner, L. (2015). The very high cycle fatigue behaviour of Ti-6Al-4V alloy. Acta Physica Polonica A, 128(4), 497–502.

Jenkins, P. J., Watts, A. C., Norwood, T., Duckworth, A. D., Rymaszewski, L. A., & McEachan, J. E. (2013). Total elbow replacement: Outcome of 1,146 arthroplasties from the Scottish Arthroplasty Project. Acta Orthopaedica, 84(2), 119–123.

Kamineni, S., & Morrey, B. F. (2004). Prophylactic antibiotics and cemented prostheses in total elbow arthroplasty. Journal of Bone and Joint Surgery. British Volume, 86(2), 250–254.

Kaufmann, R. A., D'Auria, J. L., & Schneppendahl, J. (2019). Total Elbow Arthroplasty: Elbow Biomechanics and Failure. The Journal of Hand Surgery, 44(8), 687–692.

Key M. (2016). Anatomy of the Elbow. Musculoskeletal Key. https://musculoskeletalkey.com/anatomy-of-the-elbow/.

Khan, M. A., Serpelloni, M., & Sardini, E. (2017). Optimized power harvesting module for an autonomous sensor system implanted in a total knee prosthesis. IEEE International Instrumentation and Measurement Technology Conference, 1–6.

Khanoki Arabnejad, Sajad, & Pasini, D. (2013). Fatigue design of a mechanically biocompatible lattice for a proof-of-concept femoral stem. Journal of the Mechanical Behavior of Biomedical Materials, 22, 65–83.

Kholinne, E., Altamimi, L. A., Aldayel, A., Alsabti, R., Kim, H., Park, D., Koh, K. H., & Jeon, I. H. (2020). Primary Linked Total Elbow Arthroplasty for Acute Distal Humerus Fracture Management: A Systematic Review of Clinical Outcome. Clinics in Orthopedic Surgery, 12(4), 503–513.

Kim, H. J., Kim, J. Y., Kee, Y. M., & Rhee, Y. G. (2018). Total elbow arthroplasty under unfavourable soft tissue conditions. International Orthopaedics, 42(2), 367–374.

Kim, J. M., Mudgal, C. S., Konopka, J. F., & Jupiter, J. B. (2011). Complications of total elbow arthroplasty. The Journal of the American Academy of Orthopaedic Surgeons, 19(6), 328–339.

Kincaid, B. L., & An, K. N. (2013). Elbow joint biomechanics for preclinical evaluation of total elbow prostheses. Journal of Biomechanics, 46(14), 2331–2341.

Kincaid, B. L., Varadarajan, R., Hughes, J. S., & Morrey, B. F. (2014). Modular Connection Fatigue Testing of a Linked Semi-Constrained Total Elbow Prosthesis. Orthopedic Research Society.

King, E. A., Favre, P., Eldemerdash, A., Bischoff, J. E., Palmer, M., & Lawton, J. N. (2019). Physiological Loading of the Coonrad/Morrey, Nexel, and Discovery Elbow Systems: Evaluation by Finite Element Analysis. Journal of Hand Surgery, 44(1), 61.e1-61.e9.

King, G. J. W., Richards, R. R., & Zuckerman, J. D. (2006). Total elbow arthroplasty. Journal of the American Academy of Orthopaedic Surgeons, 14(1), 15–26.

Kirking, B., Krevolin, J., Townsend, C., Colwell, C. W., & D'Lima, D. D. (2006). A multiaxial force-sensing implantable tibial prosthesis. Journal of Biomechanics, 39(9), 1744–1751.

Klug, A., Gramlich, Y., Buckup, J., Schweigkofler, U., Hoffmann, R., & Schmidt-Horlohé, K. (2018). Trends in total elbow arthroplasty: a nationwide analysis in Germany from 2005 to 2014. International Orthopaedics, 42(4), 883–889.

Kodama, A., Mizuseki, T., & Adachi, N. (2017). Kudo type-5 total elbow arthroplasty for patients with rheumatoid arthritis: a minimum ten-year follow-up study. The Bone & Joint Journal, 99-B(6), 818–823.

Kojima, T. (1991). Force-velocity relationship of human elbow flexors in voluntary isotonic contraction under heavy loads. International Journal of Sports Medicine, 12(2), 208–213.

Krukhaug, Y., Hallan, G., Dybvik, E., Lie, S. A., & Furnes, O. N. (2018). A survivorship study of 838 total elbow replacements: a report from the Norwegian Arthroplasty Register 1994-2016. Journal of Shoulder and Elbow Surgery, 27(2), 260–269.

Kudo, H., Iwano, K., & Nishino, J. (1994). Cementless or hybrid total elbow arthroplasty with titanium-alloy implants: A study of interim clinical results and specific complications. The Journal of Arthroplasty, 9(3), 269–278.

Kuen, C., & Lambert, S. (2021). Revision total elbow replacement. Journal of Clinical Orthopaedics and Trauma, 20, 101495.

Kwaees, T. A., Singhal, R., Eygendaal, D., & Charalambous, C. P. (2019). Cementation technique for elbow arthroplasty; an international survey. Journal of Orthopaedics, 16, 459–462.

Kwak, J. M., Koh, K. H., & Jeon, I. H. (2019). Total elbow arthroplasty: Clinical outcomes, complications, and revision surgery. Clinics in Orthopedic Surgery, 11(4), 369–379.

Labek, G., Thaler, M., Janda, W., Agreiter, M., & Stöckl, B. (2011). Revision rates after total joint replacement: cumulative results from worldwide joint register datasets. The Journal of Bone and Joint Surgery, 93(3), 293–297.

Leclerc, A., & King, G. J. W. (2011). Unlinked and convertible total elbow arthroplasty. Hand Clinics, 27(2), 215–227.

Li, J. (2021). Development and validation of a finite-element musculoskeletal model incorporating a deformable contact model of the hip joint during gait. Journal of the Mechanical Behavior of Biomedical Materials, 113, 104136.

Little, C. P., Graham, A. J., & Carr, A. J. (2005). Total elbow arthroplasty. Journal of Bone and Joint Surgery, 87(4), 437–444.

Liu-Bryan, R., & Terkeltaub, R. (2015). Emerging regulators of the inflammatory process in osteoarthritis. Nature Reviews Rheumatology, 11(1), 35–44.

lo, D., & Lipman, J. (2009). Retrieval and Finite Element Analysis of Coonrad-Morrey Elbow Replacements. 55th Annual Meeting of the Orthopaedic Research Society.

Maheshwari, R., Vaziri, S., & Helm, R. H. (2012). Total elbow replacement with the Coonrad-Morrey prosthesis: our medium to long-term results. Annals of The Royal College of Surgeons of England, 94(3), 189.

Malone, A. A., Taylor, A. J. N., & Fyfe, I. S. (2004). Successful outcome of the Souter-Strathclyde elbow arthroplasty. Journal of Shoulder and Elbow Surgery, 13(5), 548–554.

Maxian, T. A., Brown, T. D., Pedersen, D. R., & Callaghan, J. J. (1996). Adaptiive finite element modeling of long-term polyethylene wear in total hip arthroplasty. Journal of Orthopaedic Research, 14(4), 668–675.

Meijering, D., Boerboom, A. L., Gerritsma, C. L. E., de Vries, A. J., Vegter, R. J. K., Bulstra, S. K., Eygendaal, D., & Stevens, M. (2022). Mid-term results of the Latitude primary total elbow arthroplasty. Journal of Shoulder and Elbow Surgery, 31(2), 382–390.

Mellon, S. J., Grammatopoulos, G., Andersen, M. S., Pandit, H. G., Gill, H. S., & Murray, D. W. (2015). Optimal acetabular component orientation estimated using

edge-loading and impingement risk in patients with metal-on-metal hip resurfacing arthroplasty. Journal of Biomechanics, 48(2), 318–323.

Mori, T., Kudo, H., Iwano, K., & Juji, T. (2006). Kudo type-5 total elbow arthroplasty in mutilating rheumatoid arthritis. A 5- to 11-year follow-up. Journal of Bone and Joint Surgery - Series B, 88(7), 920–924.

Morrey, B. F. (2017). Morrey's The Elbow and Its Disorders (5th Edition). Elsevier.

Morrey, B. F., & An, K. N. (1983). Articular and ligamentous contributions to the stability of the elbow joint. The American Journal of Sports Medicine, 11(5), 315–319.

Morrey, B. F., An, K. N., & Chao, E. Y. S. (1981). Functional evaluation of the elbow joint. Journal of Biomechanics, 14(10), 659–670.

Morrey, B. F., An, K. N., & Chao, E. Y. (1998). Functional evaluation of the elbow. In B. F. Morrey (Ed.), The elbow and its disorders (3rd ed). Philadelphia, PA: W. B. Saunders.

Morrey, B. F., An, K. N., & Zobitz, M. E. (2000). Biomechanics of the Elbow. In The Elbow and its Disorders: Fourth Edition. Elsevier.

Morrey, B. F., Askew, L. J., An, K. N., & Chao, E. Y. (1978). A Biomechanical Study of Normal Functional Elbow Motion. The Journal of Bone and Joint Surgery, 4, 90–91.

Morrey, B. F., Bryan, R. S., Dobyns, J. H., & Linscheid, R. L. (1981). Total Elbow Arthroplasty A Five-Year Experience at the Mayo Clinic. The Journal of Bone and Joint Surgery, 63(7), 1050–1063.

Morrey, B. F., Glauser, S. J., Westreich, A., & An, K. N. (1993). In vitro stability of an unconstrained total elbow prosthesis. Influence of axial loading and joint flexion angle. The Journal of Arthroplasty, 8(3), 291–298.

Morris, D. L. J., Walstow, K., Pitt, L., Morgan, M., Tambe, A. A., Clark, D. I., Cresswell, T., & Espag, M. P. (2024). Discovery Elbow System arthroplasty polyethylene bearing exchange: outcomes and experience. Clinics in Shoulder and Elbow, 27(1), 18–25.

Morton, D. A., Foreman, K. B., & Albertine, K. H. (2011). The Big Picture Gross Anatomy; McGraw-Hill.

Munting, E., Smitz, R., Sante, N. Van, Nagant De Deuxchaisnes, C., Vincent, A., & Devogelaer, J.-E. (1997). Effect of a Stemless Femoral Implant for Total Hip Arthroplasty on the Bone Mineral Density of the Proximal Femur A Prospective Longitudinal Study. The Journal of Arthroplasty, 12(4), 373–379.

Murray, I. A., & Johnson, G. R. (2004). A study of the external forces and moments at the shoulder and elbow while performing everyday tasks. Clinical Biomechanics, 19(6), 586–594.

Naito, A., Sun, Y. J., Yajima, M., Fukamachi, H., & Ushikoshi, K. (1998). Electromyographic Study of the Elbow Flexors and Extensors in a Motion of Forearm Pronation/Supination while Maintaining Elbow Flexion in Humans. The Tohoku Journal of Experimental Medicine, 186(4), 267–277.

National Joint Registry (NJR). (2023). 20th Annual Report 2023: National Joint Registry for England, Wales, Northern Ireland, and the Isle of Man.

National Joint Registry (NJR). (2025). Elbows: Primary procedures – elbow components (Humeral). National Joint Registry for England, Wales, Northern Ireland, and the Isle of Man.

Neumann, Donald A. (2016). Kinesiology of the Musculoskeletal System Foundations for Rehabilitation (3rd Edition). Elsevier.

Nguyen, M. P., Chandran, S. E., Okoroha, K. R., Orandi, A., & Wright, T. W. (2023). Thirty-day complications following total elbow arthroplasty in academic centres. JSES International, 7, 451–456.

Nicol, A. C., Berme, N., & PaulJ.P. (1977). A biomechanical analysis of elbow joint function. Conference on Joint Replacement in the Upper Limb, Institution of Mechanical Engineers, London, 33, 45–51.

Nishida, K., Hashizume, K., Nasu, Y., Kishimoto, M., Ozaki, T., & Inoue, H. (2014). A 5-22-year follow-up study of stemmed alumina ceramic total elbow arthroplasties with cement fixation for patients with rheumatoid arthritis. Journal of Orthopaedic Science, 19(1), 55–63.

O'Daly, B. J., Harty, J. A., O'Malley, N., Killeen, R., McDonnell, T. J., & Quinlan, W. R. (2008). Bilateral olecranon fracture as first presentation of sarcoidosis: Case report and review of the literature. Journal of Shoulder and Elbow Surgery, 17(4), 1–5.

O'Driscoll, S. W., An, K. N., Korinek, S., & Morrey, B. F. (1992). Kinematics of semi-constrained total elbow arthroplasty. Journal of Bone and Joint Surgery - Series B, 74(2), 297–299.

O'Sullivan, L. W., & Gallwey, T. J. (2002). Upper-limb surface electro-myography at maximum supination and pronation torques: the effect of elbow and forearm angle. Journal of Electromyography and Kinesiology, 12(4), 275–285.

Park, S. E., Kim, J. Y., Cho, S. W., Rhee, S. K., & Kwon, S. Y. (2013). Complications and revision rate compared by type of total elbow arthroplasty. Journal of Shoulder and Elbow Surgery, 22(8), 1121–1127.

Pegg, E. C., Murray, D. W., Pandit, H. G., O'Connor, J. J., & Gill, H. S. (2013). Fracture of mobile unicompartmental knee bearings: A parametric finite element study. Proceedings of the Institution of Mechanical Engineers, Part H: Journal of Engineering in Medicine, 227(11), 1213–1223.

Peters, J. O., Lütjering, G., Nalla, R. K., Altenberger, I., & Ritchie, R. O. (2002). High-cycle fatigue of beta titanium alloys. Proceedings of the Eighth International Fatigue Congress, Stockholm, Sweden, 1–8.

Plaschke, H. C., Thillemann, T. M., Brorson, S., & Olsen, B. S. (2015). Outcome after total elbow arthroplasty: A retrospective study of 167 procedures performed from 1981 to 2008. Journal of Shoulder and Elbow Surgery, 24(12), 1982–1990.

Popoola, O. O., Kincaid, B. L., Mimnaugh, K., & Marqueling, M. (2017). In vitro wear of ultrahigh-molecular-weight polyethylene and vitamin E blended highly cross-linked polyethylene in linked, semiconstrained total elbow replacement prostheses. Journal of Shoulder and Elbow Surgery, 26(5), 846–854.

Prevo, S. B., Tenn, & Nashville. (1954). Prosthetic Elbow Joint. United States Patent Office.

Pritchard RW. (1983). Anatomic surface elbow arthroplasty. A preliminary report. Clinical Orthopaedics and Related Research, 179, 223–230.

Prkic, A., De Vos, M. J., Wagener, M. L., The, B., & Eygendaal, D. (2017). Total Elbow Arthroplasty: Why and How. JBJS ESSENTIAL SURGICAL TECHNIQUES, 7(1), 1–7.

Prkić, A., Van Bergen, C. J., The, B., & Eygendaal, D. (2016). Total elbow arthroplasty is moving forward: Review on past, present and future. World Journal of Orthopedics, 7(1), 44–49.

Prkic, A., Welsink, C., The, B., van den Bekerom, M. P. J., & Eygendaal, D. (2017). Why does total elbow arthroplasty fail today? A systematic review of recent literature. Archives of Orthopaedic and Trauma Surgery, 137(6), 761–769.

Quenneville, C. E., Austman, R. L., King, G. J. W., Johnson, J. A., & Dunning, C. E. (2008). Role of an Anterior Flange on Cortical Strains Through the Distal Humerus After Total Elbow Arthroplasty With a Latitude Implant. Journal of Hand Surgery, 33(6), 927–931.

Quinn, J., Mcfadden, R., Chan, C.-W., & Carson, L. (2020). Titanium for Orthopedic Applications: An Overview of Surface Modification to Improve Biocompatibility and Prevent Bacterial Biofilm Formation. IScience, 23, 101745.

Reimeringer, M., Nuño, N., Desmarais-Trépanier, C., Lavigne, M., & Vendittoli, P. A. (2013). The influence of uncemented femoral stem length and design on its primary stability: A finite element analysis. Computer Methods in Biomechanics and Biomedical Engineering, 16(11), 1221–1231.

Rosenfeld, S. R., & Anzel, S. H. (1982). Evaluation of the pritchard total elbow arthroplasty. Journal of Orthopedics, 5(6), 713–719.

Sabo, M. T., Schneeberger, A. G., & Morrey, B. F. (2002). Aseptic loosening of the humeral component in elbow arthroplasty. Journal of Bone and Joint Surgery. American Volume, 84(10), 1779–1784.

Sanchez-Sotelo, J. (2011). Total elbow arthroplasty. The Journal of Bone and Joint Surgery. American Volume, 93(14), 1437–1448.

Sanchez-Sotelo, J. (2017). Primary elbow arthroplasty: problems and solutions. Shoulder and Elbow, 9(1), 61–70.

Schneeberger, A. G., Hertel, R., & Gerber, C. (2000). Total elbow replacement with the GSB III prosthesis. Journal of Shoulder and Elbow Surgery, 9(2), 135–139.

Schneeberger, A. G., King, G. J. W., Song, S. W., O'Driscoll, S. W., Morrey, B. F., & An, K. N. (2000). Kinematics and laxity of the Souter-Strathclyde total elbow prosthesis. Journal of Shoulder and Elbow Surgery, 9(2), 127–134.

Schoch, B., Wong, J., Abboud, J., Lazarus, M., Getz, C., & Ramsey, M. (2017). Results of Total Elbow Arthroplasty in Patients Less Than 50 Years Old. The Journal of Hand Surgery, 42(10), 797–802.

Schwab, G., Bennett JB, Woods GW, & Tullos HS. (1980). Biomechanics of elbow instability: the role of the medial collateral ligament. Clinical Orthopaedics and Related Research, 146, 42–52.

Shishani, Y., & Gobezie, R. (2017). Does a short-stemmed humeral implant really make a difference? Seminars in Arthroplasty JSES, 28(1), 13–17.

Siala, M., Laumonerie, P., Hedjoudje, A., Delclaux, S., Bonnevialle, N., & Mansat, P. (2020). Outcomes of semiconstrained total elbow arthroplasty performed for arthritis in patients under 55 years old. Journal of Shoulder and Elbow Surgery, 29, 859–866.

Singh, J. A., & Ramachandran, R. (2016). Sex differences in characteristics, utilization, and outcomes of patient undergoing total elbow arthroplasty: a study of the US nationwide inpatient sample. Clinical Rheumatology, 35(3), 723–731.

Sjöden, G. O. J., Lundberg, A., & Blomgren, G. A. (1995). Late results of the Souter-Strathclyde total elbow prosthesis in rheumatoid arthritis. 6/19 implants loose after 5 years. Acta Orthopaedica Scandinavica, 66(5), 391–394.

Taylor, M., et al. (2004). An instrumented hip implant for in vivo measurement of forces and moments. Journal of Biomechanics, 37(4), 459–466.

Taylor, M., et al. (2011). An instrumented knee implant for in vivo measurement of forces and moments. Journal of Biomechanics, 44(6), 1087–1093.

Taylor, S. J. G. , Gorjon, J. , & Gorjon, A. (2000). Development of an Instrumented Tibial Tray for Knee Force Measurement In Vivo. Proceedings of the 12th Conference of the European Society on Biomechanics, 0–110.

Taylor, S. J. G. , Meswania, J. M. , Rodríguez-Arias, J. , Calle, R. , Bayley, I. L. , & Blunn, G. W. (2004). An Instrumented Implant and Calibration Technique for

Measurement of Glenohumeral Joint Forces In Vivo. Proceedings of the 14th Conference of the European Society on Biomechanics.

Taylor, S. J. G. , Perry, J. S. , Adler, J. R. , & Walker, P. S. (1994). The Telemetry of Forces In Vivo in Massive Orthopaedic Implants in Relation to Loosening. Trans. Annu. Meet. - Orthop. Res. Soc., 19–809.

Taylor, S. J. G., Perry, J. S., Meswania, J. M., Donaldson, N., Walker, P. S., & Cannon, S. R. (1997). Telemetry of forces from proximal femoral replacements and relevance to fixation. Journal of Biomechanics, 30(3), 225–234.

Taylor, S. J. G., & Walker, P. S. (2001). Forces and moments telemetered from two distal femoral replacements during various activities. Journal of Biomechanics, 34(7), 839–848.

Taylor, S. J. G., Walker, P. S., Perry, J. S., Cannon, S. R., & Woledge, R. (1998). The forces in the distal femur and the knee during walking and other activities measured by telemetry. Journal of Arthroplasty, 13(4), 428–437.

Tiusanen, R. E., Tiusanen, H. T., Saltychev, M., & Sarantsin, P. M. (2021).

Discovery elbow system arthroplasty: results of 10-year follow-up. European Journal of Orthopaedic Surgery and Traumatology, 31(6), 1207–1213.

Toulemonde, J., Ancelin, D., Azoulay, V., Bonnevialle, N., Rongières, M., & Mansat, P. (2016). Complications and revisions after semi-constrained total elbow arthroplasty: a mono-centre analysis of one hundred cases. International Orthopaedics, 40(1), 73–80.

Trail, I. A., Nuttall, D., Stanley, J. K., & Eldridge, J. D. (1999). A long-term survivorship of the Souter-Strathclyde arthroplasty. Journal of Bone and Joint Surgery. British Volume, 81(1), 80–84.

Trail, I. A., & Nuttall, D. (2002). The results of 100 Souter–Strathclyde total elbow replacements. Journal of Shoulder and Elbow Surgery, 11(6), 578–584.

Trail, I. A., Powell, J., Noble, J., & Porter, M. L. (2002). Comparison of survivorship between standard and long-stemmed Souter-Strathclyde total elbow arthroplasty. Journal of Shoulder and Elbow Surgery, 11(4), 373–375.

Triplet, J. J., Kurowicki, J., Momoh, E., Law, T. Y., Niedzielak, T., & Levy, J. C. (2016). Trends in total elbow arthroplasty in the Medicare population: a nationwide study of records from 2005 to 2012. Journal of Shoulder and Elbow Surgery, 25(11),

Valstar, E. R., Garling, E. H., & Rozing, P. M. (2002). Micromotion of the Souter-Strathclyde total elbow prosthesis in patients with rheumatoid arthritis: 21 Elbows followed for 2 years. Acta Orthopaedica Scandinavica, 73(3), 264–272.

van der Lugt, J. C., Rozing, P. M., & van Horn, J. R. (2010). A biomechanical study of torsional fatigue and fixation in the Souter-Strathclyde total elbow prosthesis. Journal of Shoulder and Elbow Surgery, 19(1), 23–29.

van der Lugt, J. C., Rozing, P. M., & van Horn, J. R. (2017). Design considerations in total elbow arthroplasty: A biomechanical perspective. Journal of Shoulder and Elbow Surgery, 26(2), 214–221.

Varadarajan, R., & Kincaid, B. L. (2019). Development and Validation of a Method for Preclinical Durability Evaluation of Linked Semiconstrained Total Elbow Replacement Prostheses. Journal of Shoulder and Elbow Arthroplasty, 3, 1–11.

Varadarajan Ravikumar, & Bernard Morrey. (2014). Fatigue Strength Evaluation of Total Humeral and Ulnar Stems. Orthopedic Research Society 2014 Annual Meeting, 1–5.

Venable, C. S. (1952). An Elbow and an Elbow Prosthesis: Case of Complete Loss of the Lower Third of The Humerus. American Journal of Surgery, 271–275.

Voloshin, I., Schippert, D. W., Kakar, S., Kaye, E. K., & Morrey, B. F. (2011). Complications of total elbow replacement: A systematic review. Journal of Shoulder and Elbow Surgery, 20(1), 158–168.

Wang, J., Chu, J., Song, J., & Li, Z. (2024). The application of implantable sensors in the musculoskeletal system: A review. Frontiers in Bioengineering and Biotechnology, 12, Article 1270237.

Wasserman, B., Kashanchi, M., Wong, K., Patel, S., & Garrigues, G. E. (2024). Short-term complications and outcomes after revision total elbow arthroplasty: An analysis of the NSQIP database. Journal of Shoulder and Elbow Surgery, 33(2), 343–350.

Węglowski, M. S., Błacha, S., & Phillips, A. (2016). Electron beam welding - Techniques and trends - Review. Vacuum, 130, 72–92.

Weiss, R. J., Ehlin, A., Montgomery, S. M., Wick, M. C., Stark, A., & Wretenberg, P. (2008). Decrease of RA-related orthopaedic surgery of the upper limbs between 1998 and 2004: data from 54 579 Swedish RA inpatients. Rheumatology, 47(4), 491–494.

Welsink, C. L., Lambers, K. T. A., Van Deurzen, D. F. P., Eygendaal, D., & Van Den Bekerom, M. P. J. (2017). Total Elbow Arthroplasty: A Systematic Review. JBJS Reviews, 5(7), 1–4.

Westerhoff, P., Graichen, F., Bender, A., Rohlmann, A., & Bergmann, G. (2009). An instrumented implant for in vivo measurement of contact forces and contact moments in the shoulder joint. Medical Engineering and Physics, 31(2), 207–213.

Willing, R., & Kim, I. Y. (2009). A holistic numerical model to predict strain hardening and damage of UHMWPE under multiple total knee replacement

kinematics and experimental validation. Journal of Biomechanics, 42(15), 2520–2527.

Willing, R., King, G. J. W., & Johnson, J. A. (2014). The effect of implant design of linked total elbow arthroplasty on stability and stress: a finite element analysis. Computer Methods in Biomechanics and Biomedical Engineering, 17(11), 1165–1172.

Wright, T. W., & Hastings, H. (2005). Total elbow arthroplasty failure due to overuse, C-ring failure, and/or bushing wear. Journal of Shoulder and Elbow Surgery, 14(1), 65–72.

Wright, T. W., Wong, A. M., & Jaffe, R. (2000). Functional outcome comparison of semiconstrained and unconstrained total elbow arthroplasties. Journal of Shoulder and Elbow Surgery, 9(6), 524–531.

Xie, J. (2013). Laser hermetic welding of implantable medical devices. In Joining and Assembly of Medical Materials and Devices (pp. 211–235). Elsevier Ltd.

Zhang, D., & Chen, N. (2019). Total Elbow Arthroplasty. Journal of Hand Surgery, 44(6), 487–495.

Zhang, X., Fouzan Iftekar, S., Aabid, A., Amir, A., Baig, M., & My, A. A.). (2023). Advancements and Limitations in 3D Printing Materials and Technologies: A Critical Review. Polymers, 15, 2519.

Zhao, J., Xu, C., Liu, L., Wang, Q., & Chen, H. (2023). Complications of total elbow arthroplasty in rheumatoid arthritis patients: A meta-analysis. Journal of Orthopaedic Surgery and Research, 18(1), 543.

Zhou, H., Orvets, N. D., Merlin, G., Shaw, J., Dines, J. S., Price, M. D., Eichinger, J. K., & Li, X. (2016). Total Elbow Arthroplasty in the United States: Evaluation of Cost, Patient Demographics, and Complication Rates. Orthopedic Reviews, 8(1), 43–46.